UNIVERSITY OF CALIFORNIA,
IRVINE

Leveraging Large, Disparate Datasets to Precisely Measure the Masses of Nearby Exoplanets

DISSERTATION

submitted in partial satisfaction of the requirements
for the degree of

DOCTOR OF PHILOSOPHY

in Physics

by

Corey Beard

Dissertation Committee:
Professor Paul Robertson, Chair
Professor Steph Sallum
Professor Aomawa L. Shields

2024

TABLE OF CONTENTS

LIST OF FIGURES

LIST OF TABLES

ACKNOWLEDGMENTS

It has been a long and fulfilling road at UC Irvine. The number of people who contributed to my success is quite large, and this thesis would likely be a hundred pages longer if I committed to thanking all of them, and recognizing their contributions. Instead, here, I will give a brief acknowledgement to those of special importance, which is less than they deserve.

First, I want to thank my parents, Mike and Carolyn Beard. You two have always supported all of my endeavors, no matter how much my path veered from your own, and you seem to take genuine pride in everything I do. For this I thank you, it would have been immeasurably more difficult without your support.

Next, I would like to think my twin brother, Bryan Beard. It goes without saying, but here I say it, that my life would be completely different without you. We were born together, grew up together, and you are an endless font of support. Truly, few can understand the depth of our relationship. I cannot imagine what the world would be like if I didn't have you to share it with, and I hope I never have to imagine, or experience it. My world would be a much, much darker place without you in it, and I doubt I would be half the person I was without you.

I want to thank Kevin Beard, my older brother, as well. Our relationship has long been complicated, as you would no doubt concede, but it has had a significant impact on my life. I wish nothing but the best for you, and I hope you know that I think your decisions, as you much as you may regret some of them, have had a huge hand in shaping my own path, and for that I am grateful.

So many other members of my family deserve praise. The Taylors, you have always been friends and supporters. Dirk, Karen, Brittany, Alyssa, and Alex: you all mean a great deal to me, and I hope you know that. Aunt Kathy, and Grandpa–Bob Cardwell–you too deserve acknowledgement. You have always been incredible sources of support. I thank you for all of it.

Family aside, I have so many wonderful friends to acknowledge. Again, I do not have enough time to sing all of your praises, so forgive me if each acknowledgement is short: it is less than you deserve.

Max, Connor, Ryan, you have all been dear friends for a long time. I wish you all the best, and I thank you for your friendship. Adam, you especially deserve thanks: aside from Bryan, you are probably the person I feel most kinship with. You are a wonderful person who has had a huge impact on my life and values. I hope we continue our friendship, and our Sunday tradition, for as long as we can.

Zane Karl, you and Cristina of course deserve recognition. I was lucky to make such a good friend in my very first year, and very first class, at UCLA. I hope I know you for a long time.

And now–since I have been going, roughly, chronologically–I come to my dear friends at UC

Irvine. Truly my graduate experience here has been life-changing. Our small group of 21 graduate students in physics has diminished somewhat over the years, some leaving, and others growing out of touch. But I am still honored to have been a part of the group.

A special thank you to Gabe Player, for all the fun we had at the gym, playing D&D, and at Mammoth. Alex Lazar deserves no less thanks, as my roommate and close friend, I wish you all success in your future endeavors, and I hope we can continue our friendship for many years yet. Olivia Dalager, you too deserve a shout out: our TV nights have long been a blast, and I hope they keep going strong.

Now of course I must thank my research group, and I didn't forget you Jack Lubin, I simply thought it would make the most sense to put you here! What can I say? We were a duo from the get-go, and yes–you were Paul's first student–but together we established the culture, creating (I argue) the best research group on campus. You were a wonderful partner in crime, and I hope very much that you continue to share your... let's say, colorful opinions, for the rest of my days. Rae Holcomb, of course, you deserve a special shout-out. While you didn't come around until a little later, you quickly became a foundational member of our group. Beyond that, you were an amazing friend to me, and I have many fond memories of our video-game sessions, D&D (of course), and Stormlight Archive cooking sessions. I know we'll continue to be friends for a long time. To the rest of Paul's research group, thank you. Jacob, Te, Pranav, Claire, and whoever else comes: you all will succeed, I'm certain, and it was wonderful knowing all of you. I hope I know you for a long time yet. To any future or prospective graduate students, good luck, if you are in Paul's group, expect to do well.

Which takes me to the last acknowledgement, but certainly not least. Paul Robertson, thank you. I have learned in graduate school, that nothing shapes one's experience more than their graduate advisor: and I have had an absolutely wonderful time at UCI, in no small part thanks to you. It is no exaggeration to say that I may not have graduated if not for your support and knowledge, and that you are truly one of the most wonderful people I have met in my life. You have already done many great things, and I know you will continue to do many more. Thank you.

Chapter 2 of this dissertation is a reprint of the material (excluding Foreward) as it appears in Beard, C., Robertson, P., Kanodia, S. et al. TOI-1696 and TOI-2136: Constraining the Masses of Two Mini-Neptunes with the Habitable-Zone Planet Finder, AJ, Volume 163, Issue 6, id.286, 20 pp, 2022. This work is used with permission from The Astronomical Journal and IOP Publishing under their authors' rights policies. The co-authors listed in this publication are, as they appear in the paper: Robertson, Paul, Kanodia, Shubham, Libby-Roberts, Jessica, Canas, Caleb I., Gupta, Arvind F., Holcomb, Rae, Jones, Sinclaire, Kobulnicky, Henry A., Lin, Andrea S. J., Lubin, Jack, Maney, Marissa, Parker, Brock A., Stefansson, Gudmundur, Cochran, William D., Endl, Michael, Hebb, Leslie, Mahadevan, Suvrath, Wisniewski, John, Bender, Chad F., Diddams, Scott A., Everett, Mark, Fredrick, Connor, Halverson, Samuel, Hearty, Fred, Metcalf, Andrew J., Monson, Andrew, Ninan, Joe P., Roy, Arpita, Schutte, Maria, Schwab, Christian, Terrien, Ryan C.

Chapter 3 of this dissertation is a reprint of the material (excluding Foreward) as it appears in Beard, C., Robertson, P., Kanodia, S. et al. GJ 3929: High-precision Photometric and Doppler Characterization of an Exo-Venus and Its Hot, Mini-Neptune-mass Companion, ApJ, Volume 936, Issue 1, id.55, 19 pp., 2022. This work is used with permission from The Astrophysical Journal and IOP Publishing under their authors' rights policies. The co-authors listed in this publication are, as they appear in the paper: Robertson, Paul, Kanodia, Shubham, Lubin, Jack, Canas, Caleb I., Gupta, Arvind F., Holcomb, Rae, Jones, Sinclaire, Libby-Roberts, Jessica E., Lin, Andrea S. J., Mahadevan, Suvrath, Stefansson, Gudmundur, Bender, Chad F., Blake, Cullen H., Cochran, William D., Endl, Michael, Everett, Mark, Ford, Eric B., Fredrick, Connor, Halverson, Samuel, Hebb, Leslie, Li, Dan, Logsdon, Sarah E., Luhn, Jacob, McElwain, Michael W., Metcalf, Andrew J., Ninan, Joe P., Rajagopal, Jayadev, Roy, Arpita, Schutte, Maria, Schwab, Christian, Terrien, Ryan C., Wisniewski, John, Wright, Jason T.

Chapter 4 of this dissertation is a reprint of the material (excluding Foreward) as it appears in Beard, C., Robertson, P., Dai, F. et al. The TESS-Keck Survey. XVII. Precise Mass Measurements in a Young, High-multiplicity Transiting Planet System Using Radial Velocities and Transit Timing Variations, AJ, Volume 167, Issue 2, id.70, 24 pp., 2024. This work is used with permission from The Astronomical Journal and IOP Publishing under their authors' rights policies. The co-authors listed in this publication are, as they appear in the paper: Robertson, Paul, Dai, Fei, Holcomb, Rae, Lubin, Jack, Akana Murphy, Joseph M., Batalha, Natalie M., Blunt, Sarah, Crossfield, Ian ; Dressing, Courtney, Fulton, Benjamin, Howard, Andrew W., Huber, Dan, Isaacson, Howard, Kane, Stephen R., Nowak, Grzegorz, Petigura, Erik A., Roy, Arpita, Rubenzahl, Ryan A., Weiss, Lauren M., Barrena, Rafael ; Behmard, Aida, Brinkman, Casey L., Carleo, Ilaria ; Chontos, Ashley, Dalba, Paul A., Fetherolf, Tara, Giacalone, Steven, Hill, Michelle L., Kawauchi, Kiyoe ; Korth, Judith, Luque, Rafael, MacDougall, Mason G., Mayo, Andrew W., Močnik, Teo, Morello, Giuseppe, Murgas, Felipe, Orell-Miquel, Jaume, Palle, Enric, Polanski, Alex S., Rice, Malena, Scarsdale, Nicholas, Tyler, Dakotah, Van Zandt, Judah.

This work was partially supported by NASA grant No. 80NSSC22K0120 to support Guest Investigator programs for TESS Cycle 4.

This work was partially support by the Future Investigators in NASA Earth and Space Science and Technology (FINESST) program grant No. 80NSSC22K1754.

VITA

Corey Beard

EDUCATION

Doctor of Philosophy in Physics — **2024**
University of California, Irvine — *Irvine, CA*

Master of Science in Physics — **2022**
University of California, Irvine — *Irivne, CA*

Bachelor of Science in Physics — **2017**
University of California, Los Angeles — *Los Angeles, CA*

RESEARCH EXPERIENCE

Machine Learning Intern — **2024–Present**
Design West Technologies — *Tustin, California*

Graduate Student Researcher — **2019–2024**
University of California, Irvine — *Irvine, California*

Data Science Intern — **2022**
Lawrence Livermore National Laboratory — *Livermore, California*

REFEREED JOURNAL PUBLICATIONS

First Author Publications

The TESS-Keck Survey. XVII. Precise Mass Measurements in a Young, High-multiplicity Transiting Planet System Using Radial Velocities and Transit Timing Variations **2024**
The Astronomical Journal

GJ 3929: High-precision Photometric and Doppler Characterization of an Exo-Venus and Its Hot, Mini-Neptune-mass Companion **2022**
The Astrophysical Journal

TOI-1696 and TOI-2136: Constraining the Masses of Two Mini-Neptunes with the Habitable-Zone Planet Finder **2022**
The Astronomical Journal

All Publications

Planet Hunters TESS. V. A Planetary System Around a Binary Star, Including a Mini-Neptune in the Habitable Zone **2024**
The Astronomical Journal

A Tale of Two Peas in a Pod: The Kepler-323 and Kepler-104 Systems **2024**
The Astronomical Journal

The TESS-Keck Survey. XII. A Dense 1.8 $R_\oplus$ Ultra-short-period Planet Possibly Clinging to a High-mean-molecular-weight Atmosphere after the First Gigayear **2024**
The Astronomical Journal

Investigating the Atmospheric Mass Loss of the Kepler-105 Planets Straddling the Radius Gap **2024**
The Astronomical Journal

TESS giants transiting giants V - two hot Jupiters orbiting red giant hosts **2024**
Monthly Notices of the Royal Astronomical Society

TOI-1670 c, a 40 day Orbital Period Warm Jupiter in a Compact System, Is Well Aligned **2023**
The Astrophysical Journal Letters

The TESS-Keck Survey. XVI. Mass Measurements for 12 Planets in Eight Systems **2023**
The Astronomical Journal

The Unusual M-dwarf Warm Jupiter TOI-1899 b: Refinement of Orbital and Planetary Parameters **2023**
The Astronomical Journal

Overfitting Affects the Reliability of Radial Velocity Mass Estimates of the V1298 Tau Planets **2023**
The Astronomical Journal

A Mini-Neptune Orbiting the Metal-poor K Dwarf BD+29 2654 **2023**
The Astronomical Journal

The TESS-Keck Survey. XV. Precise Properties of 108 TESS Planets and Their Host Stars **2023**
The Astronomical Journal

TOI-3984 A b and TOI-5293 A b: Two Temperate Gas Giants Transiting Mid-M Dwarfs in Wide Binary Systems **2023**
The Astronomical Journal

A close-in giant planet escapes engulfment by its star **2023**
Nature

The TESS Grand Unified Hot Jupiter Survey. II. Twenty New Giant Planets **2023**
The Astrophysical Journal Supplement

TOI-561 b: A Low-density Ultra-short-period "Rocky" Planet around a Metal-poor Star **2023**
The Astronomical Journal

TESS-Keck Survey. XIV. Two Giant Exoplanets from the Distant Giants Survey **2023**
The Astronomical Journal

TOI-1136 is a Young, Coplanar, Aligned Planetary System in a Pristine Resonant Chain **2023**
The Astronomical Journal

TOI-3714 b and TOI-3629 b: Two Gas Giants Transiting M Dwarfs Confirmed with the Habitable-zone Planet Finder and NEID **2022**
The Astronomical Journal

The TESS-Keck Survey: Science Goals and Target Selection **2022**
The Astronomical Journal

The TESS-Keck Survey. XI. Mass Measurements for Four Transiting Sub-Neptunes Orbiting K Dwarf TOI-1246 **2022**
The Astronomical Journal

A Close-in Puffy Neptune with Hidden Friends: The Enigma of TOI 620 **2022**
The Astronomical Journal

Rotational Modulation of Spectroscopic Zeeman Signatures in Low-mass Stars **2022**
The Astrophysical Journal Letters

TESS Giants Transiting Giants. II. The Hottest Jupiters Orbiting Evolved Stars **2022**
The Astronomical Journal

The Aligned Orbit of WASP-148b, the Only Known Hot Jupiter with a nearby Warm Jupiter Companion, from NEID and HIRES **2022**
The Astrophysical Journal Letters

TESS-Keck Survey. IX. Masses of Three Sub-Neptunes Orbiting HD 191939 and the Discovery of a Warm Jovian plus a Distant Substellar Companion **2022**
The Astronomical Journal

An Eccentric Brown Dwarf Eclipsing an M dwarf **2022**
The Astronomical Journal

The TESS-Keck Survey. VIII. Confirmation of a Transiting Giant Planet on an Eccentric 261 Day Orbit with the Automated Planet Finder Telescope **2022**
The Astronomical Journal

TOI 560 : Two Transiting Planets Orbiting a K Dwarf Validated with iSHELL, PFS and HIRES RVs **2021**
The Astronomical Journal

The TESS-Keck Survey. VI. Two Eccentric Sub-Neptunes Orbiting HIP-97166 **2021**
The Astronomical Journal

TESS-Keck Survey. V. Twin Sub-Neptunes Transiting the Nearby G Star HD 63935 **2021**
The Astronomical Journal

SOLES I: The Spin-Orbit Alignment of K2-140 b **2021**
The Astronomical Journal

TOI-532b: The Habitable-zone Planet Finder confirms a Large Super Neptune in the Neptune Desert orbiting a metal-rich M-dwarf host **2021**
The Astronomical Journal

TKS X: Confirmation of TOI-1444b and a Comparative Analysis of the Ultra-short-period Planets with Hot Neptunes **2021**
The Astronomical Journal

Stellar Activity Manifesting at a One-year Alias Explains Barnard b as a False Positive **2021**
The Astronomical Journal

The TESS-Keck Survey. IV. A Retrograde, Polar Orbit for the Ultra-low-density, Hot Super-Neptune WASP-107b **2021**
The Astronomical Journal

The TESS-Keck Survey. II. An Ultra-short-period Rocky Planet and Its Siblings Transiting the Galactic Thick-disk Star TOI-561 **2021**
The Astronomical Journal

The TESS-Keck Survey. III. A Stellar Obliquity Measurement of TOI-1726 c **2020**
The Astronomical Journal

π Earth: A 3.14 day Earth-sized Planet from K2's Kitchen Served Warm by the SPECULOOS Team **2020**
The Astronomical Journal

A Warm Jupiter Transiting an M Dwarf: A TESS Single-transit Event Confirmed with the Habitable-zone Planet Finder **2020**
The Astronomical Journal

The Multiplanet System TOI-421 **2020**
The Astronomical Journal

Persistent Starspot Signals on M Dwarfs: Multiwavelength Doppler Observations with the Habitable-zone Planet Finder and Keck/HIRES **2020**
The Astrophysical Journal

TOI-1235 b: A Keystone Super-Earth for Testing Radius Valley Emergence Models around Early M Dwarfs **2020**
The Astronomical Journal

The TESS-Keck Survey. I. A Warm Sub-Saturn-mass Planet and a Caution about Stray Light in TESS Cameras **2020**
The Astronomical Journal

A Sub-Neptune-sized Planet Transiting the M2.5 Dwarf G 9-40: Validation with the Habitable-zone Planet Finder **2020**
The Astronomical Journal

ABSTRACT OF THE DISSERTATION

Leveraging Large, Disparate Datasets to Precisely Measure the Masses of Nearby Exoplanets

By

Corey Beard

Doctor of Philosophy in Physics

University of California, Irvine, 2024

Professor Paul Robertson, Chair

The field of exoplanet science is fast approaching the capability to detect life on distant planets. The successful launch of the James Webb Space Telescope (JWST) will allow us to probe into the atmospheres of some, and the future Habitable Worlds Observatory (HWO) and thirty-meter class telescopes will allow us to directly image our closest exoplanetary neighbors. To accomplish their science goals, however, these facilities require a well-curated list of targets that are well understood. Today, most planets are not understood deeply, and the very nearest exoplanet systems—exclusively accessible via the radial velocity (RV) method—remain challenging to characterize, in no small part due contamination originating from stellar astrophysics of their host stars. The best analysis techniques for disentangling stellar noise from genuine exoplanetary signals is key to the future of exoplanet science. In this work, I focus on quantitatively comparing different ways to combine photometric data with RVs, first to deeply understand systems with minimal stellar contamination, and finally to probe into those most challenging systems. Such analyses are essential steps to finding Earth twins, a crucial prerequisite in the quest to learn if indeed we are alone in the universe. First I characterize three transiting planets, discovered by the Transiting Exoplanet Survey Satellite (TESS), and a combine RVs and ground-based photometry to improve our understanding of their nature. I then turn my focus to exoplanet systems for which stellar

variability presents a major challenge to measuring the detailed properties of the planets. My analysis of the young multiplanet system TOI-1136 combines transit times and RVs to touch upon many of the most important aspects of current exoplanet science, including atmospheres, formation, and evolution. I finally study the relationship between RVs and photometry, and I investigate the best ways to transfer knowledge of stellar variability from photometric to RV datasets in order to more reliably detect exoplanets and measure their masses.

Chapter 1

Introduction

1.1 Observational Exoplanet Astronomy

Humankind has long imagined planets orbiting distant stars, and yet our first confirmation that such planets indeed exist was very recent. The first ever discovered exoplanets were the unusual PSR1257+12 b and c, found in 1992 around a pulsar that exhibited timing variations [397]. The first exoplanet discovered around a main sequence star was found in 1995 [51 Peg b; 272]. In many ways, the discovery of 51 Peg b baffled astronomers, as the planet is a "Hot Jupiter," a Jupiter-mass planet orbiting extremely close to its host star. No such analogue exists in the solar system, and the discovery confounded planet formation models [273]. 51 Peg b was discovered using the radial velocity (RV) method, which I describe in detail in §1.1.1.

The initial push to find more exoplanets was successful, and many additional exoplanets were discovered in the following years. The launch of the *Kepler* spacecraft in 2009 [57] would eventually revolutionize the field again, as it would demonstrate the power of the transit method to find thousands of exoplanets. Careful study and follow-up would soon confirm

many of these new planets, and the transit method cinched its place as the most efficient way to find new exoplanets. I discuss transits further in §1.1.2.

Additional methods of detecting exoplanets were theorized and, often, eventually carried out, though none have yet surpassed RVs or transits in sheer number of planetary discoveries. I discuss direct imaging in §1.1.3, astrometry in §1.1.4, transit timing variations (TTVs) in §1.1.5, microlensing in §1.1.6, and pulsar timing variations in §1.1.7.

All told, the `Nasa Exoplanet Archive` currently lists 5,539 exoplanets confirmed and validated, a long way from where we began.

1.1.1 Radial Velocities

One of the original and most prominent methods for discovering and characterizing exoplanets is the radial velocity (RV) method. Newton's laws of gravitation tell us that two massive bodies bound gravitationally exert equal and opposite forces on each other, and orbit a common center of mass. This has been historically well-studied in binary and triple star systems [331, 224], and can be used to find exoplanets as well. Viewed from Earth, the presence of an exoplanet can be inferred from the variation in a star's radial velocity over time, except when the full orbital motion of the planet is perpindicular to our line of sight. We show a graphical representation in Figure 4.7.

Such velocity variations cannot be observed directly, though precise spectral measurements can detect Doppler shifts in the spectrum of the host star, and these can be translated into velocity space. Taking many RV observations results in a one dimensional time series that exhibits periodic behavior.

Kepler's equation predicts the motion of a companion bound gravitationally. It is often represented in terms of the mean anomaly, M, the eccentric anomaly, E, and the orbital

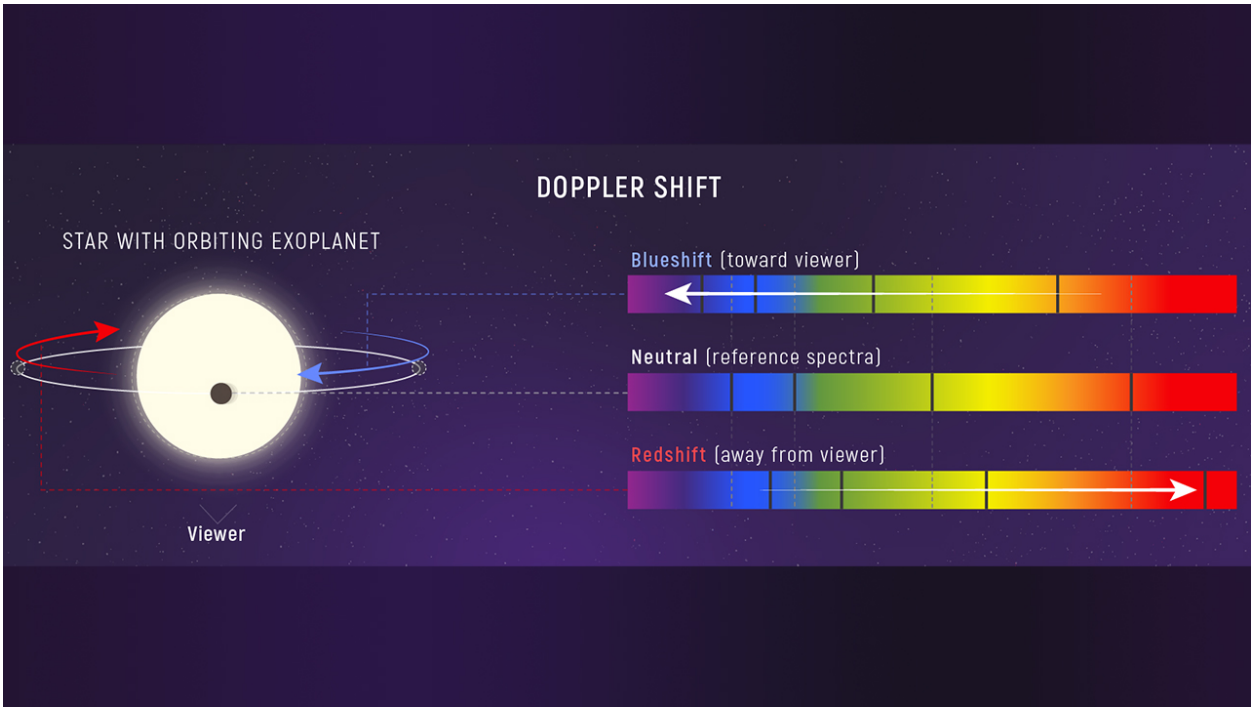

Figure 1.1: Artistic representation of the radial velocity method. As the star approaches our line of sight, its light becomes blue-shifted, and as it recedes, it appears red-shifted. Image credit: NASA, ESA, Leah Hustak (STScI).

eccentricity, e [304].

$$M(t) = E(t) - e \sin E(t) \tag{1.1}$$

This transcendental equation cannot be solved analytically, and is often solved numerically in practice. $M(t)$ describes the position of a planet in its orbit, though in general a three-dimensional planetary orbit is described by seven free parameters: semi-major axis (a), orbital period (P), eccentricity (e), periastron time (t_p), inclination (i), longitude of the ascending node (Ω), and the argument of periastron (ω) [304].

An RV time series only observes this orbit projected into one dimension, and generally cannot constrain Ω, and can only constrain $a \sin(i)$, but not a nor i individually. Kepler's laws can

be used to re-parameterize $a\,\sin(i)$ into a dependence on planetary mass times the sine of inclination, $M_p \sin(i)$, and the stellar mass, M_*. M_* can usually be measured independently from RV observations (via spectral type and luminosity). The dependence on $M_p \sin(i)$ is often re-parameterized into the direct observable, K, the RV semi-amplitude. This is given by:

$$K^2 = \frac{G}{1-e^2}\frac{1}{a\sin(i)}\frac{M_p^3 \sin^3(i)}{(M_p + M_*)^2} \tag{1.2}$$

The RV method is one of few methods that can be used to place constraints on exoplanet mass, one of the most fundamental parameters when studying exoplanets. The method is most sensitive to large planets that orbit close to their star, though RV detections have been made for Earth-sized exoplanets [40], and for very long period exoplanets [130].

The method is less efficient than the transit method, with observations restricted to a single star at a time. The advantages, however, are such that RV observations maintain their importance today, and will likely to continue to be one of the most utilized ways to study exoplanets. As mentioned above, RVs can place constraints on minimum mass, something that the transit method typically cannot do. It is also more sensitive to longer period exoplanets, as the transit probability falls off rapidly as an exoplanet's orbital distance increases. Additionally, the RV method is generally sensitive to any inclination, except for an orbit that is completely face on, allowing study of relatively inclined systems.

1.1.2 Transits

The transit method of exoplanet detection has moved to the forefront of exoplanet science today as the most successful at identifying planets orbiting distant stars. The method relies

on the continual photometric monitoring of the brightness of a star. When a planet passes between the observer's line of sight and the star, a characteristic dip in brightness appears in photometric data. We call this dip a transit. The first transit of an exoplanet was observed in 1999, for the Hot Jupiter HD 209458 [175, 78]. Originally, transit follow-up was carried out for known-exoplanet hosts at the planet's time of inferior conjunction. It was quickly determined that the more efficient method, rather than observing a single star, was to use wide-field cameras that could observe the brightness of many stars simultaneously [183]. Ground-based observations were limited in the transit depth that they could observe due to atmospheric effects, and space-based photometric missions would eventually become the gold standard for transit observations. The launch of dedicated transit missions CoRoT [19], *Kepler* [57], and TESS [318] would eventually expand our knowledge of transiting exoplanets substantially. We include a graphical representation of a transit in Figure 1.2.

When a planet transits in front of its host star, it initially blocks a portion of the stellar flux as it slowly moves in front of the disk. We call this ingress. Once the planet is completely in front of the stellar disk, the planet is transiting, and when it exits the disk, we call this egress. The amount of flux blocked by a transiting exoplanet is approximately related to the planet-star radius ratio by

$$\Delta F \approx \left(\frac{R_p}{R_*}\right)^2 \tag{1.3}$$

We call ΔF the transit depth. R_* can usually be calculated independently from the transit observation via spectral classification, and so the transit can generally constrain the radius of an exoplanet. Detecting multiple transits can be used to constrain the orbital period of a transiting exoplanet with high precision, and the transit time, or the time of inferior conjunction, can be used to tightly constrain the phase of the transiting exoplanet. The

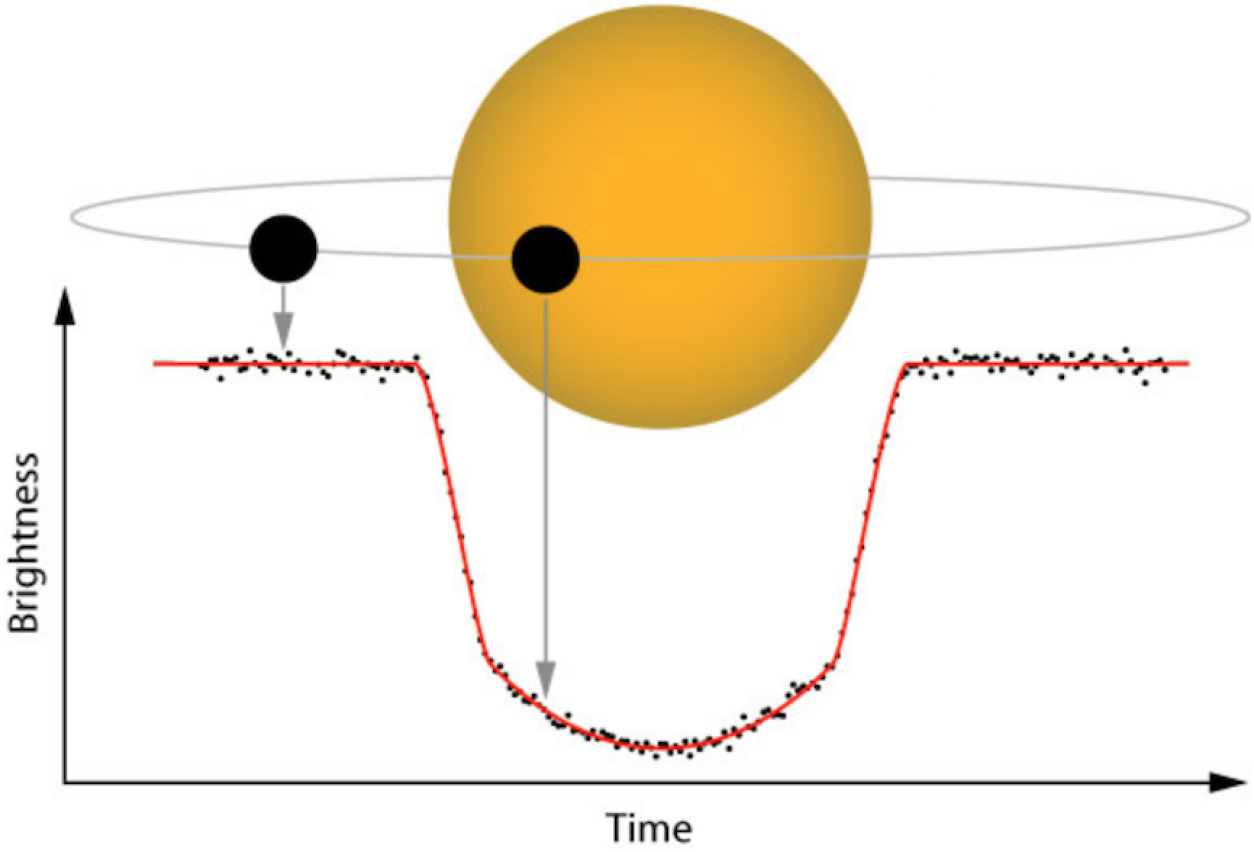

Figure 1.2: As a planet passes between our line of sight and that of a distant star, it blocks a portion of the light, creating a transit. Image credit NASA.

transit duration, usually defined as the time between the start of ingress, and the end of egress ($t_{1,4}$), is related to the semi-major axis and planetary mass by:

$$t_{1,4} = 13\left(\frac{M_*}{M_\odot}\right)^{-\frac{1}{2}}\left(\frac{a}{1\text{AU}}\right)^{\frac{1}{2}}\left(\frac{R_*}{R_\odot}\right) \text{ hours} \tag{1.4}$$

Beyond radius, orbital period, transit time, and semi-major axis, another important observable is the impact parameter, b, a dimensionless quantity that represents the distance from stellar disk center of the transiting exoplanet. The semi-major axis can be combined with the impact parameter to determine the orbital inclination. This is particularly important when combining transit and RV analysis, as one can much more firmly constrain the geometry of the exoplanet orbit [304].

The transit method is efficient, as we can photometrically monitor thousands of stars simultaneously. It also allows for the determination of planetary radius, an observable difficult to constrain via other methods, and allows for a generally much more precise constraint on orbital period and time of inferior conjunction than other methods can provide. The method relies on the very specific transit geometry for observations to be possible. The probability that a planet orbiting at a given semi-major axis, a, transits quickly falls off as a increases [59]. The probability is given in equation **??**.

$$P = \frac{R_\odot}{a} \tag{1.5}$$

It is clear, then, that most planets do not transit from our perspective. The method is heavily biased towards shorter-period, large exoplanets, much like the RV method. The

transit method, however, is generally sensitive to smaller exoplanets than the RV method at present. Consequently, while we have discovered many transiting exoplanets, they comprise a small subset of the true population of exoplanets, most of which can never be observed via transit photometry.

1.1.3 Direct Imaging

Direct imaging of an exoplanet is perhaps the simplest to conceptualize of all methods of exoplanet detection. Such an observation, as the name suggests, consists of observing the planet directly, rather than its host star. These observations can be spectroscopic or photometric. Simple to conceptualize, but far from simple to perform, direct imaging observations are generally challenged by two issues.

Firstly, the host star will be many orders of magnitude brighter than any exoplanet. As a result, any observation of light eminating from an exoplanet will need to be disentangled from the contaminating flux of its host star. Development of coronographs, instruments that block flux from the host star, have made such observations possible [118], though at present such observations are typically constrained to distant, young Jupiter-size objects that emit a great deal of light due to a high formation temperature [266]. Observations of exoplanets via light reflected from their host star are more challenging, but are expected to be the only way to directly image more mature or rocky exoplanets.

Secondly, direct imaging requires that a planet be sufficiently far from the host star that it can be geometrically resolved. The angular separation of a planet and its host star from Earth is approximately $\frac{a}{d}$ where a is the semi-major axis of the planet, and d is the distance of the system from Earth. This is typically a very small angle, and is often smaller than the minimum resolving angle of a telescope, given by the size of its Airy disk, $1.22\frac{\lambda}{D}$. λ is the wavelength of observation and D is the diameter of the optical instrument being used, in

our case a telescope.

These major limitations make observing a planet via direct imaging very challenging, and have restricted most successful observations to long-period giant planets. Currently, the lowest mass planet observed via direct imaging is 51 Eri b [2 M_j; 260], and the lowest radius exoplanet observed is TYC 8998-760-1 c [$R_p = 12^{+7}_{-3}$ $M_\oplus$; 53]. The shortest orbital period detected via direct imaging is that of HD 206893 c [2090^{+44}_{-37}; 177].

Despite challenges, direct imaging is valued because it is the primary exoplanet detection method that directly observes an exoplanet. Phase curves of thermally emitting exoplanets can be obtained photometrically [112], and high dispersion spectroscopy can recover exoplanet flux in cross-correlation space [350], though these methods are generally more restrictive. Other methods infer the existence of an exoplanet from observations of its host star. Furthermore, next generation, thirty-meter class telescopes are expected to be able to image many of Earth's closest neighbors, and will generally be sensitive to lower-mass, shorter-orbital period exoplanets [349].

1.1.4 Astrometry

Astrometry is another promising method for detecting exoplanets. Complementary to radial velocity observations, astrometry investigates the two-dimensional motion of a star in the sky plane. This subtle "wobble" of a star can be used to infer the existence of a companion exoplanet. Currently only two exoplanets have been discovered via astrometry [93, 352], and both very recently. Many more previously known exoplanets have been detected via astrometry [279, 401].

With the advent of Gaia [139], astrometric planetary observations are very likely to see a substantial uptick, as much more high-precision astrometry data is now publicly available,

and more continues to be obtained. Astrometry is a particularly valuable detection tool because it, unlike most other methods, is especially sensitive to longer period exoplanets, and could be used to probe for Jupiter analogues. Additionally, astrometric measurements of RV-detected planets can constrain the planetary orbit in three dimensions, allowing for another method to obtain true mass measurements.

1.1.5 Transit Timing Variations

Another method that can be used to discover and characterize exoplanets is to examine the transit timing variations (TTVs) of known transiting exoplanets. Normally, planetary transits are highly regular, but the presence of other perturbing bodies in the system can introduce non-linearities in the orbital period, causing transits to appear early or late, sometimes significantly so. These effects originate from that fact that planets do not only interact with their host star, but with each other as well. Typically, planets are much less massive than the host star, and often very far apart, and so the effects are negligible. Systems with massive exoplanets, however, might see TTVs occur more regularly [200]. Additionally, planets in or near orbital period resonance typically exaggerate this effect, so much so that known systems with TTVs almost always contain planets with orbital periods near resonance [149, 95].

Non-transiting companions can cause TTVs in transiting planets. These TTVs can then be used to predict the mass and orbital period of the companion. In general, TTV detections are highly valuable because they are very sensitive to orbital period and planet-planet mass ratio, and they are one of the few methods than can constrain planet mass. Furthermore, TTV mass measurements are not highly sensitive to host star brightness, and have been made on systems too dim for RV observations [149].

TTVs do not occur in every, or even many, transiting systems, with only 355 known planets

exhibiting TTVs out of 4159 known transiting planets (NASA Exoplanet Archive, November 13 2023). The TTV super-period, also, is often a very long time period, and a long baseline of photometric observations is required to constrain certain companion dynamics. Finally, TTVs occur by far most often in compact resonant systems, which, while interesting, are not representative of all exoplanet systems. I perform a detailed analysis of a TTV system, TOI-1136, in Chapter 4.

1.1.6 Microlensing

Quite distinct from the aforementioned observation methods, microlensing is a promising detection method that utilizes Einstein's theory of General Relativity to find distant exoplanets. Microlensing occurs when a distant star (the lens) passes fortuitously between our line of sight and a distant, bright object (the source). The event is transient, and lasts only a short period of time. The result is a time varying brightness profile that is highly distinct. If the lens contains a planetary companion, the varying lightcurve may see a distinctive "nano-lensing" event caused by the gravity of the planet [304].

Microlensing events are exceedingly rare, and many possible stars must be monitored at once for a chance to observe even a single event. Most surveys are focused towards the dense region of stars toward galactic center. Exoplanets detected by microlensing are typically very far from Earth, with distances typically around a few kpc, far beyond the sensitivity of most other detection methods. As a result, microlensing allows us to probe exoplanets that would normally be impossible to study, though such events are a one-time occurence only, and follow up is typically impossible.

1.1.7 Pulsar Timing Variations

Similar to transit timing variations, pulsar timing variations can be used to infer the existence of exoplanets, as was the case with the first detected exoplanets [397]. Pulsars provide extremely precise timing measurements, and slight deviations can be used to infer the existence of exoplanet companions. Planets orbiting pulsars are very rare, however, and only seven are currently known. Follow-up studies are also typically impossible.

1.2 State of the Field

The field of exoplanet science has come a long way since the first discovery of an exoplanet orbiting a main sequence star in 1995 [272]. The first exoplanet discoveries were RV exoplanets, and this continued to be the most common method of discovering exoplanets for more than a decade. The paradigm shifted with the launch of the *Kepler* spacecraft, which would discover 2778 exoplanets over the course of its four year mission. We highlight the paradigm shift in Figure 1.3. The huge increase in the number of exoplanets was a dramatic change for the field: rather than study exoplanets on a case by case basis, we could begin to *statistically* understand exoplanets. It became apparent that exoplanets are common, with an average of 0.7 planets per GK dwarf [64], and perhaps more orbiting the common M dwarfs [104].

Today we know of 5,539 confirmed exoplanet candidates, with 7,593 candidates from the *Kepler*, K2, and TESS missions yet to be confirmed or ruled out. Now, the field is dominated by a few larger questions: how do planets form and evolve? How do we explain the populations we see today? Can any planets beyond Earth host life? *Do* any planets beyond Earth host life?

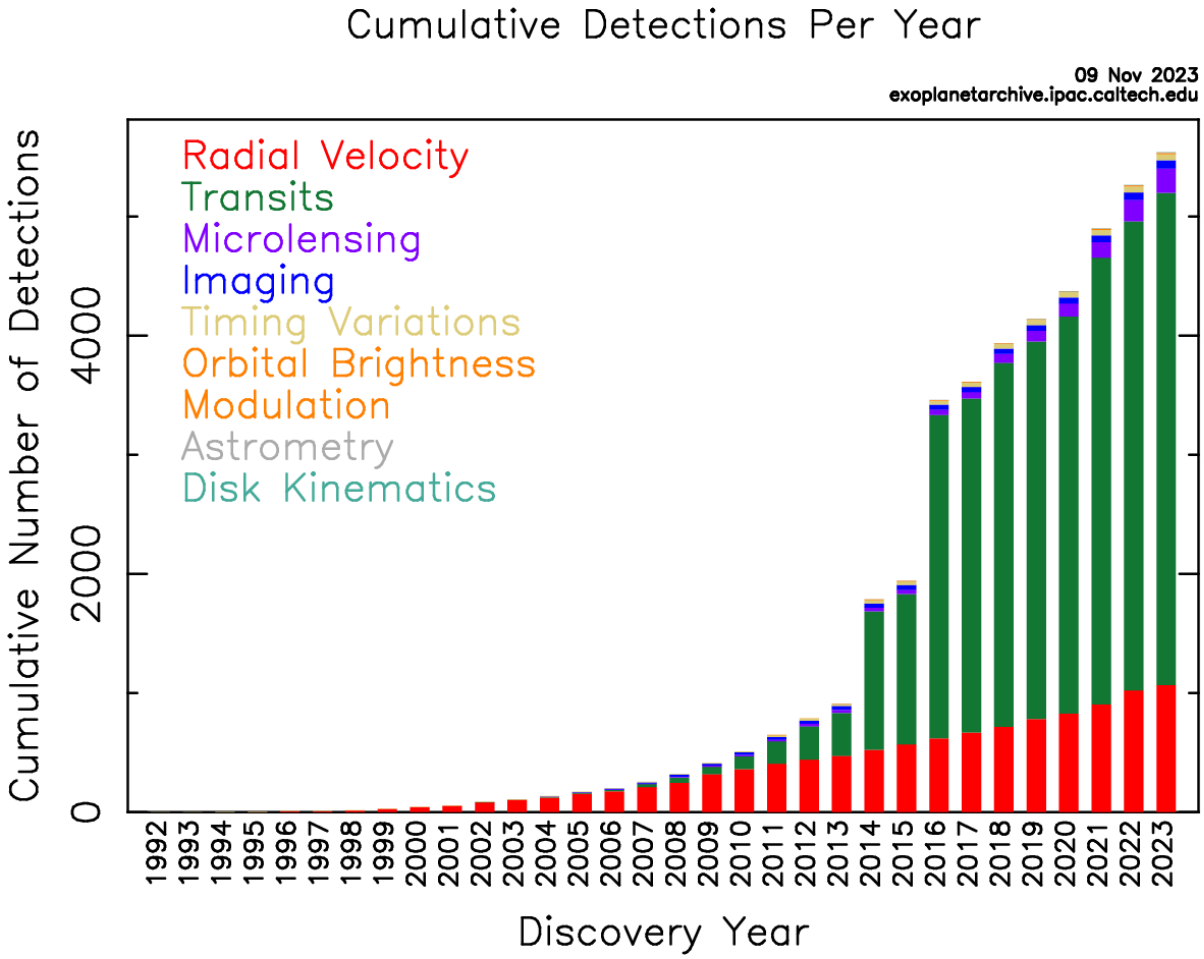

Figure 1.3: We highlight the evolution of planet discoveries by year. The RV method maintains a steady stream of discoveries, though the transit method has eclipsed it as the most efficient way of finding new exoplanets. Image `NASA Exoplanet Archive`.

1.2.1 Planet Formation and Evolution

We still have a poor idea of how planets form. Most planet formation theories are based on the solar nebula theory, first designed to describe the formation of the solar system [276]. In general there are thought to be three stages of planetary system growth. The first begins with a proto-stellar disk during star formation. A proto-planetary disk exists too at this stage, and is thought to be dominated by Van der Waals attraction as dust cools and instabilities form. The second stage sees the aggregation of cm- to km-sized particles, and is generally the least well understood, as the underlying physics is complicated and hard to predict. The third, coagulation stage, is dominated by gravitational interactions between planetesimals [304].

Pebble accretion is generally thought to influence the formation of giant planet cores during the early stages of planet formation [231]. During the planetesimal stage, gas giant cores can develop via collisions [16]. Once a planetesimal has reached a few $M_{\oplus}$, it is generally massive enough to accrete volatiles and develop an envelope or atmosphere.

All astronomical observations in human history represent only a brief snapshot when compared to the Myr to Gyr lifetimes of exoplanetary systems. Consequently, most systems have had abundant time to evolve and change throughout their incredibly long histories. To answer questions about formation, we must also answer questions about system evolution, as the current snapshot of exoplanetary systems has been inevitably shaped by both.

Inward migration is commonly predicted in system formation simulations [292]. Especially in multi-planet systems, it is expected that planets, after formation, will migrate inward and into mean-motion resonance, whether modeled using adiabatic perturbation theory [33], modified N-body integration [371], or hydro-dynamic simulations [18]. Kepler multi-planet systems reveal fewer planetary systems in pristine mean-motion resonance, however, than expected, implying the existence of Myr or Gyr processes that cause such chains to erode.

Planetesimal scattering [79], secular chaos [307], tidal dissipation [244], and orbital instability are all plausible explanations. Indeed, with the help of TESS, we are seeing young systems that maintain pristine orbital chains, suggesting this may indeed be the case [95].

Lower multiplicity systems, too, can exhibit migration, such as the well-studied population of Hot Jupiters. High eccentricity migration, for example, can often occur when a planet's orbit is perturbed into high eccentricity, and the planet circularizes due to tidal interactions with the star. This generally causes inward migration, and is a plausible explanation for some Hot Jupiters.

Beyond orbits, it is expected that the size of a planet evolves over time. The observed radius gap in the exoplant population [134] is likely caused by either atmospheric stripping from the host star or possibly outgassing of volatiles, or some combination [46]. Such processes tend to recreate the hierarchy we see in the solar system, with smaller planets on shorter orbital periods, and larger, gaseous planets further out. There are notable exceptions, however, and this process is still under study [359, 95].

But the solar system is not all stellar systems, and this had become abundantly clear as more exoplanets are discovered. Theories of formation and evolution must recreate the observed population of exoplanets, and this is no simple task. When Mayor & Queloz first discovered 51 Peg b in [272], astronomers were surpirsed to find a planet unlike any we've seen in the solar system: a Jupiter-sized planet orbiting very close to its host star.

More planets have been discovered with no clear analogues in the solar system, such as super-Earths and sub-Neptunes with radii between 1-4 $R_\oplus$ [58]. In fact, these appear to be the most common type of exoplanet, despite no representation of either type in the solar system. Furthermore, we must explain the radius gap [134], which seems to have such an effect on the divergence of these intermediate-sized planets.

The processes that cause the current exoplanet population to take the form it does now are

among the top areas of research in the field. And yet, theories require more and higher precision observations to validate or refuse their hypotheses. Atmospheric observations will be a big part of this, and to do so unambiguously we must know planet masses to better than five sigma precision [30]. Thus, methods to enhance the science return of RV observations (detailed in §1.3) are an essential part of answering these fundamental questions.

1.2.2 Life on Other Planets

Considered by some to be the top goal of exoplanets science, an area of keen interest is whether or not any exoplanets host biological life. Unable to take measurements in situ, we are restricted to observing planets from afar, and trying to infer if life indeed exists among any. The primary method for determining if a planet might host life is atmospheric observation, and a search for biosignatures or technosignatures. Two principle methods exist for determining the elemental composition of a planet's atmosphere: transmission spectroscopy [i.e. 43, 102] and direct imaging spectroscopy [i.e. 218, 330].

Transmission spectroscopy relies on measuring variations in transit depth at different wavelengths while a planet transits its host star. In principle, light from the star will be filtered through the exoplanet's atmosphere as it travels. Observing spectral features such as absorption lines can help determine precisely which elements the atmosphere is composed of. Various chemicals and combinations of chemicals have been proposed as biosignatures or technosignatures that, when detected, might suggest biotic processes happening on the surface of the planet [132, 337]. With the successful launch of JWST [143], transmission spectroscopy of smaller planets is now possible, and already observations of distant atmospheres have been executed [157, 408].

Transmission spectroscopy has a number of drawbacks. Currently, clouds and hazes are providing a serious challenge to the interpretation of transmission spectra, as they tend

to flatten spectral features, reducing the SNR with which they can be recovered [283, 113]. Additionally, high SNR observations are biased towards large planets transiting smaller stars, making observations of terrestrial planets orbiting anything other than M dwarfs a serious challenge [214]. Finally, transmission spectroscopy requires a planet to transit, which we already explained in §1.1.2 is heavily biased towards large, short period planets: not the kind thought to be amenable to life.

In principle, spectroscopic characterization of a planet's atmosphere can be obtained via direct imaging. This requires a target to be imagable, which we explained in §1.1.3 is not an easy criteria to meet. Most candidates for this observation type face the opposite problems of transmission spectroscopy: these planets are too distant and cold to plausibly host life. However, development of next generation, thirty-meter class telescopes is expected to make imaging smaller, shorter period exoplanets of the nearest stars a possibility. The Habitable Zone [220, 221] of early M dwarfs will be of particular interest in the search for biosignatures.

Upon successful detection, degenericies that exist in the interpretation of spectral data that can make a single, unambiguous atmospheric solution difficult to ascertain. An important solution is the measurement of planetary mass to better than 5σ confidence, which is expected to help distinguish different atmospheric explanations [30]. Except in the case of TTV systems like TRAPPIST-1 [149], RV measurements are typically required to measure the mass of an exoplanet. Consequently, RVs will continue to play an important role as we image the atmospheres of potentially habitable exoplanets, further motivating our need to address the problems outlined in §1.3.

Currently, no biosignatures on any exoplanet have been detected. With JWST successfully launched and thirty-meter class telescopes under development, this may change in the next decade.

1.2.3 Stellar Activity

One of the greatest challenges facing exoplanet science today is an imperfect understanding of stellar activity. With the exception of direct imaging, all exoplanet observation methods are indirect, filtered through their host star. Unfortunately, stars themselves are not perfectly predictable point sources of light, and a great deal of complicated astrophysics occurs within the star alone. Consequently, any data we obtain pertaining to exoplanets will inevitably contain physical signals that originate from the star, not the planet.

Such signals are caused by stellar magnetic activity, star spots, plage, faculae, oscillations of the stellar surface, and a variety of other effects besides. Great progress has been made in developing techniques and observation strategies that minimize the effects of stellar activity, but it is still a significant source of uncertainty in many analyses, and one of the primary hindrances to detecting Earth-sized exoplanets.

1.3 Analyzing Extremely Precise Radial Velocities

Data analysis in the field of astrophysics has evolved a great deal in the last decade, with a general shift from frequentist statistics to the newer, more powerful Bayesian approaches most astronomers utilize today. Exoplanet solutions used to be far simpler, with the earliest discoveries of high-SNR Hot Jupiters and only a handful of possible explanations of how the models fit the data. Today, we see a diversity of more challenging systems, with myriad potential models competing to explain a single time series. One exoplanet system might host half a dozen planets, and planetary signals might mix with a complicated, coherent stellar signal. Data today often come from many different sources and instruments. Such models can easily have dozens of free parameters with broad priors, and hundreds of solutions might be feasible. The advent of Bayesian statistics and machine learning models are tools that

can cut through this confusion, leading to sensible, physical results that are well motivated.

RVs in particular remain a very important discovery and characterization tool in exoplanet astronomy. Precise planet masses are essential for understanding the intricacies of exoplanet composition, and are equally important for disentangling degeneracies in the interpretation of transmission spectra and biosignatures, as described in §1.2.2.

RVs remain important as a discovery tool as well. While less efficient than the transit method, the RV method is sensitive to far more orbital geometries. Upcoming flagship imaging missions suggested by the Astro Decadal 2020 such as the Habitable Worlds Observatory [HWO; 383] will require a list of nearby, HZ worlds to perform their primary science directive. However, such nearby planets are unlikely to transit. Using an optimistic Earth-like exoplanet occurence rate ($\eta_\oplus$), [169] conclude that no such exoplanet is expected to transit within 5 pc, and only 1-20 might transit inside 20 pc. The RV method is currently the only plausible way to survey for the existence of such planets, with a few promising targets already identified [GJ 667 C, Proxima Centuari b; 15, 12].

Current candidates are all super-Earth HZ exoplanets orbiting around M dwarfs, as HZ planets orbiting FGK dwarfs have considerably smaller RV amplitudes, and strain current RV detection limits. For example, an Earth-sized planet orbiting a sun-like star would have an RV amplitude of 9 cm s^{-1}, which is approximately an order of magnitude smaller than the detection limits of high precision RV instruments [i.e. HIRES, HARPS, HARPS-N; 386, 271, 88].

Next generation instruments have been developed that can probe below the historical 1 m s^{-1} RV noise floor, with many taking data with single-measurement precisions better than 30 cm s^{-1} [ESPRESSO, NEID, KPF; 303, 336, 145]. We call these instruments Extreme Precision Radial Velocity (EPRV) instruments. Characterizing exoplanets with amplitudes below 1 m s^{-1} faces new challanges however, and much work must be done to find small

exoplanets orbiting our nearest neighbors.

1.3.1 Stellar Activity and EPRV

Historically, exoplanet signals were larger than the stellar activity present in their host stars, and as we pushed RV instruments to higher precision, we would typically avoid the most active stellar hosts. Some methods were developed to mitigate the effects of correlated noise in RV data, but more often scientists prioritized quiet stars where such noise could be avoided. In the era of EPRV, however, there are no quiet stars. Starspots and plage from magnetic activity may generate RV signals with amplitudes 1-1000+ m s^{-1} [105], stellar oscillations in Sun-like stars have typical amplitudes 10-100+ cm s^{-1} [77], and granulation may add noise at levels of 10+ cm s^{-1} [76]. We can no longer avoid stellar variability, and so we must learn how to better model and understand it. This is of paramount importance to the EPRV community, as the 2020 Astro Decadal has emphasized that "precise radial velocities will identify terrestrial exoplanets orbiting nearby stars, determine when they are situated at quadrature, and remove degeneracies from the interpretation of atmospheric spectra features," and that EPRV must "reach a single measurement precisions of 10 cm s^{-1}" [290]. Techniques must be developed to mitigate correlated noise.

Correlated noise can be mitigated in a variety of ways, and observables extracted via Doppler observations can help in the process. The simplest way to represent noise is to adopt a "jitter" term, usually Gaussian distributed and added in quadrature to each RV's uncertainty [122], though this does little to solve the problem of correlated noise, and rarely works beyond the simplest of situations. [115] took advantage of the different wavelength RVs available from HARPS data of τ Ceti: Keplerian signals are expected to be consistent across wavelength bands, but stellar activity-based signals will not. Another way to deal with stellar activity is to decorrelate the velocities to one or more indicators of stellar activity.

[158] investigated three different activity indicators in simulated RV datasets, including cross-correlation function (CCF) width, bisector span (BIS), and flux from the calcium II H&K lines ($\log R'_{HK}$). These indicators usually represent some tracer of stellar magnetic activity that isn't expected to be affected by the RV reflex motion on spectral lines. For example, $\log R'_{HK}$ is affected by rotationally-modulated atmospheric phenomena, but not by planetary orbits. These decorrelation methods can be very powerful, but still have significant limitations. Different types of activity can have different effects on these indicators, and good quality estimates of all indicators are not always available. Activity can also have effects on RVs and indicators that are out of phase, leading to results that are misleading at best.

Perhaps the current most effective technique at mitigating the effects of stellar activity on RVs is Gaussian Process (GP) Regression [10]. GP models today are a common tool for disentangling stellar signals from planetary ones, as their versatility allows them to be applied to a wide array of astrophysical situations. GPs are stochastic models consisting of a mean function $\mu_\theta(x)$ and a covariance, autocorrelation, or "kernel" function $k_\alpha(x_n, x_m)$. These functions are parameterized by the orbital parameters θ as well as additional GP "hyperparameters" α. The likelihood of a collection of data points $(y_1, y_2, ...y_N)$ corresponding to sampling times $(x_1, x_2, ...x_N)$ is given by

$$\ln \mathcal{L}(\theta, \alpha) = \ln p(y|\chi, \theta, \alpha) = -\frac{1}{2} r_\theta^T \mathcal{K}^{-1} r_\theta - \frac{1}{2} \ln \det \mathcal{K} - \frac{N}{2} \ln(2\pi) \tag{1.6}$$

where

$$r_\theta = (y_1 - \mu_\theta(x_1), ...y_2 - \mu_\theta(x_2)) \tag{1.7}$$

and the covariance matrix $\mathcal{K}$ is an $N \times N$ dimensional matrix given by

$$\mathcal{K}_{n,m} = k_\alpha(x_n, x_m) \tag{1.8}$$

Studies have consistently shown the effectiveness of GPs for modeling stellar activity, especially those where the GP is trained on photometry taken contemporaneously with RVs [e.g. 173, 312, 248]. GPs can also be trained on $\log R'_{HK}$, Hα values, or other activity indicators. Most scientists consider a GP trained on simultaneous RVs and photometry the best activity mitigation method, but the aforementioned activity indicators can be used as excellent sanity checks, or can help constrain troublesome model parameters.

1.3.2 Machine Learning in EPRV

The concept of machine learning is becoming ever more important in the field of exoplanet astronomy. As we probe for smaller and smaller signals in data, planets and other important features become far more difficult for a human to discover un-aided. Astronomical data has also grown in quantity such that no human can possibly study it all, and we must rely on algorithms and computers to identify promising exoplanets. Less sophisticated algorithms, such as the Generalized Lomb-Scargle periodogram [GLS; 404] have long been used to identify periodic signals in RV data. Photometric equivalents such as the boxed least squares [BLS; 85] and transit least squares [178] algorithms provide an automated tool to identify transit-like signals in photometric data as well.

More recently, more traditional machine learning algorithms have been deployed on exoplanet datasets, such as a deep neural network to discover the 8^{th} planet in Kepler-90 [341], or an unsupervised learning model to estimate stellar oscillations in *Kepler* stars [100].

In the context of EPRV, machine learning can be a powerful tool for modeling stellar activity that contaminates RV data. In general, our knowledge of the physical stellar parameters that imprint correlated noise in RV data is incomplete. We cannot resolve any stars beyond the Sun with current capabilities, and we cannot know their spot configurations or take in situ measurements of magnetic cycles. Consequently, modeling this unknown noise source is an unsupervised learning problem, as our model will attempt to learn the best correlated noise model that maximizes the model likelihood. As mentioned in §1.3.1, GPs are a popular choice to perform this function, and are currently the standard correlated noise model used in RV analysis. An important decision one must make when utilizing a GP is the choice of kernel function. The GP kernel, as is apparent in Equation 1.6, can have a dramatic effect on the covariance matrix and model likelihood. Dozens of GP kernels see common use in a variety of computational fields today, each with different strengths and weaknesses. For example, the documentation of `PyMC3`, a popular inference package in astronomy as well as other fields, lists about a dozen GP kernels in detail [329]. Furthermore, GP kernels can be arithmetically combined in general to generate new kernels.

The field of exoplanet astronomy utilizes a few different GP kernels regularly, though the Quasi-Periodic GP kernel is probably the most commonly used in RV science [173, 248]. GP models, in general, are not physical, and their hyperparameters do not have physical meaning. This is undesirable, as it restricts our ability to apply informed priors based on physical knowledge of the system. Thus, it is desirable to choose a GP kernel that somewhat resembles a physical model, and this is the primary reason the Quasi-Periodic GP kernel is regularly used. The kernel is given by:

$$\mathcal{K}(x_i, x_j) = \eta_1^2 \times \exp\left(- \frac{|x_i - x_j|^2}{\eta_2^2} - \frac{\sin^2\left(\frac{\pi|x_i - x_j|}{\eta_3}\right)}{2\eta_4^2} \right) \tag{1.9}$$

Where $\mathcal{K}(x_i, x_j)$ is the ijth entry of the covariance matrix, $\mathcal{K}$. η_1, also known as the GP amplitude, simply represents the amplitude of the quasi-periodic variability. In the case of RV data, this is usually in units of m s^{-1}. η_2 is approximately the lifetime of a spot on the surface of a star, often called the exponential decay length. It generally constrains the lifetime of an active region, and is given in units of time (often days). η_3 is the periodic component of the GP, and generally represents how often the structure repeats itself. This is often well represented by the stellar rotation period, or sometimes one of its harmonics. This is usually reperesented in units of days. Finally, η_4 is known as the periodic scale length, and is dimensionless. This is the least interpretable of the hyperparameters, and approximately represents the inverse of the number of mini-periods that occur inside one time scale of length η_3. For example, if η_3 were one hundred days, and $\eta_4 = 0.5$, one would expect to see a $\sim$ 50 day periodicity with some varying amplitude.

Visible in Equation 1.6, evaluating a GP likelihood requires inverting the covariance matrix, $\mathcal{K}$. In general, inverting an $N \times N$ matrix takes $\mathcal{O}(N^3)$ time, which means that GP likelihood evaluations quickly become intractable for large datasets. RV datasets are often sparse, and so the Quasi-Periodic kernel still sees a great deal of use in the community, but as time series for RV targets grow larger, and the number of free parameters (instruments) continues to grow, the Quasi-Periodic kernel may become intractable. Furthermore, photometric datasets are generally very large compared to RV, and usually impossible to model with a Quasi-Periodic kernel in any reasonable amount of time.

1.3.3 New GP Kernels

[123] have developed an alternative GP process that scales with $\mathcal{O}(N)$ in general and is far more practical for photometric datasets and large RV datasets. The drawback, however, is that GP kernels constructed using this `celerite` process are more difficult to interpret, and

are often too flexible. The result can be a process that fits the data too well, and lacks predictive ability. Our ability to constrain certain GP hyperparameters prior to modeling using physical knowledge of the system can also contribute to overfitting.

Alternatively, [74] have developed an expansion of the Quasi-Periodic kernel during their analysis of AU Mic. Unlike exoplanetary reflex motion, stellar variability is known to be chromatic [90, 323]. Most recent EPRV analysis sees data taken from multiple instruments, and many instruments extract velocity information from different wavelength regions. Consequently, even if observing an active star simultaneously, an optical RV spectrograph and an infrared RV spectrograph would likely see very different variability amplitudes. Thus, the single amplitude hyperparameter η_1 would imperfectly describe at least one dataset, and probably both. [74] introduce two new expansions of the Quasi-Periodic kernel. The first gives each RV instrument an amplitude term of its very own. It is given by

$$\mathcal{K}_{J1} = \eta_{s(i)} * \eta_{s(j)} * [...] \tag{1.10}$$

Here, $\eta_{s(i)}$ is the amplitude hyperparameter of whichever spectrograph took data at observation i, and $\eta_{s(j))}$ for observation j. The term in brackets is the exponential portion of Equation 1.9. This kernel enforces covariance between observations from different instruments, and allows for instruments to have different activity amplitudes. This is desirable as it can help prevent overfitting, and is physically motivated. This can increase the number of free parameters in a model by a fair bit, however, and can be less desirable for that reason. [74] also suggest another GP kernel as an alternative:

$$\mathcal{K}_{J2}(x_i, x_j) = \eta_0^2 * \left(\frac{\lambda_0}{\sqrt{\lambda_i \lambda_j}} \right)^{2\eta_\lambda} * [...] \tag{1.11}$$

This GP kernel requires that one assign an "effective wavelength" to each instrument, often the central wavelength, or region of highest throughput. One then chooses one of the wavelengths arbitrarily to be λ_0. This model only adds two new free parameters, η_0, the amplitude at the effective wavelength, and η_λ, a dimensionless scaling term that controls the wavelength dependence of the activity. This kernel is convenient because it enforces the expected physical dependence on wavelength of chromospheric activity, and it only adds two amplitude free parameters, regardless of how many instruments are included in the fit.

Throughout this dissertation, I use the `celerite` kernels in Chapters 2, 3, and 5, and I use the chromatic $\mathcal{K}_{J1}$ kernel during analysis in Chapters 4, 5, and 6. I use the Quasi-Periodic kernel, or its chromatic expansion $\mathcal{K}_{J1}$ when possible, though photometric datasets can only truly be utilized with `celerite`.

1.3.4 Photometric Data and EPRV

As mentioned previously in §1.3, training a GP activity model on photometry is often desirable, especially if photometry is taken simultaneously with the RV data. This is primarily because certain underlying physical processes imprint on both photometric and RV datasets, for example starspots. It can be much easier to separate the stellar variability and planetary components in photometric data than in RV data for two reasons. First, transits have a distinctive dip shape that occurs periodically in photometry, while spot induced effects on photometry tends to exhibit decaying sinusoidal behavior. These processes are much easier to distinguish in photometry than in RVs, where both activity and exoplanetary

reflex exhibit approximately sinusoidal fluctuations. Second, photometry is typically of much higher cadence than RV data. For example, TESS and *Kepler* both see short cadence observations every $\sim$ two minutes. In contrast, obtaining one RV observation of a target every day would be considered very high cadence.

Translating information from photometry to RV data can be done in a variety of ways. One can fit a GP model to photometry and use the posteriors as priors for an RV fit. In the case of the Qausi-periodic kernel, this can be applied to η_2, η_3, and η_4, though photometry cannot inform the amplitude of RV activity as it is of different dimension. The other three hyperparameters are associated with periodic structure, and should apply to both photometric and RV datasets, though with a likely phase shift. [5] provide a method for translating photometric activity amplitude to RV amplitude using a simple spot model, though it depends on knowledge of a few free parameters not generally known, such as fractional spot coverage, and has limited predictability.

Another method involves jointly fitting RV and photometric datasets. There are multiple examples of such fits in literature [173, 28], and I also perform such analyses in Chapters 4 and 5. The advantages of this method are that it generally provides the most robust picture of the stellar variability, as the model likelihood will be influenced both by RV and photometric data simultaneously, providing live feedback during inference. The main drawback is that this method is the most computationally costly, as it is high dimensional and uses all data simultaneously. We discussed in §1.3.3 that such a high dimensional dataset is not tractable to use with the Quasi-periodic kernel, and one is forced to utilize alternatives, such as `celerite`. These kernels are less interpretable, which we deem less desirable.

Even with photometric data available, it is not clear which methods or datasets are best to use to mitigate stellar variability in RV datasets. This is the primary question I seek to answer in Chapters 5 and 6. For example, older *Kepler* photometry is more precise than more recent TESS photometry, and preserves longer period signals. It is also old, however,

and may be less predictive considering that spots tend only to live for a few rotations of a Sun-like star, $\sim$ 100 days [147]. Which dataset proves superior to train upon may also be contingent upon the quality and quantity of the simultaneous RVs. I perform a series of injection recovery tests for a variety of active targets I have determined would make an excellent test case for this question. I expect the results to have lasting implications for future EPRV work, as photometric datasets are one of the most powerful ways to mitigate stellar variability in RVs, and future photometric missions will continue to provide photometry for RV targets in the future.

1.4 Dissertation Organization

My dissertation is organized into seven chapters. Chapter 2 is focused on two TESS M dwarf systems I characterized using the HPF spectrometer and ground-based follow up transit photometry. Chapter 3 is the detailed analysis of another TESS system that hosts an Earth-sized exo-Venus and a non-transiting companion. Chapter 4 is my analysis of a young TESS system with seven possibly transiting planets. This system utilized a huge quantity of RVs, a stellar activity model, and a dynamical TTV model to characterize this important, high-multiplicity system. Chapter 5 is an in-progress publication focused on the super Earth Kepler-21, the brightest known *Kepler* system. We utilize new RVs and activity models to improve the planet mass, and we test the sensitivity of the solution when trained on *Kepler*, TESS, or both. Finally, I expand my Kepler-21 analysis to eight targets chosen to test the sensitivity of photometric training datasets, as well as the utility of simultaneous, precise RVs, in Chapter 6. Chapters 2, 3, and 4 are published works that are include unadulterated, though I add a foreword to give context. I include a summary and conclusion in Chapter 7.

Chapter 2

TOI-1696 and TOI-2136: Constraining the Masses of Two Mini-Neptunes with HPF

2.1 Foreword

Today, the *Transiting Exoplanet Survey Satellite* (TESS) is providing near-constant high precision photometry of thousands of bright, nearby stars [319]. TESS has already flagged more than 7000 TESS Objects of Interest (TOIs) as potential exoplanets, but additional follow-up is necessary to validate their planetary nature. The transit method is especially susceptible to false positive scenarios [131] when utilizing the large pixels of TESS (21″), and additional data is typically required to validate the planetary nature of a TOI. Beyond ruling out false positives, additional ground-based follow-up is necessary to measure planetary parameters not typically accessible via photometry alone, such as planet mass and density.

The transit and radial velocity (RV) method together are especially sensitive to discovering

planets orbiting cooler, redder M dwarfs, the most common type of star in the galaxy [176]. Planets orbiting these late-type stars can make for unique science cases and climates [345], and are generally less studied than main sequence FGK stars, despite evidence that their population is distinct [104, 205].

Here we leverage TESS and ground-based photometry in conjunction with RV observations to validate two transiting M dwarf planets identified by TESS: TOI-1696b [282] and TOI-2136b. Both planetary systems see a refinement of their orbital parameters by utilizing knowledge from these photometric and RV datasets in conjunction.

TOI-1696 is a mid M dwarf (M4.5, V=16.8) with particularly deep transit events. The cool, small nature of the star and the relatively large transit depth suggest that this planet is an unusually large ($\sim$ 3 $R_\oplus$) mini-Neptune considering its host star's temperature (T_{eff}=3168 K)—planets larger than 2.8 $R_\oplus$ become quite rare around cool stars [104, 171, 188]. [282] highlighted several attractive features of the system: it has a high Transmission Spectroscopy Metric [TSM; 214] considering the cool nature of the star, and the planet is near the Neptunian desert [274]. An exoplanet that is unusually large, approaching the Neptunian desert, and that can be atmospherically studied can help explain or rule out planet formation scenarios, and our understanding of planetary evolution.

TOI-2136 is an early to mid M dwarf (M3, T_{eff} = 3366 K, V=14.3). The candidate planet is a small mini-Neptune ($\sim$ 2 $R_\oplus$); with an estimated equilibrium temperature of 403 K, TOI-2136b falls into a regime that allows for the existence of liquid water oceans beneath its gaseous envelope. TOI-2136's bright, close nature also puts this candidate planet in a potentially exciting region of parameter space for the detection of biosignatures: For example, TOI-2136b is an excellent candidate for a "cold Haber World," a unique environment where life could exist in oceans beneath a massive H/He envelope by combining hydrogen and nitrogen in the "Haber" process [338]. Such a process generates a detectable amount of ammonia, and TOI-2136b is not expected to produce ammonia in any other way.

In Section 4.2, we give a summary of the data used in our analysis. In Section 5.3, we detail our estimation of each system's stellar parameters. In Section 6.4, we detail the software and assumptions made during our analysis, and steps taken to measure the planetary and orbital parameters. In Section 6.5, we discuss our findings, and the implications for each system. Finally, Section 6.6 summarizes our results and conclusions.

2.2 Observations

2.2.1 TESS

TOI-1696 was observed by TESS during Sector 19 (2019 November 27 - 2019 December 24)[1]. It was observed for 27 days by CCD 2 of camera 1 in 2-minute cadence mode. It was then processed by the MIT Science Processing Operations Center (SPOC) pipeline [198], and was announced as a TOI on January 25, 2020, identifying a 2.5 day periodicity as TOI-1696.01. Photometry taken during Sector 19 is shown in Figure 2.1.

Similarly, TOI-2136 was observed in Sector 26 (2020 June 8th - 2020 July 4th) during TESS's nominal mission, and Sector 40 (2021 June 24th - 2021 July 23rd) during TESS's extended mission, in 2-minute cadence mode with CCD 1 of camera 1[2]. A 7.85 day planet candidate was identified on 2020 August 27 as TOI-2136.01. The target is also listed in Sector 14 by the Web-TESS Viewing Tool, but follow-up using the TESS-point [65] software package confirms that the target fell in a gap between CCDs during that Sector. Both observed sectors were processed using the SPOC pipeline and used for our subsequent analysis. We use the Pre-Search Data Conditioning Simple Aperture Photometry (PDCSAP) flux in our analysis. A plot of both sectors of TESS photometry for TOI-2136 is visible in Figure 2.2.

[1] 1696 DV: https://tev.mit.edu/data/atlas-signal/i165570/
[2] 2136 DV: https://tev.mit.edu/data/atlas-signal/i177995/

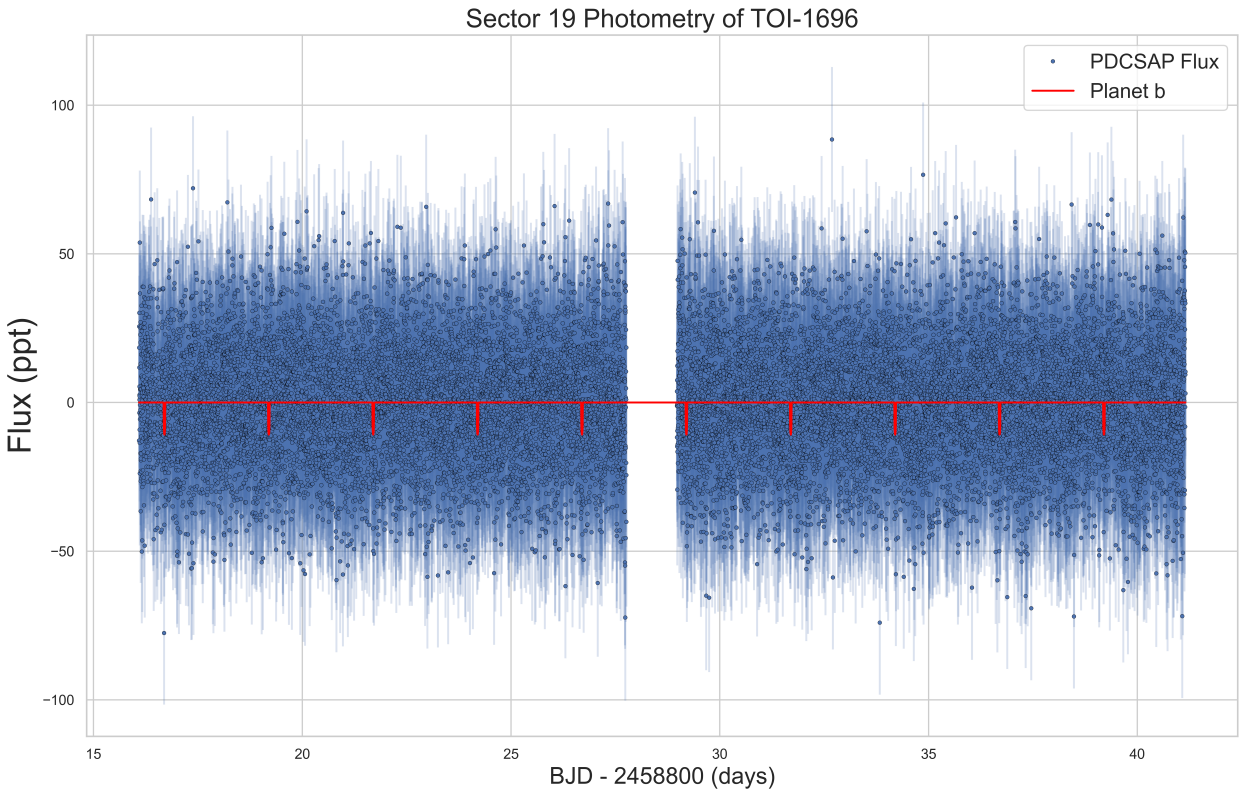

Figure 2.1: Sector 19 TESS PDCSAP flux of TOI-1696, reduced using the SPOC pipeline. A model representing the transits of planet b is indicated by a solid red line.

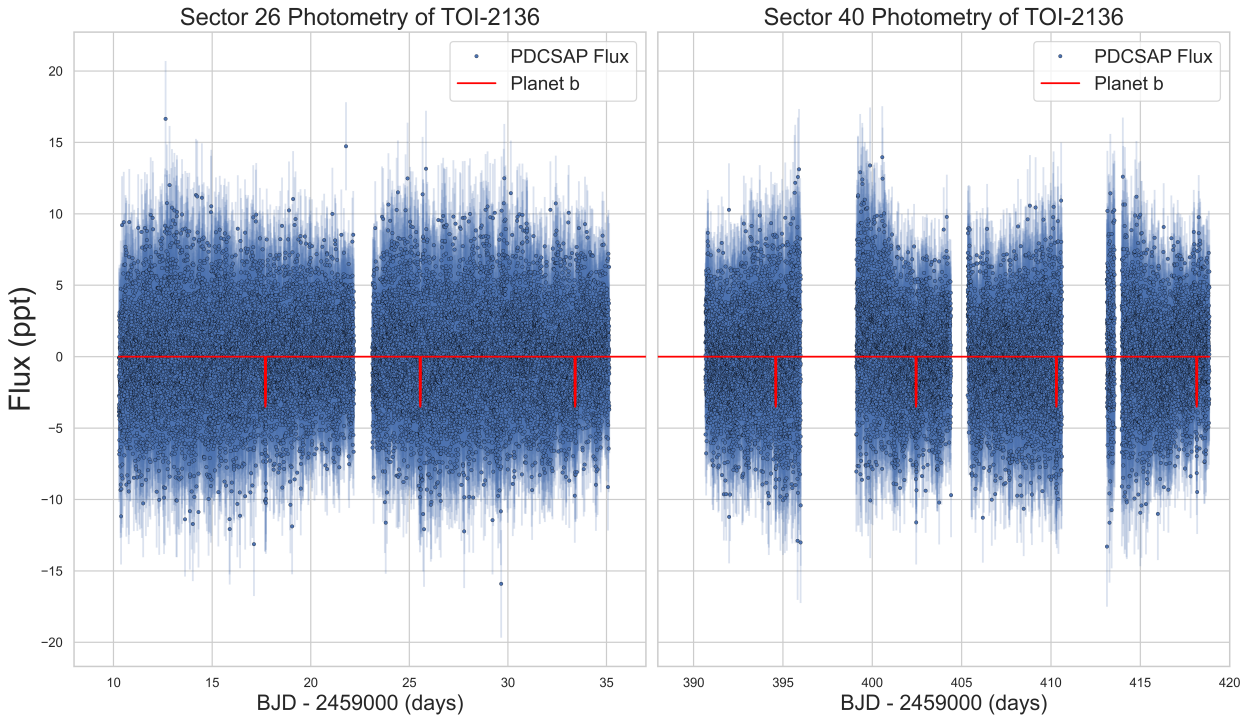

Figure 2.2: Sector 26 and 40 PDCSAP flux of TOI-2136. A model representing the transits of planet b is visible as a solid red line.

It should be noted that the Sector 40 photometry of TOI-2136 has several large gaps. The central data gap at $\sim$ BJD 2459405 is a standard data downlink. The other gaps, most notably BJD 2459396-2459399, BJD 2459411-2459413, and a small gap around BJD 2459414 are all due to an attitude adjustment of the spacecraft as described in the TESS Mission Handbook. These data were not used during the analysis.

2.2.2 Ground Based Photometric Follow-up

Ground based photometric follow-up is often necessary to validate the planetary nature of candidates flagged by TESS as TOIs [359, 72]. In addition to confirming signals, these follow-up transits provide tighter constraints on transit parameters for the candidate planets (e.g. [204]). We detail the photometric follow-up for these two planet candidates using ground based resources in the next section.

RBO

We observed a transit of TOI-1696 on the night of 2020 December 27 using the 0.6 m telescope at Red Buttes Observatory (RBO) in Wyoming [207]. The RBO telescope is a f/8.43 Ritchey-Chrétien Cassegrain constructed by DFM Engineering, Inc. It is currently equipped with an Apogee ASPEN CG47 camera.

The target rose from an airmass of 1.092 at the start of the observations to a minimum airmass of 1.009, and then set to an airmass of 1.419 at the end of the observations. Observations were performed using the Bessell I filter with 2×2 on-chip binning. We defocused moderately, which allowed us to use an exposure time of 120 s. In the 2×2 binning mode, the 0.6 m at RBO has a gain of 1.27 e/ADU, a plate scale of $1.05''$, and a readout time of approximately 2 s.

During data reduction we used a 9 pixel ($9.5''$) aperture and an annulus with an inner radius of 16 pixels ($16.8''$) and an outer radius of 24 pixels ($25.2''$).

We note that the latter observations seem to be affected by particularly high scatter. Analysis of airmass correlation doesn't resolve this issue, and so we conclude that the observations were possibly affected by clouds or poor seeing towards the end. The high scatter does not have a significant effect on our measured parameters, however, as it seems to be concentrated after egress. We leave the points for completeness.

Plots of RBO data are visible in Section 3.4.1, where they are analyzed.

ARCTIC

We observed transits of TOI-1696 and TOI-2136 on the nights of 2021 January 1 and 2020 October 5, respectively, using the Astrophysical Research Consortium (ARC) Telescope

Imaging Camera [ARCTIC; 190] at the ARC 3.5 m Telescope at Apache Point Observatory (APO). To achieve precise photometry on nearby bright stars, we used the engineered diffuser described in [360].

The airmass of TOI-1696 varied from 1.040 to 1.384 over the course of its observation on 2021 January 1. The observations were performed using the SDSS i' filter with an exposure time of 20 s in the quad-readout and fast readout modes with 4×4 on-chip binning. In the 4×4 binning mode, ARCTIC has a gain of 2 e/ADU, a plate scale of 0.468 ″/pixel, and a readout time of 2.7 s. We initially defocused to a FWHM of 4.4″. For the final reduction, we selected a photometric aperture of 8 pixels (3.7″) and used an annulus with an inner radius of 20 pixels (9.4″), and an outer radius of 30 pixels (14.0″).

The airmass of TOI-2136 varied from 1.016 to 1.420 over the course of its observation on 2020 October 5. The observations were performed using the SDSS i′ filter with an exposure time of 15.3 s in the quad-readout and fast readout modes with 4×4 on-chip binning. For the final reduction, we selected a photometric aperture of 17 pixels (8.0″), and an annulus with an inner radius of 32 pixels (15.0″) and an outer radius of 48 pixels (22.5″).

Plots of ARCTIC data are visible in Section 3.4.1, where they are analyzed.

2.2.3 Radial Velocity Follow-Up with the Habitable Zone Planet Finder

We observed both targets using HPF [262, 263], a near-infrared (8080 − 12780 Å), high precision RV spectrograph located at the 10 m Hobby-Eberly Telescope (HET) in Texas. HET is a fixed-altitude telescope with a roving pupil design. Observations on the HPF are queue-scheduled, with all observations executed by the HET resident astronomers [344]. HPF is fiber-fed, with separate science, sky and simultaneous calibration fibers [203], and

has precise, milli-Kelvin-level thermal stability [358].

To estimate the RVs, we use a modified version of the `SpEctrum Radial Velocity AnaLyser` pipeline [`SERVAL`; 405], reduced using the method outlined in [357]. `SERVAL` matches templates to the obtained spectra to create a master template from all observations, and then minimizes the χ^2 statistic to determine the shifts of each observed spectrum. This method is widely used for M dwarfs, where line blends make the binary mask technique less effective [e.g., 13]. We create a master template for each target from all it observed spectra. We mask telluric and sky-emission lines during this process. We calculate a telluric mask based on their predicted locations using `telfit` [162], a Python wrapper to the Line-by-Line Radiative Transfer Model package [83]. Despite their proximity to Earth, both targets are relatively faint. As a result, sky-fiber spectra were subtracted from the observations. Analyses were run on both sky-subtracted and non-sky-subtracted RVs to ascertain the effect of this correction. The final analysis results did not differ meaningfully between the runs. We adopt sky-subtracted RVs for both systems due to their faintness, and the long exposure times of both targets. We use `barycorrpy` to perform barycentric corrections [206].

RVs of TOI-1696 were obtained between 2020 September 27 and 2021 February 25. During this interval we obtained 30 unbinned RVs, taken over 10 observing nights. Each unbinned spectrum was observed for 650 seconds, with an average signal to noise ratio of 33.8. The average RV error was 34.7 m s^{-1} (unbinned) and 19.9 m s^{-1} (binned). The nightly binned RVs are visible in Table 2.1.

RVs of TOI-2136 were obtained between 2020 August 13 and 2021 September 19. We obtained 81 unbinned RVs of this system, taken over 27 observing nights. Each observation lasted for 650 seconds. The average signal to noise ratio was 81.7. The mean uncertainty of all of the observations is 14.1 m s^{-1} (unbinned) and 8.0 m s^{-1} (binned). A truncated list of nightly binned RVs can be seen in Table 2.2.

Table 2.1: HPF RVs of TOI-1696

BJD_{TDB} (days)	RV (m s^{-1})	σ_{RV} (m s^{-1})
2459119.84652	8	16
2459124.83479	-19	14
2459182.67317	34	17
2459187.88823	-27	19
2459210.59442	4	25
2459216.79185	15	22
2459232.76200	29	17
2459237.74584	44	19
2459238.74103	23	28
2459270.64775	-65	21

Table 2.2: HPF RVs of TOI-2136

BJD_{TDB} (days)	RV (m s^{-1})	σ_{RV} (m s^{-1})
2459074.79705	-13	7
2459087.75569	17	6
2459089.75413	9	6
2459090.74571	0	8
2459095.73448	-1	6
2459098.72963	5	8
2459118.68079	16	8
2459123.65313	-1	5

Continued on next page

Table 2.2 – continued from previous page

First column	Second column	Third column
2459125.65859	-8	6
2459129.63709	-11	7

2.2.4 High Resolution Imaging

ShARCS on the Shane Telescope

We observed TOI-1696 and TOI-2136 using the ShARCS camera on the Shane 3 m telescope at Lick Observatory [353]. TOI-1696 was observed using the K_S filter on the night of 2020 November 29. TOI-2136 was observed using the K_S filter and J filter on the night of 2021 May 28. Both targets were in a brightness regime where Laser Guide Star (LGS) mode is helpful, but this function was unavailable on both nights due to instrument repairs. Fortunately, conditions were good enough in both cases, and Natural Guide Star (NGS) mode proved to be sufficient. Both targets were observed using a 5 point dither process as outlined in [136].

The raw data are reduced using a custom pipeline developed by our team [359, 204]. Our reduction first rejects all overexposed or underexposed images, and we manually reject files we know to be erroneous from our night logs (lost guiding, shutters in frame, etc). We then apply a standard dark correction, flat correction, and sigma clip. We produce a master sky image from the 5 point dither process, and subtract this sky from each image. A final image is then produced using an interpolation process to shift the images onto a single centroid.

We then generate a 5 sigma contrast curve using algorithms developed by [110] as the final

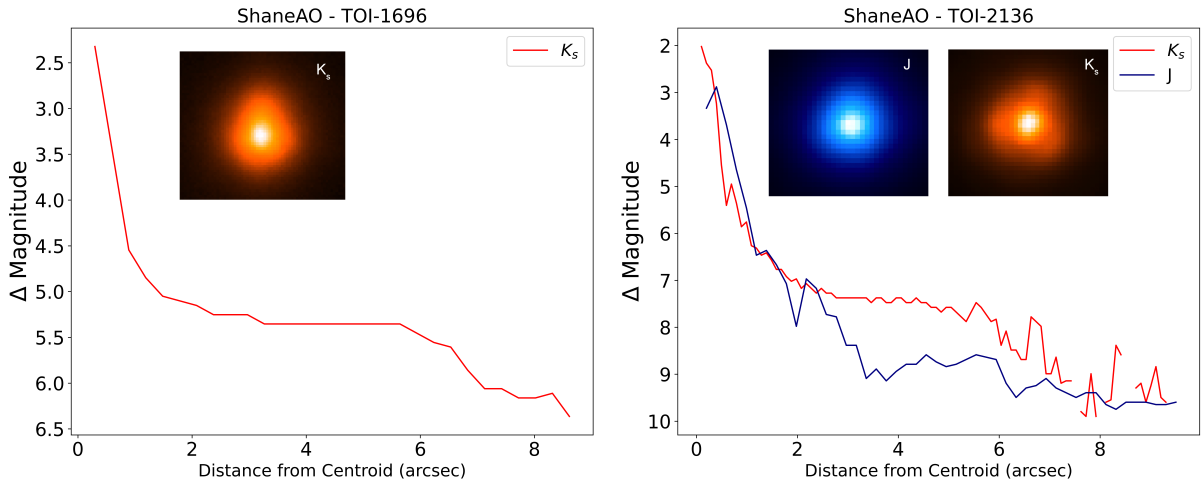

Figure 2.3: Left: 5σ contrast curve of TOI-1696 taken using the ShARCS camera at Lick Observatory on 2020 November 29 in the K_s band. Right: 5σ contrast curves of TOI-2136 taken using the K_s and J filters. The data were taken on 2021 May 28.

part of our analysis. For TOI-1696, we detect no companions at a ΔKs = 2.3 at 0.3″ and ΔKs = 5.4 at 5.9″. For TOI-2136, we rule out companions with a ΔKs = 2.4 and a ΔJ = 3.3 at 0.2″, and out to ΔKs = 7.8 and ΔJ = 8.7 at a distance of 5.9″.

NESSI at WIYN

In addition to Shane AO data, we acquired high-contrast imaging data for TOI-2136 with speckle imaging observations taken on 1 April 2021 using the NN-Explore Exoplanet Stellar Speckle Imager (NESSI) on the WIYN[3] 3.5m telescope at Kitt Peak National Observatory. To rule out additional close, luminous companions, we collected a 9 minute sequence of 40 ms diffraction-limited exposures of TOI-2136 with the r' and z' filters. As we show in Figure 2.4, the NESSI data show no evidence of blending from a bright companion down to a contrast limit of Δmag = 4 at 0.2″ and Δmag= 5.5 at 1″.

[3]The WIYN Observatory is a joint facility of the NSF's National Optical-Infrared Astronomy Research Laboratory, Indiana University, the University of Wisconsin-Madison, Pennsylvania State University, the University of Missouri, the University of California-Irvine, and Purdue University.

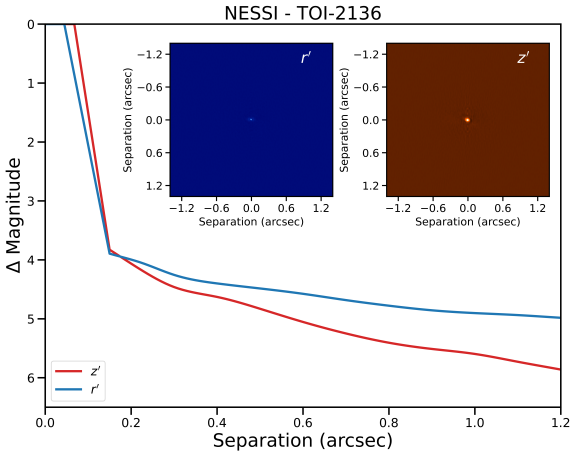

Figure 2.4: Images and contrast curves of TOI-2136 taken using the NN-Explore Exoplanet Stellar Speckle Imager (NESSI) on April 1, 2021. Data were taken in the r' and z' filters, and companions were ruled out to a distance of $1''$.

2.3 Stellar Parameters

We used a similar method to that in [357], Jones et al. (2023, in prep) to estimate $T_{\rm eff}$, $\log g$, and [Fe/H] values of the host stars from their spectra. The `HPF-SpecMatch` code, based on the `SpecMatch-Emp` algorithm from [402], compares the high resolution HPF spectra of both targets to a library of high SNR as-observed HPF spectra, which consists of slowly-rotating reference stars with well characterized stellar parameters from [402] and an expanded selection of stars from [265] in the lower effective temperature range.

We shift the observed target spectrum to a library wavelength scale and rank all of the targets in the library using a χ^2 goodness-of-fit metric. After this initial χ^2 minimization step, we pick the five best matching reference spectra for each target: GJ 3991, PM J08526+2818, GJ 402, GJ 3378, and GJ 1289 in the case of TOI-1696; GJ 251, GJ 581, GJ 109, GJ 436, and GJ 4070 in the case of TOI-2136. From these, we construct a weighted spectrum using their linear combination to better match the target spectrum (Jones et al., 2023, in prep). A weight is assigned to each of the five spectra for each respective target. We then assign the target stellar parameter $T_{\rm eff}$, $\log g$, and [Fe/H] values as the weighted average of the five

best stars using the best-fit weight coefficients. Our final parameters are listed in Table 2.3. These parameters were derived from the HPF order spanning 8670Å- 8750Å.

We artificially broadened the library spectra with a $v \sin i$ broadening kernel [155] to match the rotational broadening of the target star. We determined both TOI-1696 and TOI-2136 to have $v \sin i$ broadening values of < 2 km/s.

We used `EXOFASTv2` [108] to model the spectral energy distributions (SED) of both systems to derive model-dependent constraints on the stellar mass, radius, and age of each star. `EXOFASTv2` utilizes the BT-NextGen stellar atmospheric models [8] during SED fits. Gaussian priors were used for the 2MASS (JHK), SDSS ($g'r'i'$), Johnson (BV), and *Wide-field Infrared Survey Explorer* magnitudes (WISE; $W1$, $W2$, $W3$, and $W4$) [398]. Our spectroscopically-derived host star effective temperatures, surface gravities, and metallicities, were used as priors during the SED fits as well, and the estimates from [21] were used as priors for distance. We utilize estimates of Galactic dust by [156] to estimate the visual extinction for each system. We convert this upper limit to a visual magnitude extinction using the $R_v = 3.1$ reddening law from [116]. Our final model results are visible in Table 2.3.

Table 2.3: Stellar Parameters for TOI-1696 and TOI-2136

Parameter Name	Description	TOI-1696	TOI-2136	Reference
Identifiers				
TOI	TESS Object of Interest	1696	2136	TESS Mission
TIC	TESS Input Catalog	470381900	336128819	TICv8
Gaia	GAIA Mission	270260649602149760	2096535783864546944	Gaia EDR3
2MASS	2MASS Identifier	J04210733+4849116	18444236+3633445	2MASS
Coordinates				
α_{J2016}	Right Ascension (deg)	65.28065076(0)	281.17633745(6)	Gaia EDR3
δ_{J2016}	Declination (deg)	48.81982851(7)	36.56315642(6)	Gaia EDR3
μ_α	Proper Motion RA (mas yr^{-1})	12.87±0.03	-33.80±0.02	Gaia EDR3
μ_δ	Proper Motion DEC (mas yr^{-1})	-19.04±0.03	177.05±0.02	Gaia EDR3
Magnitudes				
V	Johnson V Magnitude	16.8±1.1	14.3±0.2	TICv8

Continued on next page

Table 2.3 – continued from previous page

Parameter Name	Description	TOI-1696	TOI-2136	Reference
B	Johnson B Magnitude	18.5±0.2	15.8±0.1	TICv8, APASS DR10
J	J-band Magnitude	12.23±0.02	10.18±0.02	TICv8
H	H-band Magnitude	11.60±0.03	9.60±0.03	TICv8
K_s	K_s-band Magnitude	11.33±0.02	9.34±0.02	TICv8
g'	Sloan g' Magnitude	17.58±0.03	14.9±0.2	APASS DR10
r'	Sloan r' Magnitude	16.2±0.1	13.2±0.3	APASS DR10
i'	Sloan i' Magnitude	14.61±0.03	11.9± 0.3	APASS DR10
W1	WISE 1 Magnitude	11.13±0.02	9.19±0.02	TICv8
W2	WISE 2 Magnitude	10.98±0.02	9.05±0.02	TICv8
W3	WISE 3 Magnitude	10.71±0.01	8.92±0.03	TICv8
W4	WISE 4 Magnitude	8.8[b]	8.76±0.02	TICv8
T	TESS Magnitude	13.966±0.007	11.737±0.007	TICv8
Spectroscopic Parameters				
$T_{\rm eff}$	Stellar Effective Temperature	3214±69	3443±69	This Work
[Fe/H]	Stellar Metallicity	0.25±0.12	-0.08±0.12	This Work
log g	Log Surface Gravity	4.96±0.04	4.91±0.04	This Work
Model Parameters[b]				
$T_{\rm eff}$	Stellar Effective Temperature	3168^{+39}_{-35}	3366^{+39}_{-41}	This Work
[Fe/H]	Stellar Metallicity	0.19±0.09	$-0.02^{+0.07}_{-0.03}$	This Work
$\log g$	Log Surface Gravity	4.96±0.03	4.92±0.03	This Work
M_*	Stellar Mass ($M_\odot$)	0.27±0.02	0.34±0.02	This Work
R_*	Stellar Radius ($R_\odot$)	0.287±0.008	0.335±0.009	This Work
L_*	Stellar Luminosity ($L_\odot$)	0.0075±0.0002	$0.0130^{+0.0004}_{-0.0005}$	This Work
ρ_*	Stellar Density (cgs)	$16.3^{+1.2}_{-1.1}$	$12.68^{+0.88}_{-0.85}$	This Work
Age	Stellar Age (Gyr)	7.1±4.6	$7.5^{+4.2}_{-4.8}$	This Work
Other Parameters				
$v \sin i$	Rotational Velocity (km s^{-1})	< 2	< 2	This Work
Δ RV	Stellar Radial Velocity (km s^{-1})	-4.1±0.1	0.0±0.1	This Work
d	Distance (pc)	64.62±0.14	33.33±0.02	This Work

2.4 Analysis

As detailed in Section 4.2, we have obtained photometry (TESS, RBO, ARCTIC) to constrain the transit events of TOI-1696 and TOI-2136, as well as RV data (HPF) to constrain the orbital parameters of each planetary system. Final parameter estimation is taken from a joint fit between the photometry and the RVs for both systems. In this joint fit, a few of the orbital parameters are shared: period, transit time, eccentricity, stellar mass, and inclination. Most of these parameters are quite well constrained prior to our joint modeling. Period and transit time are tightly constrained by the SPOC pipeline [198], the inclination must be close to 90^o by necessity, and the stellar mass is estimated to $> 15\%$ precision from our SED fits. A detailed summary of priors is visible in Table 2.4. Because most shared parameters are already tightly constrained, we do not expect a joint fit to be significantly better than individual transit and RV fits. Indeed, we did run individual RV and transit fits of this system, and found the estimated posteriors to have no significant difference from the joint fits. Nonetheless, we adopt a joint fit as our best fit, as it is the single model with the most complete description of each system.

Table 2.4: Priors Used for Various Models

Parameter Name	Prior	Units	Description
TOI-1696:			
Orbital Parameters			
P_b	$\mathcal{N}^a(2.5007, 0.1)$	days	Period
T_c	$\mathcal{N}(2458816.697706, 0.1)$	BJD (days)	Transit Time
e	0 (Fixed)	...	Eccentricity
ω	90 (Fixed)	degrees	Argument of Periastron
R_p/R_*	$\log \mathcal{N}(-2.211, 1.0)$	...	Scaled Radius
b	$\mathcal{U}^b(0.0, 1.0)$	...	Impact Parameter
K_b	$\mathcal{U}(0.01, 100)$	m s^{-1}	Velocity Semi-amplitude
Instrumental Parameters			
$\gamma_{\rm HPF}$	$\mathcal{U}(-100, 100)$	m s^{-1}	Instrumental RV Offset
$\dot{\gamma}_{\rm HPF}$	$\mathcal{U}(-100, 100)$	m s^{-1} yr^{-1}	RV Trend

Continued on next page

Table 2.4 – continued from previous page

Parameter Name	Prior	Units	Description
$\sigma_{\rm HPF}$	$\mathcal{U}(0.01, 100)$	m s^{-1}	RV Jitter
$\sigma_{\rm TESS}$	$\log\mathcal{N}(-7.58, 2)$	...	Photometric Jitter
$\sigma_{\rm ARCTIC}$	$\log\mathcal{N}(-11.68, 2)$	...	Photometric Jitter
$\sigma_{\rm RBO}$	$\log\mathcal{N}(-8.50, 2)$	...	Photometric Jitter
$\gamma_{\rm TESS}$	$\mathcal{N}(0.0, 10.0)$	...	Photometric Offset
$\gamma_{\rm ARCTIC}$	$\mathcal{N}(0.0, 10.0)$	...	Photometric Offset
$\gamma_{\rm RBO}$	$\mathcal{N}(0.0, 10.0)$	...	Photometric Offset
$u_{\rm TESS}$	$\mathcal{K}^c$	...	Quadratic Limb Darkening
$u_{\rm ARCTIC}$	$\mathcal{K}$	...	Quadratic Limb Darkening
$u_{\rm RBO}$	$\mathcal{K}$	...	Quadratic Limb Darkening
Dil$_{\rm TESS}$	$\mathcal{U}(0, 2)$	...	Dilution
s	$\mathcal{U}(0, 10)$	...	RBO Jitter Scale
TOI-2136:			
Orbital Parameters			
P_b	$\mathcal{N}(7.851866, 0.1)$	days	Period
T_c	$\mathcal{N}(2459017.704899, 0.1)$	BJD (days)	Transit Time
e	0 (Fixed)	...	Eccentricity
ω	90 (Fixed)	degrees	Argument of Periastron
R_p/R_*	$\log\mathcal{N}(-2.71, 1.0)$	...	Scaled Radius
b	$\mathcal{U}(0.0, 1.0)$	...	Impact Parameter
K_b	$\mathcal{U}(0.01, 100)$	m s^{-1}	Velocity Semi-amplitude
Instrumental Parameters			
$\gamma_{\rm HPF}$	$\mathcal{U}(-100, 100)$	m s^{-1}	Instrumental RV Offset
$\dot{\gamma}_{\rm HPF}$	$\mathcal{U}(-100, 100)$	m s^{-1} yr^{-1}	RV Trend
$\sigma_{\rm HPF}$	$\mathcal{U}(0.01, 100)$	m s^{-1}	RV Jitter
$\sigma_{\rm TESS}$	$\log\mathcal{N}(-7.94, 2)$	...	Photometric Jitter
$\sigma_{\rm ARCTIC}$	$\log\mathcal{N}(-6.21, 2)$	...	Photometric Jitter
$\gamma_{\rm TESS}$	$\mathcal{N}(0.0, 10.0)$	...	Photometric Offset
$\gamma_{\rm ARCTIC}$	$\mathcal{N}(0.0, 10.0)$	...	Photometric Offset
$u_{\rm TESS}$	$\mathcal{K}$	...	Quadratic Limb Darkening
$u_{\rm ARCTIC}$	$\mathcal{K}$	...	Quadratic Limb Darkening
Dil$_{\rm TESS}$	$\mathcal{U}(0, 2)$	...	Dilution

[a] $\mathcal{N}$ is a normal prior with $\mathcal{N}$(mean,standard deviation)

[b] $\mathcal{U}$ is a uniform prior with $\mathcal{U}$(lower,upper)

[c] $\mathcal{K}$ is a reparametrization of a uniform prior for limb darkening, outlined in [216]

2.4.1 Transit Analysis

Both systems' photometry were analyzed using the exoplanet software package [127]. First, the TESS photometry was downloaded using lightkurve [236] for both targets. Data points flagged as poor quality during the SPOC pipeline were then discarded, and we median-normalized the lightcurves of both targets and centered them at 0. Then we imported our additional ARCTIC and RBO photometry and combined the datasets.

We used exoplanet to construct a physical transit model for each system. These models consisted of mean term for each instrument, 3 for TOI-1696, and 2 for TOI-2136, to account for any offsets. The same number of jitter terms were used to account for excess white noise in each instrument.

As mentioned in Section 2.2.2, the RBO photometry exhibits a peculiar increase in scatter throughout the night. Unable to account for this by decorrelating with airmass, and with no additional explanations revealed in the night observing logs, we adopt a method in our model to increase the jitter of RBO data as the night goes on. This modified RBO jitter is given in equation 2.1. In this equation, $\sigma'_{RBO}[i]$ represents the ith component of the vector of values that we add in quadrature to the RBO errorbars. σ_{RBO} is the traditional jitter term analogous to those used in TESS and ARCTIC fits. t$_i$ is the time passed since the first RBO observation. t$_{tot,RBO}$ is the total duration of the RBO observations, and s is the RBO jitter scale, a new free parameter to control how much the error bars should increase in time.

$$\sigma'_{RBO}[i] = \sigma_{RBO}(1 + t_i/t_{tot,RBO})^s \tag{2.1}$$

The SPOC pipeline [198] performs an automatic dilution adjustment on the PDCSAP flux

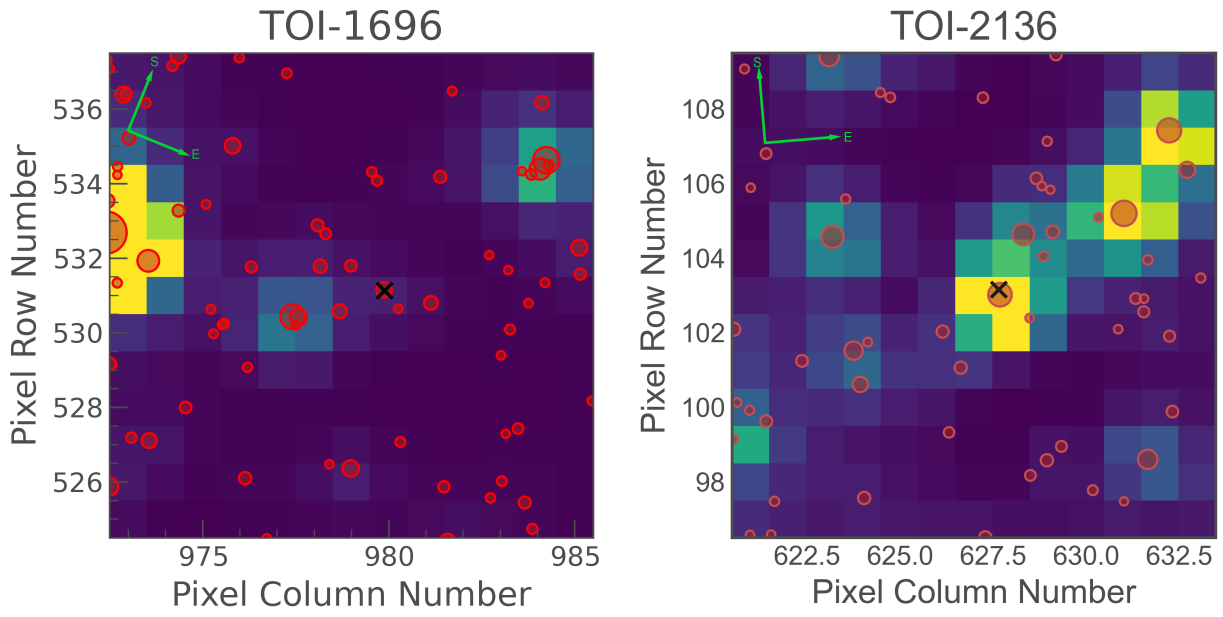

Figure 2.5: TESS pixel plots of TOI-1696 and TOI-2136 made using the eleanor software package [114]. Each square is a TESS pixel. The color of a pixel indicates the flux present. A black x near the center represents the TICv8 resolved position of the source. Red circles are Gaia resolved sources with Gaia magnitudes < 19, and the size of the circle represents the brightness of the source. The fields for both stars have many possible sources of contamination. The left field is of Sector 19, the right field of Sector 26.

of TESS lightcurves. This dilution increases the depths of transits to account for flux from nearby, adjacent stars, and is particularly important in crowded fields [67]. We include pixel images of TOI-1696 and TOI-2136 in Figure 2.5. We see from inspection that both fields are crowded, and that a dilution term might be important. TOI-1696 has an estimated contamination ratio of 0.1102, meaning that 11% of its flux is likely from nearby sources [355]. TOI-2136 has a contamination ratio of 0.1498. Both values warrant caution during analysis. Thus, we adopt as a part of our transit model a dilution term that floats between 0 and 2. A value of < 1 suggests that contamination is still present, and additional correction is required. A value > 1 suggests that the flux has been over-corrected for dilution by the SPOC pipeline. The model radius parameter is multiplied by the square root of this dilution term to allow an increase or decrease depending on dilution.

The transiting orbit model was generated using built-in exoplanet functions and the `starry`

lightcurve package [254], which models the period, transit time, stellar radius, stellar mass, eccentricity, radius, and impact parameter to produce a simulated lightcurve. We adopt quadratic limb darkening terms to account for the change in flux that occurs when a planet approaches the limb of a star [216].

A Gaussian Process (GP) model [10] was considered to account for excess correlated noise, as this is often done when analyzing the TESS photometry of even quiet stars [e.g 252]. However, both systems' photometry showed little evidence for coherent noise, and GP whitened results showed no signficant difference from models without GPs. Thus, in the pursuit of simplicity, we dispensed with any pre-fit whitening and fit transits to PDCSAP flux with no modification.

We chose to adopt fairly broad Gaussian priors with a width of 0.1 days for period and transit time to prevent any bias in our fits. Other free parameters had broad priors to reflect the wide array of possible values. A full list of the priors used is listed in Table 2.4.

Due to the proximity of both systems to their host stars, and the estimated age of each system, we attempt to determine whether eccentric fits were reasonable by calculating the circularization time for both planets. This time is calculated using equation 2.2, as detailed in [150].

$$\tau_{circ} = \frac{2PQ'}{63\pi}\left(\frac{M_p}{M_*}\right)\left(\frac{a}{R_p}\right)^5 \tag{2.2}$$

Here, P is the planet's orbital period, Q′ is a friction coefficient, M_p is the planet mass and M_* is the stellar mass. R_p is the planet radius, and a is the semi-major axis.

Because neither system has a well-constrained planet mass, we have opted to use the 3σ

upper limits of our mass estimates, since circularization time increases with planetary mass. The parameter Q' isn't known for either system, and must be estimated. This parameter represents the efficiency with which energy is lost due to tidal deformation. We adopt a similar approach to that used in [389], and attribute to each planet a $Q' = 1 \times 10^4$ since they are both in the radius regime of mini-Neptunes, though we caution that this is an assumption.

For TOI-1696, we estimate a circularization timescale of 0.062 Gyr using the 3σ upper limit of mass $M_p = 56.6\ M_\oplus$. Using the median estimate of the mass results in an even smaller timescale, 0.011 Gyr. We therefore conclude that eccentricity is unlikely to be present in this system, and can be fixed to 0.

On the other hand, for TOI-2136 we estimate a circularization timescale of 24.2 Gyr if we take its mass at a 3σ upper limit of 15.0 $M_\oplus$. Even taking the median value of 4.70 $M_\oplus$ gives a circularization timescale of 7.49 Gyr, well within the uncertainties of our stellar age. We thus conclude that eccentric fits are perfectly feasible for TOI-2136, and must be considered in our final results.

The total models for each system were then optimized using `scipy.optimize` to find a maximum a posteriori (MAP) fit to provide a starting point for posterior inference [384]. We then ran a Markov Chain Monte Carlo (MCMC) sampler to explore the posterior space of each model parameter. We use the Hamiltonian Monte Carlo (HMC) algorithm with a No U-Turn Sampler (NUTS) for efficiency [179]. We ran 10000 tuning steps and 10000 subsequent steps, and assessed convergence criteria using the Gelman-Rubin (G-R) statistic [119]. The final transit fit of TOI-1696 is visible in Figure 2.6, and of TOI-2136 in Figure 2.7. The posterior parameters of each system are listed in Table 2.6.

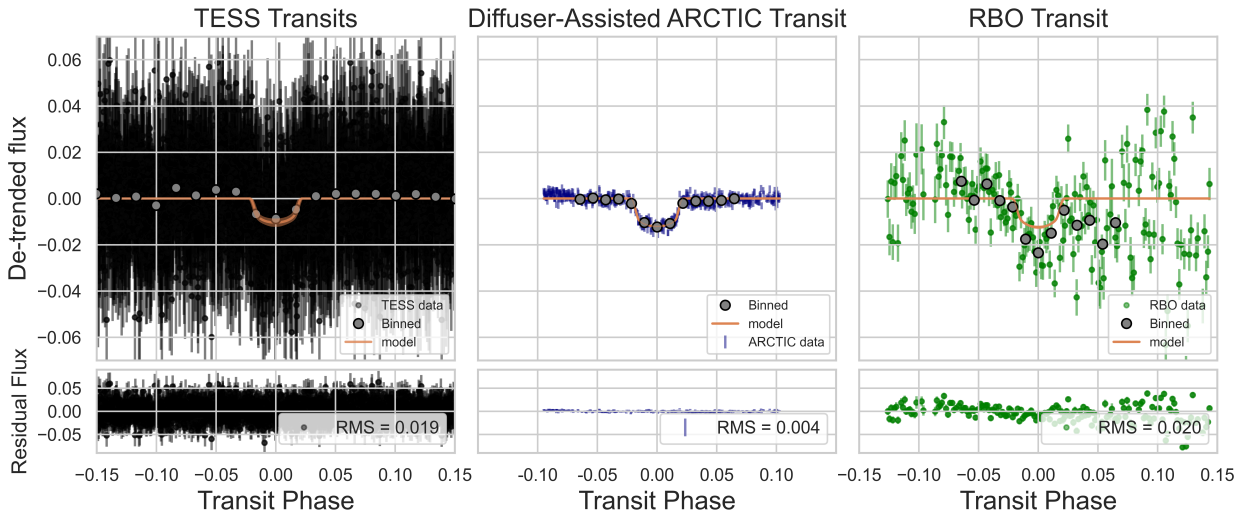

Figure 2.6: Left: phase-folded TESS transits of TOI-1696, with binned points highlighted and the median lightcurve prediction overlaid. Middle: ARCTIC transit of TOI-1696 captured on 1 January 2021. Binned photometry and the median lightcurve prediction are overlaid. Right: RBO transit of TOI-1696 captured on 27 December 2020. Binned photometry and median lightcurve prediction are overlaid.

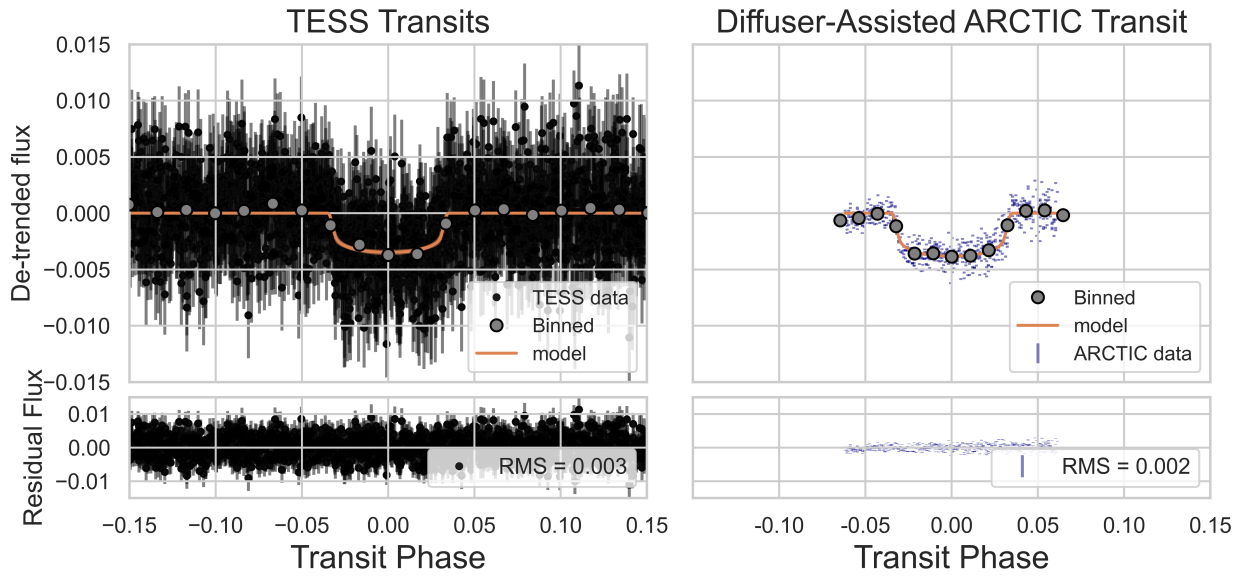

Figure 2.7: Left: TESS photometry of TOI-2136 folded to the final estimated period for planet b. Binned points are plotted in addition to the median lightcurve prediction. Right: ARCTIC transit of TOI-2136 obtained on 5 October 2020. Binned photometry is plotted in gray in addition to the median lightcurve prediction in orange.

2.4.2 Radial Velocity Analysis

Both systems' radial velocities were analyzed independently using the radvel RV fitting software [133], in addition to being used in a joint model with exoplanet. In both software packages the planet's RV signal is represented by a Keplerian orbit constrained by five planetary parameters: period, time of conjunction, RV semi-amplitude, eccentricity, and argument of periastron.

For TOI-1696, we detailed in Section 3.4.1 that an eccentric fit is unlikely for this system, but an eccentric fit is plausible for TOI-2136. Nonetheless we run eccentric fits on the RVs for both systems, and perform a model comparison, seen in Table 3.3.

For both the RV-only fits and the joint-photometry fits, a jitter term is included to account for excess white noise, and a mean term is included to account for any systematic offset in the RVs, though with only one instrument this shouldn't be significantly different from 0. Due to the well constrained ephemeris in the TESS data, tight priors were placed on the period and time of conjunction of both systems. We used broad, uninformative priors for the remaining free parameters that are not constrained by photometry. A full list of our priors can be seen in Table 2.4.

The RV only fits utilized the Powell optimization method [310] to provide an initial starting guess for every parameter. We then ran an MCMC sampler in radvel, which utilizes the ensemble sampler outlined in [125], to explore the parameter space of the model. We used the G-R statistic again to assess convergence.

The joint RV-photometry fits were performed in exoplanet in a nearly identical framework to the transit analysis described in Section 3.4.1, with the addition of the RV data and free parameters listed above. The final outputs from the joint fit are listed in Table 2.6. The final RV fits can be seen for TOI-1696 in Figure 2.8, and TOI-2136 in Figure 2.9.

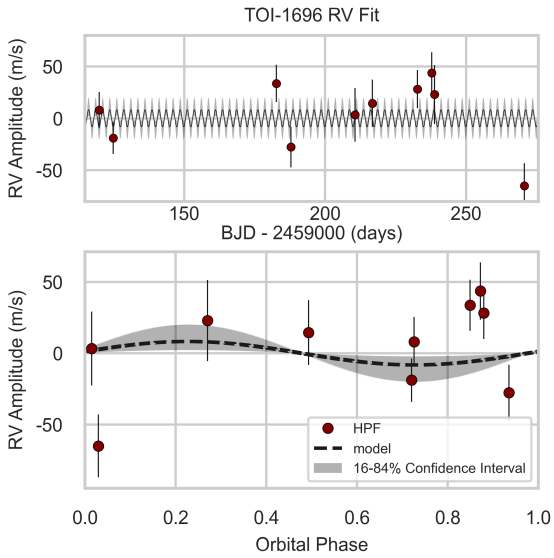

Figure 2.8: Top: Total HPF RV timeseries of TOI-1696. Bottom: Final, phase-folded RV fit for TOI-1696b. Large uncertainties and a relatively small number of points only allow us to put an upper limit on the planet's amplitude. A 1σ confidence interval is overlaid in gray.

Table 2.5: RV Model Comparisons

Fit	Free Parameters	Number of Parameters	BIC	RMS (m s^{-1})
TOI-1696:				
Circular	K, P, T_c, γ, σ, dv/dt	6	111.24	31.36
Eccentric	K, P, T_c, γ, σ, dv/dt, e, ω	8	115.82	31.36
TOI-2136:				
Circular	K, P, T_c, γ, σ, dv/dt	6	213.59	8.66
Eccentric	K, P, T_c, γ, σ, dv/dt, e, ω	8	214.64	8.10
Circular + GP	K, P, T_c, γ, σ, dv/dt, η_1, η_2, η_3, η_4	10	223.88	6.01

RV Analysis of TOI-1696

As detailed in Section 3.4.1, TOI-1696b is unlikely to have an eccentric orbit. Nonetheless, we allowed the eccentricity and argument of periastron to vary in some of our fits, and performed a model comparison to evaluate which model fits the data the best. These comparisons are visible in Table 3.3. We use the Bayesian Information Criterion [BIC; 208] to compare models. A "Bayes Factor" is computed as the half the difference in BIC of the simpler model minus the more complex model. A Bayes Factor of > 3.2 suggests a substantial preference for the more complex model.

After analysis, the circular model is slightly preferred, though the difference in BIC values is too small to be considered statistically significant. Because the circular model has fewer free parameters, and because of our circularization arguments in Section 3.4.1, we adopt a circular fit as our best solution.

RV Analysis of TOI-2136

As mentioned in Section 3.4.1, TOI-2136b has a long circularization timescale, and we cannot rule out an eccentric orbit. Eccentric and circular fits were evaluated, and compared using their BIC. Our results in Table 3.3 indicate that a more complex model cannot be justified. We go forward with a circular fit since it has fewer free parameters.

When we first chose TOI-2136 as a target, we made white-noise error estimates to determine the number of RVs that would be required to measure the mass of planet b to 3σ. Using the Mass-Radius relationship in [205], we estimated that the planet would have a semi-amplitude of 4 m s^{-1} and that we would have a photon-noise single-measurement error of 6.5 m s^{-1}. Our estimated posterior amplitude ($K_{med} = 3.02$ m s^{-1}) and median error ($\sigma_{median} = 7.87$ m s^{-1}) suggest that both estimates were reasonable. However, our final results have a much

less significant mass measurement at $K/\sigma_K < 2$. This suggests three possible explanations: the planet's mass is significantly smaller than our median prediction, activity from the star is interfering with our mass measurements, or the existence of additional planets may be confounding our models.

We used a Generalized Lomb-Scargle periodogram [GLS; 404] to analyze several activity indicators (line width, Ca infrared triplet). Results suggest that this is a quiet star, though modestly strong peaks at $\sim$ 5, 19, and 60 days in the Ca infrared triplet and line width periodograms are suggestive of possible rotation periods. It is often possible for activity present in RVs, however, to have no clear signal in one or more activity indicators [322, 251], and so we proceed forward with our investigation despite the lack of clear detections.

We have enough RVs for TOI-2136 such that we might utilize a GP without overfitting. GPs are commonly utilized to mitigate activity and improve model fits [173, 248, 106]. Our RV-only analysis utilized the robust Quasi-Periodic GP kernel [133]. The covariance matrix of this kernel is described in Equation 2.3. It contains 4 hyperparameters to model the activity: η_1 is the amplitude of covariance, η_2 is the evolution timescale, η_3 is the recurrence time scale (usually the rotation period of the star), and η_4 is the structure parameter.

$$\sigma_{i,j} = \eta_1^2 \exp\left(- \frac{|t_i - t_j|^2}{\eta_2^2} - \frac{\sin^2(\frac{\pi(t_i - t_j)}{\eta_3})}{2\eta_4^2} \right) \tag{2.3}$$

Our joint RV-Photometry-GP fits utilized the Rotation Term kernel in exoplanet, which is a combination of two Simple Harmonic Oscillator (SHO) kernels. The SHO kernel is fast and widely applicable to coherent stellar astrophysical noise sources [120]. The Fourier transform of the SHO is known as the Power Spectral Density (PSD) and can be seen in equation 2.4.

$$S(\omega) = \sqrt{\frac{2}{\pi}} \frac{S_0 \omega_0^4}{(\omega^2 - \omega_0^2)^2 + \omega^2 \omega_0^2 / Q^2} \tag{2.4}$$

The free parameters of this kernel are S_0, ω_0, and Q. S_0 represents the power of the periodicity in Fourier space, ω_0 is the angular frequency of the coherent noise, and Q is the quality factor.

The hyperparameters of the GPs were generally given wide priors when fit. η_1 was given a uniform prior from 0.1 m s^{-1} to 50.0 m s^{-1}. The η_2 and η_4 parameters were given, broad, uniform log priors from -6 to 6. The rotation period prior, η_3, can often be restricted much better due to some independent measurement of the rotation period. We performed an autocorrelation function (ACF) rotation analysis on the TESS photometry using an internally developed pipeline (Holcomb et al. 2022, in prep), and found no signficant detection of a rotation period in either sector for TOI-2136. Additionally, we analyzed publicly available photometry from the All-Sky Automated Search for Supernovae [ASAS-SN; 343, 217] and the Zwicky Transient Facility [ZTF; 267, 42] using GLS periodograms. We found no significant signals corresponding to a rotation period in the ASAS-SN photometry, but we do note a strong signal at 85.6 days in the ZTF data. This value is consistent with a rotation period described in [293]. Such a long rotation period is suggestive of a low amplitude activity signal. Regardless, analysis was performed with both tight priors around the purported stellar rotation period, and with loose, uniform priors from 1.0 - =200.0 days.

Both analyses resulted in posterior estimates nearly identical to those without the use of a GP. A comparison of the BIC of the RV-only GP fit, to other RV fits, is visible in Table 3.3.

The lower BIC (and thus higher log likelihood) of the simpler, no GP, non-eccentric model, suggest that it is the preferred model, especially considering its smaller number of free parameters. We adopt this as our final fit.

2.4.3 An Additional Planet Orbiting TOI-2136?

With a GP unable to explain our low-significance mass measurement, we turn to the next possibility: an additional planet, or planets. We began with an internally developed pipeline that utilizes a Boxed-Least Squares [BLS; 223] algorithm to search for an additional transiting planet in the TESS data. After subtracting our best-fit lightcurve model of TOI-2136b from the photometry, we ran the BLS analysis and noted no significant detections of additional transiting planets.

To probe for smaller transiting exoplanets, we used the `Transit-Least Squares` (`TLS`) python package to check for additional signals with greater sensitivity [178]. This `TLS` method is more computationally intensive than the BLS, but adopts a more realistic transit shape, and is more sensitive to small-radius transiting exoplanets.

The `TLS` package initially recovers TOI-2136b with high significance. Masking the transits of the first planet, we ran the analysis again. The result was a forest of small peaks, with no single signal standing out as a clear candidate planet. `TLS` uses the Signal Detection Efficiency (SDE) to estimate significant periods. [104] suggest that an SDE > 6 represents a conservative cutoff for a "significant" signal, though others adopt higher values [348, 245]. The original transiting signal of TOI-2136 has an SDE of 17.0, indicating a highly significant detection. After masking planet b, the forest of peaks all fall under the SDE $= 6$ threshold, with the highest having SDE $= 4.8$. We conclude that none of these signals are transiting planets.

We therefore detect no additional transiting planets in the photometry of TOI-2136b. Analysis of RV residuals, after the fitting of a single planet, also returns a forest of low significance peaks, all below the 0.01% analytical false alarm probability (FAP) [367]. This does not rule out an additional planet as an explanation for our low mass significance, especially considering that the transiting planet also falls below our significant threshold in RVs, but

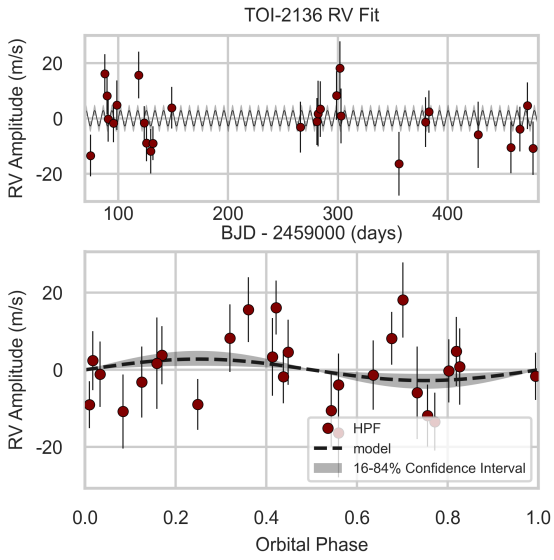

Figure 2.9: Top: Total HPF RV timeseries of TOI-2136. Bottom: Final RV fit for TOI-2136b, folded to the estimated period of the planet. A 1σ confidence interval is overlaid.

we find no definitive evidence of such a companion in RVs or photometry.

Table 2.6: Derived Parameters for Both Systems

Parameter	Units	TOI-1696	TOI-2136
Orbital Parameters:			
Orbital Period	P (days)	2.50031±0.00002	7.85191±0.00004
Eccentricity	e	0 (fixed)	0 (fixed)
Argument of Periastron ..	ω (degrees)	90 (fixed)	90 (fixed)
RV Semi-Amplitude[a]	K (m/s)	< 63.1	< 9.63
Systemic Offset	γ (m/s)	9±13	0±1.8
RV trend	dv/dt (mm/s/yr)	0.00±0.03	0.00±0.03
RV jitter	$\sigma_{\rm HPF}$ (m/s)	31^{+14}_{-10}	4.4±2.4
Transit Parameters:			
Transit Midpoint	T_C ($\rm BJD_{TDB}$)	2458816.699±0.002	2459017.7039±0.0006
Scaled Radius	R_p/R_*	0.104±0.002	0.058±0.001
Scaled Semi-major Axis ..	a/R_*	17.7±0.6	35.0±1.3
Impact Parameter	b	0.56±0.05	0.41±0.10

Continued on next page

Table 2.6 – continued from previous page

Parameter	Units	TOI-1696	TOI-2136
Orbital Inclination	i (degrees)	88.461±0.004	88.441±0.003
Transit Duration	T_{14} (days)	$0.0428^{+0.0009}_{-0.0008}$	0.0693±0.0008
Limb Darkening	$u_{1,\mathrm{TESS}}$, $u_{2,\mathrm{TESS}}$	$0.5^{+0.5}_{-0.3}$,0.1±0.4	$0.3^{+0.3}_{-0.2}$, $0.2^{+0.4}_{-0.3}$
	$u_{1,\mathrm{ARCTIC}}$, $u_{2,\mathrm{ARCTIC}}$	0.4±0.3, $0.1^{+0.4}_{-0.3}$	0.2±0.2, $0.3^{+0.3}_{-0.4}$
	$u_{1,\mathrm{RBO}}$, $u_{2,\mathrm{RBO}}$	$0.6^{+0.6}_{-0.4}$,0.0±0.5	...
Photometric Jitter	σ_{TESS} (ppm)	104^{+169}_{-79}	31^{+39}_{-21}
	σ_{ARCTIC} (ppm)	1030±91	929±28
	σ_{RBO} (ppm)	4300±1200	...
RBO Jitter Scale	s	3.1±0.6	...
Photometric Mean	$\mathrm{mean}_{\mathrm{TESS}}$ (ppm)	65±188	32±19
	$\mathrm{mean}_{\mathrm{ARCTIC}}$ (ppm) ..	440±83	1980±59
	$\mathrm{mean}_{\mathrm{RBO}}$ (ppm)	4449±1100	...
Dilution	D_{TESS}	0.86±0.14	0.92±0.07
Planetary Parameters:			
Mass[a]	M_p ($\mathrm{M}_\oplus$)	< 56.6	< 15.0
Radius.....	R_p ($\mathrm{R}_\oplus$)	3.24±0.12	2.09±0.08
Density[a]	ρ_p ($\mathrm{g/\,cm^3}$)	< 9.44	< 9.53
Semi-major Axis.....	a (AU)	0.0235±0.0006	0.054±0.001
Average Incident Flux	$\langle F \rangle$ ($\mathrm{W/m^2}$).....	18000^{+972}_{-859}	6000^{+300}_{-260}
Planetary Insolation	S ($\mathrm{S}_\oplus$).....	13.5±0.7	4.4±0.2
Equilibrium Temperature[b]	T_{eq} (K)	533±7	403±5

[a]Represents a 3σ (99.7%) confidence upper limit

[b]Estimated assuming an albedo of 0

2.5 Discussion

One of the most important open questions in the field of exoplanet astronomy is how planets retain or lose their atmospheres. This is particularly important when studying planets around M dwarf hosts. Not only are these stars the most abundant stellar type in the Galaxy [176], but their extreme UV environments likely play a significant role in sculpting their planets' atmospheres.

Mini-Neptunes present an ideal environment with which to study atmospheres of exoplanets, especially close-in ones that have excellent prospects for transmission spectroscopy. Their overall bulk densities suggest that these planets possess an atmosphere potentially dominated by a large H/He envelope. Such planets' atmospheres are easier to study, and their abundance means that we have a large number of possible systems to choose from. Mass estimates, too, become important in this regime, as there are a number of different possibilities for sub-Neptune compositions that are not well understood [406, 50, 35].

While we have only managed to place upper limits on the masses of both TOI-1696 and TOI-2136, we have measured their radii to high precision (Table 2.6). While we cannot claim to have detected a low density (and therefore large atmosphere), we can claim that it is quite unlikely for these planets not to have an extended atmosphere: for either to be primarily terrestrial, these planets would have to be truly unique in exoplanet parameter space, as any detections of such massive terrestrial planets so far have been erroneous [i.e. 313]. Thus, we will go forward under the assumption that both TOI-1696b and TOI-2136b are at the very least not terrestrial.

We have calculated the Transmission Spectroscopy Metric [TSM; 214] for both targets: 89.8 and 92.0, respectively. The TSM is a metric developed to rate the value of a target's amenability to atmospheric follow-up using the JWST. Both values are at or above the suggested cutoff for transmission spectroscopy follow-up.

2.5.1 TOI-1696

With the combination of TESS photometry and ground-based photometric follow-up, we were able to put a tight constraint on TOI-1696b's radius. With an estimated radius of 3.24±0.12 $R_\oplus$, TOI-1696b falls into a surprising region of radius-stellar effective temperature parameter space. As early as the *Kepler* mission, a relationship between planet size and stellar temperature was observed: the occurrence rate of smaller, rocky planets increases significantly for cooler stars, while the presence of larger planets ($R_p > 2.5\ R_\oplus$) falls off appreciably [104]. Later studies confirmed the veracity of this and noted that planets with radii above 2.8 $R_\oplus$ are particularly rare [287]. *Kepler* did not discover a large number of planets orbiting M dwarfs due to the nature of its mission: most observed M dwarfs were too far away and therefore dim for detailed study. It is only with the recent advent of TESS and its all-sky survey of nearby stars that we have been able to study the population of short period planets transiting these cooler stars [25].

In particular, there is more than an order of magnitude fewer exoplanets discovered around M dwarfs than there is around FGK dwarfs [45], despite the abunduance of M dwarf stars. As a result, phenemona such as the exoplanet radius valley [134, 84, 382] are difficult to discern when looking at M dwarfs alone. Thus, there is great value in validating exoplanets orbiting M dwarfs, especially cooler ones where large exoplanets become very rare. In Figure 2.10 it is clear that larger exoplanets are unusual around cooler stars, and that larger radii exoplanets become even more sparse the cooler the star. Only 10 currently confirmed planets orbit stars with $T_{\rm eff} < 3500$ K while also having a radius $> 2.8\ R_\oplus$ [219, 233, 17, 117, 24, 361, 75, 396, 301, 407]. Further, only 5 of these are close to their star, with $P_{orb} < 100$ days. An illustration of TOI-1696b's strange position in period-radius space is visible in Figure 2.11. By studying a planet on the edge of M dwarf radius parameter space, we position ourselves to better answer questions about formation processes around cool stars, and to examine any dependencies or correlations with other physical parameters (i.e. metallicity).

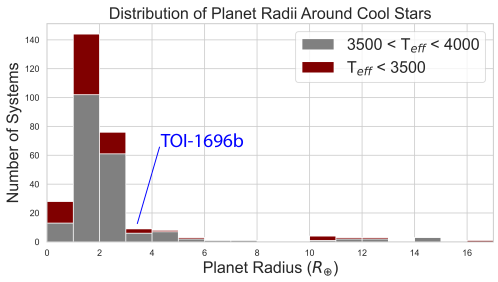

Figure 2.10: Stacked histogram of the radii of known planetary systems around cool stars, taken from the NASA Exoplanet Archive [7]. The total sample is of all planets orbiting stars cooler than 4000 K. Notable is the relative paucity of giant planets around stars in this temperature regime. The occurrence rate is inversely proportional to $T_{\rm eff}$ [104], and we further show a subset of this sample with $T_{\rm eff} < 3500$ K in red. TOI-1696b, with a radius of 3.24 $R_\oplus$ is unusually large for a star with $T_{\rm eff} = 3168$ K, and its placement in the histogram is indicated in blue.

In particular, we expect comparisons between TOI-1696b and other mini-Neptunes in more common regions of paramater space to highlight exactly what qualities make larger mini-Neptunes around cool stars unlikely.

Additionally, for sub-Neptunes, there is some degeneracy between the compositions of planets between 2 - 4 $R_\oplus$. In particular, similar masses in this range can be explained either by gaseous planets with rocky cores and large envelopes of H/He, or "water worlds" with large envelopes of H_2O fluid/ice, in addition to rock and gas [e.g. 406]. Whether or not a sub-Neptune's atmosphere has lighter elements (H/He), or heavier (H_2O/CO_2) can have important implications for its formation and the history of the protoplanetary disk of the system [379, 306, 11]. Such information can even be used to infer the existence of large companions on much wider orbits [50].

TOI-1696b also falls near the "Neptune desert," a region of parameter space where Neptune-sized objects become very rare [274]. Several possible explanations for this "Neptune desert," exist. For example, [268] suggest that this feature is a natural result of tidal circularization as high eccentricity Neptunes exchange angular momentum with their host star. On the other hand, [300] suggest that photoevaporation of short period sub-Jovians is the explanation for

this feature. Detailed characterization of systems in and near this desert is required to break degeneracies between these explanations.

Transmission spectroscopy is one approach that can be used to address these issues, and TOI-1696b is a promising candidate for atmospheric study. Following [214], we calculate a Transmission Spectroscopy Metric (TSM) of 89.8 using the median planet mass. JWST will soon be taking spectra of transiting exoplanets. In Figure 2.12 we simulate several possibilities for atmospheric observations of TOI-1696b on JWST. We use `Exo-Transmit` [215] to create atmospheric models for TOI-1696b assuming a 100× Solar metallicity composition using its median mass of 9.98 $M_\oplus$ and for its upper 3σ mass of 56.6 $M_\oplus$. We also created a "steam" atmosphere comprised of 100% water for comparison. These models assume chemical equilibrium, are cloud-free and generated with an isothermal P-T profile with a planetary equilibrium temperature of 500 K. Using `PandExo` [32], we simulate expected JWST NIRSpec/Prism observations from 0.6 to 5 microns. In general, TOI-1696b is an excellent candidate for NIRSpec observations [20] assuming the median mass limit of the planet. We will be able to identify carbon dioxide, water, and methane in its atmosphere to better than 3σ confidence with just 1 transit, and better than 5σ with 2 transits. Resolving these features will allow us to measure the metallicity of the planet as well as the C/O and C/H ratios, enabling us to constrain the disk environment where this planet initially formed [e.g. 297, 284]. At 500 K, TOI-1696b also lies in the interesting transition regime between ammonia and nitrogen dominated chemistries. Characterizing its atmospheric composition (and potentially detecting ammonia) would provide the first observations into the nitrogen-chemistries at play [285].

According to recent studies from [403, 107], the presence of aerosols (clouds or hazes) appear to be ubiquitous at this temperature regime. Therefore, it is probable that TOI-1696b also possesses an aerosol layer which could mute its absorption features in its spectrum. To test what we could observe with JWST, we add a simple (gray opacity, wavelength independent)

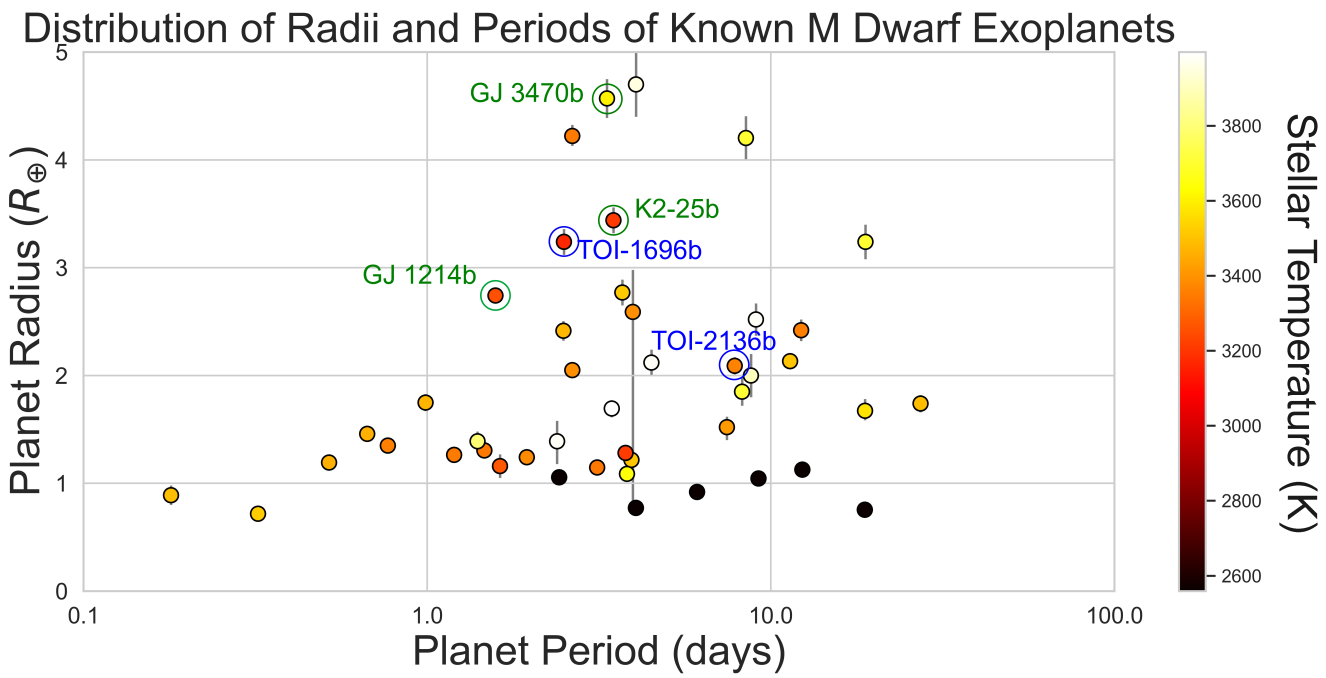

Figure 2.11: Distribution of planets orbiting M dwarfs ($T_{eff} < 4000$ K) in period-radius space taken from the *NASA Exoplanet Archive* on 8 February 2022. To emphasize the fact that we are adding additional value by constraining the mass of TOI-1696b and TOI-2136b, we include only systems with at least upper limits on their mass[1]. The most recently uploaded parameters are used. The planets studied in the paper are highlighted with blue circles, while a few notable systems are highlighted with green circles. TOI-1696b has a much larger radius than is typical considering its period, and the only stars with larger radii orbit hotter stars. Note also that with the exception of the TRAPPIST-1 planets at the bottom of the plot, TOI-1696b orbits among the coolest stars. TOI-2136b falls into a more common region of period-radius space, but has other attractive features.

1. K2-25b does not yet have a mass uploaded to the NASA exoplanet archive, but we add it manually because of its similar nature to TOI-1696b [361].

aerosol layer at various pressure levels in our 100x Solar metallicity model (assuming median mass). We find that even at pressures of 0.1 mbars [comparable to GJ 1214b 225], we will still detect the presence of water, methane, and carbon dioxide. Moreover, it is predicted that moving to longer wavelengths should diminish the effect small haze particles play on a planet's transmission spectrum [211]. We therefore do not expect the presence of aerosols to significantly hinder JWST observations of TOI-1696b. Instead, it is possible that these observations will in turn allow for a more detailed studies into the haze layer that we expect to be present in the planet's atmosphere.

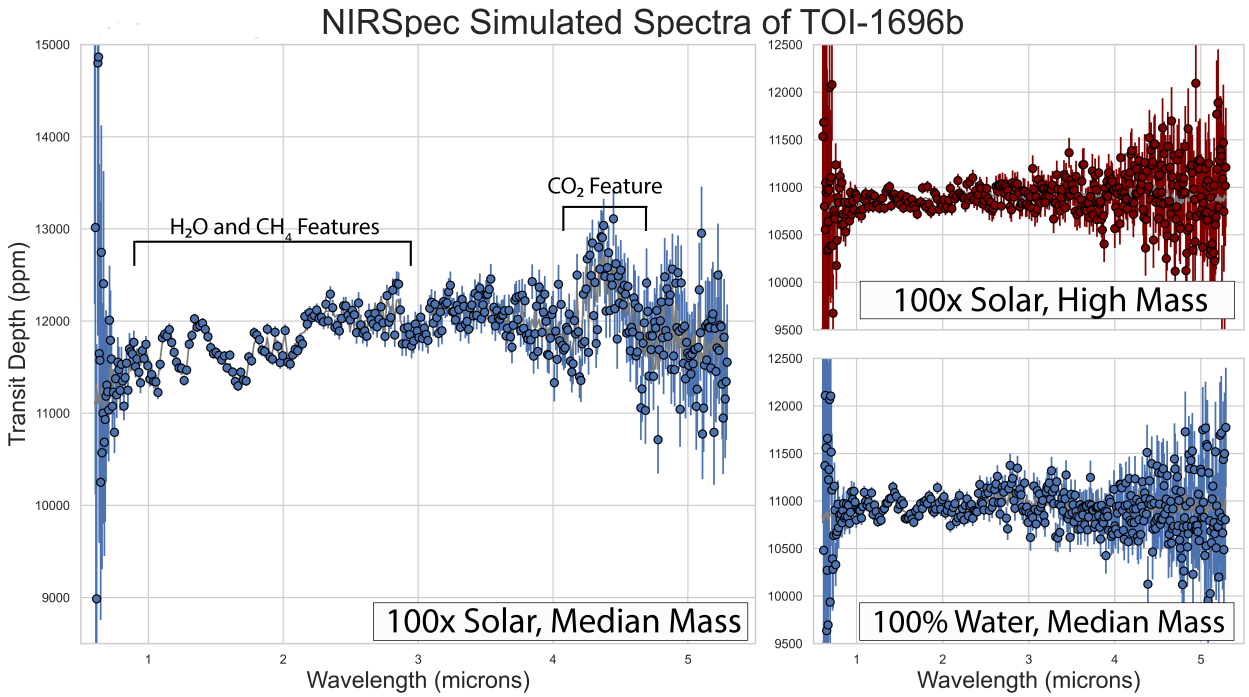

Figure 2.12: Simulations of JWST observations of TOI-1696b using the NIRSpec instrument. Gray, predicted spectra are visible under the simulated data points. Data points are simulated with a 20 ppm systematic error noise floor. Simulations where the median planet mass (9.98 $M_\oplus$) was used are colored in blue, while simulations where the 3σ upper limit (56.6 $M_\oplus$) were used are colored in red. Left: We see that a large H/He envelope with 100x solar metallicity has clearly resolvable water, carbon dioxide, and methane features. Right: Simulations of the massive H/He dominated planet, with 100x solar metallicity, above, and the less massive, but water dominated planet, below. Both make similar looking predictions, indicating the value that improving the mass measurement of TOI-1696b would add in the future.

However, we were only able to put an upper limit on the mass of this system, which can complicate the analysis of spectra obtained with JWST [31]. Simulations adopting the 3σ upper mass limit of 56.6 $M_\oplus$ were also run for NIRSpec, pictured in Figure 2.12. Far fewer atmospheric features are discernible in such a situation, due mainly to the decrease in scale height associated with a larger planet mass.

We anticipate TOI-1696b to be a system that receives much study from an atmospheric perspective in the future: its features are attractive from a wide number of scientific angles. Future RV measurements to better constrain the mass of this system would be a natural next step to understanding its composition and formation history. While the faintness of the star makes precision RVs challenging, higher precision could theoretically be obtained on future instruments for thirty-meter class telescopes. For example, using a rudimentary estimate of the performance of the Multi-Object Diffraction-limited High-resolution Infrared Spectrograph [MODHIS; 269] proposed for the Thirty-Meter Telescope (TMT), a 650 s exposure of TOI-1696 has an estimated photon-limited RV precision of ~ 6 m s^{-1}. Considering that planet b has an estimated semi-amplitude of 11.7 m s^{-1} from the mass-radius relationship in [80], we expect a more precise mass measurement for this system is well within reach of such an instrument.

2.5.2 TOI-2136

Using TESS photometry and HPF RVs, we were able to constrain TOI-2136b's radius to 2.09±0.08 $R_\oplus$, and its mass to < 15.0 $M_\oplus$. This allowed us to constrain its density to $<$ 9.53 g/cm^3. We note, however, that MCMC chains have a median of 2.5 g/cm^3, which is consistent with a planet that is significantly less dense than Earth and other rocky exoplanets, and which has a significant gaseous envelope. In addition to our discussion of the infeasability of a > 2 $R_\oplus$ planet being terrestrial in Section 6.5, we proceed under the assumption that

TOI-2136b has at least some sizable gaseous envelope.

TOI-2136b has potential as an exoplanet with detectable biosignatures. [338] first introduced the concept of a Cold-Haber World, where microbes live in liquid water environments beneath a large gaseous envelope. If such a gaseous envelope contained H_2 and even small amounts of N_2, organisms could potentially capture the energy used in the "Haber" process, where H_2 and N_2 are combined exothermically to create NH_3, which was first proposed as a potential biosignature for H_2-rich worlds in [339]. NH_3 has several attractive features: its creation from the aforementioned exothermic process is energetically favorable; NH_3 is destroyed by photolysis, meaning that sustained production would be required to register a detection; and NH_3 is only produced abiotically in limited pressure-temperature regimes.

In fact, [308] established several criteria that make exoplanet candidates attractive for NH_3 biosignature detections. First, exoplanets with radii > 1.75 $R_\oplus$ are best to ensure a gaseous envelope, but exoplanets with radii < 3.4 $R_\oplus$ are best to ensure the pressure isn't great enough to produce abiotic NH_3. Next, a $T_{eq} < 450$ K allows liquid water to exist up to 1000 bar. The existence of liquid water is thought to be a necessary ingredient for life. Finally, systems with d < 50 pc ensure adequate flux from star and planet for purposes of actually observing the biosignature with JWST. Our posterior results in Tables 2.3 and 2.6 place TOI-2136b comfortably within this regime.

We simulate NIRSpec observations of TOI-2136b using the same methods described in Section 2.5.1. Results of different simulated planet masses and metallicities are visible in Figure 2.13. Our tighter mass constraint of TOI-2136b allows us to resolve spectral features when using the median planet mass 4.64 $M_\oplus$ or when using the 3σ upper limit of 15.0 $M_\oplus$ assuming a 1x Solar metallicity composition. We expect to recover better than 3σ detections of water and methane features with just one transit, and better than 5σ with two. Our simulations do not include an NH_3 term, as TOI-2136b is not expected to produce abiotic NH_3. [308] simulated NH_3 features for a system similar to TOI-2136b: TOI-270c

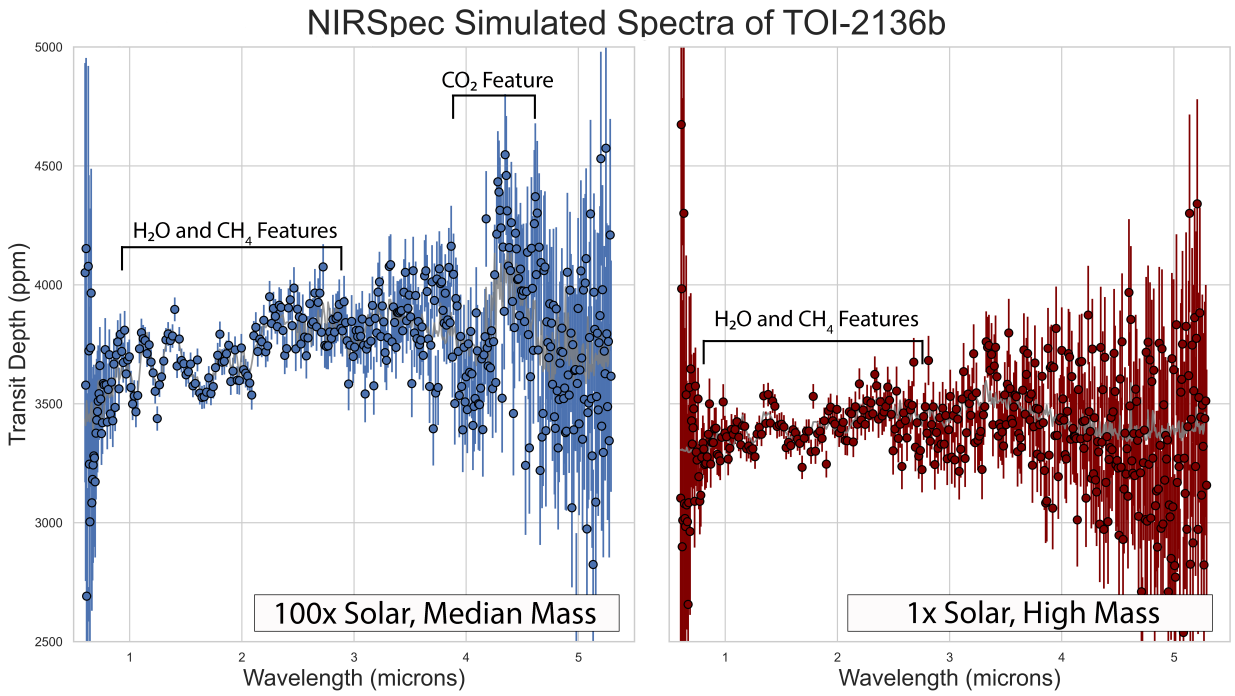

Figure 2.13: Simulations of TOI-2136b with NIRSpec. The gray, predicted spectra are visible under the simulated data points. Left: simulated spectrum of the low mass planet with 100 times solar metallicity. Spectral features are clearly resolvable, especially water and methane features. Right: the high mass planet with solar-like metallicity in its atmosphere. Our mass limits constrain the planet's atmosphere enough such that both high and low mass scenarios have recoverable features.

($M_* = 0.386$; $R_p = 2.35$ $R_\oplus$; P = 5.66 days; [163]). The TOI-270c system ranks highest in their metric for biosignature detection, and its simulated NH_3 features are recoverable in a small number of transits. This suggests that TOI-2136b will also rank very highly in future searches for atmospheric biosignatures with JWST.

We also note that during the submission of this manuscript, two additional studies were announced constraining the mass of TOI-2136b [212, 142]. Our results are consistent with both estimates, though we note that our median planet mass of 4.64 $M_\oplus$ is more consistent with the analysis in [212]. The likelihood of a future analysis utilizing all three datasets only improves the attractiveness of TOI-2136b from an atmospheric study perspective.

2.6 Summary

We refine the measured planetary, orbital, and stellar parameters of two TOI planet candidates, TOI-1696.01 and TOI-2136.01, and validate their planetary nature, using a combination of ground based photometry, high resolution adaptive optics imaging, and radial velocity measurements.

Using ground-based photometry in coordination with TESS, we measure TOI-1696b's radius as 3.24 ± 0.12 $R_\oplus$, and TOI-2136b's radius as 2.09 ± 0.08 $R_\oplus$.

Using the near-IR Habitable-Zone Planet Finder, we are able to put upper limits on the masses of both transiting planets. We constrain TOI-1696b's mass to < 56.6 $M_\oplus$, and TOI-2136b's mass to < 15.0 $M_\oplus$, with 97.7% confidence.

Both systems have high potential for future atmospheric studies, and detailed spectra of either system could answer important scientific questions. We encourage the community to continue observations on future instruments.

Chapter 3

GJ 3929: High Precision Photometric and Doppler Characterization of an Exo-Venus and its Hot, Mini-Neptune-mass Companion

3.1 Foreword

I next expanded upon my previous photometric analysis of TOI-1696 and TOI-2136 by focusing upon yet another TESS-identified transiting exoplanet system, GJ 3929. It is well known that different observational techniques are often required to accurately characterize orbital periods, rule out false positive scenarios, detect longer period or non-transiting companions, or to measure additional parameters of an exoplanet [e.g., 393, 204, 253, 72]. Unlike the previous M dwarf exoplanets TOI-1696 b and TOI-2136 b, the GJ 3929 system contained additional, challenging features.

A transiting exoplanet candidate with a 2.6 day period orbiting GJ 3929 was first identified by the TESS Science Processing and Operations Center [SPOC; 198], and was subsequently analyzed by [213]. This candidate, GJ 3929 b, is Earth-sized, but detectable in RV data due to the small size of its host star and semi-major axis. Such a detection was still very challenging, and [213] were only able to constrain the planet mass to 2.88σ confidence. This was partially due to the prescence of an additional signal in the RV data, possibly a planet or stellar variability.

We utilize precise RVs obtained with the NEID spectrograph on the WIYN[1] 3.5 m telescope at Kitt Peak National Observatory, RVs taken with the Habitable Zone Planet Finder, and previously published CARMENES RV data, in conjunction with TESS, ARCTIC, and LCOGT photometry to deeply characterize the true nature of the GJ 3929 system. From photometry we identify planet b, and we can rule out many stellar activity scenarios, verifying that the additional signal in the RV data is likely planetary. We joined this information with a variety of RV models to confirm the planetary nature of GJ 3929 c, improve the mass of GJ 3929 b, and present the most detailed understanding of the system to date.

In Section 4.2, we give a summary of the data used in our analysis. In Section 5.3, we detail our estimation of the system's stellar parameters. In Section 6.4, we detail the steps taken to measure planetary and orbital parameters, and the investigation of an additional planet. In Section 6.5, we discuss our findings, and the implications for the system. Finally, Section 6.6 summarizes our results and conclusions.

3.2 Observations

A summary of our observational data and key properties is visible in Table 4.1.

[1]The WIYN Observatory is a joint facility of the University of Wisconsin–Madison, Indiana University, NSF's NOIRLab, the Pennsylvania State University, Purdue University, and the University of California, Irvine.

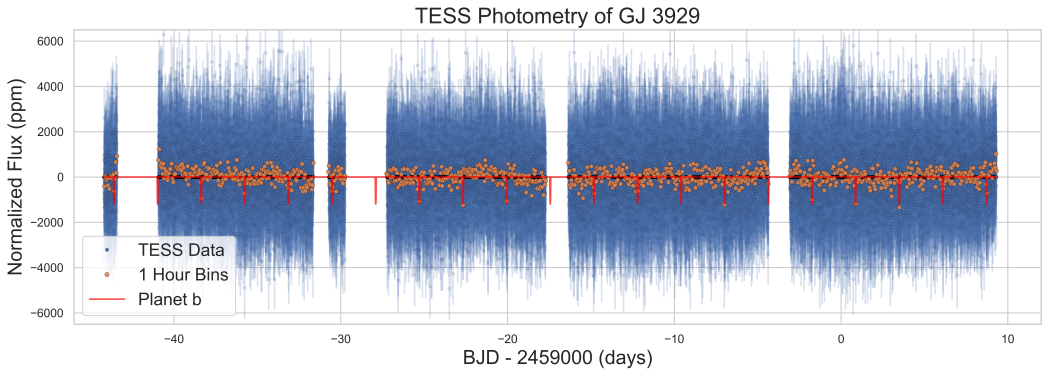

Figure 3.1: PDCSAP flux of GJ 3929 as taken during TESS Sectors 24 and 25. Overlaid is data binned into one hour intervals. Additionally, we plot a maximum a-posteriori (MAP) fit of the transits of planet b. A phase fold of the transits after our complete analysis is visible in Figure 3.4. The transit model is described in Section 3.4.1.

Table 3.1: Summary of Observational Data

Instrument	Date Range	RMS	Average Error	Type
TESS	2020 April 16 - 2020 June 8	1346 ppm	1441 ppm	Photometry
ARCTIC	2021 February 27 - 2021 April 30	1000 ppm	734 ppm	Photometry
LCO	2021 April 15	1522 ppm	692 ppm	Photometry
CARMENES	2020 July 30 - 2021 July 19	3.87 m s^{-1}	1.97 m s^{-1}	RV
HPF	2021 August 27 - 2022 March 11	8.81 m s^{-1}	8.42 m s^{-1}	RV
NEID	2021 January 6 - 2022 January 27	10.6 m s^{-1}	1.55 m s^{-1}	RV

3.2.1 TESS

GJ 3929 was observed by the TESS spacecraft between 2020 April 16 and 2020 June 8. These dates correspond to Sectors 24 and 25 of the TESS nominal mission. GJ 3929 was observed in CCD 1 of Camera 1 during sector 24, and CCD 2 of Camera 1 during sector 25.

The TESS photometry were first reduced by SPOC. After initial processing, we used the pre-search data conditioning simple aperture photometry [PDCSAP; 366] in our analysis. Data points flagged as poor quality are discarded before analysis. A plot of the TESS PDCSAP flux used in the analysis is shown in Figure 3.1.

3.2.2 Ground based photometric follow up

Ground-based follow-up can be a useful tool not only to validate the planetary nature of transiting signals, but to refine the measured parameters of transiting exoplanets. Here we detail the ground-based photometric follow-up of for GJ 3929b.

ARCTIC

We observed three transits of GJ 3929b on the nights of 2021 February 26, 2021 April 30, and 2021 September 21, using the Astrophysical Research Consortium (ARC) Telescope Imaging Camera [ARCTIC; 190] at the ARC 3.5 m Telescope at Apache Point Observatory (APO). To achieve precise photometry on nearby bright stars, we used the engineered diffuser described in [360].

The airmass of GJ 3929 varied from 1.00 to 1.66 over the course of its observation on 2021 February 26. The observations were performed using a 30 nm wide narrowband Semrock filter centered at 857 nm [described in 364] due to moderate cloud coverage, with an exposure time of 33.1 s in the quad-readout mode with 2×2 on-chip binning. In the 2×2 binning mode, ARCTIC has a gain of 2 e/ADU, a plate scale of 0.228 $''$/pixel, and a readout time of 2.7 s. We reduced the raw data using `AstroImageJ` [86]. We selected a photometric aperture of 31 pixels (7.07$''$) and used an annulus with an inner radius of 70 pixels (15.96$''$), and an outer radius of 100 pixels (22.8$''$).

We also observed a transit of GJ 3929b on 2021 April 30. The airmass during observations varied between 1.00 and 1.51. The observations were performed using the same Semrock filter as described previously, with an exposure time of 45 s in the quad-readout mode with 2×2 on-chip binning. For the final reduction, we selected a photometric aperture of 33 pixels (7.52″) and used an annulus with an inner radius of 58 pixels (13.22″), and an outer radius of 87 pixels (19.84″).

We observed a final transit of GJ 3929b on 2021 September 21. The airmass during observations varied between 1.21 and 3.22, and the resulting scatter in data points was > 3 times the values of either previous ARCTIC night ($\mathrm{rms}_{20210226} = 1000$ ppm; $\mathrm{rms}_{20210430} = 910$ ppm; $\mathrm{rms}_{20210921} = 3400$ ppm). Consequently, we chose not to use this final ARCTIC transit during analysis of planet b.

We checked for airmass correlation on each night, but found little evidence for any significant correlation. A plot of the ARCTIC transits used in our final analysis is visible in Figure 3.4.

LCOGT

We additionally use publicly available data taken by the Las Cumbres Observatory Global Telescope Network [LCOGT; 63]. These data were obtained from the Exoplanet Follow-up Observing Program (ExoFOP) website [2]. Two transits of GJ 3929b were obtained using the LCOGT. The first transit was obtained on 2021 April 10. Data were taken by both the SINISTRO CCDs at the 1 m telescopes of the McDonald Observatory (McD) and the Cerro Tololo Interamerican Observatory (CTIO). Both instruments have a pixel scale of 0.00389 pix^{-1} and a FOV of 260×260.

A second transit was obtained on 2021 April 15. These data were taken simultaneously in 4 different filters (g', i', r', and z_s') with the Multi-color Simultaneous Camera for studying

[2] https://exofop.ipac.caltech.edu/tess/

Atmospheres of Transiting exoplanets 3 camera [MuSCAT3; 289] mounted on the 2 m Faulkes Telescope North at Haleakala Observatory (HAL). It has a pixel scale of 0.0027 pix^{-1} corresponding to a FOV of 9.01×9.01.

As outlined in [213], high airmass caused the CTIO observations to exhibit higher scatter. In fact, both transits on 2021 April 10 exhibit much higher scatter (rms_{CTIO} = 3300 ppm; rms_{MCD} = 2200 ppm) than on 2021 April 15 (rms_{gp} = 1010 ppm; rms_{ip} = 850 ppm; rms_{rp} = 910 ppm; rms_{zs} = 920 ppm). Consequently, for the same reasons outlined in Section 3.2.2, we chose not to utilize either transit from 2021 April 10 in our final analysis.

The publicly available data were calibrated by the LCOGT BANZAI pipeline [277], and photometric data were extracted using AstroImageJ [86]. The resulting photometric data are the same that were utilized in [213].

3.2.3 High Contrast Imaging

High contrast imaging can be important for ruling out false positive scenarios. [213] used high-resolution images obtained from the AstraLux camera [182] at the Calar Alto Observatory to rule out false positive scenarios. They were able to rule out nearby luminous sources down to a $\Delta z' < 5.5$ at 1″. Here we detail our team's adaptive optics (AO) follow up of GJ 3929b, and add to the evidence of a planetary explanation for the transit events.

ShARCS on the Shane telescope

We observed GJ 3929 using the ShARCS camera on the Shane 3 m telescope at Lick Observatory [353]. GJ 3929 was observed using the K_S and J filters on the night of 2021 February 26. Instrument repairs prevented our observations from benefiting from Laser Guide Star (LGS) mode. Fortunately, GJ 3929 is sufficiently bright such that LGS mode

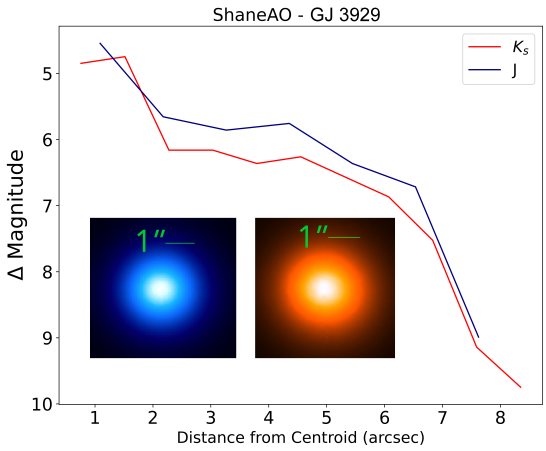

Figure 3.2: 5σ contrast curves of GJ 3929 taken using the K_s and J filters. The data were taken on 2021 February 26. The overcast conditions and poor seeing on 2021 February 26 resulted in challenges with sky-subtraction. As a result, the magnitude difference between the centroid and background don't drop as quickly as expected.

is helpful, but not necessary. Further instrument repairs prevented our observations from using a dither-routine to create master-sky images of GJ 3929. Instead, after a series of observations, we shifted several arcseconds to an empty region of sky, and took images with the same exposure time for purposes of sky subtraction.

The raw data are reduced using a custom pipeline developed by our team [described in 39]. Using algorithms from [110], we then generate a 5 sigma contrast curve as the final part of our analysis. We detect no companions at a $\Delta K_s = 4.85$ at $0.76''$ and $\Delta Ks = 9.75$ at $8.35''$. Additionally, we detect no companions at $\Delta J = 4.54$ at $1.09''$ and $\Delta J = 7.62$ at $8.99''$.

We note that observing conditions on 26 February 2021 were marginal. As a result of overcast conditions and poor seeing, the FWHM of the centroid in each reduced AO image was fairly large ($0.77''$ and $1.11''$). Consequently, our final constraints on nearby luminous companions are not as tight as they might have been. However, our high contrast images were taken in redder wavebands than than the z' filter used in [213], and so we provide additional sensitivity toward detecting redder, cooler companions. In tandem, our results and those outlined in [213] are consistent: we detect no nearby luminous companions as an explanation for the

observed transit event.

3.2.4 Radial Velocity Follow-Up

We obtained RVs of GJ 3929b in order to constrain the mass of the system and to independently confirm the planetary nature of the transiting planet. Here we detail the RV data acquired for the system GJ 3929.

The NEID Spectrometer on the WIYN 3.5 m Telescope at KPNO

We obtained RVs of GJ 3929 using the new, ultra-precise NEID spectrometer [336] on the WIYN 3.5 m telescope at Kitt Peak National Observatory (KPNO). NEID is an environmentally stabilized [358, 320] fiber-fed spectrograph [203] with broad wavelength coverage (3800 - 9300 Å). We observed GJ 3929 in High Resolution (HR) mode with an average resolving power $\mathcal{R}$ = 110,000. The default NEID pipeline utilizes the Cross-Correlation Function [CCF; 26] method to produce RVs. However, this method tends to be less effective on M dwarfs [e.g., 13], and so we use a modified version of the `SpEctrum Radial Velocity AnaLyser` pipeline [`SERVAL`; 405] as described in [362]. `SERVAL` shifts and combines all observed spectra into a master template, and compares this template with known reference spectra. We then minimize the χ^2 statistic to determine the shifts of each observed spectrum. We mask telluric and sky-emission lines during this process. A telluric mask is calculated based on their predicted locations using `telfit` [162], a Python wrapper to the Line-by-Line Radiative Transfer Model package [83].

We obtained 27 observations of GJ 3929 between 2021 January 6 and 2022 January 27. Our first two nights of observation for this system used 3 consecutive 900 s exposures, but we later changed our observation strategy to one 1800 s exposure per night. We obtained a

median SNR of 44.8 in order 102 ($\lambda = 4942$ Å) of NEID for each unbinned observation. The median unbinned RV errorbar is 1.18 m s^{-1}. The errorbars are estimated from expected photon noise. A total of 23 nightly binned RVs were obtained, though 4 were discarded because the laser frequency comb calibrator was not available on those nights, resulting in a less precise instrument drift solution that is insufficient for precision RV analysis. This left us with 19 nightly binned NEID RVs that were used in the analysis.

The Habitable Zone Planet Finder at McDonald Observatory

We observed GJ 3929 with the Habitable Zone Planet Finder [HPF; 262, 263], a near-infrared, (8080 − 12780 Å), high precision RV spectrograph. HPF is located at the 10 m Hobby-Eberly Telescope (HET) in Texas. HET is a fixed-altitude telescope with a roving pupil design. Observations on the HET are queue-scheduled, with all observations executed by the HET resident astronomers [344]. HPF is fiber-fed, with separate science, sky and simultaneous calibration fibers [203], and has precise, milli-Kelvin-level thermal stability [358].

We extracted precise RVs with HPF using the modified version of `SERVAL` [405] optimized for use for HPF data as described in detail in [357]. The RV reduction followed similar steps as outlined in Section 3.2.4.

We obtained 18 observations of GJ 3929 with HPF over the course of 6 observing nights. These data were taken between 2021 August 27 and 2022 March 11. We obtained 3 consecutive exposures on each observing night, resulting in a median unbinned RV error of 7.15 m s^{-1}. Data taken on BJD = 2459649 were excluded from our analysis due to poor weather conditions. Our dataset then consists of 5 nightly binned HPF RVs. Due to the small quantity of the HPF data, we considered fits that did not utilize HPF data. We found that model results did not differ meaningfully whether HPF data were utilized, or not, and

we include them in our final model for completeness. HPF spectra were still used to derive stellar parameters, as outlined in Section 5.3.

CARMENES RVs

Our RV modeling also utilizes CARMENES RVs published in [213]. [213] published 78 high-precision RVs as a part of their study of GJ 3929 using the CARMENES spectrograph [311]. CARMENES is a dual-channel spectrograph with visible and near-infrared (NIR) arms ($\mathcal{R}_{VIS} = 94600$; $\mathcal{R}_{NIR} = 80400$). CARMENES is located at the Calar Alto Observatory in Almería, Spain. RVs of GJ 3929 were taken between 2020 July 30 and 2021 July 19. Each observation lasted 30 minutes, with a median observation SNR of 74. 5 RVs were discarded due to a missing drift correction in [213], and we do so as well. This results in a final dataset containing 73 RVs. These RVs were taken using the visible arm of CARMENES, and have a median uncertainty of 1.9 m s^{-1}.

3.3 Stellar Parameters

We followed steps outlined in [357] and [39] to estimate $T_{\rm eff}$, $\log g$, and [Fe/H] values of GJ 3929. The `HPF-SpecMatch` code is based on the `SpecMatch-Emp` algorithm from [402], and compares the high resolution HPF spectrum of the target star of interest to a library of high SNR as-observed HPF spectra. This library consists of slowly-rotating reference stars with well characterized stellar parameters from [402] and an expanded selection of stars from [265] in the lower effective temperature range. Our analysis was run on 2022 March 3, and the library contained 166 stars during our run.

We shift the observed target spectrum to a library wavelength scale and rank all of the targets in the library using a χ^2 goodness-of-fit metric. After this initial χ^2 minimization step, we

pick the five best matching reference spectra. We then construct a weighted spectrum using their linear combination to better match the target spectrum. A weight is assigned to each of the five spectra according to its goodness-of-fit. We then assign the target stellar parameter $T_{\rm eff}$, $\log g$, and [Fe/H] values as the weighted average of the five best stars using the best-fit weight coefficients. The final parameters are listed in Table 3.2. These parameters were derived from the HPF order spanning 8670Å- 8750Å, as this order is cleanest of telluric contamination. We artificially broadened the library spectra with a $v \sin i$ broadening kernel [155] to match the rotational broadening of the target star. We determined GJ 3929 to have a $v \sin i$ broadening value of < 2 km/s.

We used `EXOFASTv2` [108] to model the spectral energy distributions (SED) of GJ 3929 and to derive model-dependent constraints on the stellar mass, radius, and age. `EXOFASTv2` utilizes the BT-NextGen stellar atmospheric models [8] during SED fits. Gaussian priors were used for the 2MASS (JHK), Johnson (BV), and *Wide-field Infrared Survey Explorer* magnitudes (WISE; $W1$, $W2$, $W3$, and $W4$) [398]. Our spectroscopically-derived host star effective temperature, surface gravity, and metallicity, were used as priors during the SED fits as well, and the estimates from [21] were used as priors for distance. We further include in our priors estimates of Galactic dust by [156] to estimate the visual extinction, though we emphasize that this is a conservative upper limit: GJ 3929 is fairly close to Earth, and is likely to be foreground to much of the dust utilized in this estimate. We convert this upper limit to a visual magnitude extinction using the $R_v = 3.1$ reddening law from [116]. Our final model results are consistent with those derived in [213], and are visible in Table 3.2.

Table 3.2: Summary of Stellar Parameters for GJ 3929

Parameter	Description	Value	Reference
Main identifiers:			
TOI	*TESS* Object of Interest	2013	*TESS* mission
Continued on next page			

Table 3.2 – continued from previous page

Parameter	Description	Value	Reference
TIC	*TESS* Input Catalogue	188589164	TICv8
GJ	Gliese-Jahreiss Nearby Stars	3929	Gliese-Jahreiss
2MASS	···	J15581883+3524236	2MASS
Gaia DR3	···	1372215976327300480	Gaia DR3
Equatorial Coordinates, Proper Motion and Spectral Type:			
$\alpha_{\rm J2000}$	Right Ascension (RA; deg)	239.57754339(4)	Gaia DR3
$\delta_{\rm J2000}$	Declination (Dec; deg)	35.40815826(2)	Gaia DR3
μ_α	Proper motion (RA; mas/yr)	-143.28 ± 0.07	TICv8
μ_δ	Proper motion (Dec; mas/yr)	318.22 ± 0.08	TICv8
d	Distance (pc)	15.8 ± 0.02	Bailer-Jones
Optical and near-infrared magnitudes:			
B	Johnson B mag	14.333 ± 0.008	TICv8
V	Johnson V mag	12.67 ± 0.02	TICv8
g'	Sloan g' mag	15.161 ± 0.006	TICv8
r'	Sloan r' mag	12.2405 ± 0.0009	TICv8
i'	Sloan i' mag	10.921 ± 0.001	TICv8
T	*TESS* magnitude	10.270 ± 0.007	TICv8
J	J mag	8.69 ± 0.02	TICv8
H	H mag	8.10 ± 0.02	TICv8
K_s	K_s mag	7.87 ± 0.02	TICv8
$W1$	WISE1 mag	7.68 ± 0.02	WISE
$W2$	WISE2 mag	7.54 ± 0.02	WISE
$W3$	WISE3 mag	7.42 ± 0.02	WISE
$W4$	WISE4 mag	7.27 ± 0.08	WISE
Spectroscopic Parameters[a]:			
$T_{\rm eff}$	Effective temperature in K	3384 ± 88	This work
[Fe/H]	Metallicity in dex	-0.02 ± 0.12	This work
$\log(g)$	Surface gravity (cm s^{-2})	4.89 ± 0.05	This work
Model-Dependent Stellar SED and Isochrone fit Parameters[b]:			

Continued on next page

Table 3.2 – continued from previous page

Parameter	Description	Value	Reference
M_*	Mass ($M_\odot$)	$0.313^{+0.027}_{-0.022}$	This work
R_*	Radius ($R_\odot$)	0.32 ± 0.01	This work
L_*	Luminosity ($L_\odot$)	$0.0109^{+0.0005}_{-0.0004}$	This work
ρ_*	Density (g/cm^3)	13.3 ± 1.1	This work
Age	Age (Gyr)	$7.1^{+4.1}_{-4.9}$	This work
A_v	Visual extinction (mag)	0.005 ± 0.003	This work
d	Distance (pc)	15.822 ± 0.006	This work
Other Stellar Parameters:			
$v \sin i_*$	Rotational velocity (km/s)	< 2	This work
ΔRV	"Absolute" radial velocity (km/s)	10.265 ± 0.008	This work
U, V, W	Galactic velocities (km/s)	-21.05 ± 0.04,10.85 ± 0.06,14.66 ± 0.08	Kemmer

References are: TICv8 [356], 2MASS [94], Gaia DR3 (Gaia Collaboration et al. 2022j, in prep), Bailer-Jones [22], WISE [398], Kemmer [213]

[a]Derived using the HPF spectral matching algorithm from [357]

3.4 Analysis

Both photometry and RV data were essential for characterizing GJ 3929, as the system may have two or more planets, though we have only detected transits of planet b. First, in Section 3.4.1, we investigate the transiting planet using our photometric data. Next, we analyze the RV data of GJ 3929 in Section 3.4.2. Then, we search for additional transiting signals. Finally, in Section 3.4.5, we combine both datasets to reach our final conclusion.

3.4.1 Transit Analysis

A 2.6 day transit signal was originally identified by the MIT SPOC pipeline on 2020 June 19, then designated TOI-2013.01. Subsequently, [213] confirmed the planetary nature of the signal in early 2022. We combine the TESS data with our follow-up transits in addition to other publicly available photometric data (detailed in Section 3.2.2) to further refine the measured parameters of the system.

Modeling the Photometry

We modeled GJ 3929's photometry using the exoplanet software package [127]. First, we downloaded the TESS PDCSAP flux using lightkurve [236]. We then performed a standard quality-flag filter, removing datapoints designated as of poor quality by the SPOC pipeline, and we median normalized the TESS data. We then combined the TESS data with our normalized ARCTIC and LCOGT data for joint analysis.

Initial fits to ARCTIC and LCOGT data appeared to have a slight residual trend, and so in our adopted fit we detrended ARCTIC and LCOGT photometry before combining the datasets. We utilized the NumPy polyfit function to fit a line for purposes of detrending [172]. This function performs a simple least squares minimization to estimate the linear trend. This detrending was performed before modeling the data, as we found that including a detrending term in the model did not meaningfully improve our results, while increasing the complexity of our model.

We found it best to partition the photometric data into four regions of interest: the TESS data (which consist of two consecutive sectors), two different nights of ARCTIC data, and a night of LCOGT data. Due to the possibility of systematic offsets between nights, and the distinct conditions during each night of ARCTIC observations, we choose to treat each

ARCTIC night separately in our model. Furthermore, the LCOGT data were taken with four different filters. Consequently, we model each filter separately. For each instrument-filter combination, then, we adopt a unique mean and jitter term. The mean terms are additive offsets to account for potential systematic shifts between nights, and are simply subtracted from all data points when fitting. The jitter terms are meant to model additional white noise not properly accounted for in the errorbars of the dataset, and are added in quadrature with the errorbars. Our model thus consists of seven total mean terms, and seven jitter terms.

The physical transit model was generated using `exoplanet` functions and the `starry` lightcurve package [254], which models the period, transit time, stellar radius, stellar mass, eccentricity, radius, and impact parameter to produce a simulated lightcurve. We adopt quadratic limb darkening terms to account for the change in flux that occurs when a planet approaches the limb of a star [216]. The two ARCTIC transits were taken using the same Semrock filter, and so we expect their limb-darkening behavior to be the same. Thus, we adopt the same limb-darkening parameters for each ARCTIC transit. We adopt distinct limb-darkening terms for the LCOGT data taken with the SDSS g′, i′, r′, and z_s' filters. We note that this results in six pairs of limb darkening terms, in contrast to seven separate jitter and mean terms, but is physically motivated.

Similar to [213], we choose not to include a dilution term in our final model. GJ 3929 does not have many neighbors, and is much brighter than all of them (Figure 3.3). GJ 3929 has an estimated contamination ratio of 0.000765, meaning that 0.08% of its flux is possibly from nearby sources [355]. This suggests that a dilution term is not necessary.

Inference

After constructing a physical transit model using `starry`, we compare it to the data after it has been adjusted to account for offsets, and we add our jitter parameters in quadrature

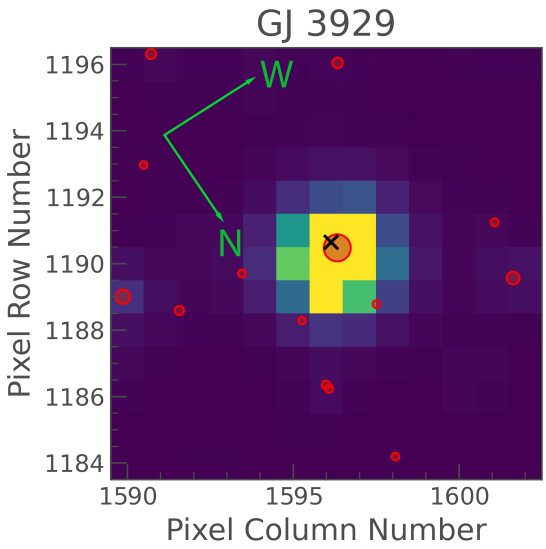

Figure 3.3: TESS pixel image of GJ 3929 taken during Sector 24, created using the `eleanor` software package [114]. The TICv8 position of GJ 3929 is indicated by a black x. Red circles correspond to Gaia resolved sources [137], with size corresponding to brightness. Because GJ 3929 does not have any bright neighbors, we do not use a dilution term.

with the errorbars during likelihood estimation. Each free parameter is given a broad prior to prevent any biasing of the model, and we summarize the priors used in Table 5.3. The model is then optimized using `scipy.optimize.minimize` [384], which utilizes the Powell optimization algorithm [310]. This optimization provides a starting guess for posterior inference. We then used a Markov Chain Monte Carlo (MCMC) sampler to explore the posterior space of each model parameter. `exoplanet` uses the Hamiltonian Monte Carlo (HMC) algorithm with a No U-Turn Sampler (NUTS) for increased sampling efficiency [179]. We ran 10000 tuning steps and 10000 subsequent steps, and assessed convergence criteria using the Gelman-Rubin (G-R) statistic [119]. We considered a chain well mixed if the G-R statistic was within 1% of unity. All the parameters in our model indicated convergence using this metric.

Our photometry-only fits are consistent with the joint fits adopted in Section 3.4.5. A final plot of the photometry, folded to the period of planet b is visible in Figure 3.4.

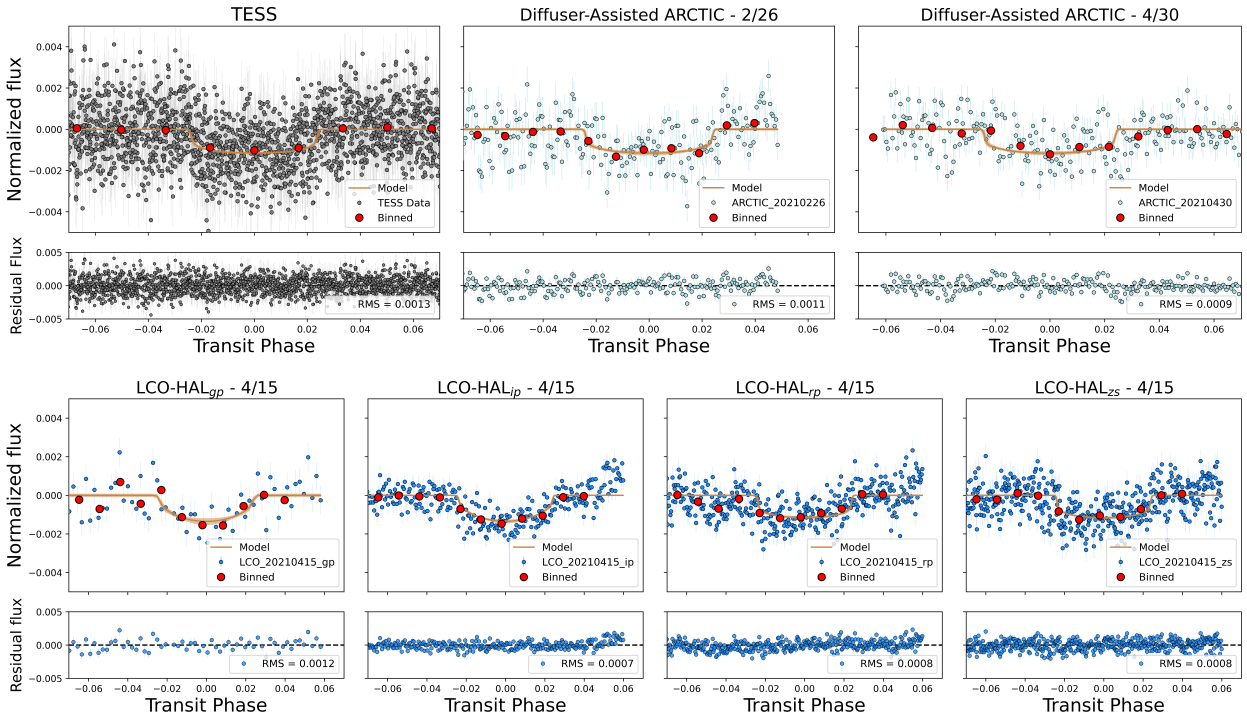

Figure 3.4: Phase folded transit fits to TESS data, ARCTIC data, and LCOGT data. We separate the 2021 April 15 transit taken with LCOGT by filter and label them accordingly. Using all of these data allow us to modify previous radius estimates of GJ 3929b.

3.4.2 Radial Velocity Analysis

Periodogram Analysis

We first used a Generalized Lomb-Scargle periodogram [GLS; 404] to analyze the RVs of GJ 3929, and to identify any periodic signals. We estimate the analytical false alarm levels and normalize the periodogram following the steps outlined in [404], which assume Gaussian noise. With this assumption, we scale the sample variance (and false alarm levels) by $\frac{N-1}{2}$ in order to reproduce the population variance, which is the quantity of interest in our analysis. Consistent with [213], we detected significant periodicities between 14-16 days. In contrast to [213], however, we find that when including the new, more precise NEID RVs (median CARMENES RV error $\sim 1.6 \times$ median NEID RV error), as well as our HPF RVs, the 15 day signal has grown in power relative to the 14 day signal, suggesting that it might be the true

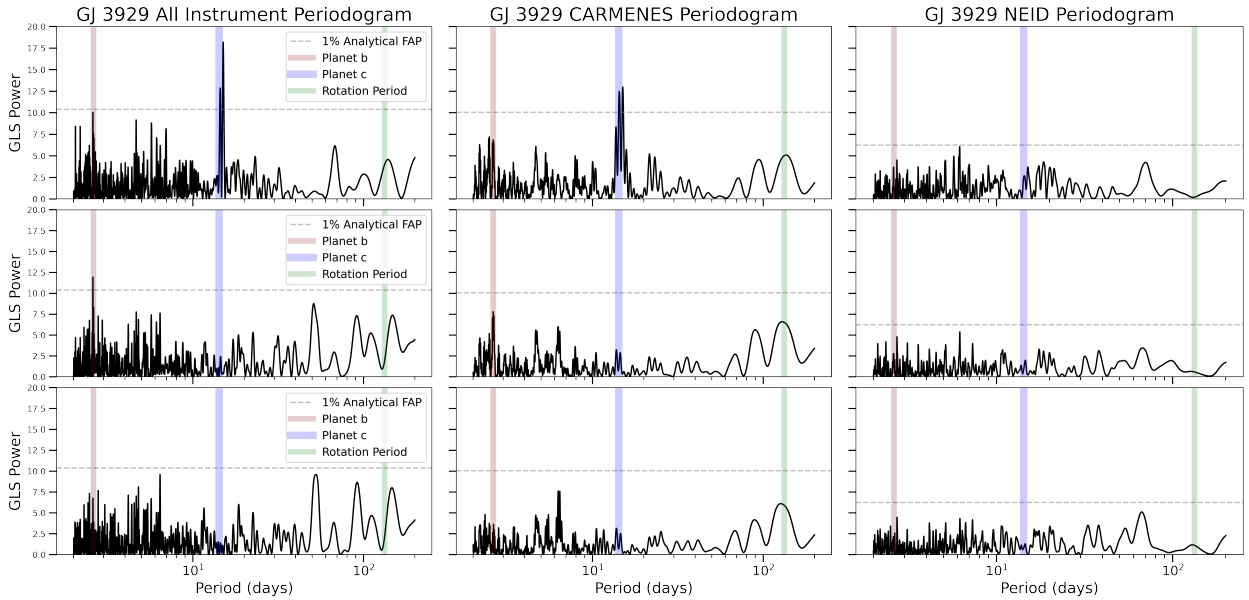

Figure 3.5: Top: GLS periodograms of the combined dataset consisting of NEID, CARMENES, and HPF RVs, CARMENES data only, and NEID data only. Data have been adjusted for offsets. Middle: data after the subtraction of planet c, assuming the values derived in our final posterior fits. Bottom: GLS periodograms of data after the subtraction of planet b and planet c. We do not include a periodogram of HPF-only data due to its sparseness.

signal. Relative peak strengths of alias frequencies in a periodogram do not always indicate the true period, however, and we detail a more formal model comparison later in the section. A plot of the combined-dataset periodogram, and periodograms on NEID and CARMENES only, are visible in Figure 3.5. After the subtraction of the longer-period planet c, the signal of the 2.6 day planet b is clearly identifiable in the periodogram.

Modeling the RVs

We used the `RadVel` software package to analyze the RVs of GJ 3929 [133]. `RadVel` models an exoplanet's orbit by solving Kepler's equation using an iterative method outlined in [98]. Each planetary orbit is then modeled by 5 fundamental parameters: the planet's orbital period (P), the planet's time of inferior conjunction (T_c), the eccentricity of the orbit (e), the argument of periastron (ω), and the velocity semi-amplitude (K). We additionally include

instrumental terms, γ and σ, which account for systematic offsets between instruments, and excess white noise.

We construct the RV model in a Bayesian context, encoding prior information about each parameter as a part of the model. Similar to the fits described in Section 3.4.1, we adopt broad priors on the free parameters of our model to prevent any bias in our results. The primary exception being that during RV-only fits, we put tight priors on P_b and $T_{con,b}$, as these are much more tightly constrained by transits than by RV fits. We emphasize, however, that our final adopted fit is a joint-fit between RVs and transits, detailed in Section 3.4.5. Detailed prior information is available in Table 5.3.

Inference

In order to estimate the posterior probability of our model, we used an MCMC sampler to explore the posterior parameter space. `RadVel` utilizes the MCMC sampler outlined in [125]. We first used the Powell optimization method to provide an initial starting guess for each parameter [310]. We then ran 150 independent chains, and assessed convergence using the Gellman-Rubin statistic [G-R; 119]. The sampling was terminated when the chains were sufficiently mixed. Chains are considered well-mixed when the G-R statistic for each parameter is < 1.03, the minimum autocorrelation time factor is ≥ 75, the max relative change in autocorrelation time $\leq .01$, and there are ≥ 1000 independent draws. All of our considered models eventually satisfied these conditions.

We additionally considered the inclusion of a Gaussian Process [GP; 10] model to account for coherent stellar activity. [213] identify a rotation period of ~ 120 days for GJ 3929. This value is derived from a combination of long-term photometry taken using the Hungarian Automated Telescope Network [HATNet; 23], the All-Sky Automated Search for SuperNovae [ASAS-SN; 342], and Joan Oró Telescope [TJO; 87], and periodogram analysis of the

CARMENES Hα values. We use the combined Hα values from CARMENES and NEID to expand upon this, plotted in Figure 3.6. While the maximum power occurs at a slightly shorter period than observed in [213], we note that rotational variability is often quasi-periodic in nature and periodograms can have trouble distinguishing longer periods [251]. Our value observed here is still consistent with the previously reported value, and we make no amendment to the system's rotation period.

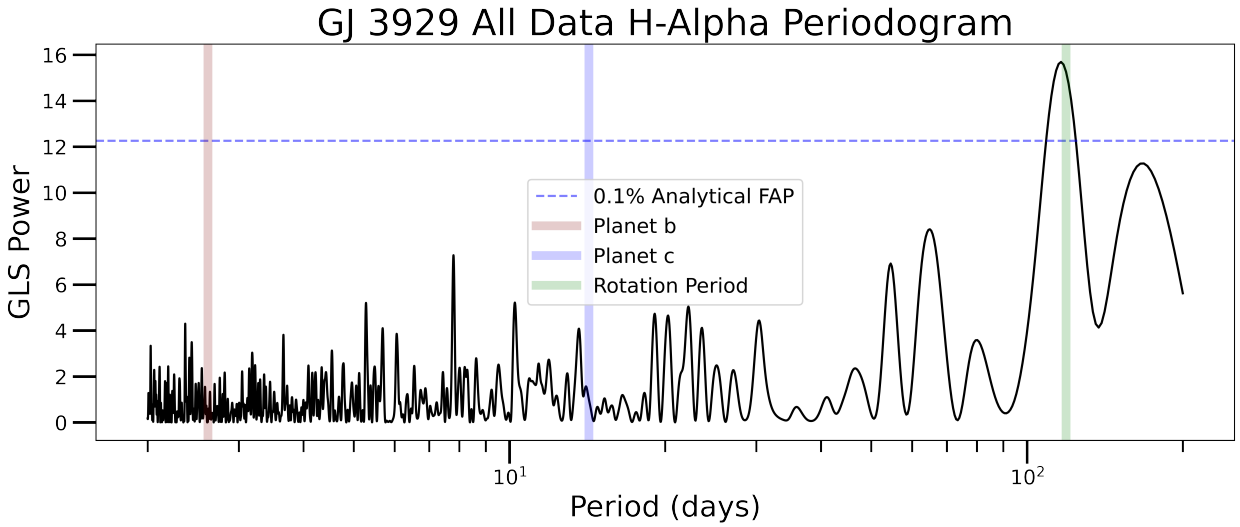

Figure 3.6: GLS periodogram of the Hα data taken by the CARMENES and NEID spectrographs. The only significant signal is at 116
days, which is most likely associated with the stellar rotation period identified in [213]. Neither of the planetary periods has any significant power in this data. We do not include HPF, as its bandpass does not include the Hα indicator.

The $>$ 100 day rotation period of this system is consistent with a quiet, slowly-rotating star, and we normally wouldn't expect a large RV signal due to activity. However, [213] found an RV fit that included a GP to be preferred to an RV-only fit, and so we proceed with a series of fits, some of which include a GP. Our GP fits utilize the Quasi-Periodic GP kernel due to its flexibility and wide application in exoplanet astrophysics [e.g. 173, 248].

We also compared fits with the GP kernel that was adopted in [213]. [213] utilized a combination of two Simple Harmonic Oscillator [SHO; 121] kernels, outlined in more detail in [222].

In order to explore the possibility of an additional planet in the GJ 3929 system, and the plausibility of stellar activity interfering with RV signals, we perform a model comparison. Model comparisons vary in the number of planets included, whether or not we include a GP to account for stellar noise, eccentric fits, and whether or not the second planet is modeled as the 14 day signal, or the 15 day signal. A full table of our model results is provided in Table 3.3. Our analysis found that both the Quasi-Periodic and dSHO GPs perform similarly in model comparison, and so we only include the Quasi-Periodic results for brevity. When comparing models, we use the Bayesian Information Criterion [BIC; 209] and the Corrected Akaike Information Criterion [AICc; 191]. The BIC of each model can be used to estimate the Bayes Factor (BF), a measure of preference for one model over another. Half the difference in BIC between two models is used to estimate the Schwarz Criterion, which itself is an approximation of the log BF. The AICc is an approximation of the Kullback-Leibler information, another metric for ranking the quality of models [191].

[209] suggest that a $\log_{10}$ BF > 2 (ln BF > 4.6) is decisive evidence for one model over another. For GJ 3929, our 2 planet ($\sim$15 day) model is preferred over the next best model, a 2 planet GP ($\sim$15 day), with a BF of 5.86 (RadVel estimates likelihoods using ln), suggesting a strong preference for the no GP case. The AICc simply prefers the model that minimizes the AICc, which is also the 2 planet model ($\sim$15 day). Both methods of estimation are only asymptotically correct, but are preferred by a wide enough margin, and agree with one another. Consequently, we use these comparisons to justify selecting the 2 planet model ($\sim$15 day) without a GP as our best model.

Table 3.3: RV Model Comparisons[a]

Fit	Number of Free Parameters	BIC	AICc
0 planet	4	566.5757	552.0607
—			

Continued on next page

Table 3.3 – continued from previous page

Fit	Number of Free Parameters	BIC	AICc
1 planet	7	569.5241	548.4207
1 planet ecc	9	578.4362	553.4362
1 planet GP	11	574.0880	545.0023
—			
2 planet (∼14 day)	10	560.2770	533.0948
2 planet (∼14 day) ecc (b)	12	567.0928	536.1688
2 planet (∼14 day) ecc (c)	12	562.6540	531.7300
2 planet (∼14 day) ecc (both)	14	567.6228	533.2274
2 planet GP (∼14 day)	14	576.62	542.2246
2 planet (∼15 day)	**10**	**545.5826**	**518.4004**
2 planet (∼15 day) ecc (b)	12	552.2589	521.3349
2 planet (∼15 day) ecc (c)	12	551.8569	520.9229
2 planet (∼15 day) ecc (both)	14	560.8289	525.8289
2 planet GP (∼15 day)	14	557.3132	522.9178

[a]Model comparison was performed on RV-only fits. This is motivated in Section 3.4.5.

3.4.3 An Additional Transiting Planet?

As elaborated further in Section 3.4.2 and detailed in [213], GJ 3929 RVs show two strong periodicities between 14-16 days. Consistent with [213], fitting either signal eliminates the other, suggesting that one is an alias of the other. Thus, we conclude that the two signals originate from a single source, though the true periodicity is originally unclear. Such a signal might be an additional planet, and if so, may be transiting. Here we search the TESS photometry for signs of additional transiting exoplanets, with a particular emphasis

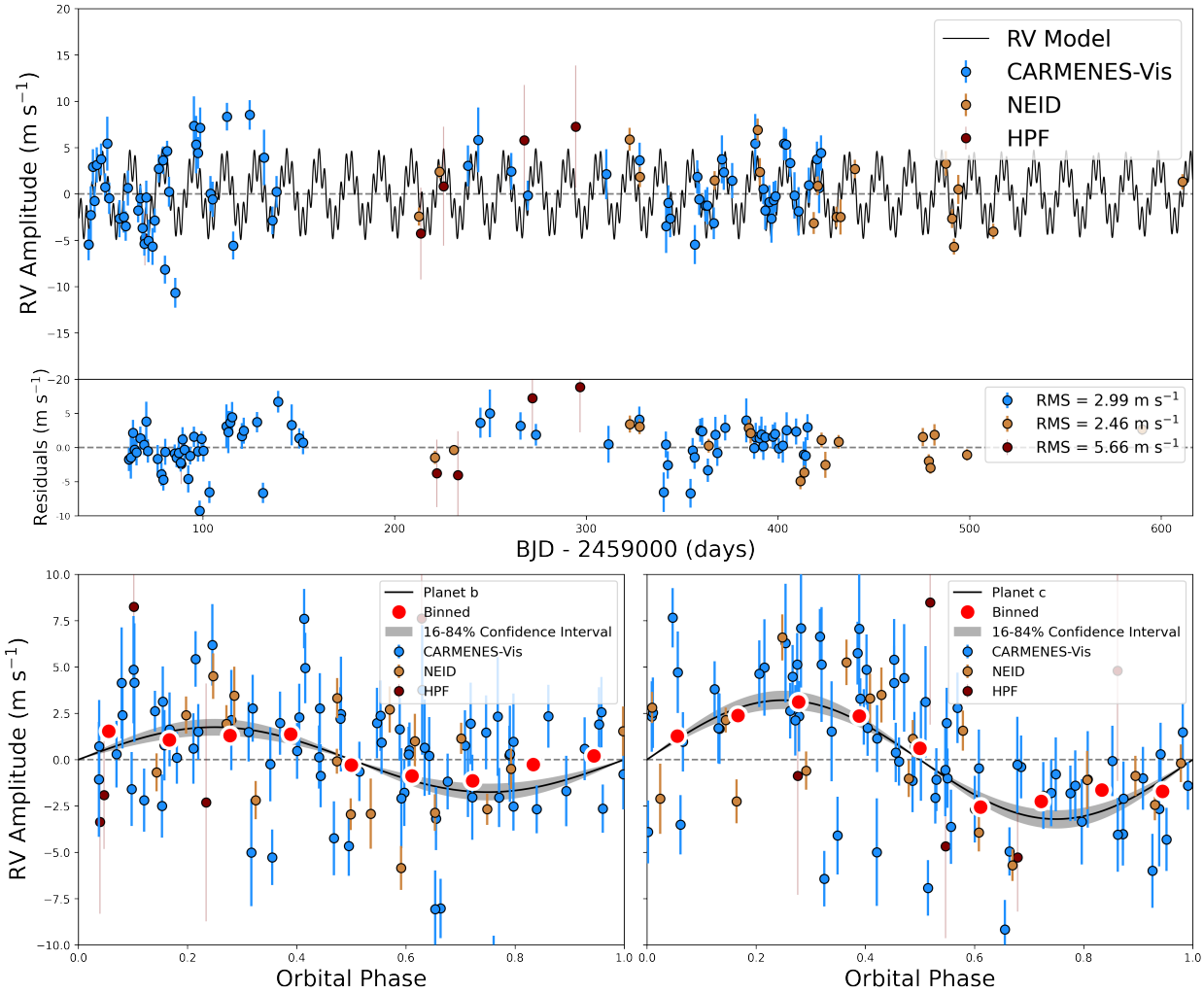

Figure 3.7: Top: RV data of GJ 3929 used in our analysis. The data has been adjusted for systematic offsets. Overlaid in black is the 2 planet model. Bottom: Phase folds of our median fit to planets b and c after subtracting the other planet, with a 1σ confidence interval overlaid. Jitter values are not included in the errors.

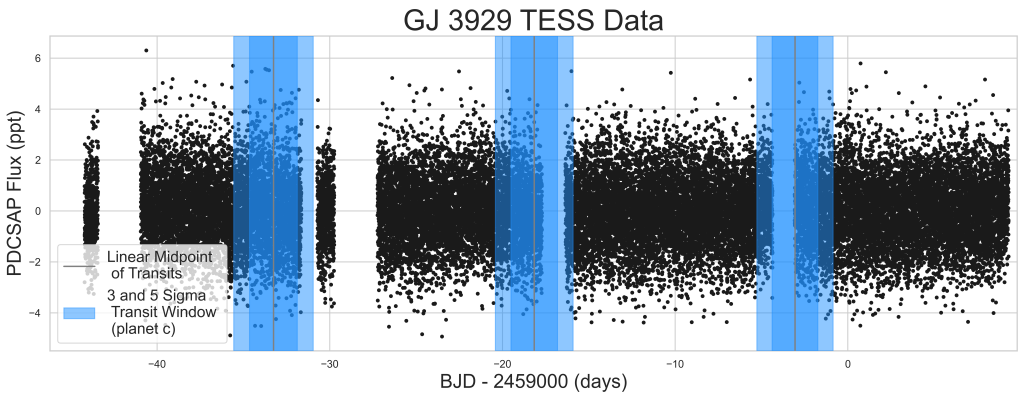

Figure 3.8: TESS PDCSAP flux of GJ 3929, taken during Sectors 24 and 25. The projected linear ephemeris of planet c is marked by a vertical gray line, with the 3σ and 5σ windows of uncertainty overlaid. It seems plausible that the second and third transits of planet c might have fallen into data gaps, though the negative detection in the first transit window cannot easily be explained if planet c is transiting. Thus, we can rule out transits of planet c with 3σ confidence.

on planets in this period range.

We use the `TransitLeastSquares` [TLS; 178] python package in order to search for additional periodic transit signals in the TESS lightcurves. Unlike a Box-Least Squares algorithm [BLS; 223], which is used frequently in transit searches, the TLS adopts a more realistic transit shape, increasing its sensitivity to transiting exoplanets, especially smaller ones. Initially, we recover GJ 3929b with a signal detection efficiency (SDE) > 35, a highly significant detection. [104] suggest that an SDE > 6 represents a conservative cutoff for a "significant" signal, though others adopt higher values [348, 245]. We then mask the transits of planet b, and continue the investigation. Our second check highlights a significant signal at 13.9 days (SDE = 12.74), somewhat close to the suspected planetary signals from the RVs. However, analysis of the candidate transit event itself seems inconsistent. Using the non-parametric mass-radius relationship from `mrexo` [205], we estimate that planet c would have a radius of 2.26 $R_\oplus$ using the minimum mass, and consequently a non-grazing transit depth of 4.19 ppt, more than 4 times as large as planet b. We caution that such mass-radius relationships are associated with a large uncertainty, though Figure 5.8 makes it clear that GJ 3929c should

at least be larger than planet b. However, this "transit" observed by TLS at $\sim$ 14 days has a depth of 0.24 ppt. It is possible that the transits of this candidate are grazing, resulting in an anomalously small transit depth. However, the duration of the transits of this signal are also much longer than expected, at 0.42 days. This is not only inconsistent with a grazing transit, but would be too long for any transit at this period. Finally, the estimated transit phase is totally inconsistent with the time of conjunction found in [213]. TLS finds a T_c = 2459867 BJD, while [213] would have expected a T_c = 2459872 BJD (scaling back the time of conjunction reported). We thus conclude that this significant $\sim$ 14 day periodicity identified by the `TLS` package is not planet c, and is most likely noise.

It is possible that planet c is transiting, but that its transits fell into TESS data gaps. In Figure 3.8, we highlight where the transits of planet c would occur relative to the TESS photometry. We identify no clear transit signals in the data.

We calculate 3 and 5σ transit windows in Figure 3.8 by using our posterior period and time of conjunction values for planet c, and back-propagating them using standard propagation of error. Consequently, from Figure 3.8, we can rule out non-grazing transits of planet c with 3σ confidence.

3.4.4 Candidate Planet, or Planet?

[213] designated the 14-15 day signal a planet candidate. While no transit signal is clearly detected at this period, we can rule out most false positive scenarios.

GJ 3929c might be a highly inclined binary or brown dwarf. While such a scenario cannot easily be ruled out, GJ 3929 has a Gaia RUWE value of 1.185, which is consistent with little astrometric motion [**?** 138, 239]. This suggests that a highly inclined binary scenario is unlikely.

Periodic or quasi-periodic RV signals can also be created by stellar magnetic activity. Our model comparison (Table 3.3) does not prefer a model that includes activity mitigation, and TESS photometry does not exhibit any obvious periodic variability (Figure 3.1). Furthermore, no strong signal near 14 or 15 days exists in the Hα indicator data (Figure 3.6). The candidate rotation period does show up very strongly in the Hα periodogram, however, and its value > 100 days is far from either planet.

The $\sim$ 15 day signal associated with planet c is stable over the time baseline and across instruments, further suggesting a planetary explanation. Performing a 2 planet fit (without a GP) on the CARMENES data, and doing the same with all data, yields consistent results ($K_{c,carmenes} = 3.20 \pm 0.58$ m s^{-1}; $K_{c,all} = 3.18 \pm 0.49$ m s^{-1}). Planetary signals are expected to remain stable over any observational baseline, while activity-sourced signals increase or decrease in amplitude over time. This analysis provides additional evidence for the true period of planet c at $\sim$ 15 days. Performing the same analysis on the $\sim$ 14 day signal yields a noticeable decrease in amplitude with the new RV data ($K_{c,carmenes} = 2.64 \pm 0.63$ m s^{-1}; $K_{c,all} = 2.38 \pm 0.52$ m s^{-1}). While the two values are consistent, the 14 day signal appears more sensitive to the new data.

3.4.5 Joint Transit-RV Analysis

Table 3.4: Priors Used for Bayesian Model Fits

Parameter Name	Prior	Units	Description
Planet b Orbital Parameters			
P_b	$\mathcal{U}^a(2.0, 3.0)$	days	Period
$T_{con,b}$	$\mathcal{U}(2459319.0, 2459320.0)$	BJD (days)	Time of Inferior Conjunction
$\sqrt{e}\cos\omega_b^*$	$\mathcal{U}(-1, 1)$	...	Eccentricity Reparametrization
$\sqrt{e}\sin\omega_b^*$	$\mathcal{U}(-1, 1)$	...	Eccentricity Reparametrization
$R_{p,b}/R_*$	$\log\mathcal{N}^b(0.0953, 1.0)$	...	Scaled Radius

Continued on next page

Table 3.4 – continued from previous page

Parameter Name	Prior	Units	Description
b_b	$\mathcal{U}(0.0, 1.0)$	...	Impact Parameter
K_b	$\mathcal{U}(0.01, 100)$	m s^{-1}	Velocity Semi-amplitude
Planet c Orbital Parameters			
P_c	$\mathcal{U}(14.5, 16)$	days	Period
$T_{con,c}$	$\mathcal{U}(2459064.0, 2459080.0)$	BJD (days)	Time of Inferior Conjunction
$\sqrt{e}\cos\omega_c^*$	$\mathcal{U}(-1, 1)$	...	Eccentricity Reparametrization
$\sqrt{e}\sin\omega_c^*$	$\mathcal{U}(-1, 1)$	...	Eccentricity Reparametrization
K_c	$\mathcal{U}(0.01, 100)$	m s^{-1}	Velocity Semi-amplitude
GP Hyperparameters			
η_1^*	$\mathcal{U}(0, 50)$	m s^{-1}	GP Amplitude
η_2^*	$\mathcal{U}(0.1, 10000)$	days	Exponential Decay Length
η_3^*	$\mathcal{U}(100, 150)$	days	Recurrence Rate (Rotation Period)
η_4^*	$\mathcal{U}(0.05, 0.6)$	...	Periodic Scale Length
Instrumental Parameters			
$\gamma_{\rm CARMENES}$	$\mathcal{U}(-100, 100)$	m s^{-1}	CARMENES Systematic Offset
$\gamma_{\rm NEID}$	$\mathcal{U}(-100, 100)$	m s^{-1}	NEID Systematic Offset
$\gamma_{\rm HPF}$	$\mathcal{U}(-100, 100)$	m s^{-1}	HPF Systematic Offset
$\sigma_{\rm CARMENES}$	$\mathcal{U}(0.01, 100)$	m s^{-1}	CARMENES Jitter
$\sigma_{\rm NEID}$	$\mathcal{U}(0.01, 100)$	m s^{-1}	NEID Jitter
$\sigma_{\rm HPF}$	$\mathcal{U}(0.01, 100)$	m s^{-1}	HPF Jitter
$\sigma_{\rm TESS}$	$\log\mathcal{N}(-9.48, 2)$	...	Photometric Jitter
$\sigma_{\rm ARCTIC-20210226}$	$\log\mathcal{N}(-9.67, 2)$	...	Photometric Jitter
$\sigma_{\rm ARCTIC-20210430}$	$\log\mathcal{N}(-11.88, 2)$	...	Photometric Jitter
$\sigma_{\rm LCO-HAL_{gp}}$	$\log\mathcal{N}(-12.41, 2)$	...	Photometric Jitter
$\sigma_{\rm LCO-HAL_{ip}}$	$\log\mathcal{N}(-13.17, 2)$	...	Photometric Jitter
$\sigma_{\rm LCO-HAL_{rp}}$	$\log\mathcal{N}(-12.96, 2)$	...	Photometric Jitter
$\sigma_{\rm LCO-HAL_{zs}}$	$\log\mathcal{N}(-12.53, 2)$	...	Photometric Jitter
$\gamma_{\rm TESS}$	$\mathcal{N}(0.0, 10.0)$	...	Photometric Offset
$\gamma_{\rm ARCTIC-20210226}$	$\mathcal{N}(0.0, 10.0)$	...	Photometric Offset

Continued on next page

Table 3.4 – continued from previous page

Parameter Name	Prior	Units	Description
$\gamma_{\rm ARCTIC-20210430}$	$\mathcal{N}(0.0, 10.0)$	...	Photometric Offset
$\gamma_{\rm LCO-HAL_{gp}}$	$\mathcal{N}(0.0, 10.0)$	...	Photometric Offset
$\gamma_{\rm LCO-HAL_{ip}}$	$\mathcal{N}(0.0, 10.0)$	...	Photometric Offset
$\gamma_{\rm LCO-HAL_{rp}}$	$\mathcal{N}(0.0, 10.0)$	...	Photometric Offset
$\gamma_{\rm LCO-HAL_{zs}}$	$\mathcal{N}(0.0, 10.0)$	...	Photometric Offset
$u_{\rm TESS}$	$\mathcal{K}^c$	...	Quadratic Limb Darkening
$u_{\rm ARCTIC}$	$\mathcal{K}$	...	Quadratic Limb Darkening
$u_{\rm LCO_{gp}}$	$\mathcal{K}$	...	Quadratic Limb Darkening
$u_{\rm LCO_{ip}}$	$\mathcal{K}$	...	Quadratic Limb Darkening
$u_{\rm LCO_{rp}}$	$\mathcal{K}$	...	Quadratic Limb Darkening
$u_{\rm LCO_{zs}}$	$\mathcal{K}$	...	Quadratic Limb Darkening

[a] $\mathcal{U}$ is a uniform prior with $\mathcal{U}$(lower,upper)

[b] $\mathcal{N}$ is a normal prior with $\mathcal{N}$(mean,standard deviation)

[c] $\mathcal{K}$ is a reparametrization of a uniform prior for limb darkening, outlined in [216]

*These parameters are not utilized in our final adopted fit. We include them for completeness.

The final step of our analysis is the combination of the transit fits and RV fits into one complete, joint analysis. We adopt this model as our best, final model as it is the most complete description of GJ 3929: it utilizes all data, and characterizes both planets that are observed in this system, while also characterizing properties of planet b that can only be gleaned from photometry, especially its radius.

We performed a model comparison in Section 3.4.2, and we use that model comparison to select our preferred model, which is a 2 planet model without the use of a GP. We performed this model comparison in the RV analysis rather than the joint analysis for one primary reason: all the free parameters of interest are primarily measured in the RVs. First, we

were interested in deciding between a 1 and 2 planet model. The second planetary signal is *only* detected in the RVs; transit searches have been unsuccessful. Second, we wanted to differentiate between a 14 or 15 day period for planet c. Again, this signal is only represented in the RV data. Thirdly, we wanted to justify the use of a GP. Our primary consideration for the use of a GP was in the RVs, as the photometry are quiet, as expected. A > 100 day rotation period would be unlikely to be observed in TESS PDCSAP flux, and the ground-based photometry are all far too short in baseline to be affected by a periodicity on even 1/100th of rotation period's timescale. Finally, we were interested in testing the veracity of eccentric models. Eccentricity, however, is much more strongly constrained by RVs than by photometry.

Our final, joint fit, then, was performed considering a 2 planet model, where the second planet period is constrained between 15 and 16 days in order to prevent the MCMC chains from clustering around the alias at 14.2 days. The model is circular, and we do not adopt any GP to account for excess noise. We use the `exoplanet` software package in the joint fit, and the transits are modeled identically as described in Section 3.4.1. The RVs are modeled in `exoplanet` as well, with two Keplerian orbital solutions that model both photometric and RV datasets simultaneously. In particular, the period and time of conjunction of each planet are shared between the datasets, while other orbital parameters are typically constrained to one dataset or another. A full list of the priors used in our model are available in Table 5.3.

We again use the HMC algorithm with a NUTS sampler for increased sampling efficiency. We again run 10000 tuning steps and 10000 subsequent steps posterior estimation steps. Our final transit fits are visible in Figure 3.4. Our final RV fit is visible in Figure 3.7. Finally, our posterior estimates for each model free parameter are listed in Table 4.3.

Table 3.5: Derived Parameters for both planets

Parameter	Units	GJ 3929b	GJ 3929c
Orbital Parameters:			
Orbital Period	P (days)	2.616235 ± 0.000005	15.04 ± 0.03
Time of Inferior Conjunction	T_C ($\mathrm{BJD_{TDB}}$)	2458956.3962 ± 0.0005	2459070.9 ± 0.4
Eccentricity	e	0 (fixed)	0 (fixed)
Argument of Periastron	ω (degrees)	90 (fixed)	90 (fixed)
RV Semi-Amplitude	K (m/s)	$1.77^{+0.44}_{-0.45}$	3.22 ± 0.51
Transit Parameters:			
Scaled Radius	R_p/R_*	0.0156 ± 0.0003	...
Scaled Semi-major Axis	a/R_*	16.8 ± 0.5	...
Impact Parameter	b	$0.11^{+0.06}_{-0.07}$	...
Orbital Inclination	i (degrees)	88.442 ± 0.008	...
Transit Duration	T_{14} (days)	$0.0495^{+0.0008}_{-0.0007}$	...
Planetary Parameters:			
Mass	M_p ($\mathrm{M_\oplus}$)	$1.75^{+0.44}_{-0.45}$	5.71^a± 0.94
Radius	R_p ($\mathrm{R_\oplus}$)	1.09 ± 0.04	...
Density	ρ_p ($\mathrm{g/cm^3}$)	7.3 ± 2.0	...
Semi-major Axis	a (AU)	0.0252 ± 0.0005	0.081 ± 0.002
Average Incident Flux	$\langle F \rangle$ ($\mathrm{W/m^2}$)	24000 ± 1000	2300 ± 100
Planetary Insolation	S ($\mathrm{S_\oplus}$)	17.3 ± 0.7	1.68 ± 0.07
Equilibrium Temperature[b]	T_{eq} (K)	568 ± 6	317 ± 3
Instrumental Parameters			
RV Jitter	$\sigma_{CARMENES}$ (m/s)	1.80 ± 0.48	
	σ_{NEID} (m/s)	2.25 ± 0.66	
	σ_{HPF} (m/s)	6 ± 7	
RV Offset	$\gamma_{CARMENES}$ (m/s)	0.97 ± 0.39	
	γ_{NEID} (m/s)	5.56 ± 0.66	
	γ_{HPF} (m/s)	8 ± 4	
Limb Darkening	$u_{1,\mathrm{TESS}}$, $u_{2,\mathrm{TESS}}$	$0.3^{+0.3}_{-0.2}$,0.3 ± 0.4	
	$u_{1,\mathrm{ARCTIC}}$, $u_{2,\mathrm{ARCTIC}}$	0.5 ± 0.3,$0.0^{+0.4}_{-0.3}$	

Continued on next page

Table 3.5 – continued from previous page

Parameter	Units	GJ 3929b	GJ 3929c
	$u_{1,\mathrm{LCO-HALgp}}$, $u_{2,\mathrm{LCO-HALgp}}$	$1.0^{+0.5}_{-0.6}$,$-0.3^{+0.5}_{-0.4}$	
	$u_{1,\mathrm{LCO-HALip}}$, $u_{2,\mathrm{LCO-HALip}}$	$1.0^{+0.3}_{-0.4}$,$-0.3^{+0.4}_{-0.3}$	
	$u_{1,\mathrm{LCO-HALrp}}$, $u_{2,\mathrm{LCO-HALrp}}$	$0.3^{+0.3}_{-0.2}$,0.3 ± 0.4	
	$u_{1,\mathrm{LCO-HALzs}}$, $u_{2,\mathrm{LCO-HALzs}}$	$0.3^{+0.3}_{-0.2}$,0.3 ± 0.4	
Photometric Jitter	σ_{TESS} (ppm)	10^{+14}_{-7}	
	$\sigma_{\mathrm{ARCTIC-20210226}}$ (ppm)	514 ± 100	
	$\sigma_{\mathrm{ARCTIC-20210430}}$ (ppm)	545 ± 60	
	$\sigma_{\mathrm{LCO-HALgp}}$ (ppm)	4^{+33}_{-4}	
	$\sigma_{\mathrm{LCO-HALip}}$ (ppm)	356 ± 42	
	$\sigma_{\mathrm{LCO-HALrp}}$ (ppm)	558 ± 40	
	$\sigma_{\mathrm{LCO-HALzs}}$ (ppm)	480 ± 40	
Photometric Mean	$\mathrm{mean}_{\mathrm{TESS}}$ (ppm)	40 ± 8	
	$\mathrm{mean}_{\mathrm{ARCTIC-20210226}}$ (ppm) .	400 ± 70	
	$\mathrm{mean}_{\mathrm{ARCTIC-20210430}}$ (ppm) .	340 ± 60	
	$\mathrm{mean}_{\mathrm{LCO-HALgp}}$ (ppm)	350 ± 100	
	$\mathrm{mean}_{\mathrm{LCO-HALip}}$ (ppm)	360 ± 40	
	$\mathrm{mean}_{\mathrm{LCO-HALrp}}$ (ppm)	350 ± 40	
	$\mathrm{mean}_{\mathrm{LCO-HALzs}}$ (ppm)	340 ± 40	

[a]Minimum mass

[b]Estimated assuming an albedo of 0

3.5 Discussion

We have refined the measured parameters for GJ 3929b ($P_b = 2.616235 \pm 0.000005$ days; $R_b = 1.09 \pm 0.04$ $R_\oplus$; $M_b = 1.75^{+0.44}_{-0.45}$ $M_\oplus$; $\rho_b = 7.3 \pm 2.0$ g cm^{-3}) and GJ 3929c ($P_c = 15.04 \pm$

0.03 days; Msin i_c = 5.71 ± 0.94 $M_\oplus$).

GJ 3929 joins a growing list of M dwarf systems that contain a short period terrestrial planet, accompanied by a non-transiting, more massive planet [i.e. 54]. Additionally, the possible existence of additional planetary companions cannot be ignored. M dwarfs in particular tend to have higher multiplicity of smaller exoplanets. [250] used metallicity correlations when studying M dwarf systems to estimate how much planet-forming material is present in an initial planetary disk. It is likely that a correlation exists between metallicity of the host star and the amount of planet-forming material in a disk, especially for late-type stars [55, 199]. [250] estimate only 9 $M_\oplus$ of material for forming planets in a metal-poor ([Fe/H] = -0.5) early M dwarf (M_* = 0.6 $M_\odot$). While GJ 3929 is smaller (M_* = 0.32 $M_\odot$) than this system, its metallicity is much closer to the Sun ([Fe/H] = -0.05), giving it $\sim$ 15 $M_\oplus$ of material to form planets, if we assume the disk-to-star mass ratio of 0.01 that [250] adopt. The sum of the median mass of GJ 3929b (1.75 $M_\oplus$) and the median minimum mass of GJ 3929c (5.70 $M_\oplus$) is significantly less than this value, implying that either planet c is significantly inclined and much more massive than we estimate, additional planets exist in the system, or the extra disk material was accreted onto the star.

We highlight the GJ 1132 system, characterized in [54], for comparison with GJ 3929. GJ 1132b is also a short period, Earth-sized rocky planet orbiting an M dwarf, with an additional non-transiting companion. GJ 3929b is denser than GJ 1132b, as seen in Figure 5.8, though it's longer orbital period makes its RV semi-amplitude a bit smaller. We include comparisons to this system further in the discussion to help frame GJ 3929 in the context of similar systems.

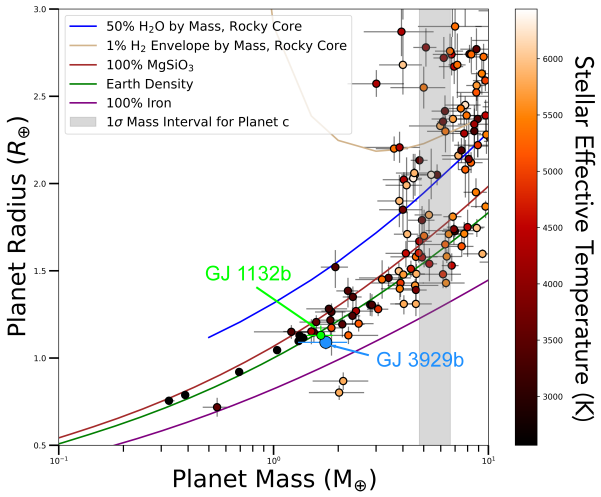

Figure 3.9: Mass-Radius diagram of exoplanets taken from the NASA Exoplanet Archive on 2022 April 5. We restricted our study to planets with measured radii and masses. Colors indicate the stellar effective temperature of the system's host star. GJ 3929b is depicted in blue, and a region spanning the possible positions of planet c is visible in gray. We also include GJ 1132b in green, as it is a similar system discussed further in the text. A few theoretical density estimates are included as outlined in [406].

3.5.1 Planet b

GJ 3929b is an Earth-sized exoplanet, placing it below the radius gap for M Dwarfs [382, 305]. Our mass and radius estimates allow us to constrain GJ 3929b's bulk density, and confirm its consistency with a composition slightly denser than Earth (Figure 5.8). Due to its proximity to its host star, GJ 3929b probably lost much of its atmosphere due to XUV flux [380]. The addition of a non-transiting second planet in the system originally confounded our RV analysis of the system, and further emphasizes the challenges discussed in [174] relating to the mass measurement of transiting planets. Since more than half of the time, the transiting planet in a system with non-transiting companions does not have the largest semi-amplitude, initial follow-up can be confusing.

GJ 3929b is Venus-like ($S_b = 17.3^{+0.8}_{-0.7}$), in that it resides in its host-star's Venus-zone. This is defined as the boundary between the runaway-greenhouse inner edge of the Habitable Zone [210, 220, 221], and an orbital distance that would produce 25 times Earth-like flux

[202, 298]. Learning more about planets in the Venus-zone is an important step towards discovering Earth-twins. Spectroscopic observations of the Solar System, for example, would have a hard time distinguishing between Earth and Venus, despite their drastically different surface environments [201]. GJ 3929b is an excellent planet for studying the differences in spectra for a system that is Venus-like, and for which we are certain that it is nothing like Earth.

Fortunately, GJ 3929b is amenable to atmospheric study with the James Webb Space Telescope [JWST; 143]. Beyond learning more about exo-Venuses, studying the atmosphere of GJ 3929b could help reveal the evolutionary history of the system, and shed light on planet formation models. GJ 3929b has an estimated Transmission Spectroscopy Metric [TSM; 214] of 14 ± 4, placing it in the top quintile of Earth-sized exoplanets amenable to JWST observations. The density of GJ 3929b does not suggest a thick atmosphere, though a thin atmosphere of outgassed volatiles, a thin atmosphere lacking in volatiles and consisting of silicates and enriched in refractory elements, or a no-atmosphere scenario are all plausible [340].

In Figure 4.10, we highlight GJ 3929b's TSM in the context of other small exoplanets. We include all exoplanets with sufficient information to calculate a TSM on the NASA Exoplanet Archive, though we caution that only exoplanets with $> 3\sigma$ mass measurements are likely to see follow-up with JWST due to a degeneracy in the interpretation of spectra [30]. GJ 3929b occupies a truly rare position in this space, as quality mass measurements are very challenging for planets of its size, and small planets with mass measurements are usually not very amenable to transmission spectroscopy. We highlight a few other small planets amenable to transmission spectroscopy. Besides the TRAPPIST-1 system [1], which is exceptional in most parameter spaces, few small planets are better for transmission spectroscopy than GJ 3929b. While GJ 1132b is a similar system to GJ 3929b, and its TSM is slightly larger, GJ 3929b is brighter, making high-SNR measurements with JWST more likely, and making it

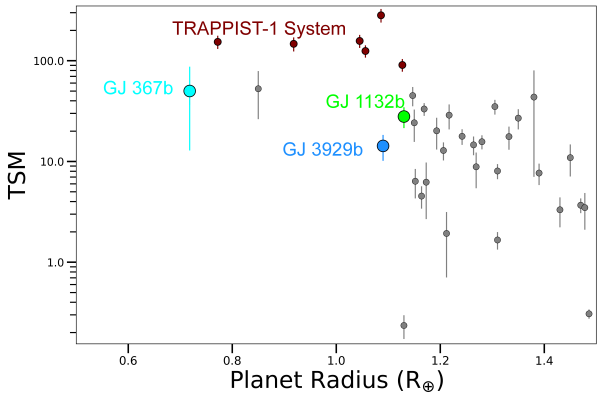

Figure 3.10: Transmission Spectroscopy Metric [TSM; 214] of various planets taken from the NASA Exoplanet Archive on 2022 April 5. We note that GJ 3929b is in a sparsely populated region of parameter space, due largely to the difficulty of studying small exoplanets. We highlight a few other small-planet systems that are amenable to transmission spectroscopy.

more attractive for ground-based follow up. On the other hand, GJ 367b is an ultra-short period (USP) planet with a much higher TSM than GJ 3929b. However, its USP nature makes the existence of an atmosphere far less likely than for GJ 3929b, and further any such atmosphere would likely exhibit very different chemistries from GJ 3929b, since its equilibrium temperature is more than 3 times hotter [$T_{eq,GJ367b} = 1745 \pm 43$; K 230].

3.5.2 Planet c

It is not clear whether or not GJ 3929c is a transiting exoplanet, though we detect no transits of this system in this study. Consequently, we cannot measure the radius of planet c, nor its bulk density.

The measured minimum mass of GJ 3929c suggests that it is at least a sub-Neptune in size when predicted from the mass-radius relationship, and perhaps larger [205]. M dwarf systems consisting of a close-in, terrestrial exoplanet and longer period sub-Neptunes are common occurrences [326, 328], though the brightness of GJ 3929 allows for a more detailed study than is often the case. GJ 3929 will not be observed by TESS during Cycle 5, though the success

of the TESS mission suggests that it will likely continue for years longer. Additionally, the advent of future photometric missions [i.e. PLATO; 261] suggest that GJ 3929 will probably receive additional photometric observations in the future, and a transit of planet c may someday be identified.

3.5.3 Comparison to Kemmer et al. (2022)

The addition of HPF and NEID RV data, as well as diffuser-assisted ARCTIC data have refined or changed various measured and derived parameters for each planet. Furthermore, our choice to use the $\sim$ 15 day signal as the period of GJ 3929c has an additional effect on several of the qualities of the planet.

The period and transit time of planet b are fully consistent with those found in [213], though the uncertainty is slightly larger in our case. This is most likely due to [213]'s use of more transit data and in general modeling more transits of planet b. We prioritized higher precision photometry, and consequently opted not to use the SAINT-EX photometry or the additional LCO data utilized in [213]. Furthermore our team did not have access to the transits obtained by the Observatorio de Sierra Nevada (OSN). Our additional ARCTIC photometry changed the radius measurement from 1.150 $\pm$ 0.04 $R_\oplus$ to 1.09 $\pm$ 0.04 $R_\oplus$, though we note that these values are 1σ consistent.

The additional RVs did not shrink the formal 1σ errorbars of the measured RV semi-amplitudes, but did modify the mean posterior values and the resulting K/σ of our mass measurements are improved. For planet b, [213] found a mass of $1.21^{+0.40}_{-0.42}$ $M_\oplus$, and we find a mass of $1.75^{+0.44}_{-0.45}$ $M_\oplus$. Similarly for planet c, [213] found a minimum mass of $5.27^{+0.74}_{-0.76}$ $M_\oplus$, while we measure a minimum mass of 5.71 $\pm$ 0.94 $M_\oplus$. We note, however, that changing the period of planet c likely played a role in this change as well, not merely the additional RVs.

Perhaps the most significant departure from [213] is that our final model did not utilize a GP. In fact, this is probably the most significant contribution to the increased mass uncertainties in our fits. When utilizing a GP, our model does yield more precise mass uncertainties than those in [213], which is expected due to our inclusion of additional data. The increased amplitudes remain, however, suggesting that their difference is not related to the use of a GP. As shown in Table 3.3, we cannot justify the use of a GP in our final fit.

3.6 Summary

We use RVs from the NEID, HPF, and CARMENES spectrographs to characterize the transiting planet GJ 3929b, and the probably non-transiting planet GJ 3929c. We use diffuser-assisted photometry from the ARCTIC telescope in combination with LCOGT and TESS photometry in order to improve the radius of GJ 3929b ($R_b = 1.09 \pm 0.04$ $R_\oplus$), and we use RVs from CARMENES, NEID, and HPF to measure the mass of both planets ($M_b = 1.75 \pm 0.45$ $M_\oplus$; $M \sin i_c = 5.70 \pm 0.92$ $M_\oplus$). We conclude that GJ 3929 is a 2 planet system with a 2.61626 ± 0.000005 day transiting exo-Venus that is highly amenable to transmission spectroscopy. GJ 3929c is a more massive planet orbiting with a period of 15.04 ± 0.03 days that is unlikely to transit.

Chapter 4

The TESS-Keck Survey. XVII. Precise Mass Measurements in a Young, High Multiplicity Transiting Planet System using Radial Velocities and Transit Timing Variations

4.1 Introduction

Planet formation and evolution are still poorly understood: pebble accretion could form planets in situ [231, 193], or planets might form beyond the ice line and migrate inward [151, 99, 316, 194]. Atmospheric sculpting from stellar flux [232] might sculpt the observed exoplanetary population, or the outgassing of volatiles [325] might dominate.

Answering these questions requires us to study young systems, still undergoing either formation

or evolution. Unfortunately, such systems are among the most contaminated by stellar variability [i.e. 74, 51]. Furthermore, challenges comparing the formation and evolution of different exoplanetary systems are compounded by the various natures of host stars: while it is possible to control for aspects such as age, stellar type, and metallicity when studying formation history, the probable dependence of system evolution on a variety of the host star's parameters makes wider study difficult. It follows that multiple-planet systems are very attractive when studying planetary characteristics such as atmospheric evolution, as they all share a host star, allowing for the removal of degeneracies between different stellar parameters. Higher multiplicities are even better, as they allow for a larger sample size that shares system parameters. Targets that are young, highly multiple, and amenable to follow-up study are exceedingly rare. Here I present my in-depth analysis of TOI-1136, one such system.

TOI-1136 has at least six transiting planets [96] (hereafter D23), and a candidate seventh. TOI-1136 is a young (700 $\pm$ 100 Myr), bright (V=9.5) G dwarf and its photometric data show signs of transit timing variations (TTVs), allowing for the precise characterization of most planet masses with photometry alone. The planets are in deep Laplace resonance (P_b = 4.1727 d; P_c = 6.2574 d; P_d = 12.5199 d; P_e = 18.801 d; P_f = 26.321 d; P_g = 39.545 d), suggesting a distinct formation history [short scale type-I migration; 347, D23]. TOI-1136 was observed by the Transiting Exoplanet Survey Satellite [TESS; 318] for six non-consecutive sectors. The relatively short baseline of TESS limits the precision with which we can constrain planetary masses using TTVs, especially for the longer-period outer planets. Furthermore, adding RVs in conjunction with TTVs can help prevent conflict between TTV-only and RV-only measured masses [365, 281].

I utilize over 400 RVs taken with the High Resolution Echelle Spectrometer [HIRES; 387], Levy Spectrometer on the robotic Automated Planet Finder [APF; 388] Telescope, and the High-Accuracy Radial velocity Planetary Searcher North [HARPS-N; 89] spectrograph in

conjunction with TESS data to refine the parameters of the TOI-1136 system. I combine these observations with TTVs and perform a detailed RV + TTV + GP analysis of TOI-1136, which is likely the most complicated mass-retrieval model for an exoplanet in literature to date.

The chapter is organized as follows. A summary of our observations and data is given in §4.2. A brief description of the stellar parameters of TOI-1136 is given in §5.3. A study of the candidate seventh planet is given in §4.4. Our analysis is detailed in §6.4. Finally, the results and their interpretation are placed into context in §6.5, and the paper is summarized in §6.6.

4.2 Observations

4.2.1 TESS Photometry

TOI-1136 was first observed by TESS during Sector 14 (18 July - 15 August 2019) and Sector 15 (15 August - 11 September 2019) of Cycle 2. TOI-1136 was later re-observed during Sectors 21 and 22 (21 January - 18 March 2020), and in two subsequent sectors (41: 23 July - 20 August 2021; 48: 28 January - 26 February 2022). The star was first declared a TESS object of interest [TOI; 161] on 27 August 2019, and the science processing and operations center [SPOC; 198] pipeline would eventually identify 4 candidate planets in the system. Additional community observers would later identify two more community TOIs (CTOIs), increasing the number of candidate planets in the system to 6.

No additonal TESS photometry has been acquired since the system was studied in D23. Nonetheless, the TESS photometry is incorporated in multiple aspects of our analysis of the system. We build on the individual transit times of the TOI-1136 planets determined in

D23 by jointly modeling these transit times with RVs in §6.4. We also analyze the TESS Presearch Data Cleaning Simple Aperture Flux [PDCSAP; 198] photometry to measure the stellar rotation period, to fit a single transit to the candidate planet in §4.4.1, and to calculate FF′ values utilized in §4.5.1 by multiplying the PDCSAP Flux (F) by its first derivative [F′; 5].

4.2.2 RVs with Keck/HIRES

Between 1 November 2019 and 16 July 2022, we obtained 155 high-resolution spectra of TOI-1136, resulting in 103 nightly binned RV observations, using the High-Resolution Echelle Spectrometer (HIRES, **(author?)** 387) located at Keck Observatory. Precise radial velocities were extracted using a warm iodine cell in the light path for wavelength calibration, as described in [70]. We extracted precise RVs from the echelle spectra using the California Planet Search (CPS) pipeline [184].

We typically achieved a signal-to-noise ratio of ≈ 200 at visible wavlengths for each spectrum by capping the HIRES built-in exposure meter at 250,000 counts. resulting in a median nightly binned RV uncertainty of 1.75 m s^{-1}, and a median SNR of 214 for the wavelength order centered at 540 nm.

4.2.3 HARPS-N RVs

We also utilized 51 RV observations of TOI-1136 obtained using the HARPS-N spectrograph at the Telescopio Nazionale Galileo, a 3.6-m telescope located in the Canary Islands, Spain under the observing programs, CAT19A_162, ITP19_1 and CAT21A_119. Observations had a median exposure time of 1000 s and a median SNR of 74.6 at 550 nm.

HARPS-N RVs were reduced using the standard cross-correlation function mask method

outlined in [26] and [302]. After reduction, HARPS-N RVs had a mean uncertainty of 2.63 m s^{-1}.

4.2.4 RVs with the Automated Planet Finder

Essential to characterizing the stellar activity were additional RV observations taken using the APF Telescope, located at Lick Observatory on Mount Hamilton, CA. The automated nature of the APF allowed for much more consistent, high cadence observations than were possible using HIRES or HARPS-N. The smaller aperture of APF, however, restricted us to lower SNR and correspondingly less precise observations. Between 1 November 2019 and 16 July 2022, we carried out 320 APF observations over the course of 256 observing nights. APF spectra are calibrated using an iodine cell and are extracted using a process very similar to that of HIRES RV extraction [135].

A preliminary analysis of APF spectra motivated our choice of a minimum SNR threshold of 55, as spectra with lower SNR were subject to very large uncertainties. Our final collection of APF observations have a mean binned RV uncertainty of 4.92 m s^{-1} and a mean SNR of 94.1 estimated across its full wavelength coverage, centered at 596 nm.

4.3 Stellar Parameters

We utilize the stellar parameters of TOI-1136 as adopted in D23. D23 used `SpecMatchSyn` [306] on 3 iodine-free, high resolution HIRES spectra obtained as a part of TKS's observing program to derive $T_{\rm eff}$, $\log g$, and [Fe/H]. These results were then combined with Gaia parameters [139, 140] in the `Isoclassify` software package to obtain stellar mass, radius, and other relevant parameters for our models [189, 47]. The full list of stellar parameters is identical to those used in D23, and we refer readers to Table 1 in D23 for the full parameter

list, though for convenience we note that the star is a G5 dwarf with $M_* = 1.022 \pm 0.027$ $M_\odot$ and $R_* = 0.968 \pm 0.036$ $R_\odot$. We detail our independent measurement of the system's stellar rotation in the next subsection.

4.3.1 Stellar Rotation Period

Identifying the frequency of stellar rotation is an important part of characterizing systems with spot modulation, as a quasiperiodic signal can mask known exoplanet signals [248] or mimic real ones [251]. Young systems, like TOI-1136, are particularly susceptible to large activity signals that dwarf planetary signals [74].

D23 used a Lomb-Scargle periodogram [LS; 246, 334] to identify a rotation period of 8.7 ± 0.1 days for TOI-1136 based on TESS photometry. Because the quasi-periodic rotation signature often leads to significant peaks at harmonics of the true rotation period, we performed an independent analysis of the stellar rotation. We utilized the new SpinSpotter software package to fit an autocorrelation function (ACF) to TESS photometry [181], which is more robust than LS for detecting accurate stellar rotation periods [4]. We analyzed the ACF on all six Sectors of TESS data. We identified a rotation period of 8.42 ± 0.09 days using SpinSpotter, which is consistent with the previously identified rotation period (as opposed to a harmonic). The uncertainty is estimated by taking the standard deviation of the variations in parabola vertex locations from the expected position predicted by the found rotation period, which can underestimate uncertainties and likely contributes to the $> 1\,\sigma$ discrepancy with D23. However, [181] suggest that detecting at least 5 peaks in the ACF (seen in Figure 4.1) is strong evidence that the rotation estimate is reliable.

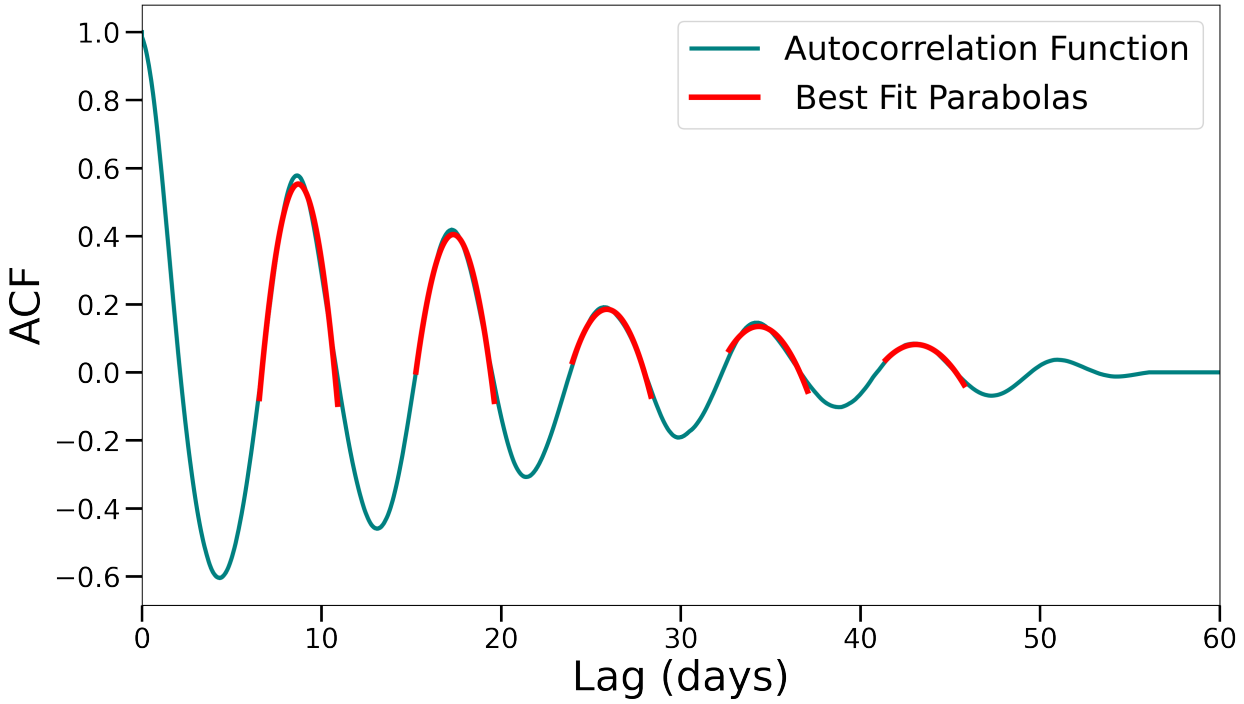

Figure 4.1: An autocorrelation function (ACF) of TOI-1136's TESS photometry. A clear frequency pattern with well-defined parabolas fit to the peaks of the ACF indicates a solid detection of the system's rotation period.

4.4 A Seventh Planet?

D23 identified a single transit that was distinct from those corresponding to planets b-g as a possible seventh planet in the TOI-1136 system. D23 were unable to identify any additional transits of this candidate planet in the TESS photometry, and so the period remained unclear.

D23 did not include a detailed analysis of the transit, mainly noting that the estimated radius was around 2.5 $R_\oplus$ and that the transit duration suggested a possible $\sim$ 80 day orbital period, consistent with a 2:1 resonance with planet g.

Without additional transits, it is difficult to conclude that the event is necessarily an exoplanet. False positive transit signatures were rare in NASA *Kepler* photometry, but are more common in the TESS photometry due to a large pixel size [369]. D23 ruled out visual, spectroscopic, co-moving, and astrometric companions, but this does not exclude

every possible false positive scenario. For example, an unresolved background eclipsing binary could potentially create such a signature. False positives from background eclipsing binaries are extremely unlikely in the high-multiplicity planetary systems characterized by *Kepler* [242], but the incidence of eclipsing binary FPs is likely higher for TESS planet candidates due to the larger pixel size. Another possibility is that the transit-like event is a false alarm, i.e., an instrumental artifact or spurious event that is non-astrophysical. To mitigate our uncertainty of the veracity of planet candidate seven, we tested both a seven-planet and a six-planet model in our full TTV + RV analyses, with constraints on the orbit of the seventh planet based on the RVs.

4.4.1 Identifying the Period of the Candidate

D23 estimate an orbital period near 80 days for the seventh planet candidate based on the transit duration. Such an estimate can be inaccurate, however, especially when factors such as eccentricity and impact parameter are also unknown. We explore other methods of estimating an orbital period for the single-transit candidate.

The period might be inferred from the RVs, as their quantity and cadence would be sufficient to find medium to longer-period planets with modest amplitudes in many planetary systems. A periodogram analysis is often fruitful when first trying to identify the orbital periods of planets in the RVs.

We first used a generalized Lomb-Scargle (GLS) periodogram [404] to identify significant periodicity in the RV data. Unfortunately, the GLS does not identify the periods of any of the known transiting planets, and it is unlikely that any of the high power periods correspond with the candidate planet. The highest-power periods are all close to, or aliases of, the known rotation period of TOI-1136. This is mainly caused by the prominent stellar activity in the system. Due to the quasi-periodic nature of the rotation signal, however, standard

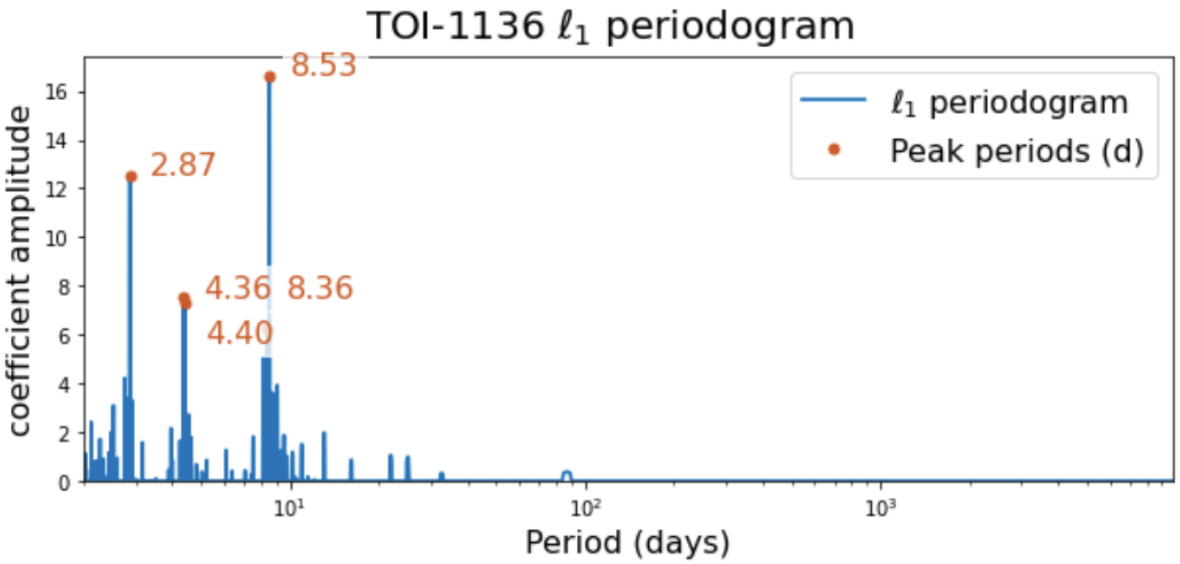

Figure 4.2: We computed an $l1$ periodogram of TOI-1136 RV data, determining the best white noise value for the noise model through cross-validation. Instrument offsets are fit by the compressed sensing model. Unlike other periodograms, multiple peaks can have significance. However, the rotation period (8.53 days), signals near the rotation period (8.36 days), and aliases of the rotation period (4.40, 4.36, 2.87 days) dominate the periodogram. Once again, planet periods are not significantly detected, and a more complicated model is required to remove the activity and uncover the planet signals.

sinusoidal fits are an imperfect match, and one cannot easily subtract the highest power signal for investigation of lower amplitude signals.

We next try the correlated noise model present in the Bayes Factor periodogram (BFP) with 1 moving average term introduced in [115], but this too proved insufficient to clearly detect the orbital period of any planet exterior to planet g. Most likely, the red-noise model used by the BFP, while consistently recovering true stellar variability signals, was not capable of detecting the relatively small amplitude of the planets in the system.

The $l1$ periodogram established in [167] searches all frequencies simultaneously rather than sequentially, and might succeed where other frequency analysis attempts have failed. However, as is visible in Figure 4.2, the $l1$ periodogram once again only identifies the rotation period and its aliases, probably due to their much more significant amplitudes.

Another method we might use to predict the period of the candidate planet exploits the resonance of TOI-1136. For example, a similar method was used to predict the orbital period of TRAPPIST-1 h when only one transit of the planet was known [256]. The idea is that trios of neighboring planets in compact, resonant systems tend to satisfy equation 4.1 for small-integer values of p, q.

$$pP_1^{-1} - (p+q)P_2^{-1} + qP_3^{-1} \approx 0 \tag{4.1}$$

Here P_1, P_2, and P_3 are the orbital periods of any three adjacent planets. We solved for P_3 for a variety of combinations of p and q, ranging from one to three. Many of the predictions were implausible. Some combinations predicted orbital periods interior to planet g's $\sim$ 39 day orbital period (e.g. $p = 1$, $q = 2$, $P_3 = 32.89$ days), which would have been seen in photometry, and are unlikely in such a compact, resonant system. Some predictions were close enough to planet g for stability concerns to make the period unlikely (e.g. $p = 2$, $q = 2$, $P_3 = 43.86$ days). Two period predictions stand out as plausible when using equation 4.1: $p = 2$, $q = 1$, $P_3 = 131.47$ days and $p = 3$, $q = 2$, $P_3 = 65.71$ days. The first is somewhat close to 4:1 resonance with planet g at 156 days, and the second is close to 3:2 resonance at 58.5 days, or perhaps a 2:1 resonance at 79.1 days. Motivated by the $\sim$ 80 day period prediction from transit duration, we deem the 65.71 day period the more likely of the two. We proceed assuming the candidate planet is either in 3:2 or 2:1 resonance with planet g.

4.4.2 Fitting the Transit of the Candidate Planet

We have not identified any additional transits of the candidate, though our RV analysis in section 4.5.2 does shed additional light on the planet. In order to frame the candidate in

context with the other planets in TOI-1136, we perform a single transit fit to formalize an estimate of the radius and other transit-related parameters.

We use the `exoplanet` software package [128, 129] on the detrended photometry from D23, which is detrended using a simple 0.5 day cubic spline. We used only photometry within one day of the reported transit time in D23.

We used `PyMC3` [329] to create a model context for the single transit of the candidate, and we used `starry` to generate the light curve model [254]. `starry` uses a quadratic limb-darkening law when modeling transits. Eccentricity was modeled using a reparametrization detailed in [381], and the orbital period and transit time were given normal priors from the posteriors of our nested sampling fits. Earlier fits were plagued by bimodal solutions related to transit depth, duration, and transit time. An in-transit region of slightly lower flux (visible in Figure 4.3) would sometimes confuse the model, shifting the transit time to the right and increasing the planet radius. To prevent this, we put a minimum transit duration of 0.2 days.

We then utilized a Hamiltonian Monte Carlo algorithm with the No-U-Turn Sampler [NUTS; 179] to efficiently sample the posterior parameter space. We ran 4 chains, each with 5000 tuning steps and an additional 10000 parameter estimation steps. Our final fit is visible in Figure 4.3, and our posterior values are listed in Table **??**.

Table 4.1: TOI-1136(h) Transit Posteriors

Parameter	Posterior Value	Units	Description
$P_{(h)}$	507^{+303}_{-324}	Days	Orbital Period
T_c	$2459435.10^{+0.006}_{-0.007}$	BJD	Transit Time
R_p	$2.68^{+0.20}_{-0.18}$	$R_\oplus$	Planet Radius
e	$0.04^{+0.05}_{-0.03}$	...	Eccentricity
Continued on next page			

Table 4.1: TOI-1136(h) Transit Posteriors

Parameter	Posterior Value	Units	Description
ω	0±120	Degrees	Arg. of Peri.
$i_{(h)}$	89.68±0.02	Degrees	Inclination
t_{14}	$0.26^{+0.02}_{-0.01}$	Days	Transit Duration

The single-event nature of this possible planetary transit makes assessment of its veracity difficult. We use the single event statistic (SES, **(author?)** 196) to quantify the quality of this candidate transit:

$$\mathrm{SES} = \frac{d \cdot s}{\sigma\sqrt{s^T s}} \tag{4.2}$$

Above, d is the detrended flux data, and s is the predicted transit signal at each flux timestamp. σ is the out-of-transit scatter. T indicates transposing a matrix. We use a subset of the detrended flux in D23, which removed correlated noise using a cubic spline of 0.5 days. Some correlated noise was still present even after such a detrending, especially near the wings of the transit. We mask the transit and additionally use a univariate spline with a smoothing factor of s=1400 to remove ther remainder of the out-of-transit variability. The SES is often expanded upon as a multi-event statistic (MES) in *Kepler* systems [378], though such an expansion is not possible in the case of a single transit. [195] suggest 4.0 as a more conservative cutoff to call a single event significant, and 3.5 as sufficient. We estimate an SES of 12.3 for the single transit of this candidate planet, suggesting that the single transit is indeed statistically significant, and not likely due to white noise. We attempt to recover

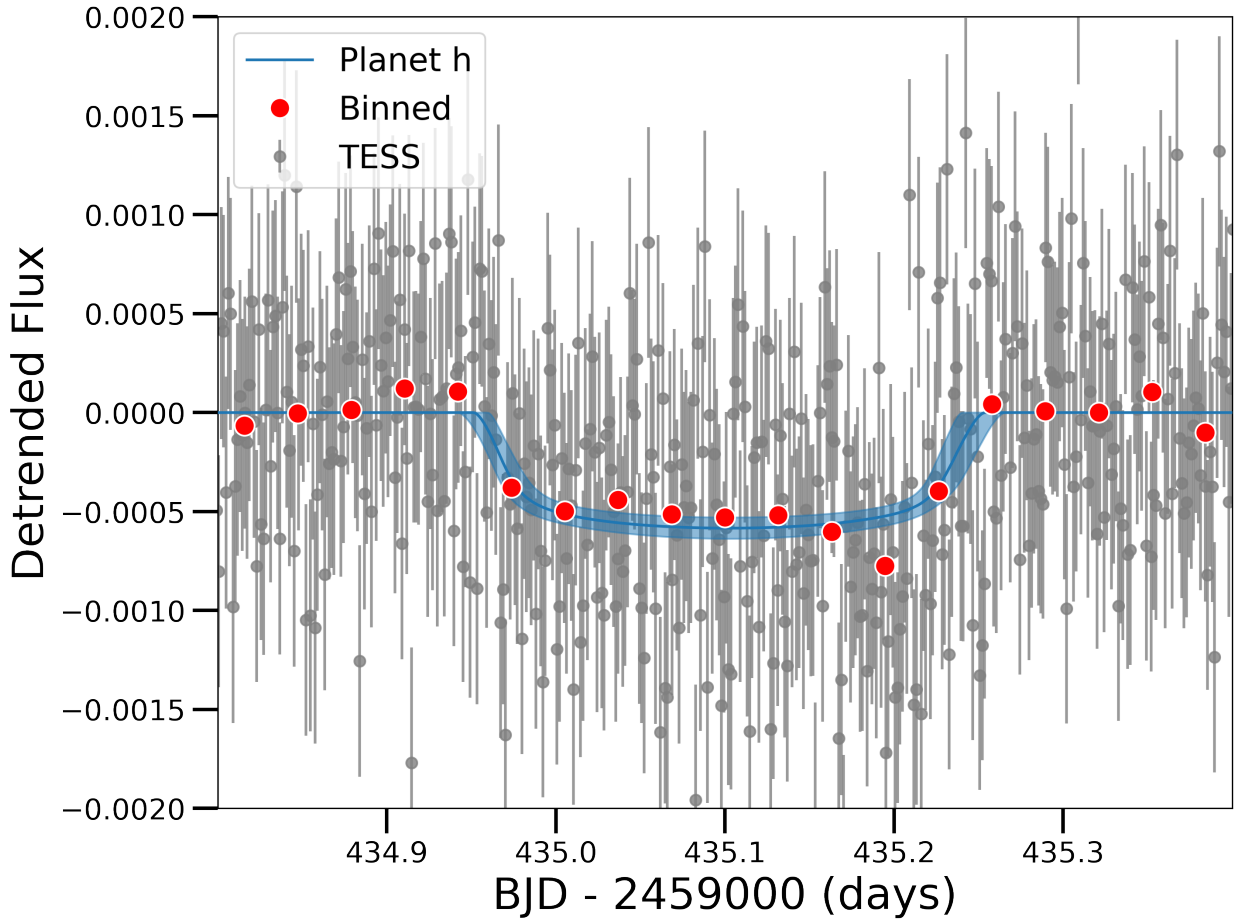

Figure 4.3: Our posterior transit fit to the single transit of the candidate planet. Fits indicate that the planet likely has a radius near 2.68 $R_\oplus$. We use the SES (equation 4.2) to verify the significance of the transit.

the mass of this candidate in the next section.

Our conclusion then is that a single transit was most likely detected in the photometry that is not consistent with any of the known planets in the system, but any other parameters for this candidate planet are difficult to discern without a more in-depth analysis, or additional photometry. Additionally, we can rule out most false positive scenarios, as mentioned in D23.

4.5 Analysis

The high multiplicity of the system generates a large number of free parameters in the model to describe the planetary orbits. The youth of the system suggests that large amounts of magnetic activity are likely occurring on the surface and within the star. This magnetic activity is likely to generate variability in the RVs and photometry not related to planetary motion. Indeed, examination of the quasi-periodic modulation of the TESS photometry confirms this expectation, and the high scatter of the RVs (RMS = 43.5 m s^{-1}) could not come from any of the known planets, even in the implausible event that they were all pure iron. Thus, some model to account for stellar variability in the RVs that is many times larger than the exoplanet signals is an essential part of modeling the RVs.

A detailed photometric analysis of TOI-1136 was carried out in D23, including the identification of individual transit times at each transit epoch for each planet. In this work, we jointly model the transit times determined in D23 and our newly collected RVs.

We performed RV-only analyses of TOI-1136, but we failed to significantly detect the system's exoplanets for two reasons. First, the proximity of the stellar rotation period (8.4 days) to several planetary periods (P_b = 4.17, P_c = 6.26, P_d = 12.52 days) made distinction challenging. Additionally, the significantly larger amplitude of the spot-induced

variability ($\sim$ 50 m s^{-1}) compared to the expected planetary semi-amplitudes [estimated from a mass-radius relationship; K_{M-R} = 0.3 - 3.0 m s^{-1}; 80] further hindered detection. TTV fits alone were much more successful at measuring planet masses, as the photometry is significantly easier to disentangle from stellar variability. It is expected that combining both TTV-predicted masses and RV-predicted masses would yield the best results, as the independent datasets can be combined in likelihood space to give the largest quantity of information about the system. We detail activity model training in §4.5.1, our complete RV + TTV model in §4.5.2, and detail our cross-validation in §4.5.3.

4.5.1 Training the Activity Model

We do not choose to include photometry in our final TTV + RV fit, but we can still use the 6 sectors of TESS data to inform our activity model. The RV contribution of the stellar activity can be predicted from photometry using the FF′ method outlined in [5]. This method is best at predicting quasi-periodic modulations from starspots or plage, which is likely the biggest contribution to TOI-1136's stellar activity. We fit the Quasi-Periodic kernel as described in RadVel documentation to the predicted RV activity signal [133]. We divide this signal into four "seasons," corresponding to continuous TESS coverage. Season 1 is Sectors 14 and 15; season 2 is Sectors 21 and 22; season 3 is Sector 41; and season 4 is Sector 48. We then performed GP fits to each season individually, as well as a single run on all the FF′ predictions together. An example plot of our fit to season 2 is visible in Figure 4.4.

We performed an MCMC fit on the FF′ data using RadVel, which assesses convergence by determining when the Gelman-Rubin (G-R) statistic is less than 1.01 and the number of independent samples is greater than 1000 for all free parameters for at least five consecutive checks [119].

The FF′ spot model is relatively simple, and does not take into account all physical processes

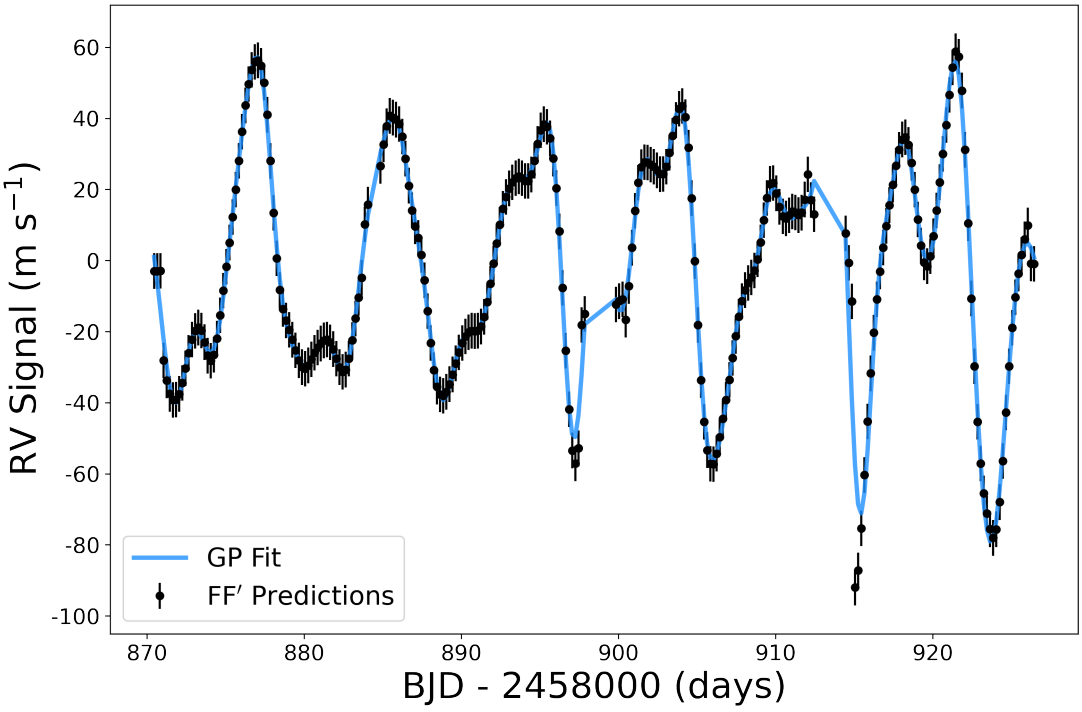

Figure 4.4: A plot of the GP fit to the RV activity signal of TOI-1136, calculated from photometry. This activity prediction is estimated via the FF′ method described in [5]. The above plot illustrates our fit to season 2. After assessing convergence, we use the frequency posteriors of this GP fit as priors on the GP hyperparameters for our TTV + RV fits in the next section.

that occur in a magnetically active star. Additionally, it is known to break down in multi-spot cases. The model is based on photometry, which is expected to have a shared frequency structure with the RVs, though the phase may not be consistent. Consequently, we utilize only the posteriors of the terms associated with frequency (η_2,η_3, η_4) as priors in our full TTV + RV model, and we maintain broad, uniform priors on GP amplitude terms.

4.5.2 TTV + RV Model

We used TTVFast [101] to jointly model the transit times and the RVs of TOI-1136. TTVFast is a symplectic N-body integrator that uses Keplerian interpolation between N-body time steps to predict transit times [101]. TTVFast uses seven free parameters per planet to integrate the dynamical motion of the system: planet mass, orbital period, eccentricity, argument of periastron, orbital inclination, mean anomaly at reference epoch, and the longitude of the ascending node. During our analysis of TOI-1136, we fixed the longitude of ascending node to zero for all planets, as our current data is not generally good at constraining this parameter, and this is commonly done [e.g. D23, 159]. All other parameters were left free to vary during our fits, resulting in six free parameters per planet. We perform fits on six and seven-planet models in order to better quantify the plausibility of including the candidate planet, as well as to examine the sensitivity of posteriors to including a seventh planet. Thus, there are 36 and 42 free parameters corresponding to Keplerian motion in each model.

We integrated using a timestep suggested by [101] by dividing the shortest orbital period by 25. Consequently, our integration time step used was 0.125 days. After integration, we use the predicted transit times from the TTVFast model and the observed transit times (taken from D23) to calculate a likelihood associated with the TTVs ($\mathcal{L}_{TTV}$):

$$\log\mathcal{L}_{TTV} = -\frac{1}{2}\sum_{j=1}^{n}\sum_{i}\left(\frac{T_{ob,i,j} - T_{pr,i,j}}{\sigma_{ob,i,j}}\right)^2 + \log(2\pi\sigma_{ob,i}) \tag{4.3}$$

where i is the i^{th} transit of planet j, and n is the number of transiting planets in the model.

The N-body integration performed by TTVFast models planet positions at each integration time step, which is sufficient to calculate the predicted radial velocity signal of the modeled system. The presence of additional, non-Keplerian signals in the RVs, most likely coming from spots or plage, requires the inclusion of an activity model. We utilize a GP to model the correlated noise of the stellar activity. A GP creates a covariance matrix from its kernel that models the covariance between each RV data point with each other data point. This is ideal for modeling the expected quasi-periodic behavior of the activity signal. This matrix can be used with the residuals of the planet fit to completely model the system. This is represented in the RV likelihood function in Equation 4.4.

$$\log\mathcal{L}_{RV} = -\frac{1}{2}\big(r^T\mathcal{K}r + \log|\mathcal{K}| + N\log(2\pi)\big) \tag{4.4}$$

Above, $\mathcal{K}$ is the covariance matrix of our GP, N is the number of RV data points, and r is a vector of residuals to the TTVFast predicted RV model given by Equation 4.5.

$$r = RV_{obs} - RV_{pred} - \gamma \tag{4.5}$$

Above, γ corresponds to a linear offset subtracted from the model. A different offset is fit

for each instrument, and subtracted from velocities of each instrument uniformly.

Our choice of GP kernel is the chromatic $\mathcal{K}_{J1}$ kernel outlined in [74]. This GP kernel is an expansion of the commonly used Quasi-Periodic GP kernel [173, 248]. The $\mathcal{K}_{J1}$ kernel utilizes a different amplitude parameter for each instrument used in the fit, which is particularly useful for RV instruments of different wavelength regimes, as stellar activity is expected to be chromatic [90, 323]. This is not highly relevant in the case of TOI-1136, as the central wavelength bands of all three instruments used (HIRES, APF, HARPS-N) are close in wavelength-space (Though HARPS-N is not an iodine instrument, and this might have a significant effect). However, this $\mathcal{K}_{J1}$ kernel can be used to model all three instruments simultaneously in one covariance matrix, rather than the traditional method of calculating a likelihood for each instrument and summing them. Consequently, RVs from each instrument maintain a covariance even between RVs of other instruments. This is particularly useful for preventing overfitting of the GP, which is a serious problem, especially in a model with so many free parameters. This is discussed more in §4.5.3.

Our total joint model log likelihood is

$$\log\mathcal{L}_{tot} = \log\mathcal{L}_{TTV} + \log\mathcal{L}_{RV} + \log\mathcal{P}, \tag{4.6}$$

where $\mathcal{P}$ is the product of all priors.

We generally adopted broad priors on the free parameters of TOI-1136, with a few exceptions. The inclinations, while constrained by TTVs, are also informed by transit shapes, which we did not fit for in our model, but which were fit in D23. To leverage this information without including transit fits in our model, we use a Gaussian prior on the inclination of the inner 6 planets, with values corresponding to the posteriors of D23. To prevent the perfect

degeneracy between inclinations on either side of 90 degrees, we also put an upper limit of 90° on all the inclination priors, preventing chains from crossing that threshold. Technically, we are restricting mutual inclinations between planets to minimum values, when two planets could have inclinations on either side of the 90 degree threshold but still exhibit the same transit shape. However, this difference in mutual inclination is limited to only a few degrees, and is unlikely to affect our fit results, so we ignore it. We estimate the minimum and maximum inclinations possible for the candidate planet to transit, and use these values as uniform priors for TOI-1136 (h). The GP hyperparameters, too, can be informed by the photometry. This is particularly important due to the flexibility of GPs, and our model's susceptibility to overfitting. Uninformative priors on GP terms give the GP the flexibility to modify the model until residual scatter is minimized, even if the results are unphysical. We use the posteriors of a GP fit to the FF′ predictions, detailed in §4.5.1, as priors on the GP hyperparameters. A full list of our priors is visible in table 5.3.

Table 4.2: Priors Used for Various Fits

Parameter Name	TTVFast Prior	FF′ Prior	Units	Description
Planet Priors (b-g):				
P_{orb}	$\mathcal{U}^a(0.99 * \mu^*_{D23}, 1.01 * \mu_{D23})$	-	days	Period
$\sqrt{e}\cos\omega$	$\mathcal{U}(-1, 1)$	-	...	Eccentricity Reparametrization
$\sqrt{e}\sin\omega$	$\mathcal{U}(-1, 1)$	-	...	Eccentricity Reparametrization
$\frac{m_p}{m_s}$	$\mathcal{U}(0.0, 0.01)$	-	...	Planet-star Mass Ratio
M	$\mathcal{U}(-180, 180)$	-	degrees	Mean Anomaly
i	$\mathcal{BN}^b(\mu_{D23}, sd_{D23}, 80, 90)$	-	degrees	Inclination
TOI-1136(h) Priors:				
P_{orb}	$\mathcal{U}(1, 1000)$	-	days	Period
$\sqrt{e}\cos\omega$	$\mathcal{U}(-1, 1)$	-	...	Eccentricity Reparametrization
$\sqrt{e}\sin\omega$	$\mathcal{U}(-1, 1)$	-	...	Eccentricity Reparametrization
$\frac{m_p}{m_s}$	$\mathcal{U}(0.0, 0.01)$	-	...	Planet-star Mass Ratio
M	$\mathcal{U}(-180, 180)$	-	degrees	Mean Anomaly
i	$\mathcal{U}(89.5, 90)$	-	degrees	Inclination
GP Hyperparameters				
$\eta_{1,\mathrm{HIRES}}$	$\mathcal{U}(1, 100)$	-	m s^{-1}	HIRES GP Amplitude
$\eta_{1,APF}$	$\mathcal{U}(1, 100)$	-	m s^{-1}	APF GP Amplitude

Continued on next page

Table 4.2 – continued from previous page

Parameter Name	TTVFast Prior	FF′ Prior	Units	Description
$\eta_{1,HARPS-N}$	$\mathcal{U}(1, 100)$	-	m s^{-1}	HARPS-N GP Amplitude
$\eta_{1,FF'}$	-	$\mathcal{J}^c(0.001, 100.0)$	m s^{-1}	FF′ GP Amplitude
η_2	$\mathcal{N}^d(9.6188, 0.871)$	$\mathcal{J}(8.54, 10^{10})$	days	Exponential Scale Length
η_3	$\mathcal{N}(8.429, 0.094)$	$\mathcal{N}(8.429, 0.094)$	days	Periodic Term
η_4	$\mathcal{N}(0.4402, 0.0499)$	$\mathcal{J}(10^{-5}, 1)$	...	Periodic Scale Length
Instrumental Parameters				
$\gamma_{\rm HIRES}$	$\mathcal{U}(-100, 100)$	-	m s^{-1}	HIRES offset
$\gamma_{\rm APF}$	$\mathcal{U}(-100, 100)$	-	m s^{-1}	APF offset
$\gamma_{\rm HARPS-N}$	$\mathcal{U}(-100, 100)$	-	m s^{-1}	HARPS-N offset
$\gamma_{\rm FF'}$	...	$\mathcal{U}(-100, 100)$	m s^{-1}	FF′ offset
$\sigma_{\rm HIRES}$	$\mathcal{U}(0.01, 100)$	-	m s^{-1}	Instrumental Jitter, HIRES
$\sigma_{\rm APF}$	$\mathcal{U}(0.01, 100)$	-	m s^{-1}	Instrumental Jitter, APF
$\sigma_{\rm HARPS-N}$	$\mathcal{U}(0.01, 100)$	-	m s^{-1}	Instrumental Jitter, HARPS-N
$\sigma_{\rm FF'}$	-	$\mathcal{U}(0.01, 100)$	m s^{-1}	Instrumental Jitter, FF′

[a] $\mathcal{U}$ is a uniform prior with $\mathcal{U}$(lower,upper)

[b] $\mathcal{BN}$ is a bounded normal prior with $\mathcal{BN}$(mean, standard deviation, minimum, maximum)

[c] $\mathcal{J}$ is a Jeffreys prior with $\mathcal{J}$(lower,upper)

[d] $\mathcal{N}$ is a normal prior with $\mathcal{N}$(mean, standard deviation)

* μ_{D23} refers to the mean posterior taken from Table 10 in D23. sd_{D23} refers to the 1σ uncertainty taken from Table 10 in D23.

– indicates a free parameter that was not fit in that particular model.

We initially perform a simple least-squares optimization on our model using `lmfit` [294]. We let all parameters vary during this optimization step, except for the GP hyperparameters which are fixed. This is partially to prevent some measure of overfitting, which a least-squares optimization may do for a complicated model, and is additionally unceccessary: our FF′ fits detailed in §4.5.1 already provide a good estimate of our GP hyperparameter values, and their uncertainties.

To model the posterior probability of our TTV + RV model, we used the `emcee` software package to perform Markov-Chain Monte Carlo (MCMC) inference [125]. We utilize Differential Evolution MCMC (DEMCMC) sampling with the DEMove in `emcee` documentation [370]

as well as the affine-invariant sampler proposed in [154] for faster MCMC convergence, referred to in `emcee` documentation as the StretchMove. We experimented with different hyperparameter values to tune the sampling, and we settled on sigma=2e-8 and gamma0=0.33 for the DEMove, as this combination produced the desired acceptance rate near 30%. We set the single hyperparameter for the StretchMove to a=1.2, as this value produced the highest acceptance. Both methods produced consistent results, though we report our results from the DEMove.

We estimated convergence via the method proposed in [154] and further endorsed in [125], by estimating the integrated autocorrelation time, τ. This value is approximated by `emcee` during the MCMC process, and the estimate asymptotically approaches the correct value as more steps in the sampling are computed. `emcee` documentation suggests using a large number of simultaneous walkers, or chains, to more efficiently sample parameter-space, and to more accurately estimate τ. The sampler should be run for multiple lengths of τ to ensure that final results are not subject to sampler uncertainty, and that final results sufficiently reflect measured uncertainties of the data and model.

Less complicated models that utilized `TTVFast` in the literature were able to achieve precise results using only dozens of walkers and tens of thousands of sampler steps [e.g. 41, 375]. Due to its increased complexity, however, we utilized 1000 simultaneous walkers for TOI-1136, and we ran for 300,000 MCMC steps for both models. Our models estimate τ at ~ 25000 model steps, suggesting that our model has run for > 10 autocorrelation timescales. We also compute the G-R statistic to compare inter-chain and intra-chain variability [119]. Our model meets convergence criteria (G-R < 1.01 for all parameters) according to the G-R statistic, though we caution that the this is considered less robust than autocorrelation times when using the StretchMove ensemble in `emcee`.

Our final posterior parameter values are listed in Table 4.3. A plot of our RVs and TTVs modeled to these values is visible in Figures 4.7 and 4.8. To encourage reproduction, we

provide a public github repository with our analysis code and encourage others to use and test it[1].

Beyond the TTV + RV models described above, we ran a TTV-only model as well. This will help us to quantify the effect RVs are having on our models more directly, and additionally help when comparing results with D23. We only performed such a fit for a six planet model, as a TTV-only fit with a single transiting planet is not highly meaningful. These results are reported in Table **??**, and are discussed further in §6.5.

4.5.3 Cross Validation

Our joint model (described in §4.5.2) has a large number of free parameters with respect to the size of the dataset, and is consequently susceptible to overfitting. In principle, a dataset is overfit when it learns the training data too well, and starts to recreate the statistical noise of the data in its predictions, rather than information about a physical system. When training a physically motivated model on data, the training likelihood of the model should initially improve as the model learns the features of the data. However, the training likelihood will often continue to improve (as the model learns the noise properties of the data it sees), as its predictive ability on data it doesn't see (the test dataset) begins to fall. When the model likelihood increases at the expense of predictivity, we call this overfitting. We are most interested in determining whether our final hyperparameters from the model in §4.5.2 are contributing to overfitting, and our intention is not to estimate model parameters in this section.

We perform cross validation to assess our model's predictive ability on data it has not seen before. Ideally, we would follow the method proposed in [51], reserving 30% of our radial velocity data as a "test dataset" and only training our model on 70%. We could, at fixed

[1] `https://github.com/CCBeard/TOI-1136_Analysis_Code` [36]

intervals, check our model's predictive ability and determine when the test likelihood starts worsening. This method is not ideal for TOI-1136, however, for a number of reasons. Despite our large model with 52 free parameters, our actual dataset contains a relatively small number of points (87 transit times, 410 RVs, 497 datapoints). Removing 30% of our dataset would largely reduce the size of a dataset already worryingly close to the number of free parameters. Furthermore, shrinking this percentage would likely result in a test dataset that is not well representative of the whole. Lastly, such tests often work best when repeated many times to ensure that the randomly drawn test dataset is representative of the whole sample. Our models are already extremely expensive to run (taking around 5000 CPU-hours to converge), and repeating them dozens or hundreds of times would be prohibitively so. Additionally, our model requires large amounts of random access memory (RAM) to manipulate the long (300,000 steps) and wide (1000 chains) samples object, and our access to specialized high-memory CPUs is additionally limited. Because of these constraints, we make a compromise between a simpler cross-validation utilized in [166] and the more complicated method utilized in [51].

[166] utilize cross-validation of their GP model by creating a grid of GP hyperparameter values, and optimizing planet models with GP hyperparameters fixed at these values. This optimization is performed on 70% of the data, and the authors then evaluate the likelihood of the 30% test dataset.

When applying this to TOI-1136, we focus on the hyperparameters of the $\mathcal{K}_{J1}$ GP kernel. GP parameters often cause overfitting, as GPs are incredibly flexible. Because the rotation period of TOI-1136 is clearly detected in §4.3.1, we focus only on the parameters η_1, η_2, and η_4, known as the GP amplitude, exponential decay length, and periodic scale length, respectively (described in [97]). We perform a grid search using these three parameters, performing fits with them fixed at certain values. We prioritize values distributed around the posterior of our model. The amplitude term was tested at values of 10, 50, 75, and 100

m s^{-1}. The exponential decay length was allowed values of 5, 10, 50, 100, 1000. Finally, the periodic scale length was tested with values of 0.1, 0.2, 0.3, 0.4, 0.5. For comparison, our final 7 planet model values, listed in Table 4.3, are $\eta_{1,HIRES} = 36.9$ m s^{-1}, $\eta_{1,APF} = 43.8$ m s^{-1}, $\eta_{1,HARPS-N} = 37.4$ m s^{-1}, $\eta_2 = 13.5$ days, and $\eta_4 = 0.25$.

For each combination of hyperparameter values, we set up the model described in §4.5.2, except with these three hyperparameters fixed at their selected value. We then split the RV data into a training dataset (70%) and test dataset (30%) randomly. We do so by instrument so that there is always the same number of APF, HIRES, and HARPS-N points. We then optimize the free parameters of the model using lmfit [294] on the training dataset only. After optimization, we estimate the likelihood of the training and test datasets. The training and test datasets are then recreated again via random draw, and this process is repeated 100 times for each parameter trio, and we take the average result. Note that we only perform a least-squares optimization to the model, rather than a full MCMC. This is to prevent this check from being prohibitively expensive.

We perform the same calculation with the three hyperparameters fixed at the values taken from our full MCMC posteriors. With a representative test likelihood value and training likelihood value for each combination of GP hyperparameters and for our final model, we scale each likelihood by the number of datapoints used to estimate. The result is a variety of likelihoods that can be compared on the same scale. The idea is that if the training likelihood is much better than the test likelihood, the model is probably overfitting. Ideally, the scaled test and training likelihoods should be close to the same value, suggesting that the model makes predictions on both datasets equally well.

We additionally follow [51] and check the predictivity of our activity model. We do so by measuring scatter of the residuals of our training datasets compared to the scatter of the residuals of the test datasets.

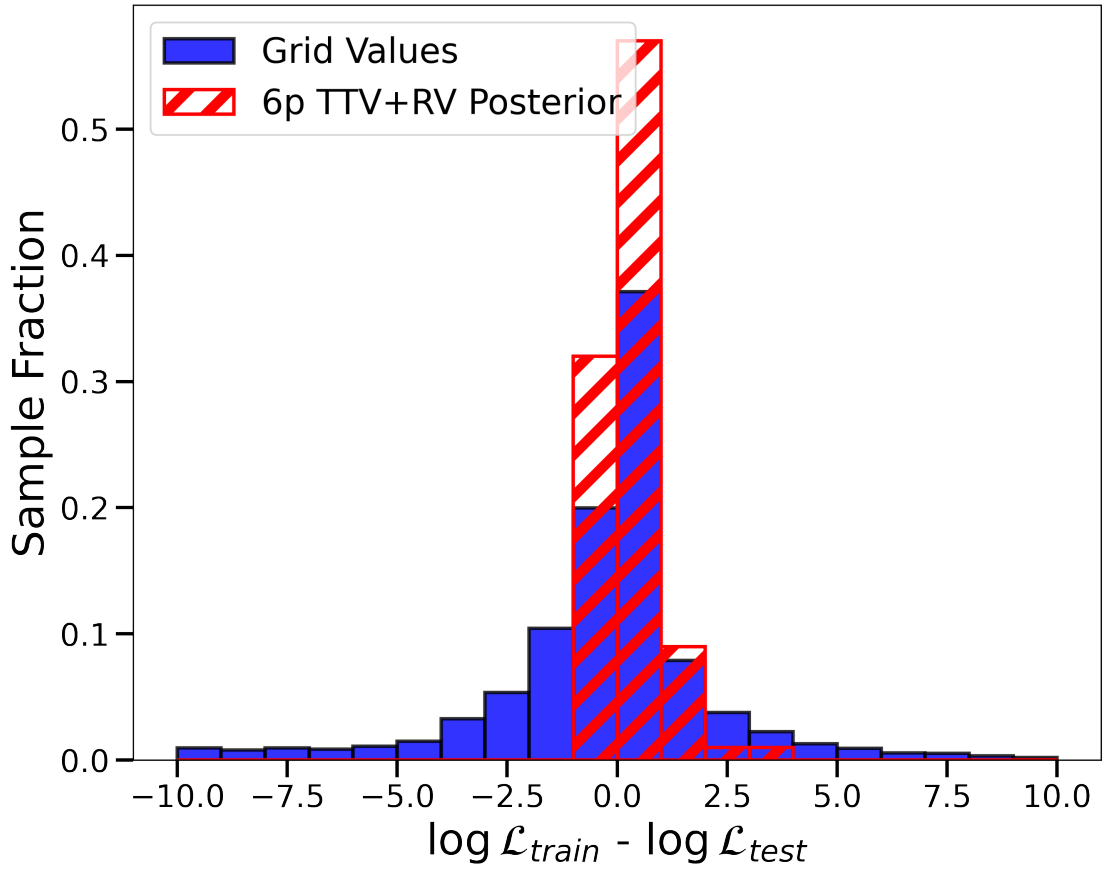

Figure 4.5: Histogram of the difference between the scaled log-likelihood of the training datasets described in §4.5.3 and the scaled test datasets. As a model becomes overfit to data, the training likelihood should become much higher than the test likelihood. Positive values indicate overfitting, and negative values indicate underfitting. A histogram of our grid search results is shown in blue, and a histogram of the 100 samples using our 6 planet TTV+RV posterior are shown in red hatches. Our model likelihood differences skew slightly into overfitting, but they are much more highly concentrated around 0 than our grid search.

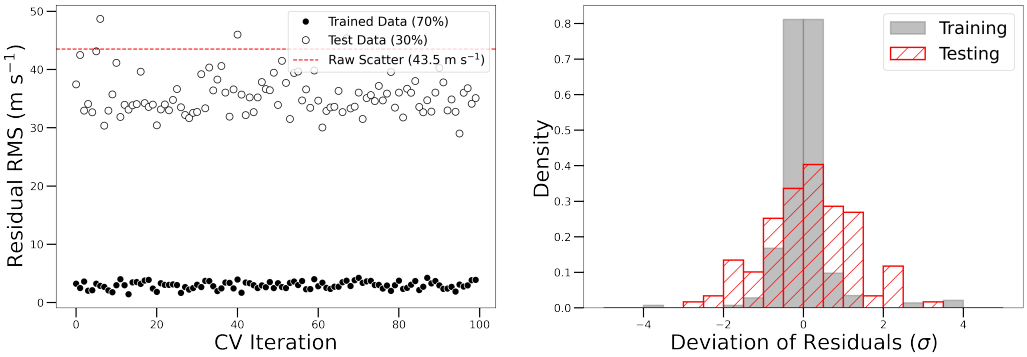

Figure 4.6: Left: A comparison of the RMS of the training and test residuals during our cross validation. The test datasets exhibit higher scatter, but their GP uncertainty is also high, indicating that the model has trouble predicting the held-out, test dataset. Right: a histogram of the residuals/uncertainty of the training and test datasets. Despite the large RMS of the test dataset, its associated uncertainty is also high. Consequently, the predictions are not unreliable, though imprecise. This again indicates slight overfitting, though it is less than in [51].

Our final results in Figure 4.5 suggest that our final values might be slightly overfitting the data, but that the posterior GP hyperparameter values are well within a normal range, and most of our models are concentrated around zero (neither under or over-fitting). In Figure 4.6, we see the difference in residual RMS between the training and test dataset. The test dataset exhibits much higher scatter than the training dataset, which is expected, but may indicate overfitting considering the degree of difference. We recreate Figure 2 from [51] by picking an iteration at random and plotting a histogram of the prediction value divided by its uncertainty (1σ GP standard deviation + RV error, added in quadrature). While the test dataset exhibits higher scatter than the training dataset, it is not as anomalous as the result demonstrated in [51]. This result agrees with the earlier likelihood estimation that our model may be slightly overfit, but that it is not likely to be extreme.

Overfitting might alter posterior parameters into unphysical regimes, or cause under or over-estimated posterior errors. Our general median agreement with D23 suggest that the former is not likely happening, though our improved errors over D23 suggest that error under-estimation may be happening. A combined RV/TTV analysis is expected to improve

precision, however, and MCMC convergence checks, as well as our cross validation above suggest that if this is happening, it is not extreme.

Table 4.3: TTV+RV Posteriors of TOI-1136[†]

Parameter Name	6p TTV+RV Posterior	7p TTV+RV Posterior	Units	Description
Planet b				
Fit Parameters				
P_b	4.1727 ± 0.0003	$4.1728^{+0.0003}_{-0.0002}$	days	Orbital Period
$\sqrt{e}\cos\omega_b$	$0.15^{+0.02}_{-0.03}$	$0.18^{+0.02}_{-0.03}$	...	Eccentricity Reparametrization
$\sqrt{e}\sin\omega_b$	$0.07^{+0.03}_{-0.04}$	0.04±0.06	...	Eccentricity Reparametrization
M_b	$51.9^{+12.0}_{-10.3}$	$64.9^{+17.7}_{-18.7}$	degrees	Mean Anomaly
i_b	86.4±0.6	86.4±0.3	degrees	Inclination
$m_{p,b}$	$3.50^{+0.8}_{-0.7}$	$3.68^{+0.61}_{-0.54}$	$M_\oplus$	Planet Mass
Derived Parameters				
ρ_b	2.80±1.00	2.95±0.96	g/cc	Bulk Density
e_b	0.027±0.009	0.03±0.01	...	Eccentricity
ω_b	25±11	12.5±9	Degrees	Argument of Periastron
K_b^*	1.37±0.29	1.44±0.22	m s^{-1}	RV Semi-amplitude
a_b	0.05106±0.0009	0.0511±0.0008	AU	Semi-Major Axis
$T_{eq,b}^{**}$	1216±12	1216±11	K	Equilibrium Temperature
Planet c				
Fit Parameters				
P_c	6.2574±0.0002	$6.2577^{+0.0003}_{-0.0002}$	days	Orbital Period
$\sqrt{e}\cos\omega_c$	-0.11±0.01	-0.08±0.02	...	Eccentricity Reparametrization
$\sqrt{e}\sin\omega_c$	-0.31±0.02	-0.29±0.02	...	Eccentricity Reparametrization
M_c	$62.9^{+2.2}_{-2.4}$	$57.3^{+3.6}_{-3.5}$	degrees	Mean Anomaly
i_c	$88.8^{+0.7}_{-1.0}$	$89.3^{+0.5}_{-0.4}$	degrees	Inclination
$m_{p,c}$	$6.32^{+1.1}_{-1.3}$	$7.41^{+0.98}_{-1.20}$	$M_\oplus$	Planet Mass
Derived Parameters				
ρ_c	1.45±0.29	1.71±0.28	g/cc	Bulk Density
e_c	0.11±0.01	0.09±0.01	...	Eccentricity
ω_c	70±2	74±4	Degrees	Argument of Periastron
K_c	2.16±0.41	2.54±0.38	m s^{-1}	RV Semi-amplitude
a_c	0.0669±0.0005	0.0669±0.0007	AU	Semi-Major Axis
$T_{eq,c}$	1062±7	1062±8	K	Equilibrium Temperature
Planet d				
Fit Parameters				
P_d	12.5199±0.0004	$12.5195^{+0.0003}_{-0.0004}$	days	Orbital Period

Continued on next page

Table 4.3 – continued from previous page

Parameter Name	6p TTV+RV Posterior	7p TTV+RV Posterior	Units	Description
$\sqrt{e}\cos\omega_d$	-0.10±0.01	-0.07±0.02	...	Eccentricity Reparametrization
$\sqrt{e}\sin\omega_d$	0.10±0.01	0.18±0.02	...	Eccentricity Reparametrization
M_d	$140.6^{+3.8}_{-3.4}$	$165.0^{+5.1}_{-5.0}$	degrees	Mean Anomaly
i_d	89.2±0.5	89.4±0.3	degrees	Inclination
$m_{p,d}$	$8.35^{+1.8}_{-1.6}$	$5.6^{+0.9}_{-1.0}$	$M_\oplus$	Planet Mass
Derived Parameters				
ρ_d	1.81±0.35	0.31±0.06	g/cc	Bulk Density
e_d	0.042±0.004	0.04±0.01	...	Eccentricity
ω_d	-67±3	-68±6	Degrees	Argument of Periastron
K_d	2.27±0.46	1.52±0.27	m s^{-1}	RV Semi-amplitude
a_d	0.1062±0.0008	0.1062±0.0007	AU	Semi-Major Axis
$T_{eq,d}$	843±6	843±5	K	Equilibrium Temperature
Planet e				
Fit Parameters				
P_e	18.801±0.001	18.802±0.001	days	Orbital Period
$\sqrt{e}\cos\omega_e$	0.08±0.01	0.08±0.01	...	Eccentricity Reparametrization
$\sqrt{e}\sin\omega_e$	-0.19±0.01	-0.22±0.01	...	Eccentricity Reparametrization
M_e	$175.5^{+2.1}_{-2.2}$	$175.5^{+2.8}_{-3.5}$	degrees	Mean Anomaly
i_e	89.2±0.5	89.3±0.3	degrees	Inclination
$m_{p,e}$	$6.07^{+1.09}_{-1.01}$	$3.31^{+0.46}_{-0.39}$	$M_\oplus$	Planet Mass
Derived Parameters				
ρ_e	1.81±0.35	0.99±0.16	g/cc	Bulk Density
e_e	0.0425±0.004	0.0548±0.005	...	Eccentricity
ω_e	-67±3	-70±2.4	Degrees	Argument of Periastron
K_e	1.44±0.25	0.78±0.102	m s^{-1}	RV Semi-amplitude
a_e		0.139±0.002	AU	Semi-Major Axis
$T_{eq,e}$	737±6	736±6	K	Equilibrium Temperature
Planet f				
Fit Parameters				
P_f	26.321±0.001	26.3213±0.001	days	Orbital Period
$\sqrt{e}\cos\omega_f$	-0.02±0.01	-0.04±0.02	...	Eccentricity Reparametrization
$\sqrt{e}\sin\omega_f$	0.02±0.01	0.05±0.02	...	Eccentricity Reparametrization
M_f	$51.4^{+4.3}_{-4.4}$	$52.4^{+10.1}_{-9.2}$	degrees	Mean Anomaly
i_f	89.3±0.4	$89.4^{+0.2}_{-0.3}$	degrees	Inclination
$m_{p,f}$	$9.7^{+3.9}_{-3.7}$	$8.22^{+2.8}_{-2.4}$	$M_\oplus$	Planet Mass
Derived Parameters				
ρ_f	0.89±0.22	0.77±0.25	g/cc	Bulk Density
e_f	0.001±0.001	0.0±0.003	...	Eccentricity

Continued on next page

Table 4.3 – continued from previous page

Parameter Name	6p TTV+RV Posterior	7p TTV+RV Posterior	Units	Description
ω_f	-45±20	-51±18	Degrees	Argument of Periastron
K_f	2.01±0.46	1.74±0.55	m s^{-1}	RV Semi-amplitude
a_f	0.174±0.002	0.174±0.002	AU	Semi-Major Axis
$T_{eq,f}$	658±5	658±5	K	Equilibrium Temperature
Planet g				
Fit Parameters				
P_g	39.545±0.002	$39.544^{+0.001}_{-0.002}$	days	Orbital Period
$\sqrt{e}\cos\omega_g$	0.03±0.01	0.02±0.01	...	Eccentricity Reparametrization
$\sqrt{e}\sin\omega_g$	-0.19±0.02	-0.20±0.02	...	Eccentricity Reparametrization
M_g	$-119.5^{+2.3}_{-2.5}$	$-118.5^{+3.0}_{-2.6}$	degrees	Mean Anomaly
i_g	89.5±0.3	89.7±0.2	degrees	Inclination
$m_{p,g}$	$5.6^{+4.1}_{-3.2}$	$12.0^{+5.2}_{-3.2}$	$M_\oplus$	Planet Mass
Derived Parameters				
ρ_g	1.9±1.3	4.07±1.52	g/cc	Bulk Density
e_g	0.04±0.01	0.04±0.01	...	Eccentricity
ω_g	-81±3	-84±3	Degrees	Argument of Periastron
K_g	1.03±0.68	2.22±0.78	m s^{-1}	RV Semi-amplitude
a_g	0.229±0.003	0.229±0.002	AU	Semi-Major Axis
$T_{eq,g}$	574±5	574±4	K	Equilibrium Temperature
TOI-1136 (h)***				
Fit Parameters				
$P_{(h)}$	-	77	days	Orbital Period
$\sqrt{e}\cos\omega_{(h)}$	-	0.15	...	Eccentricity Reparametrization
$\sqrt{e}\sin\omega_{(h)}$	-	-0.24	...	Eccentricity Reparametrization
$M_{(h)}$	-	120.3	degrees	Mean Anomaly
$i_{(h)}$	-	89.7	degrees	Inclination
$m_{p,(h)}$	-	<18.8	$M_\oplus$	3σ Mass Upper Limit
Derived Parameters				
$\rho_{(h)}$	-	0.34	g/cc	Bulk Density
$e_{(h)}$	-	0.002	...	Eccentricity
$\omega_{(h)}$	-	63	Degrees	Argument of Periastron
$K_{(h)}$	-	0.6	m s^{-1}	RV Semi-amplitude
$a_{(h)}$	-	0.36	AU	Semi-Major Axis
$T_{eq,(h)}$	-	460	K	Equilibrium Temperature
GP Hyperparameters				
$\eta_{1,HIRES}$	$36.9^{+4.5}_{-3.6}$	$33.9^{+2.2}_{-1.7}$	m s^{-1}	HIRES GP Amplitude
$\eta_{1,APF}$	$43.8^{+4.3}_{-3.9}$	$41.2^{+2.7}_{-2.8}$	m s^{-1}	APF GP Amplitude
$\eta_{1,HARPS-N}$	$37.4^{+6.2}_{-5.2}$	$33.2^{+3.5}_{-3.0}$	m s^{-1}	HARPS-N GP Amplitude

Continued on next page

Table 4.3 – continued from previous page

Parameter Name	6p TTV+RV Posterior	7p TTV+RV Posterior	Units	Description
η_2	$13.5^{+1.5}_{-2.3}$	$13.9^{+0.8}_{-0.9}$	days	Exponential Scale Length
η_3	8.55±0.011	$8.58^{+0.05}_{-0.06}$	days	Periodic Term
η_4	$0.25^{+0.04}_{-0.06}$	0.26±0.02	...	Periodic Scale Length
Instrumental Parameters				
$\gamma_{\rm HIRES}$	9.1±6.6	$10.0^{+3.6}_{-3.9}$	m s^{-1}	HIRES offset
$\gamma_{\rm APF}$	4.2±7.0	3.9±3.9	m s^{-1}	APF offset
$\gamma_{\rm HARPS-N}$	$7.8^{+7.5}_{-7.4}$	$5.4^{+4.3}_{-5.0}$	m s^{-1}	HARPS-N offset
$\sigma_{\rm HIRES}$	$1.1^{+0.9}_{-0.7}$	$2.1^{+2.8}_{-1.7}$	m s^{-1}	Instrumental Jitter, HIRES
$\sigma_{\rm APF}$	13^{+4}_{-10}	$16.5^{+2.3}_{-3.0}$	m s^{-1}	Instrumental Jitter, APF
$\sigma_{\rm HARPS-N}$	$4.7^{+3.9}_{-3.3}$	$7.9^{+5.5}_{-5.8}$	m s^{-1}	Instrumental Jitter, HARPS-N

* Although K is usually an observed parameter, it is computed in this analysis because our model parameterizes the planet masses directly.

** Estimated using an albedo of 0.

† All of the orbital parameters presented in this table are osculating elements computed at BJD 2458680 days.

*** We do not report uncertainties, as our model fits report overly-confident estimates that we consider unlikely to be accurate. We do not significantly detect planet (h), and so these values are not likely precise.

4.6 Discussion

4.6.1 Adopted Model

We have run a total of three large analyses: a 6 planet TTV + RV fit ($\mathcal{A}1$; Table 4.3), a 7 planet TTV + RV fit ($\mathcal{A}2$; Table 4.3), and a 6 planet TTV only fit ($\mathcal{A}3$; Table **??**). Not all of these results agree. For example, $\mathcal{A}1$ finds a mass of $5.6^{+4.1}_{-3.2}$ $M_\oplus$ for planet g, while $\mathcal{A}2$ finds a mass of $12.0^{+5.2}_{-3.2}$. Another example has the mass of planet d in $\mathcal{A}2$ as $5.6^{+0.9}_{-1.0}$ $M_\oplus$ and in $\mathcal{A}3$ as 9.4±1.2 $M_\oplus$. We feel that it is worthwhile to include all of these results, especially to emphasize how differences in assumption can change model results significantly. We also feel it is best to select a single result as the primary focus of the discussion, and to choose an adopted model.

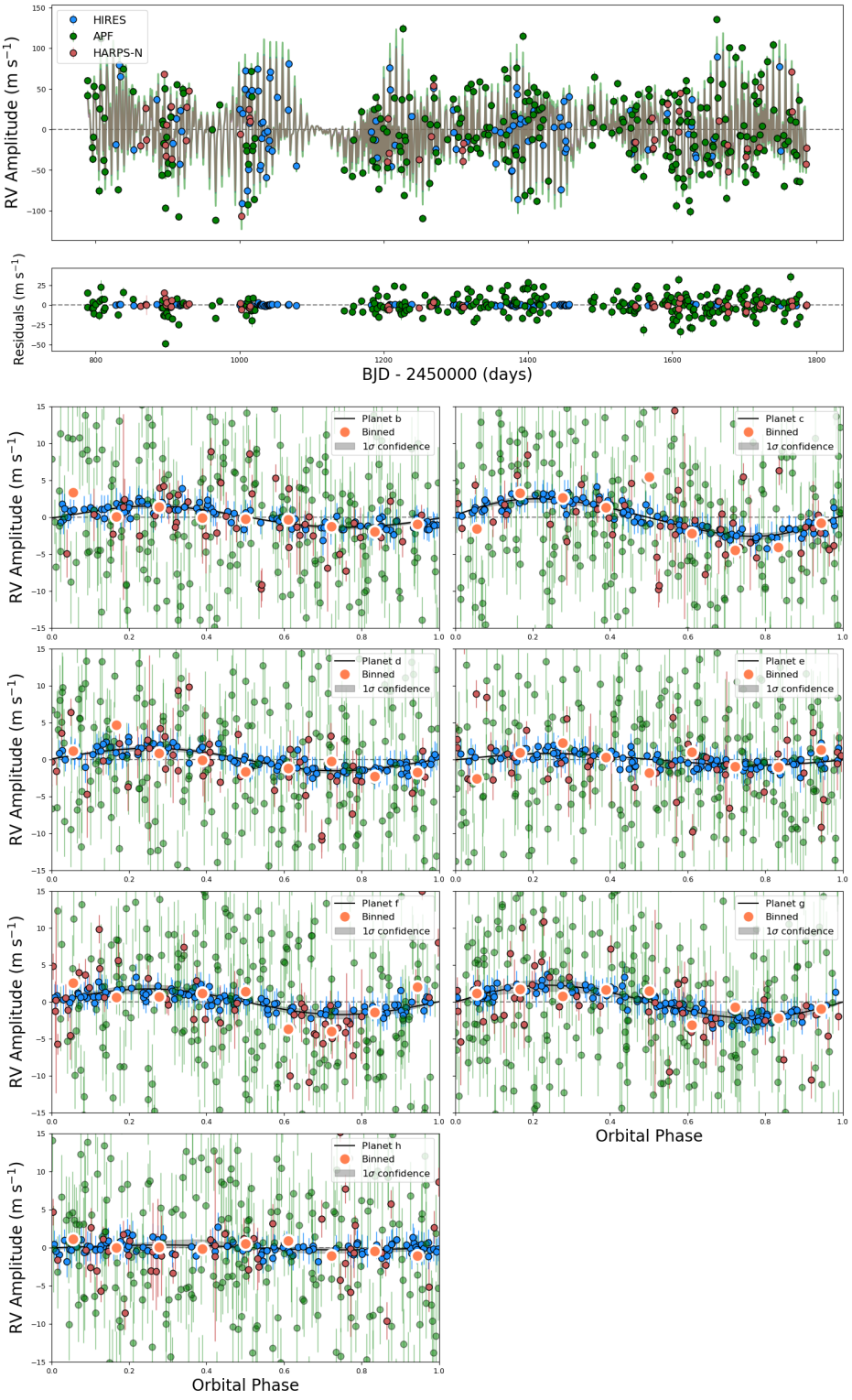

Figure 4.7: Top: Total RV model to TOI-1136, planets and GP. Middle: Residuals to seven planet GP fit. Bottom: Phase folds to each planet in TOI-1136 after subtracting the activity model and each other planet. RVs are adjusted for instrumental offsets. We note that APF's lower precision was not ideal for tracking planetary reflex, but helped to constrain the stellar activity. The RV data used in our analysis are available as "data-behind-the-figure".

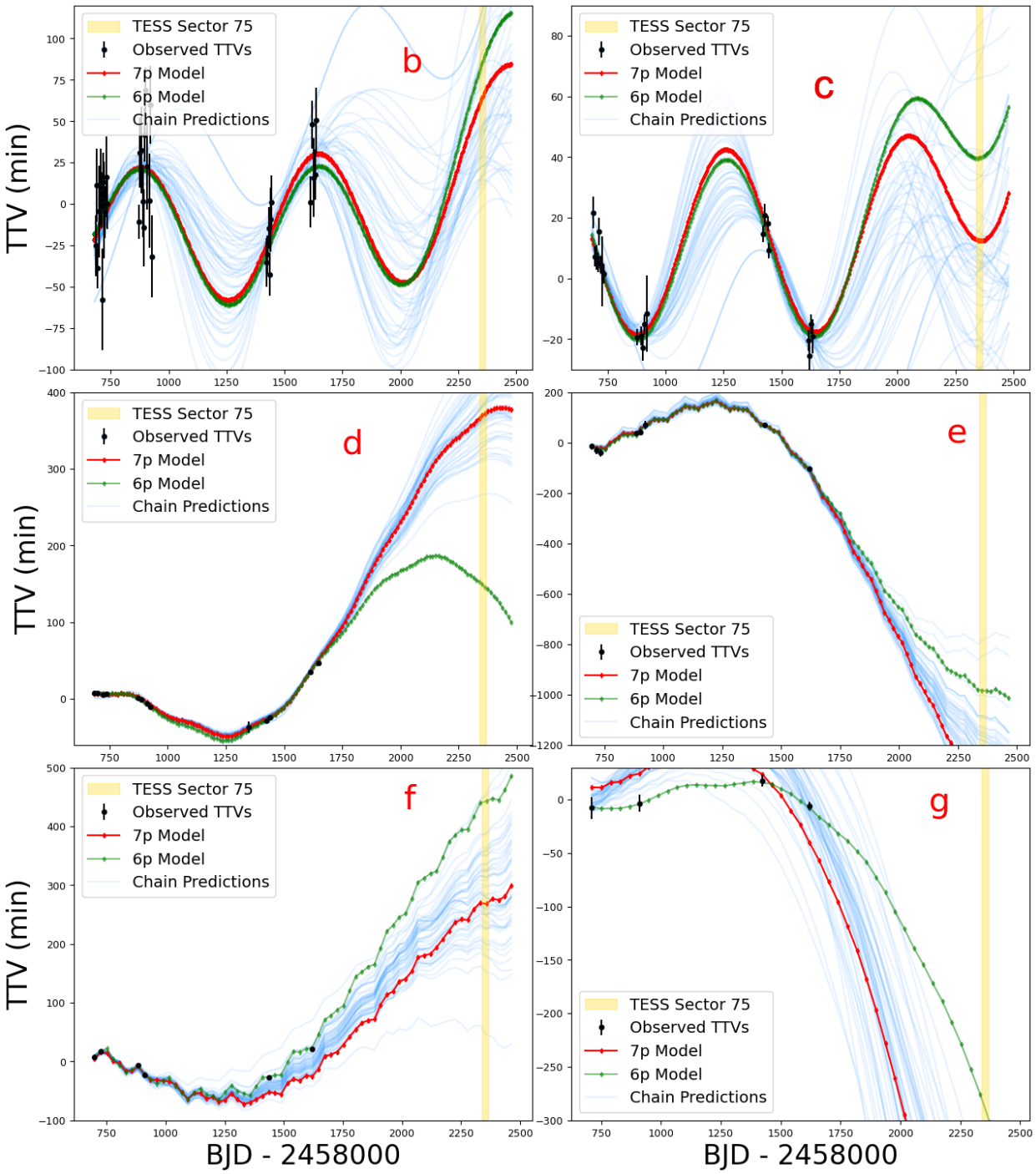

Figure 4.8: TTV O-C plots for each of the six inner transiting planets (b-g), from top to bottom, left to right. Red lines indicate the maximum likelihood TTV model predictions from a seven planet model, while green lines indicate a six planet model. Light blue lines indicate the final prediction of 100 randomly selected chains. We do not include a fit to the single transit of TOI-1136 (h). We also highlight TESS sector 75, where TOI-1136 will receive additional observations. The two models predict significant TTV differences during this Sector.

Going forward, we will mainly talk about the 6 planet TTV + RV model, $\mathcal{A}1$, and we choose this as our adopted model. We choose this over $\mathcal{A}3$ because it utilizes all of the data we have on hand, and because a TTV+RV analysis should be less susceptible to certain biases in mass measurement [365, 281]. Additionally, as remarked later, the TTV+RV+GP analysis is unique and interesting for such a high multiplicity system, and selecting this model further differentiates from the detailed analysis of a 6 planet TTV-only model already carried out in D23. We reject $\mathcal{A}2$ as our preferred model because of the non-detection of planet (h) in the model, and the unreliable estimates of the planet's parameters.

4.6.2 A Seven Planet System?

While we identify a statistically significant transit in §4.4.2 that may correspond to a seventh planet, we do not significantly detect a mass for TOI-1136 (h) in our 7 planet model. Consequently, while the single transit is evidence for an additional planet in the system, we cannot confidently report its orbital period or mass. Thus, we will call this a candidate planet for the remainder of the discussion.

We spend the next sections frequently comparing TOI-1136 to the highest multiplicity exoplanet systems. We feel the comparison is appropriate because of the serious possibility that a seventh planet exists in TOI-1136, but we emphasize its status as a candidate. To reflect this nature, we will refer to the candidate at TOI-1136 (h) in various plots.

4.6.3 Unique High Multiplicity Architecture

The TOI-1136 system currently stands as a particularly unique planetary system. It is among the highest multiplicity exoplanet systems known, tied with TRAPPIST-1 [7 known transiting planets; 148, 1] if we include the candidate planet, and just below Kepler-90 [8

known transiting planets; 73, 341] and the solar system. None of these systems are alike beyond multiplicity, and TOI-1136 continues to buck the trend of similarity.

TRAPPIST-1 is an ultra-cool M dwarf with a compact architecture of planets. The planets are all terrestrial in size ($R_p < 1.2$ $R_\oplus$) and are all on short orbital periods, close to their host star ($P_{orb} < 19$ days). While the TRAPPIST-1 system has multiple potential habitable zone planets [220], making it independently interesting, their small radii suggest that they may only have small atmospheres, and their study via transmission spectroscopy may be impossible. Already, analyses of the atmospheres of TRAPPIST-1 b and c are consistent with a no-atmosphere model [157, 192, 238], though [227] maintain that the outer planets are still likely to have at least a small atmosphere.

Kepler-90 orbits a slightly evolved, early G dwarf, and has several longer period transiting planets. Unlike TOI-1136, Kepler-90 follows a fairly clear demarcation, with smaller, super Earth and sub-Neptune planets on shorter orbital periods, and larger gas giants on exterior orbits.

TOI-1136 consists entirely of sub-Neptune sized planets, likely none of them terrestrial. Further, none are large enough to call gas giants, either, and the planet sizes do not follow any clear sequence or demarcation, with the largest planet third from the star. We highlight the architectural differences in Figure 4.9. TOI-1136's youth is yet another distinguishing feature that adds to the system's value.

Kepler-11 is perhaps the most similar *Kepler* system to TOI-1136, with six transiting planets orbiting a G dwarf [241]. Additionally, its six planets are all similar in size (R_p = 1.8 - 4.2 $R_\oplus$) and density (ρ = 0.58 - 1.4 g/cc) to TOI-1136. As with many *Kepler* systems, the low brightness of Kepler-11 makes RV observations difficult, making any combined analysis like that of TOI-1136 more challenging, though a TTV + RV analysis was done in [392]. This system is also likely not young, making some science cases less promising.

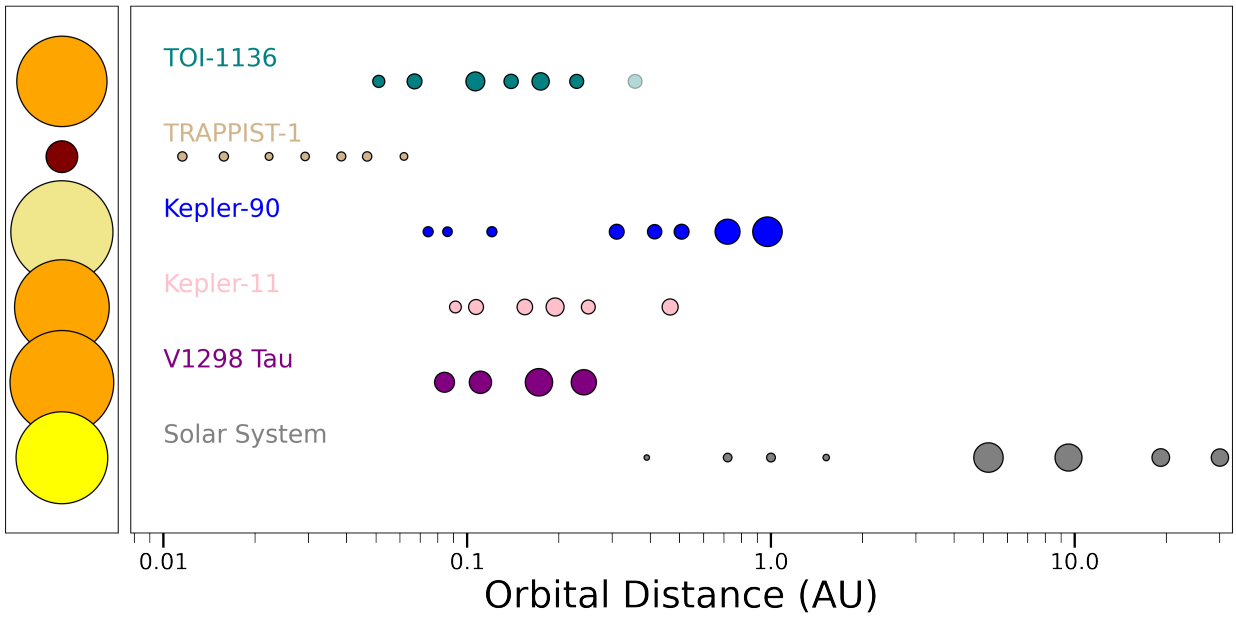

Figure 4.9: We highlight the disparate architectures of the highest-known multiplicity planetary systems, as well as a few systems similar to TOI-1136. We highlight that the candidate seventh planet in TOI-1136 does not have a confidently detected orbital distance. Planet and stellar radii are scaled for comparison to other systems, though we emphasize that the planet-star size is not to scale. None of the systems exhibits a clear analog to any of the others, and all have the potential for very interesting, future study.

We finally compare TOI-1136 to V1298 Tau, a very young system with four transiting exoplanets [368]. The system is even brighter than TOI-1136, and the star is even younger ($\sim$ 20 Myr). V1298 Tau's RVs are much more contaminated with stellar activity than even TOI-1136, making its study very challenging [51]. The system does not appear to exhibit TTVs, however, making its mass extraction much more difficult than TOI-1136.

While many systems exhibit many of the attractive features present in TOI-1136 (multiplicity, youth, TSM), few others have all in the right combination to allow for precise mass measurement, as is possible with TOI-1136.

4.6.4 Resonance Gives Insight into Formation

D23 performed an extensive analysis of TOI-1136, especially considering the resonant orbital properties of neighboring planets, and the overall dynamical stability of the system. Unlike most *Kepler* systems, the orbital periods of TOI-1136 do not deviate from resonance by more than 1%. Particularly strange is the existence of a second-order resonance between planets e and f, which is rare and usually unstable. The youth of TOI-1136 ($\sim$ 700 Myr) suggests the possibility that TOI-1136 is a young precursor to more mature *Kepler* systems, and perhaps suggests that higher order resonances are more common than observed, but become unstable on shorter timescales.

This unique characteristic of TOI-1136 allows us to make more sophisticated guesses about the system's formation and evolution. The system can in many ways be likened to a snapshot of a younger *Kepler* system. Our constraints on eccentricity and argument of periastron, in particular, may shed light beyond the analysis in D23. When experiencing Type-I migration, planets will often form far from the star, and move inward via mutual interactions and disk torque. Theory suggests that such migration results in opposite arguments of periastron to minimize mutual interactions [34]. We include a similar figure to Figure 19 in D23 (Figure C.3). With the exception of planets c and d, and the candidate, posteriors are highly suggestive of Type-I migration. Future atmospheric studies would likely help confirm if indeed the planets in TOI-1136 migrated inward, possibly from the beyond the ice line.

4.6.5 Improved Mass Precisions?

TKS began observations of TOI-1136 well before its true multiplicity was known, and before any significant transit time variations were detected. As our knowledge of the system evolved, the large number of RVs acquired for the system became less obviously useful: with the high mass precisions measured in D23 for the 6 planets using TTVs alone, the RVs seemed

unlikely to improve our mass constraints by a great deal. RV-only fits were hindered by several challenges, preventing significant detections of most of the planets. Mainly, the stellar variability amplitude was many times larger than the expected RV semi-amplitudes, and the stellar rotation period was close to several of the planet orbital periods. With the relatively poor cadence of RV data (compared with photometry), disentangling Keplerian signals from stellar variability became very hard to do with confidence.

Our adopted model generally extracts mass precisions and values consistent with D23. Planet's c, d, and g see slightly improved mass precisions, while the others see slightly worse. Our 7 planet model and our TTV-only models, however, see generally much more precise masses, and in some cases masses quite distinct from D23. It may be that including a seventh planet improves the model significantly, though we consider this unlikely considering its insignificant detection and possibly incorrect orbital period. Additionally, the inclusion of RVs may not be the only contribution to our adopted model's differing posterior parameters. Figure C.4 shows our results, compared with a TTV-only model run using `TTVFast` and `emcee`. It is clear that, especially for the inner planets, the fits which include RVs are not more precise. They are, in fact, typically less well constrained than a TTV-only fit. This suggests that the resulting differences are more likely caused by a different N-body integrator, sampler, or both. D23 utilized `JAX` [60] for N-body integration, and a No U-Turn Sampler [NUTS; 49] for inference. We utilized `TTVFast` for N-body integration and `emcee` for sampling.

An analogous situation may be the mass measurements of TRAPPIST-1 in [391], which utilized `TTVFast` and `emcee`, that were later rectified in [1] using a NUTS sampler. The situation is not perfectly analogous, however, as the masses reported in [391] were highly discrepant with those in [1], which is not the case between our mass estimates here, and the values reported in D23. Additionally, the uncertainties reported in [391] were much larger than the values reported in [1], which is only the case for three planets in our adopted model,

and the difference is not large. Additionally, we know of at least two multi-planet systems with a TTV + RV analysis that utilize `TTVFast` and `emcee` in conjunction [Kepler-11; WASP-47; 392, 9], suggesting that the combination is not necessarily unreliable. Convergence and other sanity checks do not suggest issues during inference, and so we report our results here with a caution that the 7 planet fit and the TTV-only fit have discrepancies with D23, and we are not entirely certain of the cause. Our adopted model, however, is generally consistent.

The high amounts of correlated noise in the RVs are the most likely culprit lowering the precision of our TTV + RV models. Despite this, we include them in our model for a number of reasons. A 6 planet TTV + RV model is generally more consistent with D23. Including RVs also prevents our results from biasing towards the known systematic differences between TTV masses and RV masses [365, 281]. Further, the additional complication added to the analysis by utilizing a TTV + RV + GP model, we feel, is a useful case study for the field, regardless of the result.

Few exoplanet studies are capable of utilizing both RVs and dynamical TTVs, and those systems that are amenable typically have lower multiplicity. Many high-multiplicity systems are analyzed by their TTVs alone [e.g. 241, 1], or their RVs alone [i.e. 286, 115, 332, 253, 377], and lower-multiplicity systems have seen combined analyses [i.e. 395, 9, 394]. The only other high multiplicity system (> 5 planets) for which RVs and TTVs are jointly modeled is Kepler-11 [392]. [392] found that including RVs did not improve mass measurements of Kepler-11 appreciably compared to TTV-only fits, though a comparison is imperfect as this analysis only utilized 27 RVs, in contrast to the 410 RVs used in our analysis of TOI-1136. Our analysis appears to be the first for which an N-body forward model with Gaussian process is jointly fit to the TTVs and RVs. A full photodynamical analysis of the photometry jointly with the RVs, including a model for stellar activity in both the photometry and the RVs, might further improve the planet mass and orbit determinations, but such an effort is enormously computationally costly and is beyond the scope of this paper.

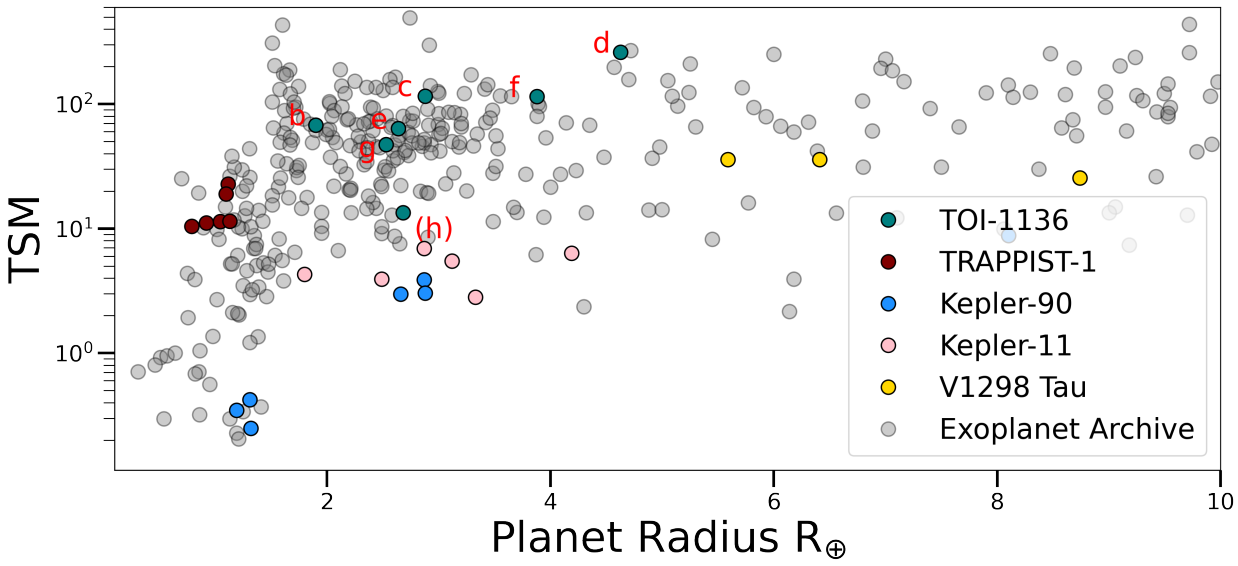

Figure 4.10: TSM versus planetary radius of known exoplanets, taken from the `Exoplanet Archive` on 25 October 2023. We also highlight TRAPPIST-1, Kepler-90, Kepler-11, and V1298 Tau, the systems we discussed as most relevant for comparison with TOI-1136. None of these other systems have TSM values as high as TOI-1136. While several planets in TOI-1136 have only average TSM values, planets c and d are very good for follow up. We emphasize that the probable existence of an atmosphere on all planets in the TOI-1136 system inflates the system's TSM values, and the system would be less useful for a study focused on terrestrial planets.

4.6.6 Prospects for Atmospheric Studies

The potential for future atmospheric studies is a significant portion of TOI-1136's value to the scientific community. The bulk densities of all six transiting planets, and the candidate seventh, are consistent with appreciable atmospheric envelopes, suggesting that atmospheric features may be detected on all seven planets. The transmission spectroscopy metric [TSM; 214] is a useful metric for assessing the value of transmission spectroscopy for a variety of planet regimes. Planets b-g have TSM values of 68, 116, 260, 64, 115, and 47, respectively. These values are estimated assuming an albedo of 0, as is often done [e.g. 40]. TOI-1136 c and TOI-1136 d both rank higher than the follow-up cutoffs suggested in [214], and planet d is particularly good, ranking in the second quartile of large planets. A comparison of TOI-1136 TSMs with other published exoplanets is shown in Figure 4.10.

The true value of studying TOI-1136 via transmission spectroscopy comes from a combination of its multiplicity and its youth. Multiplicity allows for comparative exoplanetology between planets in the same system. This is advantageous because the formation environment of a planetary system is a considerable source of uncertainty, and studying multiple planets in the same system allows for the removal of this uncertainty [299]. Comparing the different environments and atmospheres between the planets of TOI-1136 would provide a great deal of information about the processes that formed the planets in the system, especially their dependence on non-stellar parameters. Is the composition of all the planets the same? If they differ, does it depend on orbital period or eccentricity? Have interior planets been noticeably depleted of volatiles by XUV sculpting?

The youth of TOI-1136 suggests that the system is likely still evolving. Some studies suggest atmospheric stripping may occur on Myr timescales [333], while others suggest that it continues into the Gyr regime [48]. For example, the high insolation received by many of the planets in the system might plausibly strip the atmospheres of the inner planets, if it has not done so already. The largest planet in the system, however, is third closest to the star, in contrast to the typical architectures seen in multi-planet systems [243]. This suggests that atmospheric stripping may be ongoing in this system. Preliminary atmospheric observations of TOI-1136 d detect Hα absorption, a possible sign of atmospheric stripping (Orell-Miquel et al., in prep). Furthermore, the stellar type of TOI-1136 is very similar in parameter space to the Sun, which offers particularly strong motivation for additional study. While the planetary environment does not appear at all similar to the Solar system, the evolution of TOI-1136 could inform predictions about the evolution of our own home.

The youth of TOI-1136, while adding to the potential scientific interest of transmission spectroscopy, might also hinder spectral models. Spectral contamination, however, most strongly hinders low-resolution spectroscopy of late type stars, and earlier type stars mainly see contamination in optical wavebands, which is less of an issue for JWST [144]. Additionally,

such contamination can be mitigated by high resolution spectroscopy, which we have in abundance for TOI-1136.

Comparing the various planets of TOI-1136 with other known planets can be highly suggestive of their compositions. We put the 6 known planets, and the candidate planet, on a mass-radius diagram in Figure 5.8.

The possible compositions of the planets in TOI-1136 depend strongly on the insolation. Planets in TOI-1136 are hot, with insolations of 365, 213, 84, 49, 31, and 18 $S_\oplus$. [247] only estimate compositions curves for a limited number of insolations, the closest being 10 $S_\oplus$ and 1000 $S_\oplus$. Despite these caveats, the placement of the planets in mass-radius space suggests a wide variety of possible compositions for every planet in the system, and follow-up study with JWST would likely reveal a great deal about the chemicals in the atmospheres of these plaents.

Planet b is in the radius gap [134], and might realistically have a terrestrial or gaseous composition. Figure 5.8 suggests a large envelope of water vapor may be the best description of TOI-1136 b's atmosphere, though a variety of volatile envelopes could presumably describe the planet as well. D23 made a strong case that TOI-1136 has experienced Type-I migration, which makes planet b an excellent water world candidate. The resonance of the system suggests that planets likely migrated inward, which is one of the primary ways an exoplanet so close to its host star might still contain significant amounts of water. Our new constraints on the argument of periastron of the planets in the system further suggest Type-I migration (Figure C.3), as neighboring planets are expected to have anti-aligned arguments of periastron [34].

Planet c, d, e, and f, on the other hand, seem consistent with a large gaseous envelope of H_2 or some other volatiles. Even among these planets, compositions vary appreciably, with planets d and f likely containing larger envelopes of H_2, while planets c and e are notably

less "puffy". Stellar winds may have stripped some of their atmospheres, but it remains a mystery as to why planet e would experience such stripping at an increased rate as compared to planets d and f.

TOI-1136 (h) does not have stringent mass or orbital period measurements, and we cannot say much about its potential composition, except that it likely contains a gaseous envelope of some kind. Future studies that confirm or refute the planetary nature of this signal could shed a great deal of additional light on its theoretical composition.

4.6.7 Bridging the Radius Gap

A dearth of exoplanets with radii between 1.5 $R_\oplus$ and 2.0 $R_\oplus$ was first identified in [134], and since has been of great interest to the exoplanet community. This line seems to demarcate terrestrial planets from more gaseous sub-Neptunes, and exoplanets within the gap, in particular, could be subject to either composition. Studying systems with planets on either side of the radius gap can give special insight to the formation, and a number of such studies have been carried out in the literature [92, 295]. TOI-1136 is an extremely useful system to include in such studies, as it has 1 planet within the radius gap (b), 5 planets above the radius gap (c, d, e, f, g), and a candidate planet above the radius gap (h). A great deal of information might be gleaned from a follow-up study examining each planet's expected role in such a configuration, though it is beyond the scope of our analysis here.

4.6.8 Future Work

We expect TOI-1136 to receive continued observations and scientific interest. Many of the most attractive features of the system, such as its amenability to transmission spectroscopy, are due to the possibility of future observations. TOI-1136 makes for an extremely compelling

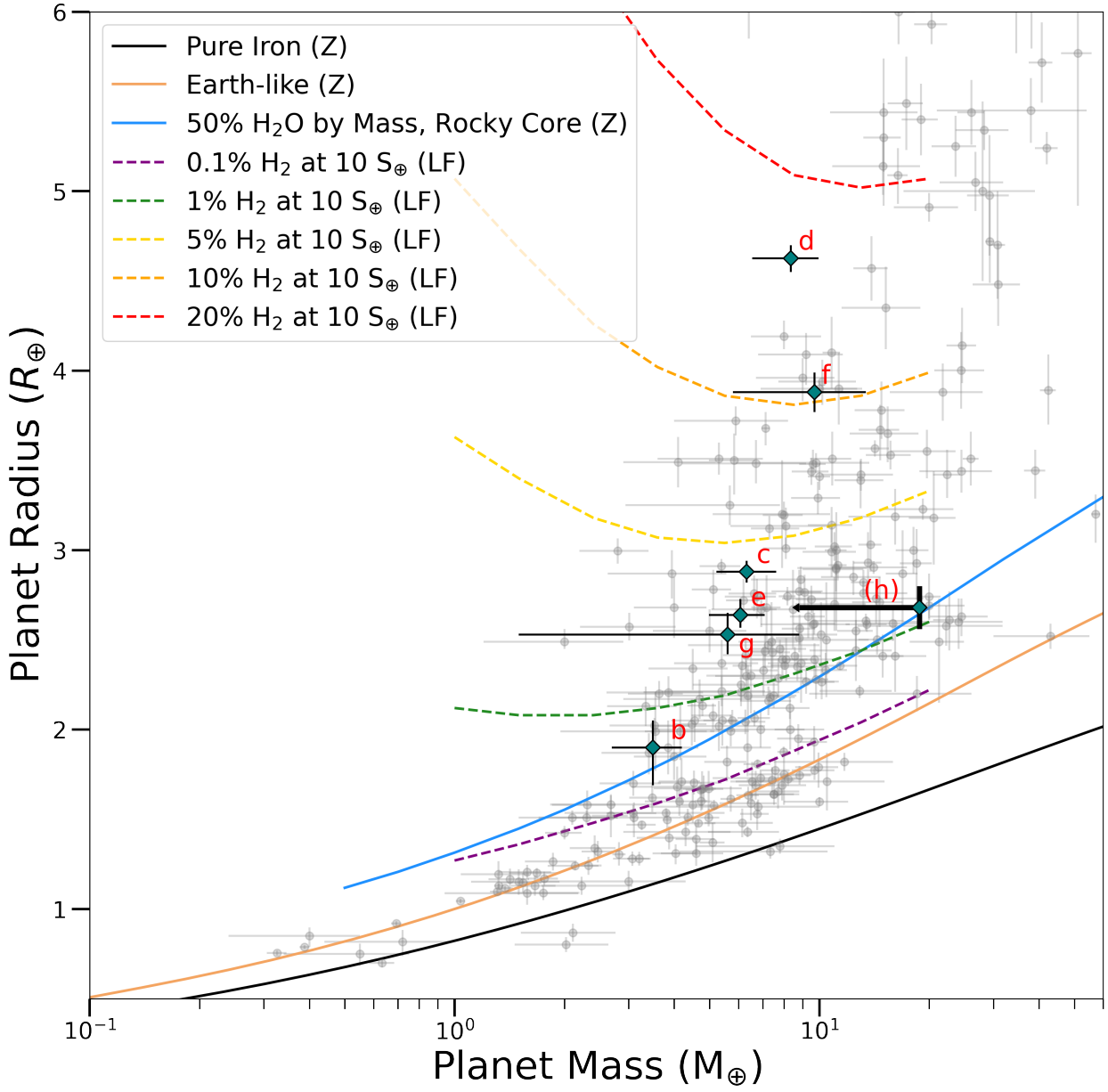

Figure 4.11: Mass-radius diagrams of known exoplanets taken from the `NASA Exoplanet Archive` on 12 May 2023 in gray, with the planets in TOI-1136 highlighted. We include only exoplanets with better than 2σ mass precision. We include composition profiles taken from [406] for rock, water, and iron compositions, indicated by a solid line in the figure, and a (Z) in the legend. We include H_2 envelopes of different percentages taken from [247], as the [406] profiles may not be as accurate in the regime of large gaseous envelopes [324]. These are indicated by dashed lines, and are notated with a (LF) in the plot legend. A wide variety of compositions might explain the bulk density of the planets in TOI-1136, and planet b in particular might have either a small volatile envelope, or could be consistent with a "water world". We place TOI-1136(h) at its 3σ upper limit, and use a downard arrow to indicate our uncertainty in its mass.

target for JWST.

Future RV observations might better constrain the mass of the system, though future TESS observations are likely to be more fruitful. TTVs seem to contribute a great deal to the mass precision of the system's exoplanets, and more transits should only further refine our knowledge. Other parameters, such as radius, orbital period, and time of conjunction will see improvements with more TESS observations. Observing additional transits of the candidate planet would be the best way to confirm its planetary nature. Fortunately, TESS will be re-observing TOI-1136 in Sector 75, which starts on 30 January 2024.

This system is particularly interesting in the context of the observed discrepancy between TTV and RV measured exoplanet masses [365, 281]. Very few exoplanet systems with TTV masses are also amenable to RV follow-up (< 7; `NASA Exoplanet Archive`). Recovering significant mass measurements with RVs alone, while preventing GP overfitting, would be a challenging task, probably requiring many more observations, but could potentially shine light on this discrepancy. It might additionally alleviate concerns raised in §4.5.3 about model overfitting, as it would be interesting to ensure the two methods are consistent.

4.7 Summary

We utilize a combination of TTVs, RVs, and a GP to measure the mass of the six-planet system TOI-1136, and place constraints on the orbital properties of a potential seventh planet. This detailed analysis will inform future studies of TOI-1136, as the system is a top candidate for transmission spectroscopy, and is a huge source of potential information about planetary formation.

Chapter 5

Utilizing Photometry from Multiple Sources to Mitigate Stellar Variability in Precise Radial Velocities: A Case Study of Kepler-21

5.1 Foreword

Radial Velocities (RV) have long been an important method for discovering and characterizing exoplanets. Initial discoveries of Hot Jupiters were executed using RV instruments with precision near ten meters per second [272, 68, 69]. Improvements in instrument design, pipelines, and analysis methods have allowed us to detect smaller signals, such as those with lower masses and longer orbital periods [275, 374]. Later, the Kepler mission [57] would reveal that the dominant population of exoplanets consists of intermediate-sized exoplanets between the size of Earth and Neptune, dubbed Super-Earths and Sub-Neptunes [e.g., 185].

Measuring the masses of this common type of exoplanet is a more challenging prospect than discovering them via transits. As a transit survey, the Kepler mission could only measure planet masses for a small number of systems that exhibited transit timing variations [TTVs; 164]. RV follow-up continues to be the most reliable method for measuring planet masses, and the field continues to push RV sensitivity to smaller and smaller values, with the longstanding 1 m s^{-1} noise floor recently being breached by new instruments.

New RV instruments with on-sky (or expected on-sky) precisions well below 1 m s^{-1} are available today, though they still are generally unable to characterize exoplanets with RV semi-amplitudes similar to Earth's [10 cm s^{-1}; 399]. This is due primarily to correlated noise in the RVs from a variety of stellar astrophysics that interfere with small planetary signals, sometimes many times larger than the planetary signal in question [76, 77, 105]. These astrophysical noise sources can manifest as uncorrelated white noise, or "jitter," at the $\sim$ 1 m s^{-1} level [e.g. 29], or more frustratingly, they can create correlated noise that resembles false planetary signals, creating false positives [251]. Hence, to detect planets at the limits of our technological capacity, we must first deal with astrophysical noise sources many times larger than our instrumental variability.

High-cadence stellar lightcurves from transit surveys such as Kepler and TESS offer a powerful diagnostic tool for correcting activity contamination in RV data caused by a multitude of stellar astrophysics. For example, [5] developed a diagnostic, FF', that is an excellent predictor of RV variability induced by rotating active regions on Sun-like stars. More recently, [76] predicted that high-cadence photometry may also help diagnose RV jitter from granulation at amplitudes below 1 m s^{-1}.

Why should stellar variability in photometry inform variability in RV data at all? Spot modulation in particular can have large effects on both datasets. Spots and plages represent regions of enhanced magnetic activity, and they show up as extra bright or dim regions in photometry. These features affect RV data by creating an anomalous red or blue shift for

some small region of the star, reducing or increasing the total measured Doppler velocity [105]. Spots typically rotate into and out of view, creating a periodic, or quasi-periodic, variation of both photometric brightness and measured RV.

Importantly, while there may be phase offsets between a spot's signature in photometric or RV data, the two datasets should modulate with a related frequency, since this modulation is caused by a real, physical rotation of the star. Thus, the frequency structure of photometry and RV data should be related, if not identical.

These stellar surface features come and go, with typical lifetimes varying depending on spectral type [147, 146]. Consequently, the frequency structure of the stellar activity will typically evolve over time, and we may not be able to enforce a strong relationship between photometry and RV data taken temporally far apart. Hence the general opinion in the field of exoplanet science that RV data taken contemporaneously with photometry is more informative for mitigating stellar activity than data taken much earlier or later [173].

Temporal proximity to RV data is not the only consideration when examining photometric datasets. Kepler, for example, was a much more precise instrument than TESS (For Kepler-21: $\sigma_{\mathrm{Kepler,med}}$=4.38 ppm; $\sigma_{\mathrm{TESS,med}}$=38.38 ppm), and was sensitive to brightness variations that TESS cannot detect. Further, the observing strategy of Kepler allowed it to typically constrain periodic signals near 45 days or less [278], while TESS's mission strategy prevents rotation estimates much greater than 12 days [181]. Even if simultaneous, TESS may not be able to constrain magnetic activity in RV data if its periodicity is longer than this limit. All of these considerations have motivated us to study the tradeoffs of utilizing different photometric datasets.

We set out to study a handful of Kepler targets with the NEID spectrograph [336, 165] at Kitt Peak National Observatory (KPNO), located on the WIYN telescope[1], while TESS

[1]The WIYN Observatory is a joint facility of the University of Wisconsin-Madison, Indiana University, the National Optical Astronomy Observatory and the University of Missouri.

was observing them. We were interested in studying the utility of simultaneously acquired precision RVs, and how these can best be combined with photometric data to mitigate stellar variability.

Here we present a deep dive into the RV and photometric data of one of our targets, Kepler-21, and explore the best ways to mitigate the stellar variability in its RVs using photometry. Kepler-21 was first studied by [186], and later in **(author?)** [249, hereafter LM16], and has seen extensive interest in the community for a variety of reasons. [56] recently released a catalog of RV systems that further improved the mass precision of Kepler-21 b to $> 5\sigma$ precision, though they did not discuss the system in depth. Kepler-21 is the brightest planet-hosting Kepler system (V = 8.5) and hosts one of the first detected exoplanets with a composition similar to Earth. Kepler-21 b also resides in the exoplanet radius valley [134], which, due to the paucity of planets in the region, and our incomplete knowledge of planet formation and evolution, makes it a compelling target for atmospheric study. Despite the variety of attractive features, stellar magnetic activity (RV RMS = 5.32 m s^{-1}) has long challenged our ability to precisely measure the mass of Kepler-21 b, and to explore other features of the system. Utilizing a variety of new, precise RVs, Kepler-21 presents an ideal target to test the sensitivity of different activity mitigation models trained on Kepler and TESS, as well as to refine the orbital parameters of an important planetary system. We additionally place constraints on the orbital period and mass of a candidate super-Jupiter outer companion to Kepler-21 b, which we designate Kepler-21 (c).

We present an overview of the data used in our analysis in §6.3. We briefly discuss our utilized stellar parameters in §5.3. We next present an analysis of the data in §6.4. We discuss our results in §6.5, and provide a final summary in §6.6.

5.2 Data

5.2.1 Photometric Data

Kepler Photometry

Kepler-21 was observed for the entire duration of the primary Kepler mission [57]. The Kepler spacecraft utilized a 1.4 m primary mirror to observe > 190,000 main sequence stars using its 115 square degree field of view. Kepler-21 was observed from 2 May 2009 to 11 May 2013, spanning 1470 days, or just over four years.

Kepler-21 saw both long-cadence (29.4 min) and short-cadence (58.85 s) observations. Short and long cadence data are available for all 17 Kepler quarters, with the exception of Q1, Q3, and Q4, where only long-cadence data are available. We, like LM16, utilize long-cadence data during our photometric fits, for the sake of uniformity. We utilize the Presearch Data Conditioning (PDC) flux, estimated with the Kepler Science Processing Pipeline [KSPP; 197]. We use the lightkurve package (v. 2.4.1) to download Kepler PDCSAP flux data [237] for use in our transit analysis and training. The Kepler long-cadence data have an median errorbar of 4.4 ppm. Kepler data quality does vary from quarter to quarter, though not at levels that are relevant to our analysis. We utilize the `lightkurve` NaN/outlier removal functions to remove datapoints flagged as unreliable [237].

TESS Photometry

Kepler-21 was observed by the Transiting Exoplanet Survey Satellite [TESS; 318] during Sectors 14 (18 July - 15 August 2019), Sectors 40-41 (24 June - 20 August 2021), and Sectors 53-54 (13 June - 5 August 2022). We use the presearch data conditioning simple aperture (PDCSAP) flux reduced from by the TESS science processing operations center

[SPOC; 198] pipeline during our analysis.

We again utilize built in `lightkurve` functions to remove TESS datapoints flagged as unreliable. Kepler-21 was observed both with short-cadence (2 min) and long-cadence (30 min) observations. We utilize TESS short-cadence data, which has an median error of 38 ppm.

5.2.2 Radial Velocity Data

HIRES RVs

We utilize 49 archival and 20 newly acquired RVs of Kepler-21 taken with the High-Resolution Echelle Spectrometer [HIRES, 387], mounted on the Keck-I telescope at W.M. Keck Observatory. RVs were extracted using the iodine-cell method described in [70], and we utilized archival data from [71] for the older RVs. This archival data was run through the California Planet Search [CPS; 184] pipeline in conjunction with our newly acquired HIRES RVs before analysis.

After binning observations taken on the same night, our HIRES dataset consists of 36 RVs. While more sparse than the other RV datasets, the HIRES RVs span by far the longest observation baseline, greatly expanding our sensitivity to the long period companion discussed in §5.4.6. HIRES observations span from 31 August 2010 to 14 July 2023. Binned HIRES RVs have an average SNR of 200, estimated as a per-pixel average at peak blaze in the middle of the iodine region (500-550 nm). This corresponds to an internal average error of 2.4 m s^{-1}.

HARPS-N RVs

Our analysis utilizes 98 RV observations of Kepler-21 using the High-Accuracy Radial Velocity Planetary Searcher North [HARPS-N; 89] located at the Telescopio Nazionale Galileo. 82 of these RVs were first published in LM16 after their analysis of Kepler-21 b, and an additional 16 were published in [56].

HARPS-N RVs have an average SNR of 167 at 550 nm, which corresponds to an average RV errorbar of 1.39 m s^{-1}. LM16 originally noted that this value is higher than the expected ~ 1 m s^{-1} uncertainty for a star of this spectral type at this SNR, and this is likely a consequence of line broadening due to the high $v \sin i$ of Kepler-21 (detailed more in §5.3).

NEID RVs

We obtained 22 high cadence observations of Kepler-21 with the NEID spectrometer located at Kitt Peak National Observatory. NEID is an extremely stable instrument capable of obtaining RV precisions of better than 50 cm s^{-1} on bright stars [336, 165]. Our observations range from 15 April 2021 to 13 June 2022, with most concentrated around TESS observation windows. Indeed, our observing strategy was to obtain as many high-cadence RVs of Kepler-21 as possible during, or near, TESS observing windows. Particularly poor weather in 2021 prevented us from obtaining as many simultaneous observations as would have been ideal, and the Contreras fire shut down Kitt Peak mere days after our observing sequence began in 2022. Despite this, we obtained seven NEID RVs simultaneous with TESS observations, with most of the rest of our RVs nearly simultaneous. Our coverage relative to TESS observations is visible in Figure 5.1.

We reduced the NEID RVs using the SpEctrum Radial Velocity AnaLyser [`SERVAL`; 405] software package, modified for use with NEID [see 363]. Our NEID data has a mean SNR

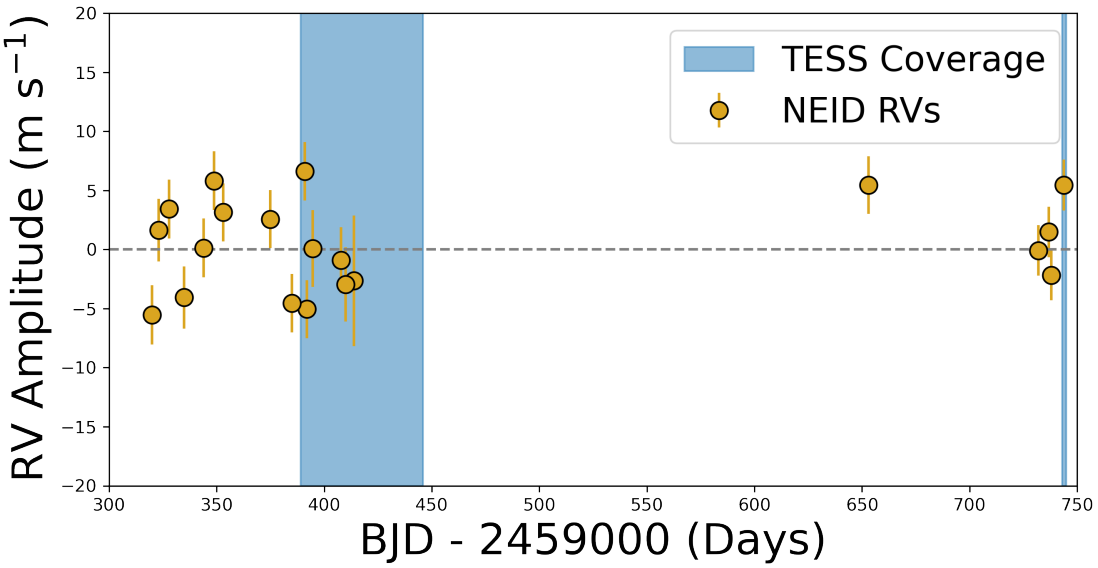

Figure 5.1: A plot of our NEID RV coverage as a function of time. TESS simultaneous veiwing is highlighted with a light blue streak. All of our NEID RVs were obtained near in time, or simultaneously, with TESS observations.

of 102 at 490 nm, and a mean RV precision of 2.2 m s^{-1}.

5.3 Stellar Parameters

Kepler-21 is a bright (V = 8.5), slightly evolved F5 subgiant. We follow LM16 and use the stellar parameters of Kepler-21 taken from [346], who derived stellar properties for 33 Kepler systems. Kepler-21 also saw study via asteroseismology, which allows us to constrain its age (2.84 ± 0.35 Gyr) and provides a separate measure of the system's rotation period [14.83 ± 2.41 days; 186].

Because it is a slightly evolved star with a short stellar rotation period, we expect a high $v \sin i$. LM16 measure $v \sin i = 8.4 \pm 0.5$ km s^{-1}. This value is sufficiently high to create an effective noise floor for our most precise RVs. Indeed, the average error of our HARPS-N and NEID RVs do seem hindered by a precision limit near 1.5 m s^{-1}. This is especially notable

for NEID, as the NEID exposure time calculator estimates a precision of 0.47 m s^{-1} on a G star with a small (< 2 km s^{-1}) $v \sin i$ of equal brightness and exposure time. Our full stellar parameters are visible in Table 6.1.

Table 5.1: Stellar Parameters

Parameter	Estimated Value	Units	Reference
M_*	$1.408^{+0.021}_{-0.030}$	$M_\odot$	1
R_*	$1.902^{+0.018}_{-0.012}$	$R_\odot$	1
L_*	$5.188^{+0.142}_{-0.148}$	$L_\odot$	1
ρ_*	$0.287^{+0.004}_{-0.005}$	cgs	1
$\log g_*$	4.026 ± 0.004	cgs	1
$T_{\rm eff}$	6305 ± 50	K	1
[Fe/H]	-0.03 $\pm$ 0.10	...	1
Age	2.84 $\pm$ 2.41	Gyr	2
1 refers to [346]. 2 refers to [186].			

5.4 Analysis

5.4.1 Training Our Models

Throughout the paper, and in the following sections, we will often use the terms "Kepler-trained", or "TESS-trained." As mentioned in §6.1, training activity models on different photometric datasets is expected to have different effects on RVs. Precision, temporal proximity, and observing baseline are expected to have the largest effect. To explore these

tradeoffs, we train on Kepler and TESS photometry independently. This training consists of fitting a Gaussian Process [GP; 10] to photometry prior to utilizing the posteriors of these fits as priors for RV fits.

Because RV data is more sparse than photometry, our Kepler and TESS datasets need not be used at their full temporal resolutions. We bin our photometric data using 0.1 day bins. We also restrict our training to Sectors 40 and 41 of TESS, and Quarters 6 and 7 of Kepler. Sectors 40 and 41 were chosen because our NEID RVs were taken contemporaneously with these Sectors, and Quarters 6 and 7 of Kepler were chosen because of their simultaneity to HARPS-N RVs. Our intent is to give each dataset the best possible chance of informing the RV model most accurately, and temporal proximity is likely a deciding factor. A plot of our training data is visible in Figure 5.2.

An important part of training a GP model is the kernel function one chooses to employ. We choose to use the $\mathcal{K}_{J1}$ GP kernel [74], where the i$^{\text{th}}$ and j$^{\text{th}}$ elements of its covariance matrix are given in equation 6.1.

$$\mathcal{K}_{J1} = \eta_{\sigma,s(i)}\eta_{\sigma,s(j)} \exp\left(\frac{-|t_i - t_j|^2}{2\eta_\tau^2} - \frac{1}{2\eta_l^2}\sin^2\left(\frac{\pi|t_i - t_j|}{\eta_p}\right)\right) \tag{5.1}$$

Above, t_i and t_j refer to the i$^{\text{th}}$ and j$^{\text{th}}$ timestamps of our RV observations, η_τ refers to the exponential decay timescale, η_l is the periodic scale length, and η_p is the recurrence timescale of the GP. $\eta_{\sigma,s(i)}$ refers to the amplitude hyperparameter associated with spectrograph s, utilized for observation i. This $\mathcal{K}_{J1}$ kernel is an expansion of the Quasi-Periodic (QP) GP kernel utilized frequently in RV exoplanet science [e.g., 173, LM16]. The QP kernel is a convenient choice not only due to its wide use, but also because of the *interpretability* of its hyperparameters. η_p is usually a good approximation of the stellar rotation period, η_τ can

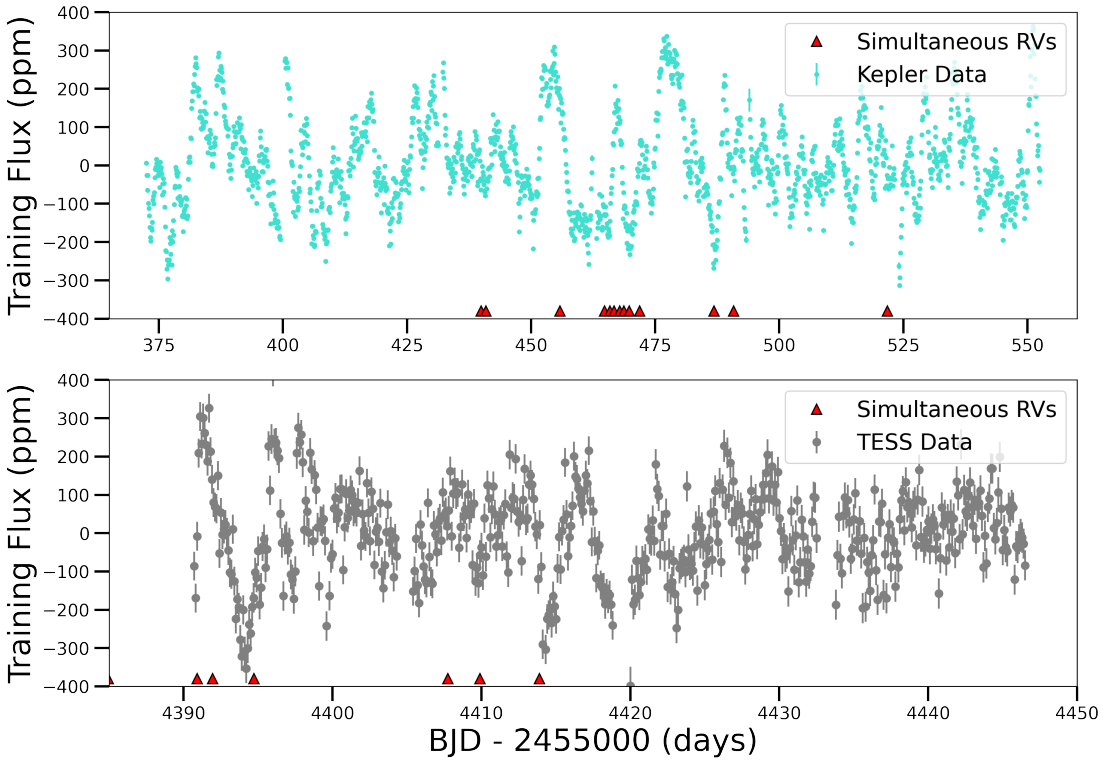

Figure 5.2: Top: Kepler Quarters 6 and 7 PDCSAP Flux, binned to 0.1 days. Bottom: TESS Sectors 40 and 41 PDCSAP Flux, binned to 0.1 days. Both datasets exhibit clear, quasi-periodic variability caused by stellar magnetic activity. Simultaneous RVs are marked with red triangles.

be approximated as the active region decay lifetime, and η_σ is the amplitude of variability. η_l, sometimes called the structure parameter, is more difficult to interpret physically, though it is related to the number of intra-period variations the GP sees inside of a single rotation period, as LM16 explain.

We use the $\mathcal{K}_{J1}$ kernel instead of the QP kernel because it 1) utilizes all instruments in a single covariance matrix, and 2) it utilizes a different amplitude parameter for each spectrograph. The former can make the model less susceptible to overfitting, which can be a serious problem when utilizing GPs on sparse datasets [51]. The latter is useful because the different instruments used in our analysis do not all extract RV information from the same wavelength-space, and stellar variability can be chromatic [90].

We run our training using the `RadVel` software package [133]. While not designed for fitting photometry, we have modified the software to use the $\mathcal{K}_{J1}$ kernel for our RV fits in §5.4.3, and it is trivial to evaluate a GP-only fit on a time series of any dimension. We assessed model convergence using the default method in `RadVel`, which assesses convergence by determining when the Gelman-Rubin (G-R) statistic [119] < 1.03 for all parameters, the minimum autocorrelation time factor ≥ 75, and a max relative change in autocorrelation time is $\leq .01$, and ≥ 1000. We adopted broad priors on the GP hyperparameters, summarized in Table 5.3.

The posteriors of the GP fit to Kepler and TESS photometry are used as priors in Kepler-trained and TESS-trained RV fits, respectively. The amplitude posterior from training is not used as a prior in RV fits, as its dimension is flux, not velocity, and would not make meaningful sense when applied to RV data.

Kepler-21 has a known rotation period, measured via asteroseismology to be 14.83 ± 2.41 days [186], and from Kepler photometry to be 12.62 ± 0.03 days (LM16). To prevent biasing our training toward Kepler, we use the asteroseismological estimate as an initial

guess. Interestingly, as seen as priors in Table 5.3, our Kepler training produces a 22 day periodic term that we know to be erroneous. TESS training finds a 15.8 day periodicity, though with a large uncertainty. Both of these results highlight the fact that the periodic term of a GP is not strictly the same as the stellar rotation period. Rather than modify our training until we achieve a desired result, we proceed as if we do not know the true rotation period of the system. Interestingly, the Kepler-trained RV fits do recover a less precise planetary mass, as seen in Table 5.4. It should be noted that our joint fits in Table 5.5 do recover the correct rotation period in Kepler, and its second harmonic in TESS. This might suggest a reason to prefer joint fits to RV fits trained on photometry.

5.4.2 Transit Analysis

Kepler-21 photometry was first obtained by the Kepler mission, with observations spanning 4.25 years. Consequently, LM16 were able to extract highly precise planetary parameters, such as orbital period and radius, by fitting only the Kepler data.

Kepler-21 was observed with TESS for a comparatively small amount of time, only six sectors of 27 days each, adding 150 additional days of photometric data. TESS photometry is less precise than Kepler, meaning that it is unlikely to improve measured planetary parameters such as radius or impact parameter on its own.

Utilizing both datasets together, however, is expected to improve some of the previously measured parameters. In particular, orbital period and measured time of inferior conjunction might see genuine improvements due to the significantly increased total observation baseline when including TESS data.

In §5.4.4, we utilize *all* Kepler quarters and TESS sectors during analysis, as we are extracting planetary parameters from the lightcurves as well. In §6.4.1 we use only the subsets described

therein, as we are only extracting RV variability information.

Our transit model utilizes a mean offset for Kepler and TESS photometry and two photometric jitter terms to account for uncorrelated white noise. Kepler-21 has an estimated background contamination ratio of 8.1%, suggesting that the TESS photometry is probably slightly contaminated by nearby stars [356]. To account for this, we scale the generated TESS light curve by the square root of a dilution term, which floats between 0 and 2 [39].

We use the `exoplanet` software package [129, 127] to create an orbit model of Kepler-21 using its orbital period, transit time, impact parameter, stellar radius, and stellar mass. exoplanet utilizes this orbit model with `starry` [254] to generate the light curves for Kepler and TESS, which requires a planet radius and limb darkening coefficients. We use a quadratic limb darkening law [2], and different limb darkening terms for Kepler and TESS. We use the limb darkening terms estimated from [81, 82] as our initial guess.

Both Kepler and TESS photometry exhibit quasi-periodic fluctuations, likely due to stellar magnetic activity. Consequently, some model to account for this coherent noise is an essential part of modeling the photometry. We again utilize a GP to model the coherent noise, though we do **not** utilize the $\mathcal{K}_{J1}$ kernel described in §6.4.1 or 5.4.3. Instead, we use the `celerite2` RotationTerm, also called the double simple harmonic oscillator (dSHO) [124, 120]. We do so because the $\mathcal{K}_{J1}$ kernel is more computationally expensive, scaling $\mathcal{O}(N^3)$ with number of data points, while the dSHO kernel scales as $\sim \mathcal{O}(N)$, even for large datasets. While the dSHO kernel is still widely used [e.g. 222, 6], we find that its hyperparameters are more difficult to interpret physically. The dSHO is a combination of two simple harmonic oscillator (SHO) terms, given in equation 5.2.

$$\mathrm{SHO_n}(\omega) = \sqrt{\frac{2}{\pi}} \frac{\mathrm{S_0}\omega_\mathrm{n}^4}{(\omega^2 - \omega_\mathrm{n}^2)^2 + \omega_\mathrm{n}^2\omega^2/\mathrm{Q_n^2}} \tag{5.2}$$

In the dSHO case, our total power spectral density is the sum of SHO_1 and SHO_2. The actual GP fit sees a slight reparameterization using free parameters σ_{GP}, Q_0, dQ, f, and P_{GP}, and it restricts the frequency of the second oscillator to be twice that of the first. These are related to the above parameters by the following equations:

$$Q_1 = 1/2 + Q_0 + dQ \tag{5.3a}$$

$$\omega_1 = \frac{4\pi Q_1}{P_{GP}\sqrt{4Q_1^2 - 1}} \tag{5.3b}$$

$$S_1 = \frac{\sigma_{GP}^2}{(1+f)\omega_1 Q_1} \tag{5.3c}$$

$$Q_2 = 1/2 + Q_0 \tag{5.3d}$$

$$\omega_2 = 2\omega_1 \tag{5.3e}$$

$$S_2 = \frac{f}{2} S_1 \tag{5.3f}$$

The free hyperparameters of this kernel are σ_{GP}, the standard deviation of the process, P_{GP}, which is approximately the stellar rotation period, Q_0, the quality factor of the undamped harmonic oscillator, dQ, the difference in quality factors between SHO_1 and SHO_2, and f, the fractional amplitude difference of the two oscillators. While we prefer the $\mathcal{K}_{J1}$ kernel because of the more readily interpretable hyperparameters, the dSHO kernel is sufficient to model the variability in the photometry of Kepler-21.

We generate a model context using the `PyMC3` software package [329], which uses `theano` tensors for fast likelihood computations [372]. We put generally broad priors on all the free parameters of our model, with a summary in Table 5.3. We then explore the posterior parameter space of our model via Markov chain Monte Carlo (MCMC) inference. `exoplanet` uses the Hamiltonian Monte-Carlo (HMC) method in conjunction with a No U-Turn Sampler (NUTS) to explore the posterior parameter space efficiently [179]. We run our model with two chains for 2000 tuning steps and 2000 sampling steps, confirming that our parameters are converged by ensuring their GR statistic is less than 1.001 for each. Our results are visible in Figure 5.3 and Table 5.2.

Table 5.2: Transit Posteriors

Parameter Name	Posterior Value	Units
Planet Parameters		
P_{orb}	2.785823±3e-6	Days
T_c	2459793.521±0.005	BJD
e	0.13±0.09	-
ω	-10.6±45	Degrees
Transit Parameters		
R_p	1.66±0.03	$R_\oplus$

Continued on next page

Table 5.2: Transit Posteriors

Parameter Name	Posterior Value	Units
b	0.64±0.08	-
$u_{1,Kepler}$	0.35±0.08	-
$u_{2,Kepler}$	0.21±0.09	-
$u_{1,\mathrm{TESS}}$	0.36±0.10	-
$u_{2,\mathrm{TESS}}$	0.23±0.10	-
$\mathrm{dil}_{\mathrm{TESS}}$	0.8±0.2	-
Derived Parameters		
T_{14}	0.14±0.01	Days
a	0.043	AU
i	88.557±0.006	Degrees
S	2752.356±0.004	$S_{\oplus}$
T_{eq}	2015.5472±0.0008	K
GP Hyperparameters		
σ_{Kepler}	127±2.9	ppm
σ_{TESS}	129±7.4	ppm
$\log Q0_{\mathrm{Kepler}}$	-4.73±0.21	-
$\log Q0_{\mathrm{TESS}}$	-5.33±0.37	-
$\log dQ_{\mathrm{Kepler}}$	-1.11±0.14	-
$\log dQ_{\mathrm{TESS}}$	-1.10±0.70	-
$P_{\mathrm{rot,Kepler}}$	5.78±0.21	Days
$P_{\mathrm{rot,TESS}}$	3.48±0.48	Days
f_{Kepler}	0.016±0.002	-
f_{TESS}	0.32±0.07	-

Continued on next page

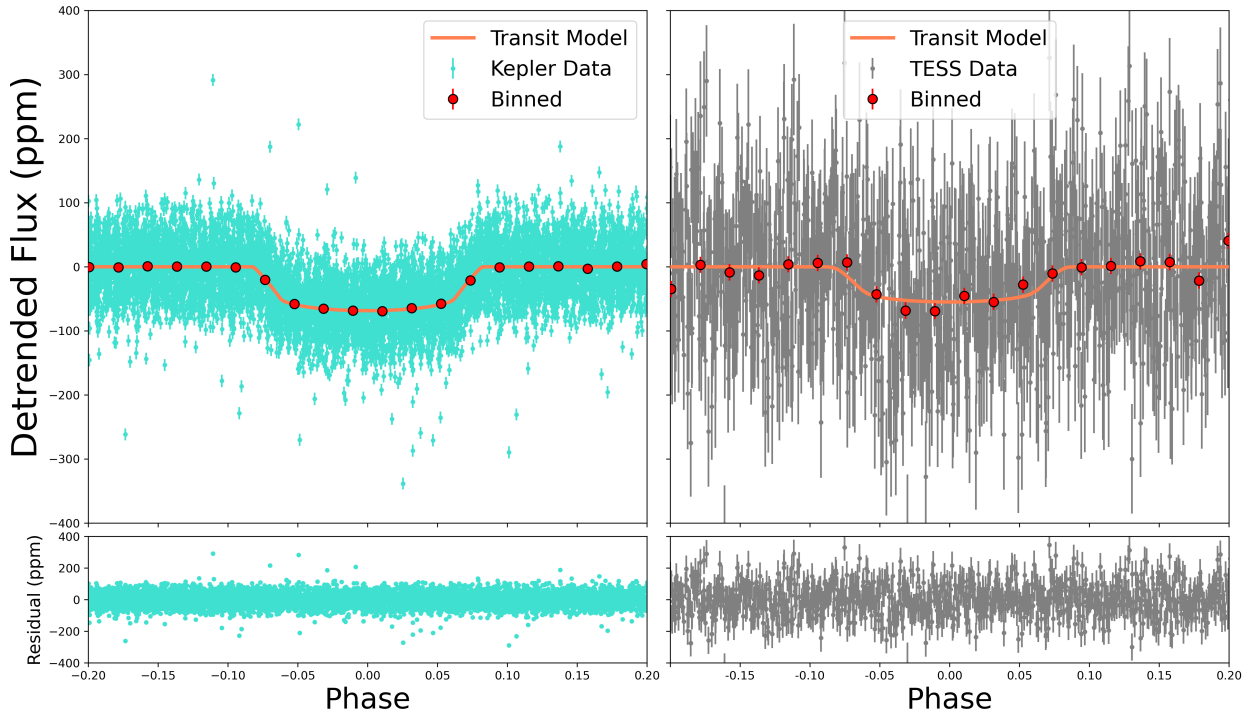

Figure 5.3: Left: phase folded Kepler transit of planet b, and the fit residuals below. Right: phase folded TESS transit of planet b, with residuals below. Unsurprisingly, we recover the previously reported transits in Kepler, but we also include for the first time a fit using TESS. Considering that the planet has a radius of 1.618 $R_\oplus$ and is orbiting a larger star ($R_* = 1.902\ R_\odot$), the transit depth is quite small, and difficult to discern from an individual transit, especially in TESS. Nonetheless, folding multiple transits and binning the data clearly reveals a transit-like structure, even in TESS.

Table 5.2: Transit Posteriors

Parameter Name	Posterior Value	Units
Instrumental Parameters		
γ_{Kepler}	1e6±4	ppm
$\gamma_{\rm TESS}$	1e6±24	ppm
σ_{Kepler}	50.000±0.003	ppm
$\sigma_{\rm TESS}$	95±2	ppm

Table 5.3: Priors Used for Various Fits

Parameter Name	Transit Fit Prior	Kepler Trained RV Fit	TESS Trained RV Fit	Joint Fit	Description
Planet Priors					
P_{orb} (days)	$\mathcal{N}^a(2.785, 0.1)$	$\mathcal{N}$(2.7858212,3e-6)	$\mathcal{N}$(2.7858212,3e-6)	$\mathcal{N}(2.785, 0.1)$	Orbital Period
T_c (BJD)	$\mathcal{N}(2455093.8, 0.1)$	$\mathcal{N}(2456798.7188, 0.0009)$	$\mathcal{N}(2456798.7188, 0.0009)$	$\mathcal{N}(2455093.8, 0.1)$	Transit Time
R_p ($R_\oplus$)	$\mathcal{U}^b(0.5, 2.0)$	-	-	$\mathcal{U}(0.5, 2.0)$	Radius
K (m s^{-1})	-	$\mathcal{U}(0.1, 10.0)$	$\mathcal{U}(0.1, 10.0)$	$\mathcal{U}(0.1, 10.0)$	RV Amplitude
Transit Priors					
b	$\mathcal{U}(0.5, 1.0)$	-	-	$\mathcal{U}(0.5, 1.0)$	Impact Parameter
$u_{1,Kepler}$	$\mathcal{N}(0.3451, 0.1)$	-	-	$\mathcal{U}(0.3451, 0.1)$	Limb Darkening
$u_{2,Kepler}$	$\mathcal{N}(0.216, 0.1)$	-	-	$\mathcal{U}(0.216, 0.1)$	Limb Darkening
$u_{1,TESS}$	$\mathcal{N}(0.3451, 0.1)$	-	-	$\mathcal{U}(0.3451, 0.1)$	Limb Darkening
$u_{2,TESS}$	$\mathcal{N}(0.216, 0.1)$	-	-	$\mathcal{U}(0.216, 0.1)$	Limb Darkening
Photometric Priors					
γ_{Kepler}	$\mathcal{U}(0.9, 1.1)$	-	-	$\mathcal{U}(0.9, 1.1)$	Mean Offset
γ_{TESS}	$\mathcal{U}(0.9, 1.1)$	-	-	$\mathcal{U}(0.9, 1.1)$	Mean Offset
σ_{Kepler}	$\mathcal{BLN}^c$(5e-5,1e-3,1e-5,7.4)	-	-	$\mathcal{BLN}$(5e-5,1e-3,1e-5,7.4)	Jitter
σ_{TESS}	$\mathcal{BLN}$(5e-5,1e-3,9e-5,7.4)	-	-	$\mathcal{BLN}$(5e-5,1e-3,9e-5,7.4)	Jitter
RV Priors					
γ_{HIRES}	-	$\mathcal{U}(-100, 100)$	$\mathcal{U}(-100, 100)$	$\mathcal{U}(-100, 100)$	Mean Offset
$\gamma_{HARPS-N}$	-	$\mathcal{U}(-100, 100)$	$\mathcal{U}(-100, 100)$	$\mathcal{U}(-100, 100)$	Mean Offset
γ_{NEID}	-	$\mathcal{U}(-100, 100)$	$\mathcal{U}(-100, 100)$	$\mathcal{U}(-100, 100)$	Mean Offset
σ_{HIRES}	-	$\mathcal{U}(0.1, 10)$	$\mathcal{U}(0.1, 10)$	$\mathcal{U}(0.1, 10)$	Jitter
$\sigma_{HARPS-N}$	-	$\mathcal{U}(0.1, 10)$	$\mathcal{U}(0.1, 10)$	$\mathcal{U}(0.1, 10)$	Jitter
σ_{NEID}	-	$\mathcal{U}(0.1, 10)$	$\mathcal{U}(0.1, 10)$	$\mathcal{U}(0.1, 10)$	Jitter
GP Priors					
$\eta_{\sigma,HIRES}$	-	$\mathcal{J}^d(0.1, 100)$	$\mathcal{J}(0.1, 10)$	-	GP Amplitude
$\eta_{\sigma,HARPS-N}$	-	$\mathcal{J}(0.1, 100)$	$\mathcal{J}(0.1, 10)$	-	GP Amplitude
$\eta_{\sigma,NEID}$	-	$\mathcal{J}(0.1, 100)$	$\mathcal{J}(0.1, 10)$	-	GP Amplitude
η_τ	-	$\mathcal{N}(17.5, 1.6)$	$\mathcal{N}(15.7, 1.3)$	-	Spot Decay Timescale
η_P	-	$\mathcal{N}(22.0, 0.1)$	$\mathcal{N}(15.8, 2.3)$	-	Periodic Term
η_l	-	$\mathcal{N}(0.09, 0.03)$	$\mathcal{N}(0.136, 0.045)$	-	Recurrence Timescale
$\sigma_{GP,Kepler}$	$\mathcal{LN}^e$(1e-5,7.4)	-	-	$\mathcal{LN}$(1e-5,7.4)	GP Standard Deviation
$\sigma_{GP,TESS}$	$\mathcal{LN}$(9e-5,7.4)	-	-	$\mathcal{LN}$(9e-5,7.4)	GP Standard Deviation
$\sigma_{GP,HIRES}$	$\mathcal{U}$(0.1,100)	-	-	$\mathcal{U}$(0.1,100)	GP Standard Deviation
$\sigma_{GP,HARPS-N}$	$\mathcal{U}$(0.1,100)	-	-	$\mathcal{U}$(0.1,100)	GP Standard Deviation
$\sigma_{GP,NEID}$	$\mathcal{U}$(0.1,100)	-	-	$\mathcal{U}$(0.1,100)	GP Standard Deviation
P_{rot}	$\mathcal{LU}^f$(1,200)	-	-	$\mathcal{LU}$(1,200)	GP Standard Deviation
Q0	$\mathcal{LU}$(0.002, 400)	-	-	$\mathcal{LU}$(0.002, 400)	Quality Factor
dQ	$\mathcal{LU}$(0.002, 400)	-	-	$\mathcal{LU}$(0.002, 400)	Difference Quality Factor
f	$\mathcal{U}$(0.1, 1.0)	-	-	$\mathcal{U}$(0.1, 1.0)	Fractional Amplitude

[a] $\mathcal{N}$ is a normal prior with $\mathcal{N}$(mean, standard deviation)

[b] $\mathcal{U}$ is a uniform prior with $\mathcal{U}$(lower,upper)

[c] $\mathcal{BLN}$ is a bounded log normal prior with $\mathcal{BLN}$(lower, upper, mean, standard deviation)

[d] $\mathcal{J}$ is a Jeffrey's prior with $\mathcal{J}$(lower,upper)

[e] $\mathcal{LN}$ is a log normal prior with $\mathcal{LN}$(mean, standard deviation)

[f] $\mathcal{LU}$ is a log uniform prior with $\mathcal{LU}$(lower,upper)

[–] indicates a free parameter that was not fit in that particular model.

5.4.3 Radial Velocity Modeling

We perform an RV-only analysis of Kepler-21, in addition to a joint RV + Photometry analysis in §5.4.4, for a number of reasons. First, we are interested in comparing the results of an RV fit when trained on Kepler or TESS data, in addition to joint fits **with** Kepler and TESS data. Joint fits are much more computationally expensive, so are they worth doing? Or can training on photometry first, and then fitting RV data give just as precise results? Does the precision or temporal proximity of the training photometry affect this? Most RV systems do not have the abundance of photometric data that Kepler-21 has, making joint fits of questionable value. Finally, many exoplanet systems do not transit, and it is not clear that a joint photometric fit is the right approach for such systems.

We utilize the `RadVel` software package to fit the RV data of Kepler-21. To account for stellar variability, we use the $\mathcal{K}_{J1}$ GP kernel described in §6.4.1.

`RadVel` models Kepler-21 b by solving Kepler's equation via a method outlined in [288]. The orbit of each planet in the model is modified by five Keplerian parameters: orbital period (P), time of inferior conjunction (T_c), eccentricity (e), argument of periastron (ω), and the RV semi-amplitude (K). Previous studies have found that Kepler-21 b has minimal eccentricity and generally fix this parameter at 0 (LM16, [56]). We do the same, as well as fix ω to zero.

Our model also includes a constant offset for each RV instrument, γ_{inst}, and a white noise jitter term for each instrument, σ_{inst}. This jitter term is added in quadrature with error bars when used in the likelihood computation. We also experiment with including linear and quadratic acceleration terms, as our long-baseline HIRES RVs are especially sensitive to these terms, and a preliminary analysis suggests that these may be necessary(§5.4.6). We run our RV fits to convergence using the same metrics in §6.4.1.

We run two RV-only fits, one trained on Kepler photometry, and one trained on TESS

photometry. This training changes the priors on the GP hyperparameters, but otherwise, the initial fit parameters are identical. We include a full list of priors in Table 5.3. The posterior estimates of our fits are detailed in Table 5.4, and our best RV-only fit is visible in Figure 5.4.

5.4.4 Joint Modeling

Finally, we attempt joint fits of the photometry and RVs. Such fits are the most computationally expensive option, though they can shed light where other methods do not [e.g. 38]. One particular advantage is the ability to fit an activity model to photometric data and RV data simultaneously. In our RV-only fits, we train the models on the photometry, and transfer this information as informative priors. A joint fit transfers more information, as an adjustment to a shared GP parameter can immediately respond to the likelihoods of the RVs and photometry together. Planetary parameters such as orbital period and time of inferior conjunction are more strongly constrained by photometry than RV data, so we expect no difference in result due to a joint fit of these parameters. However, some GP hyperparameters can be shared between the datasets, because we expect the frequency structure of photometric and RV variability to be related.

We use `exoplanet` to create an orbit model, and we use `starry` to generate light curves as described in our transit analysis. Due to the large quantity of data, we again utilize the dSHO kernel rather than the $\mathcal{K}_{J1}$. Planet orbital period, time of inferior conjunction, eccentricity, argument of periastron, and orbital inclination are shared between the RV and photometric datasets. Offset and jitter terms are included for each instrument (Kepler, TESS, HIRES, HARPS-N, NEID), as described in previous sections. Our joint fits are most similar to our transit fits in §5.4.2, mainly due to choice of GP kernel.

The primary new feature is the treatment of GP hyperparameters between the datasets. We

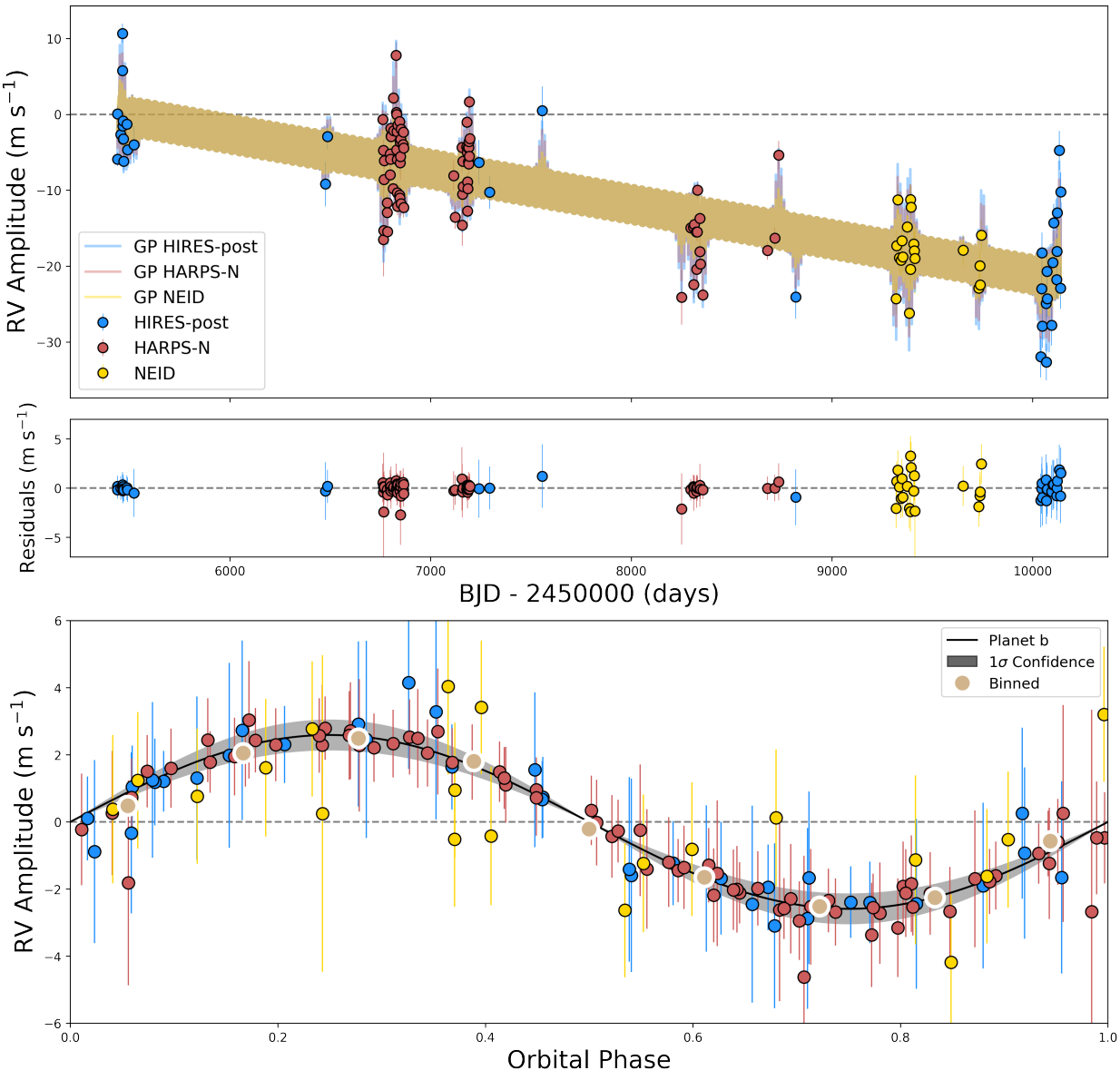

Figure 5.4: Top: RV time series of Kepler-21 spanning more than a decade. Light colors reflect the GP model used for each instrument. Middle: Residuals of a one planet, trend, and GP fit to the data. Bottom: phase folded RVs to planet b.

perform three different joint fits, which we call Kepler-RV, TESS-RV, and Kepler-TESS-RV. Each fit is performed on the same dataset utilizing all RVs and photometry. Each name emphasizes how GP hyperparameters are shared. The Kepler-RV joint fit is run such that the frequency hyperparameters of the Kepler GP are shared with the RV GP (P_{GP}, Q_0, dQ, f). We alternatively perform a TESS-RV joint fit where, again, all data are used, but the TESS GP hyperparameters (except amplitude) are shared with the RV GP. Finally, we perform a fit where all GP hyperparameters are shared between Kepler, TESS, and RV data, with the exception of an amplitude term for each.

We use an HMC MCMC algorithm with a NUTS sampler, as described in §5.4.2. Due to the efficiency of the HMC, we find that our runs converge after 2000 tuning and 2000 sampling steps executed in two independent chains. Our final fit posteriors are described in Table 5.5, and the priors of our joint fits are given in Table 5.3.

Table 5.4: RV Fit Posteriors

Parameter	RV Fit (Kepler Trained)	RV Fit (TESS Trained)
Orbital Parameters		
P_{orb} (days)	2.7858212±3e-6	2.7858212±3e-6
T_c (BJD)	2456798.7188±0.0008	2456798.7188±0.0009
$\sqrt{e}\cos\omega$	-	-
$\sqrt{e}\sin\omega$	-	-
K (m s^{-1})	2.54±0.57	2.55±0.47
$\dot{\gamma}$ (m s^{-1} d^{-1})	-0.0046±0.0005	-0.0046±0.0005
GP Hyperparameters		
$\eta_{\sigma,\mathrm{HIRES}}$ (m s^{-1})	4.8±1.8	5.6±1.4
$\eta_{\sigma,\mathrm{HARPS-N}}$ (m s^{-1})	4.0±0.7	4.0±0.5
Continued on next page		

Table 5.4: RV Fit Posteriors

Parameter	RV Fit (Kepler Trained)	RV Fit (TESS Trained)
$\eta_{\sigma,\mathrm{NEID}}$ (m s^{-1})	2.8±1.2	2.7±1.3
η_τ (days)	16.7±1.5	16.0±1.3
η_P (days)	22.03±0.11	13.5±0.5
η_l	0.091±0.003	0.19±0.03
Instrumental Parameters		
γ_HIRES (m s^{-1})	7.8±1.7	7.7±1.9
$\gamma_\mathrm{HARPS-N}$ (m s^{-1})	6.5±1.1	6.3±1.3
γ_NEID (m s^{-1})	20.8±2.2	20.6±2.4
σ_HIRES (m s^{-1})	3.7±2.1	2.2±2.1
$\sigma_\mathrm{HARPS-N}$ (m s^{-1})	1.4±1.3	1.3±0.81
σ_NEID (m s^{-1})	2.3±1.4	2.6±1.4

Table 5.5: Joint Fit Posteriors

Parameter	Joint Fit (Kepler-RV)	Joint Fit (TESS-RV)	Joint Fit (Kepler-TESS-RV)
Orbital Parameters			
$\mathrm{P_{orb}}$ (days)	2.785823±3e-6	2.785823±3e-6	2.785823±3e-6
$\mathrm{T_c}$ (BJD)	2455093.8364±0.0009	2455093.8364±0.0009	2455093.8365±0.0009
$\sqrt{e}\cos\omega$	-	-	-
$\sqrt{e}\sin\omega$	-	-	-
K (m s^{-1})	2.48±0.48	2.66±0.57	2.41±0.49
$\dot{\gamma}$ (m s^{-1} d^{-1})	-0.0049±0.0005	-0.0047±0.0005	-0.0046±0.0005
Transit Parameters			
$\mathrm{R_p}$ ($\mathrm{R_\oplus}$)	1.65±0.02	1.65±0.02	1.65±0.02
b	0.620±0.014	0.620±0.014	0.620±0.014
$\mathrm{u}_{1,Kepler}$	0.35±0.07	0.35±0.08	0.34±0.08
$\mathrm{u}_{2,Kepler}$	0.21±0.09	0.21±0.09	0.21±0.09

Continued on next page

Table 5.5: Joint Fit Posteriors

Parameter	Joint Fit (Kepler-RV)	Joint Fit (TESS-RV)	Joint Fit (Kepler-TESS-RV)
$u_{1,\mathrm{TESS}}$	0.36±0.10	0.36±0.10	0.36±0.10
$u_{2,\mathrm{TESS}}$	0.23±0.10	0.23±0.10	0.23±0.10
$\mathrm{dil}_{\mathrm{TESS}}$	0.80±0.18	0.80±0.18	0.75±0.15
Derived Parameters			
M_p ($M_\oplus$)	6.9±1.3	7.4±1.6	6.68±1.4
T_{14} (days)	0.144±0.002	0.1442±0.002	0.144±0.002
a (AU)	0.0434281±3e-8	0.0434281±3e-8	0.0434281±3e-8
i (degrees)	88.556±0.003	88.556±0.003	88.556±0.003
S ($S_\oplus$)	2752.356±0.004	2752.356±0.004	2752.356±0.004
T_{eq} (K)	2015.5472±0.0008	2015.5472±0.0008	2015.5473±0.0008
ρ (g/cc)	8.92±1.96	9.18±1.86	8.38±1.62
GP Hyperparameters			
$\sigma_{\mathrm{GP,Kepler}}$ (ppm)	151±5	127±3	145±4
$\sigma_{\mathrm{GP,TESS}}$ (ppm)	129±7	131±7	278±2
$\sigma_{\mathrm{GP,HIRES}}$ (m s^{-1})	6.33±1.0	6.0±0.9	7.5±1.3
$\sigma_{\mathrm{GP,HARPS-N}}$ (m s^{-1})	4.2±0.5	4.1±0.5	4.9±0.7
$\sigma_{\mathrm{GP,NEID}}$ (m s^{-1})	3.3±1.2	3.4±1.2	3.3±1.6
$\log Q0_{\mathrm{Kepler}}$	-4.8±0.21	-4.73±0.14	-2.31±0.07
$\log Q0_{\mathrm{TESS}}$	-5.3±0.4	-5.6±0.3	-2.31±0.07
$\log dQ_{\mathrm{Kepler}}$	-1.1±0.1	-1.1±0.3	3.35±0.30
$\log dQ_{\mathrm{TESS}}$	-1.1±0.7	-1.6±0.6	3.35±0.30
$P_{\mathrm{rot,Kepler}}$ (days)	5.8±0.2	5.77±0.22	12.53±0.14
$P_{\mathrm{rot,TESS}}$ (days)	3.5±0.5	4.01±0.61	12.53±0.14
f_{Kepler}	0.016±0.002	0.015±0.002	0.94±0.05
f_{TESS}	0.32±0.7	0.30±0.06	0.94±0.05
Instrumental Parameters			
Photometric			
γ_{Kepler} (ppm)	1e6±4	1e6±4	1e6±4
γ_{TESS} (ppm)	1e6±10	1e6±12	1e6±24
σ_{Kepler} (ppm)	119.256±0.007	50.003±0.003	50.000±0.003
σ_{TESS} (ppm)	82±2	83±2	95±2
RV			
γ_{HIRES} (m s^{-1})	-3.2±1.2	-3.2±1.1	-3.13±1.2
$\gamma_{\mathrm{HARPS-N}}$ (m s^{-1})	-4.7±0.7	-4.6±0.6	-4.6±0.7
γ_{NEID} (m s^{-1})	9.9±1.3	9.8±1.2	9.7±1.2
σ_{HIRES} (m s^{-1})	5.0±2.9	5.0±2.9	5.7±2.9
$\sigma_{\mathrm{HARPS-N}}$ (m s^{-1})	3.6±2.4	4.1±2.8	3.8±2.6

Continued on next page

Table 5.5: Joint Fit Posteriors

Parameter	Joint Fit (Kepler-RV)	Joint Fit (TESS-RV)	Joint Fit (Kepler-TESS-RV)
$\sigma_{\rm NEID}$ (m s^{-1})	4.9±2.9	5.5±2.9	5.1±2.5

5.4.5 Injection Recovery Analysis

We perform injection-recovery tests to explore the value of photometric training datasets. Kepler photometry is more precise than TESS, and its longer baseline provides many advantages. It is also temporally separated from newer RV data by more than ten years. This is particularly concerning given that stellar variability is known to evolve on much shorter time scales [147, 146]. We can begin to evaluate the training datasets by noting which produced the most precise orbital parameters in the previous section, though comparing recovered mass precisions is not necessarily the best way to determine the best activity mitigation method. In particular, such a method could not be expanded to systems with no known planets, despite interest in knowing which photometric dataset would be best for *searching* for planets in such systems.

We follow a method similar to [74] by injecting circular planet signals into the data at a variety of orbital periods and RV amplitudes. We choose ten RV amplitude bins ranging between 0 to 10 m s^{-1}, uniformly spaced. For orbital periods, we create ten bins between 1 and 1000 days with log-uniform spacing. We then inject signals randomly drawn from within these two dimensional bins into our data, and fit both a one- and two-planet model. Targets are also injected with a random time of periastron, drawn from a distribution with a width equal to the injected period. Especially for longer period planets, this is an important step to take to simulate the effects of favorable or unfavorable phase coverage. This process is executed with models trained on Kepler and TESS, as well as on "untrained" datasets

where broad, uninformative GP hyperparameter priors are used. Each fake signal is added to the existing Kepler-21 RV data to create a fake dataset, and we do this 100 times in each period-K bin.

We use the Bayes Factor [BF; 209] for model comparison to determine if an injected planet is recovered successfully. The BF is produced by taking the ratio of the evidence of two competing models, with a value > 1 indicating preference for the numerator. Typically, we require that a more complicated model be substantially better than a simpler model to warrant adoption. This threshold is not important during our injection-recovery tests where we are interested only in comparing which training method recovers a higher BF, though in §5.4.6 we do require a $\log_{10}(\mathrm{BF}) > 5$ to prefer a more complicated model, which is a commonly adopted threshold [i.e. 376, 258, 40].

Continuing to follow [74], we explore two different cases of injected planet. First, we explore the case of a "transiting" injected planet, where the orbital period of the injected planet is known, and we fix it to the correct, injected value. Second, we explore the "RV detected" injected planet, where the period and time of inferior conjunction of the injected planet is not known a priori. The results of these two tests are visible in Figures 5.5 and 5.6.

We generate our injected signals using the `RadVel` software package. Because of the large number of RV fits required for our analysis, we make a few simplifying assumptions during injection-recovery. In contrast to the RV fits in §5.4.3, we fix the orbital period and time of conjunction of Kepler-21 b. We only inject circular planets, and always fix our model eccentricity at zero. An exploration of how our results are sensitive to eccentricity would be interesting, but is beyond the scope of our work. We use the injected orbital periods and RV semi-amplitudes as starting guesses for all of our two planet models. In the case of "RV detected" planets, we place generally broad priors on the orbital period and time of inferior conjunction of the second planet. The orbital period has a Gaussian prior centered at P_{inj} with a standard deviation of $\mathrm{P}_{inj}/2$. The time of inferior conjunction has a uniform prior

centered at the injected value with a width of the injected period.

With a 10×10 grid of bins, and 100 signals injected in each bin, we perform 10,000 signal injections for the Kepler-trained models and TESS-trained models respectively, as well as an untrained RV fit. Since we are fitting both a one and two planet model to each injected signal, we perform two RV fits per signal, resulting in 20,000 RV fits for Kepler-trained, TESS-trained, and untrained models, or 60,000 total. Performing these analyses on the "transiting" and "RV-detected" cases brings our final number of RV fits to 120,000.

Performing an MCMC or nested sampling fit to each model would be prohibitively expensive in terms of CPU-hours, and so we approximate the evidence of each model using the Laplace approximation, given in equation 5.5 [291]. The Laplace approximation allows us to estimate the evidence of each model fit, rather than integrating it numerically. The evidence is defined in equation 5.4, [209].

$$\mathcal{E} = \int \mathcal{L}(d,\theta)\pi(d,\theta)d\theta \tag{5.4}$$

Here, $\mathcal{E}$ is the evidence of a model, $\mathcal{L}(\theta)$ is the likelihood of the model with data d and parameters θ. $\pi(\theta)$ is the prior probability of the parameters. This integral is typically intractable to calculate, and the Laplace approximation circumnavigates this computation. It is convenient to rewrite the right term $\mathcal{L}$ as an exponentiated logarithm, $\exp(\log(\mathcal{L}(d,\theta)\pi(\theta)))$. Then we can say that it is equal to

$$\left[\frac{(2\pi)^2}{|\det(H(d,\theta_0)|}\right]^{1/2} \exp(\log(\mathcal{L}(d,\theta_0)\pi(\theta_0))) \tag{5.5}$$

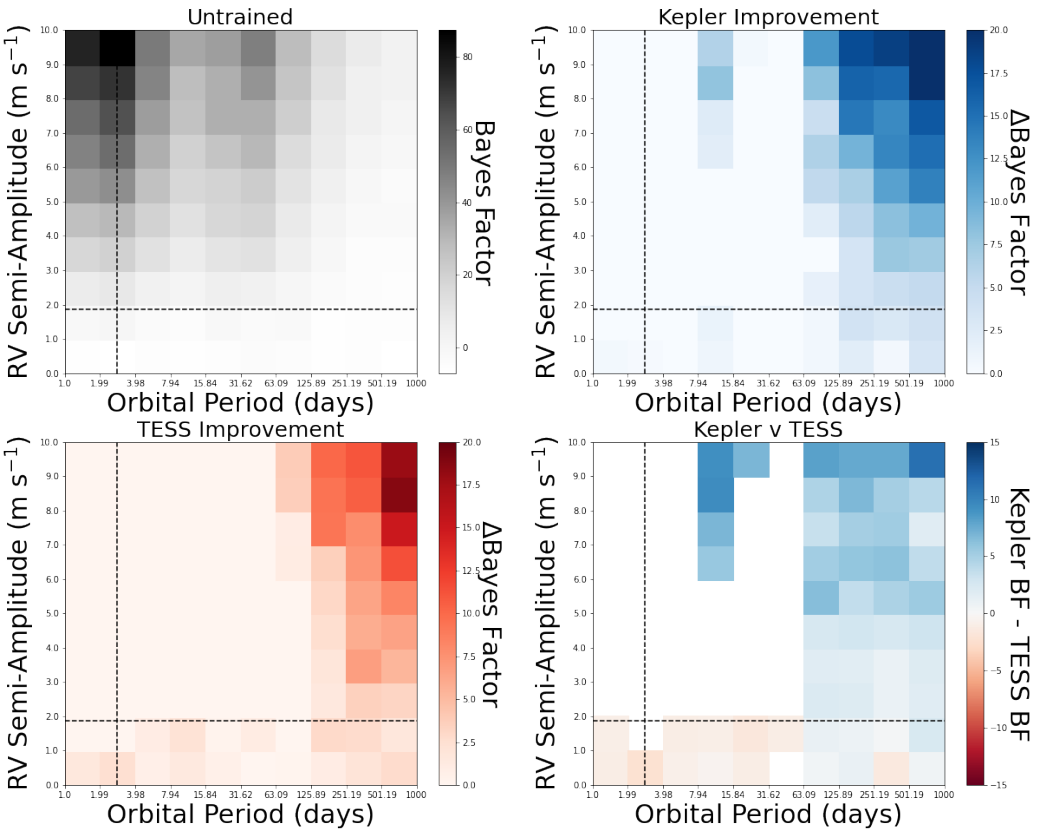

Figure 5.5: Injection recovery results for fits with an injected "transiting" planet. The amplitude and period of the known planet are denoted by a black dashed line. Top Left: Injection recovery tests run with no GP training. Top Right: differential preference for recovering the injected planets between Kepler and untrained fits. Bottom Left: differential preference for recovering the injected planets between TESS and untrained fits. Bottom Right: differential BF improvements between the training methods. Longer orbital periods are consistently recovered more robustly when training on Kepler.

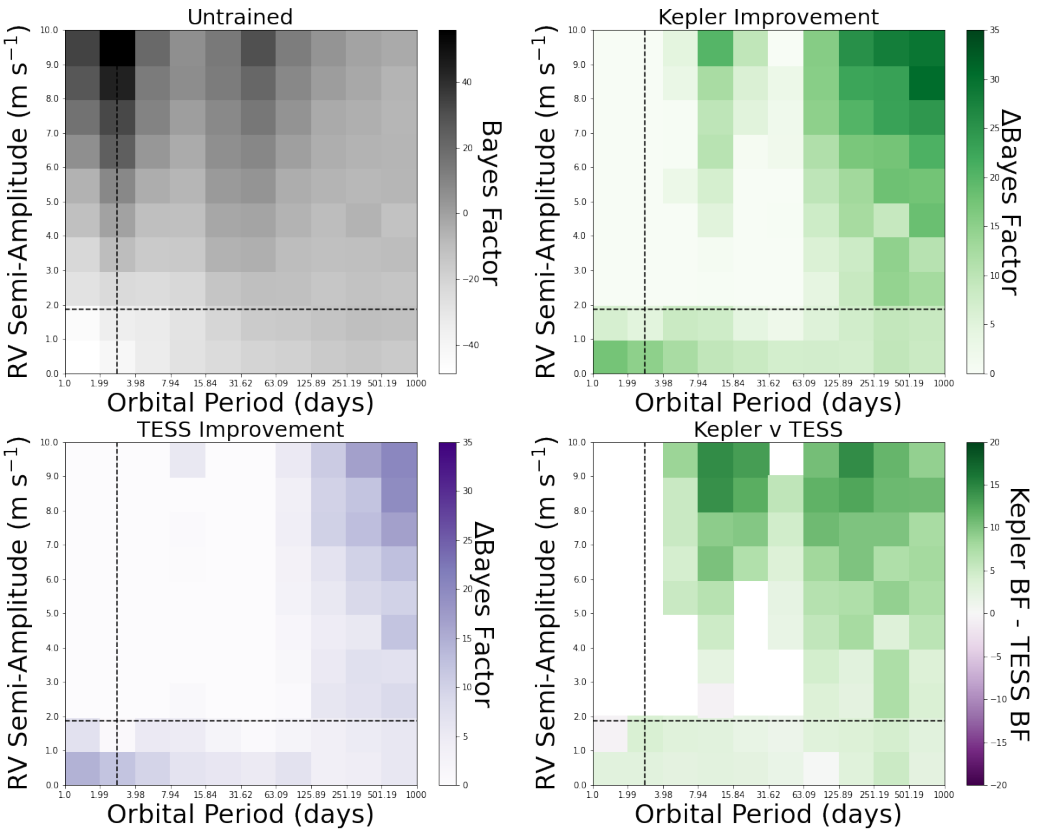

Figure 5.6: Injection recovery results for fits with an injected "RV-detected" planet. The amplitude and period of the known planet are denoted by a black dashed line. Top Left: Injection recovery tests run with no GP training. Top Right: differential preference for recovering the injected planets between Kepler and untrained fits. Bottom Left: differential preference for recovering the injected planets between TESS and untrained fits. Bottom Right: differential BF improvements between the training methods. The vast majority of injected planets were recovered more strongly when training on Kepler.

where H is the Hessian matrix of the function $\log(\mathcal{L}(d,\theta)\pi(\theta))$, and θ_0 is a set of parameters that produce a local maximum. This approximation is generally true for a function where the dominant mode is well separated from the integration domain, which is true for our analysis. We first optimize our initial values using a least squares fit in `scipy.optimize.minimize`, and then we estimate the evidence at this point. We take the average ΔBF in each bin and report them in Figures 5.5 and 5.6.

5.4.6 Additional Bodies in the System?

The Kepler spacecraft observed Kepler-21 for more than four years, and only identified transits of Kepler-21 b. It is not feasible that TESS would observe two or more planetary transits that Kepler missed, but it is possible that a single, long-period planet transits in TESS, but not Kepler. We use the Transit Least Squares [TLS; 178] Python package to search for additional transits in Kepler-21. Due to the correlated noise present in the photometry, we applied a UnivariateSpline to the Kepler and TESS photometry to remove the noise while minimally affecting the transits [103]. After recovering and masking the transits of Kepler-21 b, we run the TLS algorithm on the collective photometry, but we detect no significant additional transit events. We conclude that there are no additional observed transiting planets in Kepler-21 up to the limits of our photometric sensitivity.

Our analysis adds to the already significant ($\sim$ 10 years) RV baseline of the system, extending our sensitivity to longer period, non-transiting planets. The observing baseline of HIRES allows us to constrain the RV offsets present in other instruments. The data seem strongly suggestive of either a trend or curvature, and we perform a series of RV fits to determine which explanation is best. In Table 5.6, we compare a variety of models exploring no trend, a linear trend, a fit with a linear and quadratic term, and a two planet model. We use the Bayesian Information Criterion [BIC; 209, 235] to approximate the BF between our

models. Although a TESS-trained linear + quadratic model has the lowest BIC value, it is not low enough to justify adopting the more complicated model. The linear trend fits are significantly better than the no-trend cases, however, and so we adopt a linear trend. Our best fits recover a $\dot{\gamma}$ value of -0.0046±0.0005 m s^{-1} day^{-1}, which is 9.2σ significant. This could be caused by a long period activity cycle, though analysis of the HIRES S_{HK} values reveals no such corresponding trend. We conclude that this trend is suggestive of either an additional, long-period planet, or perhaps a substellar companion.

To identify the source of the linear RV trend, we searched the Gaia database for possible bound stellar companions. Gaia reports Kepler-21 to have a renormalized unit weight error [RUWE; 240] consistent with unity, a strong indicator that Kepler-21 is not an unresolved stellar multiple. We do not find any co-moving stars with similar parallaxes in Gaia [259], suggesting that the cause of this apparent RV slope is the result of a substellar object.

A combination of RVs and Gaia astrometry [141] can be used to constrain the parameters of long period companions [e.g., 253, 109, 352]. Since we only observe a linear drift in RVs, formal statistical analyses like MCMCs cannot reliably converge on a two-planet fit, and would produce poorly constrained posteriors. In order to make a reasonable estimate for the parameter space in which an outer companion could exist, we implement a model based on rejection sampling [52] that considers many randomly sampled trial orbits and accepts those that pass our acceptance criteria. We also use the same acceptance criteria, which accepts a trial if the likelihood, estimated as $0.5*\exp(-\chi^2/2)$ is higher than a random number between 0 and 1. We stop our sampling once 1000 trial orbits have been accepted. In addition to our residual RV slope, our rejection sampling imposes an agreement between a trial orbit's induced astrometric signal and the calibrated absolute astrometry from the Hipparcos-Gaia Catalog of Accelerations [HGCA; 61, 62]. The low astrometric signature of Kepler-21 rules out most high mass objects, and we can constrain mass and period modestly well. We perform fits where the companion has a fixed 90 degree inclination, and where its inclination

is allowed to float. We show a plot of our rejection sampling in Figure 5.7. We estimate a mass of $3.7^{+2.5}_{-1.3}$ M_J and an orbital period of $70.0^{+52.7}_{-26.4}$ yr in the first case, and a mass of $4.0^{+2.4}_{-1.3}$ M_J and period $62.7^{+49.6}_{-21.8}$ yr in the latter case. In both cases, more than 97% of our samples are less than 10 M_J, which justifies designating the object imposing the long-term RV trend on Kepler-21 a candidate super-Jupiter planet, Kepler-21 (c).

Table 5.6: RV Model Comparisons

Fit	Kepler-Train BIC	TESS-Train BIC
No Trend	953.27	899.82
Linear Trend	**890.06**	**878.89**
Linear + Quadratic Trend	906.12	875.95
Two Planet Model	906.49	895.98

5.5 Discussion

Our investigation and analysis of Kepler-21 had two goals: an updated, more precise description of the Kepler-21 system, and an investigation into the use of photometry to mitigate stellar variability in RVs.

5.5.1 Adopted Fit

We focus on one set of posteriors when discussing the Kepler-21 planetary system. Two fits, TESS-trained RV and Joint Kepler-TESS-RV, stand out as the most successful at

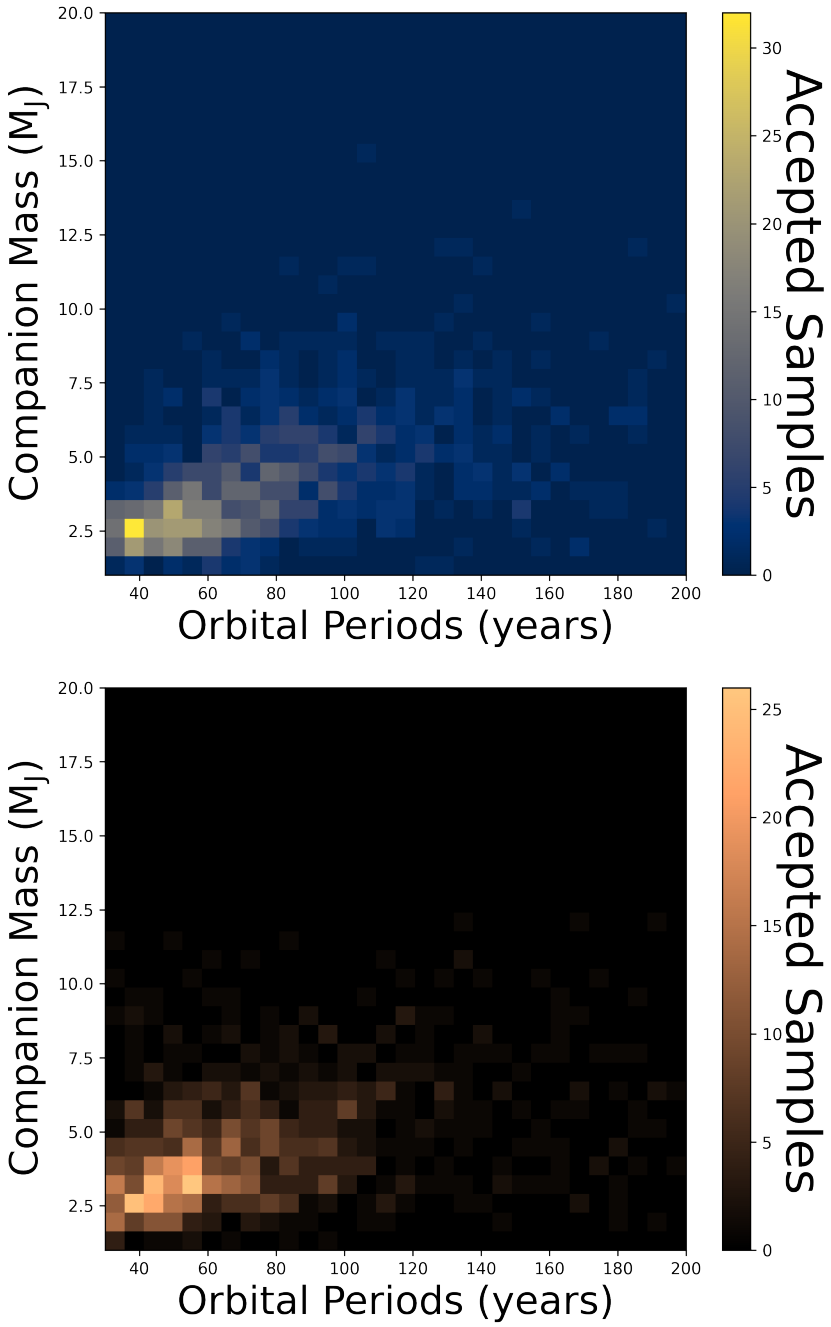

Figure 5.7: Top: rejection sampling for a variety of masses and orbital periods of the long period companion, where inclination is fixed at 90 degrees. Bottom: same as above, but with inclination allowed to vary. Due to the lack of sizable astrometric signatures in Gaia data, we can rule out many long period and high mass objects.

constraining the mass of Kepler-21 b. We choose the latter as our "adopted fit," as it is more complete than the former, utilizing more data and returning a larger set of posteriors. It also more correctly identifies the rotation period of the system. Consequently, our plots in Figure 5.4 and 5.8 utilize this set of posterior values.

5.5.2 Refining Fits for Kepler-21 b

The photometry of Kepler-21 was first analyzed in [186], and a joint photometry-RV fit was performed in LM16. Despite a large number of RVs, stellar variability made precise recovery of the planet mass challenging. The final mass recovered in LM16 using a joint HIRES + HARPS-N RV fit was 5.08 $\pm$ 1.72 $M_{\oplus}$, which is slightly less than 3σ significant, often considered the minimum for a "significant" detection. One of our goals was to raise this to a higher significance threshold, and to better understand where Kepler-21 b falls in parameter space. [56] recently improved the mass measurement of Kepler-21 b to $> 5\sigma$ in a survey focused on Kepler systems.

Our fits utilize additional HIRES RVs and NEID data. While we cannot claim an improved mass precision, we do characterize the system with the most detail to date, and we provide significantly improved constraints on the additional companion described in §5.4.6. Our full fit posteriors are available in Tables 5.4 and 5.5.

As explained in §5.4.2, including TESS photometry did not improve the measured orbital parameters, in particular the orbital period and time of inferior conjunction. The design of Kepler already allowed for pristine recovery of both values, with errors reported in LM16 of 0.24 seconds and 71 seconds, respectively. Our orbital period precision is identical to that in LM16, and the uncertainty in our measured transit time is actually worse. Why might this be? We first ran our exact same model, but with Kepler only, to see if adding TESS indeed improved our recovered parameters. When not utilizing TESS, our orbital period and

transit time measurements are actually less precise than in LM16, despite using the same photometric dataset. We conclude that adding TESS does indeed improve precision on both posterior values, and that something about our model or parameter estimation is performing worse than in LM16.

One explanation is our treatment of stellar variability. LM16 utilized the data validation (DV) lightcurve produced by the Kepler DV pipeline in their analysis. This lightcurve sees aggressive detrending for any periodic signals longer than the transit duration [197, 400]. The result is a pristine lightcurve, but stellar astrophysics cannot be extracted. We utilize a newer version of this reduction that does not remove long period variability, and we use a GP model to remove the residual, non-transit signals. Our motivation is to extract information about the stellar variability in the RVs from the photometry, and so we require the preservation of longer period signals. As a result, our model fits see a simultaneous GP + transit fit, which increases the uncertainty in the exact transit time.

With a newly measured planetary mass, we can rule out Kepler-21 b as a "water world." (Figure 5.8). Its mass (6.68±1.4 $M_\oplus$) and radius (1.65±0.02 $R_\oplus$) place it on the upper edge of "water world" candidates, which [257] denote as a regime of planet mass between 3 and 6 $M_\oplus$ and 1.5 - 2.0 $R_\oplus$. Kepler-21 b might have formed beyond the ice line and migrated inwards throughout its lifetime, retaining water and falling into this regime [406, 257]. Such planets retain an atmosphere composed partially of gaseous water, and can even retain water in their core. [3] model theoretical compositions for highly irradiated water worlds, and we plot selected curves in Figure 5.8. Kepler-21 b is too massive for it to contain any significant quantity of water in its atmosphere or in its core. Most likely, the evolution of its host star stripped the atmosphere of the planet, leaving it a bare rock.

Atmospheric observations might provide an independent verification that the system lacks appreciable quantities of water, though Kepler-21 b is not a strong candidate for JWST. We estimate a transmission spectroscopy metric [TSM; 214] of 16.4 for Kepler-21. The TSM is

a simple, first order approximation for amenability to JWST atmospheric observation. In its radius regime, [214] suggest at least a TSM of 92 to justify study, making Kepler-21 b far from ideal. The biggest contributor to Kepler-21 b's low TSM is the large radius of its evolved F type host star, which makes any atmospheric signal small.

5.5.3 RVs Trained with Photometry

Our second goal was to investigate the effectiveness of mitigating stellar variability in RVs using different photometric datasets. This exploration of Kepler-21 is a precursor and test case for a wider analysis of Kepler/K2/TESS targets that saw simultaneous NEID RV observations.

A few of the questions we are interested in exploring are 1) How long are lightcurves useful for dealing with astrophysical RV noise? Are Kepler lightcurves still valuable? By extension, will TESS lightcurves be useful years from now? 2) Does the simultaneity of our NEID data mitigate the limitations of TESS baseline and precision? 3) Do joint Kepler-TESS models improve mass precision, or do the differences in sampling, age, and reduction make the noise models too different?

The broader analysis mentioned above will eventually shed more light on all of these questions, though with Kepler-21 we explore a single case deeply.

First, our analysis indicates that Kepler lightcurves are still useful. Joint fits with Kepler GP parameters sharing information with RV GP parameters typically recover the most precise mass for planet b. In the RV-only fits, training on Kepler photometry is noticeably worse than training on TESS, though as we discuss in §6.4.1, this is probably due to the Kepler training adhering to the wrong rotation period. As seen in Figures 5.5 and 5.6, Kepler training helps recover additional planets broadly across RV amplitude and orbital period

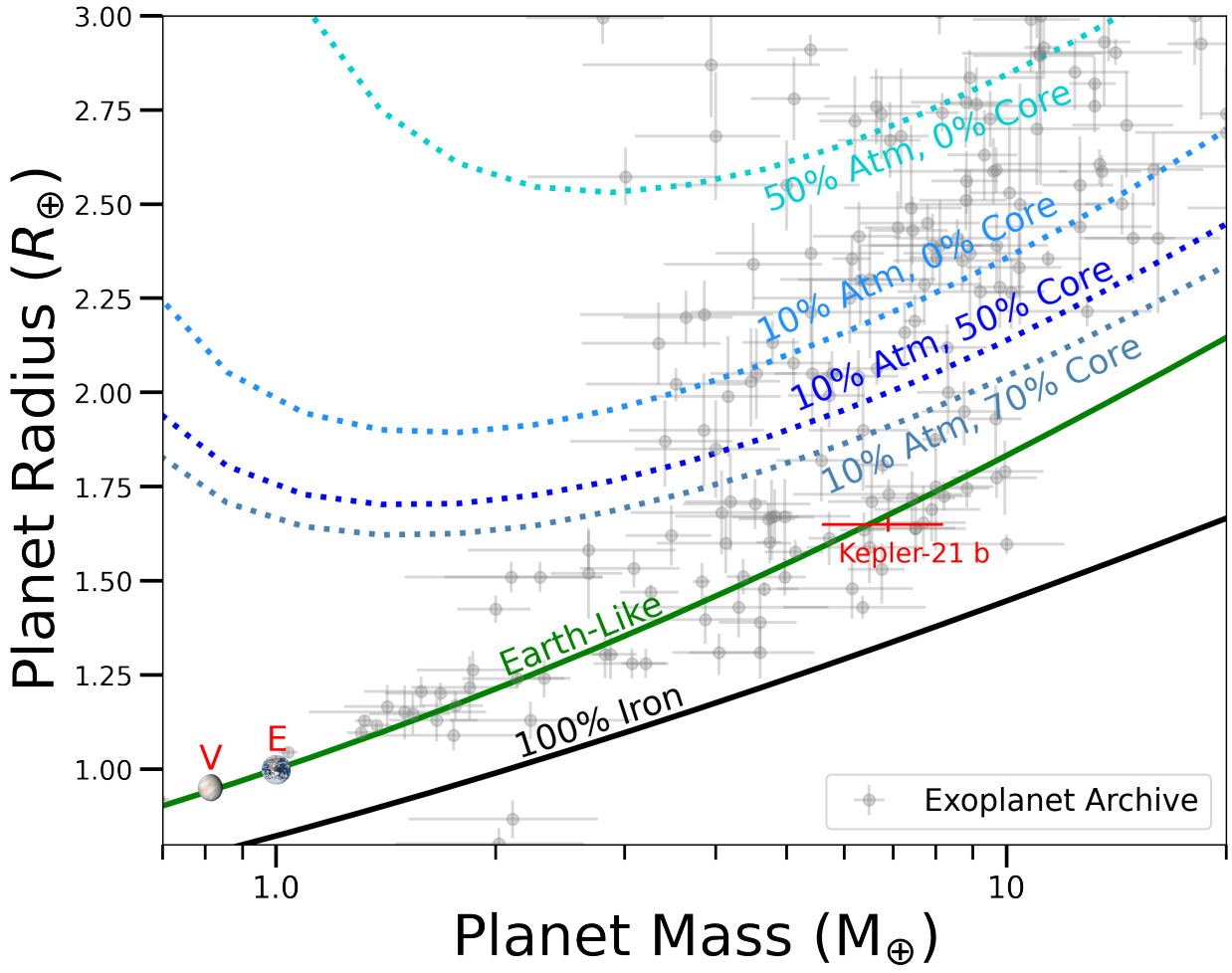

Figure 5.8: Correlation between mass and radius of known exoplanets with a measured mass and radius, taken from the `NASA Exoplanet Archive` on 12 August 2023. We only use planets with precisely measured masses ($M_p/\sigma > 3$). We add our new mass and radius measurements for Kepler-21 b in red. We additionally add theoretical planet compositions. Earth and iron compositions are taken from [406], and we extract irradiated water compositions from [3]. We use "Atm" to indicate the percentage of water in the atmosphere, and "Core" to indicate the percentage in the planet core. Kepler-21 b's placement in the radius valley made it a candidate "Water World," though it seems such scenarios can likely be ruled out.

space.

Despite being over ten years old, Kepler photometry is highly precise, and huge in quantity. This trumps the more recent TESS data, at least for this system. This may not be true for every system, however. We did not achieve as many simultaneous NEID RVs as would have been ideal, and unlike many Kepler systems, Kepler-21 has precise RVs simultaneous with Kepler. Due to the higher rotational velocity of Kepler-21, NEID is not seeing higher precision than older RVs, such as HARPS-N or HIRES. We can also conclude that TESS photometry may still be useful ten or more years in the future, though TESS's specific usefulness will likely depend on the existence of other photometric datasets [e.g. PLATO; 315] at the time.

Second, does the simultaneity of NEID with TESS mitigate some of the downsides of TESS photometry? PDCSAP photometry removes longer period signals, especially those on the order of half a 27-day TESS cycle. With a rotation period of 12.6 days, Kepler-21 is near the upper limit of what might be possible to find in TESS PDCSAP. This obviously makes TESS less useful for constraining stellar variability in RVs, since longer period signals in RVs still remain. However, unlike older Kepler photometry, TESS photometry can give us information about spot complexes as the RV data are taken, which might be advantageous. Indeed the RV fits trained on TESS photometry were typically more precise than those trained on Kepler, though this may be the result of the erroneous period detection mentioned in §6.4.1. Nonetheless, we can say that training on TESS certainly can be effective, though training on both jointly has its advantages.

Third, should we use a joint Kepler-TESS model when informing RVs? We examine our model that performs such a fit, and how it compares to alternatives. In particular, we ask the question: should we train an activity model on photometry, and then perform an RV-only fit? Or is there an advantage to performing these steps simultaneously? We use the recovered RV semi-amplitude as our primary comparison point, because we are most

interested in which method best removes stellar activity contamination in the RVs. This activity contamination has the most pressing effect on the recovery of this observable.

Comparing the most precise mass measurements in each case, our TESS-trained RV fit has a semi-amplitude of 2.59±0.46 m s^{-1}, while joint Kepler-TESS-RV fits have an amplitude of 2.49±0.47 m s^{-1}. The former fit has a strictly higher precision, though the two results are extremely close. The methods recover the RV amplitude indistinguishably well. However, joint fits are generally more computationally costly, and so this may be seen as an endorsement of RV fits trained on photometry. On the other hand, the joint fits recover the true rotation period of the system, and this may be seen as an endorsement of that method.

5.5.4 Kepler-21 (c)?

If it is a planet, Kepler-21 (c) would have the longest known orbital period of any planet with a known transiting planet companion. We estimate the orbital separation of Kepler-21 (c) in the more general non-fixed-inclination case as 17.7±1.6 AU. Kepler-21 is 108.5±0.4 pc [22, 141] from Earth, giving Kepler-21 (c) an angular separation of 160 mas. Other giant planets have been imaged at this separation [PDS 70 b; 175.8 mas 390], though the age of Kepler-21 makes that prospect more challenging. Unlike most planets imaged today, Kepler-21 (c) has likely lost most of its heat of formation, and would likely need to be imaged using reflected light from its host star. We calculate the contrast Kepler-21 (c) would likely exhibit with respect to its host star using equation 5.6 [234].

$$\epsilon = A * \frac{1}{\pi} * \frac{R_p^2}{a^2} \tag{5.6}$$

Above, A is the albedo of the planet, a its semi-major axis, and R_p its radius. We use the

mass-radius relationship in [80] to estimate a planet radius for Kepler-21 (c) of $1.16^{+0.24}_{-0.20}$ R_J. Using the calculated semi-major axis of 17.7±1.6 AU, we estimate a contrast of 3.1e-11±1.6e-11 using an albedo of 0.1. In the highly reflective case of albedo=1, this only increases the contrast by one order of magnitude, 3.1e-10±1.6e-10. This is below the expected atmospheric contrast limit for even extremely large telescopes [1e-8; 354], and Kepler-21 (c) will not likely ever be imaged from the ground, though the proposed Habitable Worlds Observatory (HWO) has a targeted contrast limit of 1e-10 [290, 168], making the high-albedo case potentially observable.

While both transmission spectroscopy of the inner planet, and direct imaging spectroscopy of the outer candidate are at the edge of even future detection limits, it is possible that both observations might be taken someday. An intra-system comparison of the atmospheric compositions of the two bodies could reveal a great deal about the formation and evolution of the system, and would be highly valuable.

5.6 Summary

We revisit the Kepler-21 system and perform an in-depth analysis of the best methods to mitigate stellar activity with photometry. We compare the results of RV fits trained on Kepler and TESS data, as well as a variety of joint fits. We also perform an injection recovery test to determine if Kepler or TESS photometry is better at disentangling injected planet signals from stellar activity. Our results show that training activity models on Kepler benefits in the discovery of new planets, though our TESS-trained models recover a more precise mass for Kepler-21 b. We further confirm the nature of Kepler-21 b as a rocky, terrestrial planet in the radius valley, and we strongly identify a long-period companion in the system.

Chapter 6

Utilizing Photometry to Mitigate Stellar Variability in RVs: A Wider Look

6.1 Foreword

Radial velocity (RV) analysis of stars is one of the oldest [272] and most successful [229, 317, 326] methods for discovering and characterizing exoplanets. RV observations additionally provide an excellent means of validating transiting exoplanets [e.g. 309, 39, 40], providing mass measurements [173, 249, 314], and probing regions of parameter space that transit observations rarely can [i.e. long-period, distant planets 253]. Measuring exoplanet masses is especially relevant in the era of the James Webb Space Telescope [JWST; 143], as a precise mass measurement is necessary to interpret atmospheric transmission spectra [30]. Further, the discovery of exoplanets around the nearest stars is an essential precursor to a future Habitable Worlds Observatory [HWO; 290, 264] mission to image Habitable Zone [HZ;

210, 220] planets around the nearest stars, and the vast majority such planets are unlikely to transit [170]. To maximize the efficiency of future missions such as HWO, a curated list of known, nearby planets is required, and RV detection remains our only plausible method for discovering such nearby, imagable exoplanets.

RV exoplanet science faces serious challenges, however, especially in the era of extreme precision RV (EPRV) observations [399]. As we push instrument stability below the historical 1 m s^{-1} noise floor, a variety of physical processes in stellar atmospheres contaminate our RV data at amplitudes larger than the instrumental precision, making it difficult to identify low-amplitude exoplanets [e.g. 249, 51, 38]. This contamination can vary widely in amplitude and frequency. Cool spots or hot plage on the surfaces of stars can quasi-periodically deform stellar spectra, producing undesired red or blue shifts in our spectra that do not originate from gravitational reflex, having effects up to 1000+ m s^{-1} [327, 280]. Granulation and stellar p-mode oscillations are another class of contamination that can have effects up to 10 m s^{-1} [77].

A variety of methods exist for modeling out or otherwise accounting for stellar contamination of RV data, varying in complexity and effectiveness. Adding a "jitter" term in quadrature with RV uncertainties is perhaps the simplest method, though ineffective in cases where noise is correlated and large in amplitude. Another common technique is decorrelating RVs to some stellar activity indicator, metrics extracted from spectra to track the activity of the host star [321, 228]. Unfortunately, the correlation between RV activity contamination and activity indicators is not always well-governed by a simple relationship [i.e. time delays between the datasets 66]. Further, many analyses today utilize data from multiple instruments, and it is common that different instruments do not track the same activity indicators. Gaussian Process [GP; 10] regression is one of the most common and effective ways to remove the effects of stellar magnetic activity from RV data [173, 249, 38], though how exactly to utilize it is not always clear. GPs are flexible and non-physical, and imposing bounds on their flexibility

can be extremely helpful for separating quasi-periodic stellar variability from true exoplanet signals. GPs can be trained on stellar activity indicators, or fit with them simultaneously [312, 314]. Utilizing photometry is another popular method for removing stellar variability from RV data [5, 160, 375], especially if taken contemporaneously. Photometric data, unlike spectroscopic stellar activity indicators, are often much higher in cadence and precision, allowing for a better characterization of the current stellar astrophysics. Additionally, large photometric datasets exist for many systems, and photometry can often be acquired for thousands of targets simultaneously. Astronomers generally agree that simultaneous photometry is a powerful tool when mitigating stellar variability in RVs, but how powerful? Multiple photometric datasets exist, with different precisions and observing baselines. Are there clear reasons to use one over another, or is utilizing all available photometry the best course?

In this work we seek to study the effectiveness of photometric datasets when used to correct for stellar variability in RVs. We also wish to understand the importance of simultaneous, or near-simultaneous photometry and RV data. Doing so will require answering several key questions. Firstly, which stellar properties are constrained by which lightcurves? TESS's 27-day baseline for most stars suggests that TESS might be superior for constraining shorter-lived activity, while Kepler's long baseline makes it ideal for longer activity cycles.

Secondly, which lightcurves should be used to correct for stellar activity? RV noise may be suppressed using a joint model to data from Kepler, TESS, or both. Most likely, this will depend upon the temporal proximity of RVs and photometry.

Finally, how well can photometry remove stellar activity contamination from RVs. Newer instruments such as NEID are capable of achieving RV precision better than 30 cm s^{-1} [336] for bright targets, allowing us to constrain photometric variability and Doppler jitter more precisely than was possible for Kepler systems. The most complete analysis relating Kepler photometric variability to RV jitter was conducted using Keck/HIRES, which has an

instrumental noise floor of 2-3 m s^{-1} [29].

To gain insights into these questions, we chose a variety of bright targets with either Kepler or K2 photometry, and we observed them with NEID and TESS simultaneously. We detail our selection criteria, targets, and their stellar parameters in §6.2, the data we use in §6.3, our primary analysis in §6.4, and we discuss the results in §6.5.

6.2 Target Selection

Over the course of this study, we chose targets with particular features. Targets were chosen for the express purpose of studying photometry's ability to mitigate stellar variability in RVs. Two criteria were mandatory: first, we chose targets that had existing Kepler or K2 photometry. Comparing the value of TESS training versus older Kepler/K2 training forms a core part of this analysis, and could not be done without such archival data. Second, we were interested in achieving simultaneous NEID observations during TESS observations. Consequently, when choosing targets for a NEID observing semester, we required that they be observed by TESS at a time that NEID, too, could observe them.

We then chose a number of other optional, but desirable, features. We wanted bright targets to minimize the amount of telescope time required to observe our targets at high precision. We imposed a general magnitude cut of $V < 10$. We also chose targets that had archival HIRES, HARPS, or HARPS-N RVs. This allowed us to 1) confirm that these targets were amenable to precise RV observations, and 2) approximate to first order the level of activity contamination that would likely exist in the RV data.

We mainly restricted our observations to main sequence FGK stars, for a number of reasons. Firstly, these were the most abundant stars observed during the Kepler mission. Secondly, more evolved stars begin to see non-spot dominated forms of stellar activity emerge as

highly significant, such as p-mode oscillations and granulation. These generally reduce our RV precision and interfere with our analysis, which is primarily focused on spot modulation. Finally, M dwarf targets typically require a different treatment, as many relational metrics such as [5]'s FF′ method are not applicable to M dwarfs. Furthermore, stellar activity can function very distinctly from that on FGK dwarfs and should not be lumped into a single analysis [180].

The above restrictions left us with a pool of targets to choose from. We prioritized the brightest, with special weight given to those that exhibited spot-induced stellar variability in their Kepler or K2 photometry. We discuss our eight targets briefly in the next subsections.

HD 173701

HD 173701 is a bright Kepler star with no known exoplanets. Because it is a solar analogue in age, radius, and mass, it has seen previous study [373]. The star is known to exhibit differential rotation, with rotation rates at 45^o latitude $\sim$ 50% slower than at the equator [44]. and a number of archival HIRES RVs have been taken to study the star [326]. We additionally obtained new APF RVs of HD 173701 and use them as as part of our analysis.

A generalized Lomb-Scargle [GLS; 405] periodogram on HD 173701 Kepler photometry reveals high powered signals between 32 and 36 days, suggesting a possible rotation period somewhere in this range, though the system is known to differentially rotate. The same analysis on TESS photometry highlights a strong signal near 12 days, most likely a harmonic of the longer period signal identified in Kepler. TESS is generally insensitive to signals near or longer than half a TESS sector in length ($\sim$12 days), though TESS can sometimes identify physical signals at the top end of this range [181]. The system likely has a rotation period near 32 days, and TESS only detects a harmonic.

Kepler-21

Kepler-21 is the brightest known Kepler system with a transiting planet, and has a variety of scientifically interesting features. The system was first studied in [186], where a small, transiting exoplanet was discovered orbiting the star with a period near 2.7 days. [249] performed a joint photometric-RV analysis of the system, and determined the composition of the planet to be consistent with that of Earth. Their mass estimate, however, was hindered by stellar variability, as the system is known to be contaminated with stellar activity (K_b = 2.46±0.48 m s^{-1}; RV RMS = 4.95 m s^{-1}). More recently, [56] obtained more data and significantly increased our confidence in the planet mass measurement, placing it near 7.5 ± 1.3 $M_\oplus$, and consistent with an Earth-like density. We perform a detailed study of Kepler-21 during a precursor analysis (Beard et al. 2024b, submitted), though we summarize the system briefly here.

Kepler-21 is actually a slightly evolved F4-6 IV star (6250 ± 250 K). Despite this fact, we still include it in our observations because it is historically important to the community, is very bright, has a known rotation period $\sim$ 12.7 days, and has an abundance of archival RVs.

Kepler-37

Kepler-37 is the dimmest star in our sample [V = 9.77±0.03; 314], but still relatively bright. The system has three known transiting exoplanets, with a fourth controversial candidate [314]. Most remarkable about the system is the size of its exoplanets, with Kepler-37 b smaller than Mercury, approximately the size of the Earth's Moon [27]. Planets b and c have RV amplitudes far too small for study with even the highest precision instruments today ($K_b < 1$ cm s^{-1}, $K_c < 14$ cm s^{-1}), though [314] were able to constrain the RV signal of Kepler-37 d (1.22±0.31 m s^{-1}), one of the smallest ever detected RV amplitudes at the

time.

The Kepler photometry of Kepler-37 is contaminated with a quasi-periodic signal suggestive of spot modulation, and the system has a likely rotation period of 29 days. Consequently, Kepler-37 makes an interesting test case to compare activity training between Kepler and TESS, especially with a suspected rotation period longer than the baseline of a single TESS sector. All three transiting exoplanets have small RV semi-amplitudes, though Kepler-37 d is plausibly detectable with NEID, and was detected using HARPS-N. Consequently, when modeling Kepler-37 in our analysis, we treat it as a one planet system containing Kepler-37 d, and ignore the other two planets, far below our sensitivity.

HD 4256

HD 4256 is a bright (V = 8.00) K3 dwarf with no known exoplanets that was observed during the K2 mission. It has a long history of HIRES observations [326], and a clear, long period, periodic signal is apparent from the RVs. This signal is strongly correlated with the Calcium II H&K S index (S_{HK}), however, suggesting this cycle is not planetary, but likely related to stellar variability. After subtracting this signal, modest residual scatter remained, suggesting planets or additional stellar variability. The presence of the long-term activity cycle, clearly seen in S_{HK} values, motivated us to test if, in fact, such a correlation existed for photometry as well.

HD 31966

HD 31966 is a bright G2 dwarf that saw observations during the K2 mission. The system has no known exoplanets, though it has been considered as a promising target for asteroseismology [335]. The target was chosen for our project mainly because it is extremely bright, has archival HIRES RVs [326], and we detected scatter in the RVs suggestive of either stellar

variability, or an undetected exoplanet.

HD 24040

HD 24040 is a bright (V = 7.51) G1 star with a long history of HIRES RV observations. The system has two known RV-detected exoplanets with very long periods, one larger than Jupiter, and the other near Saturn in size. The system also has a long term linear trend that has begun to show signs of curvature [326]. The trend/curvature is of sufficiently low amplitude that it may well be a long period planet.

The system was also observed during the K2 mission, making it a potentially fruitful target for study. Often, when selecting targets, we would look at the archival Kepler or K2 photometry to get a first order estimate of stellar activity contamination. This is somewhat difficult in K2 photometry, due to K2's ubiquitous systematic contamination issues (mentioned further in §6.3), though an analysis of archival RV data suggests that after subtracting the three known signals in the RVs, there was a few m s^{-1} of residual scatter, suggesting either stellar variability or additional planets. We are interested in exploring activity near the historical 1 m s^{-1} noise floor in addition to more obvious spot modulation, and so we included HD 24040 in our target list.

HD 106315

HD 106315 is a bright (V=8.95) K2 system with two known sub-Neptune transiting exoplanets [91]. [28] measured the masses of the transiting exoplanets using HARPS radial velocities. The system's host star is an F5 star with a suspected rotation period near 5 days. Due to the rapid rotation and early spectral type of the star, line broadening typically reduces the precision of RV observations. Nonetheless, due to its brightness, HD 106315 b and c are excellent targets for atmospheric observations [226].

After systematic correction, K2 photometry exhibit a clear quasi-periodic signal, likely due to spot modulation, making it a useful addition to our study.

HD 119291

HD 119291 is a K2 star with no known transiting exoplanets. The target is very bright [9.24±0.03; 355], and we observed that the K2 photometry exhibits distinctive quasi-periodic modulation that is likely due to spot modulation. HD 119291 has also seen archival observations with the HARPS spectrograph, mainly with respect to Gaia radial velocity standard stars [351].

6.2.1 Stellar Parameters

As alluded to previously, all of our targets are very bright, and have characterized in previous works. Rather than repeat such analyses, we summarize the stellar parameters of our targets in Table 6.1. While such a heterogeneous collection of stellar properties is unsuitable for demographic studies of stellar or exoplanetary populations, it is sufficient to describe the basic properties of targets for our study, which is primarily focused on time-series analysis.

Table 6.1: Stellar Parameters

System	T_{eff} (K)	Spectral Type	R_* ($R_\odot$)	M_* ($M_\odot$)	L_* ($L_\odot$)	V Magnitude	$\log R'HK$	P_{pred} (days)	Reference
HD 173701	5337±105	G8V	0.96±0.04	0.92±0.11	0.67±0.01	7.54±0.03	-4.94	41.38	A
Kepler-21	6305±50	F6IV	$1.902^{+0.018}_{-0.012}$	$1.408^{+0.021}_{-0.030}$	$5.188^{+0.142}_{-0.128}$	8.25±0.03	-5.19	14.83	B
Kepler-37	5406±28	G8V	$0.787^{+0.033}_{-0.031}$	0.87±0.15	0.479±0.001	9.77±0.03	-4.93	26.5	C
HD 4256	5017±141	K3V	0.77±0.06	0.83±0.11	0.33±0.01	8.045±0.013	-4.95	46.2	A
HD 31966	5715±108	G2IV-V	1.61±0.07	1.02±0.12	2.48±0.06	6.74±0.02	-5.06	29.0	A
HD 24040	5776±84	G1V	1.38±0.03	1.10±0.05	0.27±0.01	7.515±0.009	-5.05	27.7	D
HD 106315	6321±50	F5V	$1.27^{+0.17}_{-0.13}$	$1.12^{+0.05}_{-0.04}$	0.388±0.004	8.951±0.003	-5.14	5.9	E
HD 119291	4510±137	K7V	0.69±0.06	0.71±0.08	0.178±0.009	9.24±0.03	-4.95	46.2	F

A is [355], B is [249], C is [314], D is [326], and E is [270].

We predict rotation periods using an estimate from the $\log R'_{HK}$ activity indicators given in [296]. We call these $P_{\rm pred}$ in Table 6.1. A few of our targets have known rotation periods (Kepler-21: 12.6±0.03 days [249]; Kepler-37: 29±1 days [314]; HD 106315: 5.15±0.28 days [28]) and most of the others show clear signs of periodic modulation in photometry and RVs. Photometry can often produce more reliable estimates of stellar rotation periods [278, 181], though we utilize a non-photometric method to prevent "double fitting" photometry, which we use later in §6.4. We have found that the estimate in [296] is generally close to the known or suspected rotation periods of our targets. We note that Kepler-21's predicted rotation period using [296] was 0.05 days, far from the known, true value. This might be caused by the relationship in [296] failing for a more evolved star. Instead, we use the asteroseismological estimate from [186] for our predicted rotation estimate for Kepler-21.

As mentioned above, we observe primarily main sequence FGK stars. The primary exception to this rule is Kepler-21, as well as the slightly evolved HD 31966. We adopt stellar parameters from planet discovery papers for those with known planets, and use the TICv8 catalog for the remainder [355].

6.3 Survey Data

6.3.1 Photometric Data

We chose targets with an abundance of photometric data. Kepler targets that were able to be observed simultaneously with NEID and TESS were prioritized, but TESS pointing constraints forced us to choose several targets with K2 photometry instead of Kepler.

Kepler Photometry

Three of our targets were Kepler targets, meaning that they were observed as a part of the primary Kepler mission that launched on 6 March 2009, with observations beginning 2 May 2009. All three of these targets–Kepler-21, HD 173701, and Kepler-37–were observed until 11 May 2013, spanning 1470 days [57]. The Kepler spacecraft utilized a 1.4 m primary mirror to observe $\sim$ 150,000 main sequence stars using its 115 square degree field of view.

Kepler observations were divided into "quarters," 90 days in length. Both short and long cadence observations were taken by Kepler, with exposure times of 58.85 s and 29.4 minutes respectively. Long cadence data is available for all Kepler quarters, while short cadence data is only available for quarters 2, and 5-17. We choose to use long cadence data during our analysis, as our RV cadence is insensitive to activity on sub-hour timescales.

We utilize the Presearch Data Conditioning (PDC) flux, produced by the Kepler science processing pipeline [KSPP; 197]. This pipeline reduces raw data into a processed form, removing known instrumental and erroneous effects, and flagging datapoints of suspicious quality. Reductions can remove genuine physical signals from the photometry on periods near the length of a Kepler quarter (90 days), though our targets are either known to, or suspected to, have rotation periods far less than this length. A summary of our Kepler data is visible in Table 6.2.

Table 6.2: Median Uncertainty in Observation Data

Instrument	HD 173701	Kepler-21	Kepler-37	HD 4256	HD 31966	HD 24040	HD 106315	HD 119291
Photometric Data								
Kepler	2.92 ppm	4.38 ppm	7.79 ppm	-	-	-	-	-
K2	-	-	-	3.77 ppm	4.83 ppm	6.50 ppm	13.14 ppm	13.10 ppm
TESS	23.89 ppm	38.83 ppm	79.62 ppm	27.44 ppm	17.27 ppm	24.64 ppm	489 ppm	61.01 ppm
RV Data								
HIRES-pre	-	-	-	1.27 m s^{-1}	1.27 m s^{-1}	1.30 m s^{-1}	-	-

Continued on next page

Table 6.2: Median Uncertainty in Observation Data

Instrument	HD 173701	Kepler-21	Kepler-37	HD 4256	HD 31966	HD 24040	HD 106315	HD 119291
HIRES-post	1.07 m s^{-1}	2.45 m s^{-1}	2.38 m s^{-1}	0.86 m s^{-1}	1.26 m s^{-1}	1.17 m s^{-1}	-	-
HARPS	-	-	-	-	-	-	2.84 m s^{-1}	0.84 m s^{-1}
HARPS-N	-	1.23 m s^{-1}	0.91 m s^{-1}	-	-	-	-	-
APF	0.99 m s^{-1}	5.47 m s^{-1}	-	-	-	-	-	-
NEID	0.49 m s^{-1}	2.02 m s^{-1}	1.36 m s^{-1}	0.56 m s^{-1}	0.39 m s^{-1}	0.71 m s^{-1}	5.19 m s^{-1}	0.73 m s^{-1}

K2 Photometry

We utilize K2 photometry for our remaining five targets, HD 24040, HD 31966, HD 106315, HD 4256, and HD 119291. The K2 mission was a successor mission to Kepler after a failure of two of its reaction wheels prevented the spacecraft from continuing its primary mode of operation [187]. The follow-up K2 observations started on 30 May 2014 and ended on 30 October 2018, and targeted Earth's ecliptic stars, rather than those in the Kepler field.

The K2 observing strategy was significantly different than that of Kepler, as it could not point continuously at a single region of stars. Instead it would observe a field for ∼83 days and move to a different ecliptic region. Consequently, most of our targets have only a single ∼ 83 day span of photometry taken with K2, rather than the extensive four year time span of our Kepler targets.

K2 observations were taken in short (∼1 minute) and long (∼30 minute) cadence mode. We used short cadence data in our analysis when available, though, as we mention in §6.4.1, we typically bin data into regions of size 0.1 days, and so their should be no discernable difference between cadence types.

Most important when analyzing K2 data is the treatment of systematic trends in the data.

Due to the failed reaction wheels, K2 observations were consistently drifting off target, requiring thruster fires to keep stars in the field of view [270]. This would consistently change the pixel that each star fell on, introducing myriad systematic effects into the raw data.

A variety of different correction methods were devised for the purpose of removing systematic trends. In our analysis we utilize `EVEREST` [255] for all of our K2 targets, with the exception of HD 4256, as the default `EVEREST` reduction included with `lightkurve` was hardly improved from the raw flux. For HD 4256 we utilize pixel level decorrelation (PLD) built into the `lightkurve` software package to produce a lightcurve that saw much reduction in the artificial signals common in K2 photometry [237].

With the exception of HD 119291, all of our K2 targets still showed signs of long-period systematic contamination after `EVEREST`, or PLD, corrections. To remove these signals, we used a 1D spline in the `SciPy` interpolation module, `scipy.interpolate.BSpline` [385]. The smoothing factor, s, is a dimensionless parameter that controls the closeness (low values) and smoothness (high values) of the spline fit. We used large smoothing factors to prevent the spline from overfitting and removing short-period signals, typically ranging from 10^7 - 10^9.

It is likely that the K2 photometry, after `EVEREST` and spline corrections, still contains systematics. Nonetheless, we go forward with our analysis with these first and second-order corrections: a more in-depth reduction would be beyond the scope of our analysis.

TESS Photometry

The Transiting Exoplanet Survey Satellite [TESS; 318] began its primary mission on 18 April 2018, and continues to take data today. While the primary purpose of the TESS mission is to find transiting exoplanets, much like Kepler and K2, its observing strategy is significantly

different. TESS is an all-sky survey, starting in the Southern Hemisphere and pointing at most stars for only a ~ 27 day sector before moving on to another region of sky. While not as precise as Kepler, the TESS mission is especially focused on finding exoplanets orbiting the brightest, nearest stars. To date, TESS has confirmed 446 transiting planets, though over 7,000 candidates are currently under some form of study (Taken from the NASA Exoplanet Archive on 25 May 2024).

Because of its all-sky nature, most bright stars will receive TESS observations at some point. All of our targets were chosen during NEID observing semesters where simultaneous NEID RVs and TESS photometry were available. Because of their brightness, all of our targets recieved observations at two-minute cadence, and some even at faster cadence.

We use TESS Pre-Search Data Conditioning Simple Aperture Photometry (PDCSAP) flux processed by the TESS Science Processing and Operations Center [SPOC; 198] pipeline. This processing removes troublesome features from raw flux data such as instrumental effects and scattered light. However, it also tends to remove astrophysical signals longer than about half a TESS sector in period-space. This might plausibly hinder TESS's utility as a training dataset for our RV analysis, and is one of the key differences between TESS and Kepler data. We include a summary of TESS precision for each of our targets in Table 6.2.

6.3.2 Radial Velocity Data

RV data utilized consists of archival data, as well as newly acquired observations. RVs taken with the NEID spectrometer and the Automated Planet Finder (APF) spectrograph (detailed in §6.3.2 and §6.3.2) are all newly utilized, and non-archival. All other instrument data is purely archival. We detail each instrument's RV data in more detail ahead.

RVs with Keck/HIRES

All of our targets, with the exception of HD 119291 and HD 106315, saw observations taken using the High Resolution Echelle Spectrometer [HIRES; 387] located on the Keck 1 telescope in Hawaii. Precise radial velocities are taken from [71].

The HIRES spectrograph recieved an instrument upgrade in 2006 that likely introduced a systematic offset between data taken before and after. In our analysis, HD 173701, HD 4256, HD 24040, and HD 31966 all have HIRES observations on either side of this maintenance. Consequently, when modeling the data, we treat pre-upgrade HIRES data and post-upgrade HIRES data as separate instruments. HD 173701's pre-upgrade HIRES data appeared to exhibit a strong trend not seen in any of the other data, which we deem likely systematic in origin. We consequently exclude it from the analysis.

Our observation statistics are detailed in Table 6.2.

RVs with HARPS-N

Kepler-21 and Kepler-37 were both observed using the High-Accuracy Radial velocity Planet Searcher-North [HARPS-N; 89] spectrograph. HARPS-N is located at the Telescopio Nazionale Galileo, a 3.6-m telescope in the Canary Islands, Spain.

[314] utilized a pairwise Gaussian Process reduction during their analysis of Kepler-37, producing a different set of HARPS-N RVs. Such a process was not used in [56], though they include additional HARPS-N RVs. We utilize the data from [56] for all of our targets. In particular, we do *not* uses Kepler-37 data from [314] for 1) consistency with our other targets, and 2) we are interested in studying post-processing methods for removing stellar variability, while [314] utilized a pre-processing method to do so.

Our observation statistics are detailed in Table 6.2.

RVs with HARPS

Two of our targets, HD 106315 and HD 119291 were observed by the High Accuracy Radial velocity Planet Searcher [HARPS; 271]. HARPS is a high precision spectrograph utilized by the European Southern Observatory 3.6 m telescope, located at La Silla Observatory, Chile. HARPS is capable of achieving a spectral resolving power of $R \sim 115,000$.

Our observations statistics are detailed in Table 6.2.

RVs with the Automated Planet Finder

We obtained RVs of HD 173701 using the Levy Spectrometer on the 2.4 m Automated Planet Finder [APF; 388] Telescope. APF is a fully robotic telescope at Lick Observatory on Mt. Hamilton, CA.

Our APF observations of HD 173701 are comprised of 61 observations taken over a 1902-day baseline extending from July 2013 to September 2018. We used an exposure meter to achieve consistent SNR sufficient to achieve ~ 1 m s^{-}1 precision; exposure times range from 322-1800s.

The Levy spectrometer is equipped with an iodine vapor cell to provide a stable wavelength reference and track variations in the instrument profile. RVs were extracted using the method described in [71]. The APF RV time series has an RMS scatter of 4.7 m s^{-}1 and a median uncertainty of 0.99 m s^{-}1.

RVs with the NEID Spectrometer

We obtained RV observations for all targets with the extremely precise NEID spectrograph, located on the WIYN 3.5 m telescope at Kitt Peak National Observatory[1] [336] . NEID is extremely stable, with a resolving power of $R > 100\,000$ and capable of achieving RV precisions as low as 25 cm s^{-1}. RVs were obtained via the standard NEID reduction pipeline, which utilizes a cross correlation function [CCF; 14] to generate precise RVs.

One of the main goals of our analysis was to explore how photometry can help mitigate stellar activity in the era of extreme precision radial velocities (EPRV). Thus, obtaining NEID data simultaneously with TESS was an essential part of our experimental design.

Obtaining RV observations simultaneously with any photometric instrument can be very challenging, but is especially so for TESS. The TESS observing strategy typically only observes a single star for a 27 day sector, limiting the ability to obtain RVs simultaneously. This is complicated by the fact the NEID instrument is not used every night at the WIYN telescope, and that scheduled NEID observations are often competing with other programs for limited observing time. The difficulty is alleviated by the queue-observing system employed by WIYN staff, allowing for high-cadence observations that are impossible in a classically scheduled system [152].

Our observing programs faced several challenges. We were originally allocated NEID time during Sector 26 of the TESS primary mission, the first sector where Kepler stars were to be observed and NEID was operational. However, Kitt Peak underwent a full observatory shut down due to the SARS Cov-2 pandemic during Sector 26, making data acquisition impossible. Observations for our program continued nominally in 2021, thanks in part to the NEID queue system, and we initially had great success observing during Sectors 40 and

[1]The WIYN Observatory is a joint facility of the University of Wisconsin–Madison, Indiana University, NSF NOIRLab, the Pennsylvania State University, Purdue University, and Princeton University.

41. The latter saw a particularly bad patch of weather at Kitt Peak, and few of our final observations were able to be executed.

TESS then moved to the Southern hemisphere for year three of its mission (Sectors 27-39), and we could no longer observe Kepler targets simultaneously with TESS. Fortunately, some ecliptic targets could be observed with NEID and TESS simultaneously, and we obtained RVs of our K2 targets. After a year in the Southern Hemisphere, TESS would return to the North and the Kepler field. As is visible in Figure 6.1, these observations quickly ceased due to the Contreras wildfire, which threatened Kitt Peak National Observatory, halting observations for several months.

Despite the many setbacks our program faced, we obtained many NEID RVs simultaneously, or nearly simultaneously, with TESS observations. We include a plot of our simultaneous observations in Figure 6.1.

Our observation statistics are detailed in Table 6.2.

6.4 Analysis

6.4.1 Training Activity Models

Much of our analysis is devoted to determining which photometric datasets can be used to glean the most information about stellar activity contamination in the RVs. Kepler data has a much longer baseline than TESS, but is comparatively old, and may not well predict the current stellar activity structure. K2 data, while longer baseline than TESS, has its own disadvantages, as the data include difficult-to-remove instrumental signals that might negate any advantage from the longer observing baseline. Future photometric missions such as PLATO [315] will likely provide different advantages and disadvantages still. To the

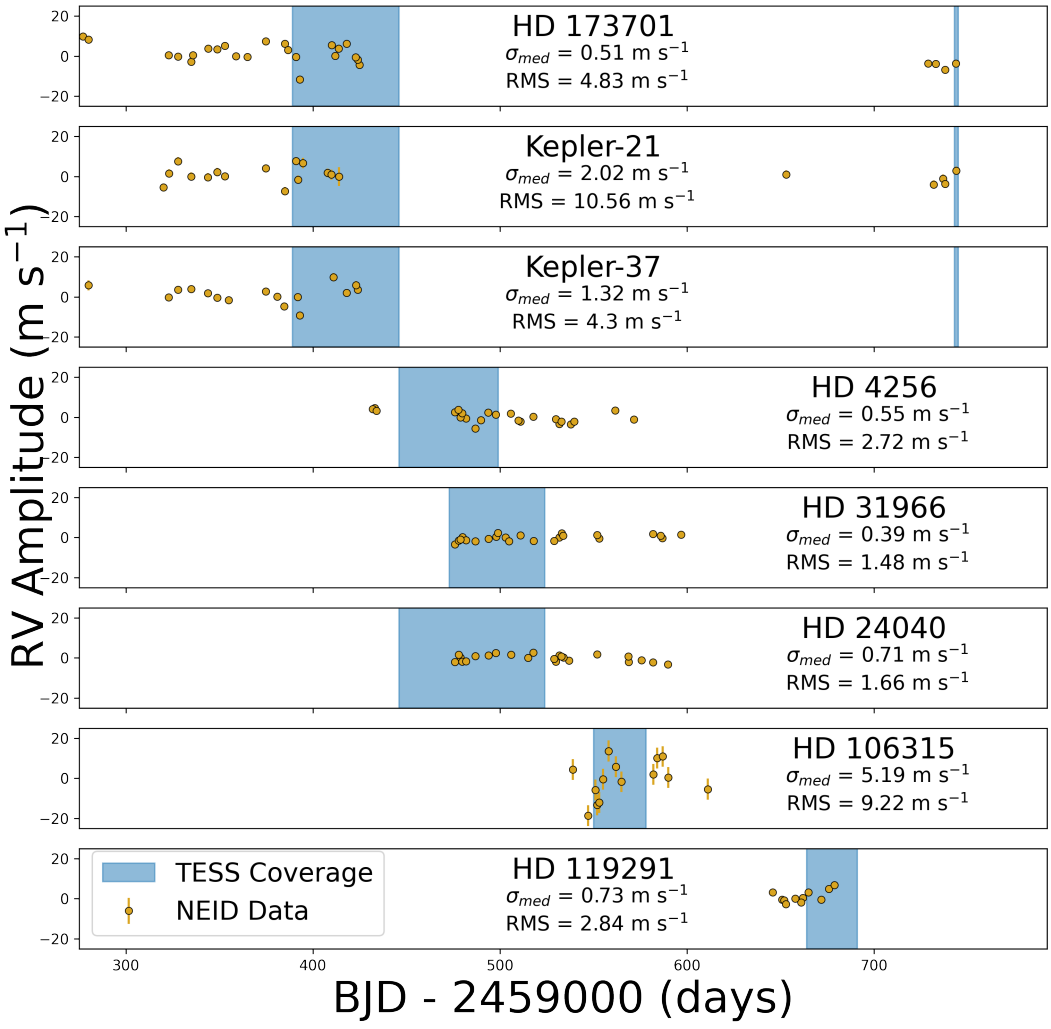

Figure 6.1: NEID observations of our eight targets. TESS observations are overlaid in blue. Bad weather hindered observations of Kepler targets at first, and the Contreras fire would eventually prevent observations toward the end of our program, hence the small window of TESS observations which then ended abruptly for the Kepler targets. We generally had high success observing K2 targets.

end of quantifying advantages and disadvantages, we carry out analyses that are trained on Kepler/K2 photometry, or TESS photometry, as well as untrained analyses, and scrutinize the results.

Our training involves fitting an activity model to each photometric dataset, and using Markov-chain Monte Carlo [MCMC; 126] sampling to determine the best fit posteriors. We then use these posteriors as priors when performing RV-only fits, or when performing injection-recovery fits. We choose as our activity model the $\mathcal{K}_{J1}$ chromatic GP kernel, detailed in [74]. This kernel is an expansion of the commonly used quasi-periodic (QP) kernel, with a few advantages not implemented in the QP kernel by default. The $\mathcal{K}_{J1}$ kernel is given in equation 6.1.

$$\mathcal{K}_{J1} = \eta_{1,s(i)}\eta_{1,s(j)} \exp\Big(\frac{-|t_i - t_j|^2}{2\eta_2^2} - \frac{1}{2\eta_4^2}\sin^2\big(\frac{\pi|t_i - t_j|}{\eta_3}\big)\Big) \tag{6.1}$$

The first advantage we expect from this kernel is that it utilizes a different activity amplitude term for each instrument, which is generally physically motivated, as different RV and photometric instruments often extract information from different bandpasses, and stellar activity is chromatic [90]. Additionally, the $\mathcal{K}_{J1}$ GP kernel models all instruments in a single covariance matrix, allowing covariances *between instruments* to be enforced, whereas the traditional QP kernel models each instrument independently.

The advantages of the $\mathcal{K}_{J1}$ kernel are not as obvious when training on photometric data, but we expect real benefit to come from RV fits utilizing this kernel. For consistency, we do all our training and model evaluation using this kernel, though on single-instrument photometry, the $\mathcal{K}_{J1}$ kernal is identical to the QP kernel. The calculation of the chromatic GP likelihood scales with number of data points by $\mathcal{O}(\mathrm{N}^3)$, making the computation impractical for very

large datasets, like photometry. To circumvent this problem, we train on binned subsets of photometry. We use 30 minute time bins, as RV cadence is much sparser than this, and stellar activity that evolves on shorter timescales is not likely to be detected in the RVs.

We additionally use subsets of the photometric data to speed computation. For Kepler, we chose quarters 6 and 7 for this analysis. This choice was originally motivated by the availability of simultaneous Kepler-21 RV data in these quarters, and we continue to adopt it for our other Kepler targets for the sake of consistency. K2 targets saw much shorter baseline observations, and we use all available K2 data for each target.

TESS photometry for some targets is highly abundant, but often spread out over many years with large gaps of no observation. During survey development, we chose targets where simultaneous NEID observations could be acquired with TESS observations. Consequently, we generally choose TESS photometry closest to our NEID observations for photometric training. A full table of which datasets for which targets were used for training is given in Table 6.3.

Table 6.3: Photometric Training

Target	Kepler	K2	TESS
HD 173701	Q6, Q7	-	S40, S41
Kepler-21	Q6, Q7	-	S40, S41
Kepler-37	Q6, Q7	-	S40, S41
HD 4256	-	C8	S42, S43
HD 31966	-	C13	S43, S44
HD 24040	-	C4	S42, S43, S44
HD 106315	-	C10	S46
HD 119291	-	C17	S50

We chose broad, uninformative priors for our fits, to maximize the amount of "learning" that could be done. For η_1, we implemented a Jeffreys prior with minimum 10 ppm, and maximum 1,000,000 ppm. For η_2, we implemented a wide Jeffreys prior with a minimum equal to the predicted rotation period, and a maximum of 10,000 days, as suggested by Polanski et al., 2024 (submitted). For η_3, which is often a good approximation of the stellar rotation period, we utilize a Gaussian prior centered at the predicted rotation period (Table 6.1), and with a width of 20% of this estimate. Finally, we follow [249] and Polanski et al., (submitted) concerning η_4 by utilizing a Gaussian prior for centered at 0.5, with a standard deviation of 0.05.

We run each training dataset through an MCMC inference process to measure, primarily, its GP hyperparameters. We generate an activity-only GP model using the `RadVel` software package [133]. We follow the default `RadVel` convergence criteria to assess convergence, which assesses convergence by determining when the Gelman-Rubin (G-R) statistic [119] is less than 1.01 and the number of independent samples is greater than 1000 for all free parameters for at least five consecutive checks. After inference is completed, we use the posteriors of all the hyperparameters as priors for our RV fits, with the exception of amplitude. This is because photometry and RV data have completely different dimensions, and photometric amplitude cannot be reliably converted into RV amplitude. We implement posteriors as priors by taking the posterior mean and standard deviation, and using these as Gaussian priors in our RV fits. A summary of our training posteriors is given in Table 6.4.

Table 6.4: Trained Values

Target	Kepler	K2	TESS
HD 173701			
η_2 (days)	41.7±0.5	-	51±11
η_3 (days)	32.81±0.07	-	42.0±5.6
η_4	0.098±0.003	-	0.049±0.009
Kepler-21			
η_2 (days)	17.5±1.6	-	15.7±1.3
η_3 (days)	22.03±0.11	-	15.8±2.3
η_4	0.090±0.003	-	0.14±0.05
Kepler-37			
η_2 (days)	27.7±1.2	-	30±4
η_3 (days)	26.5±0.2	-	17.6±0.22
η_4	0.22±0.01	-	0.27±0.07
HD 4256			
η_2 (days)	-	55±1	60±15
η_3 (days)	-	50±6	18.4±0.3
η_4	-	0.5±0.05	0.42±0.05
HD 31966			
η_2 (days)	-	31.9±3.2	809±2100
η_3 (days)	-	26.0±0.6	27.9±5.4
η_4	-	0.42±0.05	0.51±0.05
HD 24040			
η_2 (days)	-	38±12	66±29
η_3 (days)	-	29.8±2.8	8.35±0.09

Continued on next page

Table 6.4: Trained Values

Target	Kepler	K2	TESS
η_4	-	0.52±0.05	0.48±0.05
HD 106315			
η_2 (days)	-	6.2±0.37	9±51
η_3 (days)	-	5.36±0.64	4.52±0.41
η_4	-	0.51±0.05	0.48±0.05
HD 119291			
η_2 (days)	-	41.9±2.7	61±24
η_3 (days)	-	24.71±0.15	14.86±0.15
η_4	-	0.26±0.02	0.28±0.15

6.4.2 Injection-Recovery Tests

We utilize an injection-recovery test to explore which training method best removes stellar activity contamination. For each target, we take its RV data and inject a variety of planetary signals with known orbital period, RV semi amplitude, and phase. We then fit an RV model with the injected planet included and an RV model with it excluded, and compare the results. In particular, we elect to use model comparison to determine with what level of confidence that the injected planet is recovered.

Another possible metric for model effectiveness is the recovered RV semi-amplitude of a simulated planet, divided by its uncertainty. However, due to the high computational cost of our injection-recovery tests detailed later in the section, we were unable to perform true inference, and thus could not achieve a reliable estimate of our amplitude uncertainty.

Consequently, we opt to use model comparison rather than recovered amplitude significance.

We follow a similar method as used in [74] by injecting planets with a variety of periods and amplitudes. We create 10 bins linearly spaced between 1 and 10 m s^{-1} for RV amplitudes, and 10 bins with log-uniform spacing between 0.1 days and 1000 days for injected orbital period. The result is 100 bins for a range of amplitudes and orbital periods. When injecting signals, for each bin, we generate a fake planet with RV amplitude and orbital period randomly selected inside each bin, and with zero eccentricity. Additionally, we then randomly pick a phase for the injected planet to prevent our results from being biased by RV phase coverage. We do this 100 times in each bin, and average the results.

Following [74], we explore two cases: first, where the injected planet is "transiting," and we know the orbital period and time of conjunction precisely. In these cases, these parameters are fixed when fitting, and only the RV amplitude K of the injected planet is fit. The second case is an "RV detected" planet, where we do not know the precise orbital period or phase, and these parameters must also be fit.

To determine the effectiveness of our training, we compare the results of RV fits that include the injected planet, and those that do not. To do so, we perform N and N+1 planet fits for each system and training dataset, where N is the number of planets known in the system. We compare the results of the fit using the evidence of each model, which is calculated by integrating the product of the model likelihood and its priors over the entire parameter space [209]. A higher evidence value indicates a better fit to the data, and we use the concept of the Bayes Factor (BF) to quantify the improvement gained by adopting the higher evidence model. This is usually defined as the ratio of the evidences, though it is more often the logarithm of the BF that is computed and referenced, as the log of the evidence is much less likely to overflow a computer's floating point precision.

The primary issue with utilizing evidences to explicitly calculate the BF is that they are

very computationally expensive, and often completely impractical to estimate. A variety of methods exist for approximating the evidence or the BF [BIC, AIC, Nested Sampling; 235, 111], though all have their drawbacks. BIC and AIC typically require a full MCMC sampling process before they can be reliably calculated, and even then are considered imperfect approximations of the evidence. Nested sampling can be used to calculate the evidence of a model without taking the complicated integral, but is itself a sampling process that can be time-consuming.

The problem is especially severe in our case, as our injection-recovery tests are performed for 100 different grids, and with 100 simulated phases inside each grid. These 10,000 calculations have to be performed six times for each target: fits without training, trained on Kepler/K2, trained on TESS, and in each case fits including the injected planet in the model, or not. Thus, 60,000 model evidences have to be calculated for each of our targets, a totally infeasible task using the above methods.

Instead, we approximated the evidence using the Laplace approximation (detailed in [291] A3). Essentially, the Laplace approximation leverages the fact that a complicated integral, decomposed into an exponential

$$Z = \int \exp(f(x))\, dx \tag{6.2}$$

can be approximated as

$$\left[\frac{(2\pi)^2}{\det|H(x_0)|}\right]^{\frac{1}{2}} \times \exp(f(x_0)) \tag{6.3}$$

where H is the Hessian matrix of $f(x)$, and x_0 is a region of high probability, far from the bounds of integration. We utilize a lightweight python package, `LApprox` [37], to estimate the evidence for each of our runs.

We include a summary figure for each of our targets in the appendix, though highlight HD 173701 in the main text in Figure 6.2. These include plots of our GP fits to the photometry, as well as summary plots of the injection recovery results for the "transiting" and "RV-detected" cases.

6.4.3 Non-Simultaneous TESS Fits

Beyond determining which training dataset improves RV fits most significantly, we are interested in quantifying the effectiveness of simultaneously obtained RV data. Such data is widely considered ideal for constraining RV activity models using photometry, but is often difficult to acquire in practice.

To do so, we perform another injection-recovery test on a model that has been trained on non-simultaneous TESS photometry. In Table 6.3, we note the TESS sectors that were used for training our activity models in our main analysis. These were selected because they were the TESS sectors simultaneous with our acquired NEID RV data, and we hypothesized that a model trained on this data would be most effective at separating stellar activity signals from exoplanet signals. To test this hypothesis, we train on non-simultaneous TESS sectors, and we compare the result. HD 106315 and HD 119291 have no additional TESS photometry, and could not be included in this analysis, but we were still able to analyze six targets. We used sectors 53 and 54 for the three Kepler targets, sector 70 for HD 4256, sector 71 for HD 31966, and sectors 70 and 71 for HD 24040. For the Kepler targets, this is a median RV-photometry separation of 356, 352, and 362 days for HD 173701, Kepler-21, and Kepler-37, respectively. For the K2 targets, this corresponds to a median RV-photometry distance of

HD 173701

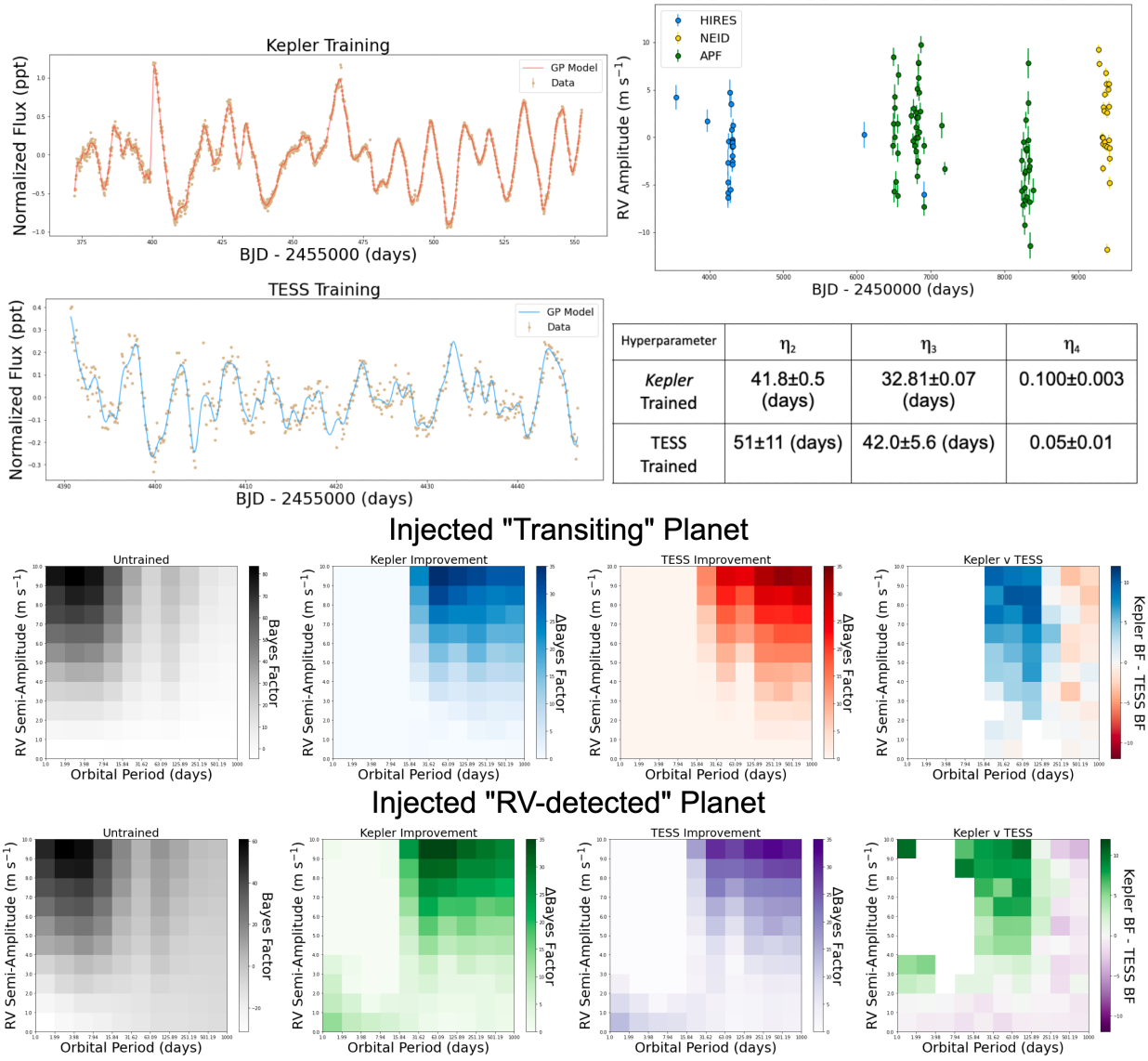

Hyperparameter	η_2	η_3	η_4
Kepler Trained	41.8±0.5 (days)	32.81±0.07 (days)	0.100±0.003
TESS Trained	51±11 (days)	42.0±5.6 (days)	0.05±0.01

Figure 6.2: We include a variety of plots summarizing our training and analysis of HD 173701. Top Left: Kepler and TESS training data, as well as our best fit GP model overlaid. Top Right: RV time series and training posteriors. Bottom: Results of our injection-recovery analysis in the two cases described in §6.4. The left plots show the preference for models including the injected planet when no GP training is applied. The middle two plots show the improvements gained when training on Kepler or TESS. The rightmost plots highlight the differences between Kepler and TESS training.

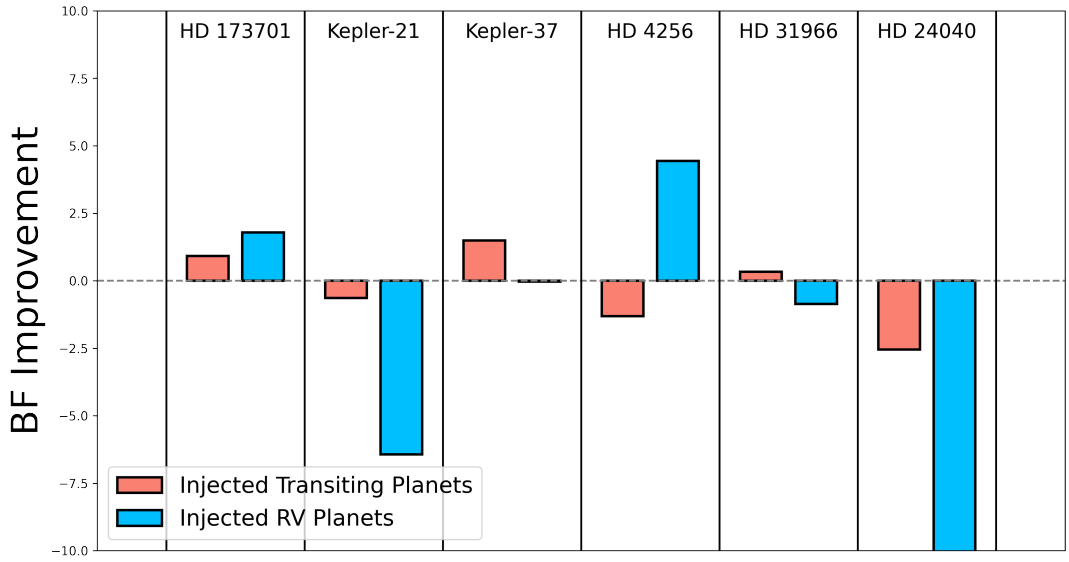

Figure 6.3: We show the increased or decreased performance of our activity models when trained on simultaneous data instead of non-simultaneous data. The y-axis indicates ΔBF between models trained on simultaneous versus non-simultaneous photometry. Positive values indicate that the simultaneous photometry is improving sensitivity to injected planets, while negative values indicate worse performance. Red bars correspond to our "transiting" planet runs, and the blue bars correspond to "RV-detected" injected planets. There is not consistent improvement gained from simultaneous photometric training. We note that for HD 24040, the negative preference goes far below our axes limits, which we set for a clearer analysis of the other systems. As mentioned in the text, we believe these fits may not be reliable.

709 days for HD 4256, 719 days for HD 31966, and 684 days for HD 24040.

We train activity models on these non-simultaneous TESS sectors just as in §6.4.1, and we compare the differences in effectiveness in Figure 6.3.

6.5 Discussion

6.5.1 Which Photometric Dataset?

Our injection-recovery tests shine some light on the advantages of training on a photometric dataset. Furthermore, we highlight the strengths of either Kepler or TESS training. We provide summary plots for each of our eight targets in Figures 6.2 and D.1 through D.7. These plots contain the Kepler and TESS training timeseries, the RV time series, the results of our training, and the results of injection-recovery tests. We focus on the bottom two panels of each plot in this section.

The leftmost injection-recovery panels show the level of preference for a fit with the injected planet over a fit without the injected planet when the GP model is not trained. We use the Bayes Factor (BF) as described in §6.4 to quantify this value. The middle panels quantify the level of improvement gained by training on Kepler or on TESS, as compared to no GP training at all. Finally, the rightmost panels show the difference between the middle two, emphasizing which photometric dataset improves the BF by the greatest amount. We discuss each target briefly before our final summary just after.

HD 173701

The results of our HD 173701 analysis are visible in Figure 6.2. The system is one of our brightest targets, and its photometry exhibits very clear quasi-periodic modulation. We predict a rotation period of 41.38 days from the $\log R'_{HK}$ value in §6.4.1, though GLS and autocorrelation analysis of the Kepler photometry suggest a $\sim$ 32-36 day rotation period [405, 181]. Like the other Kepler targets, the injected planet sensitivity is generally highest when the model has been trained on Kepler photometry, though at longer periods TESS occasionally performs modestly better. Interestingly, shorter period injected planets,

especially with larger amplitudes, do not appear to benefit from training an activity model. This trend appears for several targets, and we discuss it in §6.5.1.

Kepler-21

A more detailed discussion relating to Kepler-21 is available in Beard et al. 2024b in prep, though we summarize here. The results of our analysis are visible in Figure D.1. Kepler-21 exhibits a fairly clear $\sim$ 12 day rotational modulation in its Kepler photometry, though the rotation term of our GP model does not adhere to this value during training. TESS training recovers a value closer to the true rotation period, though with a larger uncertainty. Training on Kepler photometry still recovers injected planets more often than when training on TESS photometry. This suggests that some genuine stellar activity contamination likely exists near 22 days, and that this contamination exists in the RVs as well. The source of such a periodic signal is difficult to ascertain considering the system's known rotation period, though this affirms the importance of utilizing an entire dataset to mitigate stellar variability, rather than a single number for a stellar rotation period.

Kepler-37

Kepler-37 results are visible in Figure D.2. The system exhibits clear rotational modulation on a $\sim$ 29 day time scale, too long for TESS to plausibly recover. As with the other Kepler targets, GP models trained on Kepler photometry consistently recover injected planets with higher confidence.

Unlike with the other Kepler targets, training on Kepler much more significantly recovers the higher amplitude, shorter period planets injected during our analysis than when the GP model is not trained, or when it is trained on TESS. It may be that some higher frequency signal in the RVs confuses any attempt to recover planets, but is more easily distinguished

when trained on Kepler photometry.

HD 4256

The K2 photometry of HD 4256 likely still contain systematic contamination, despite the efforts in §6.3. The system also maintains higher levels of stellar variability in photometry and RVs, evident from TESS and S_{HK} values. We expect that this contributes to the fact that TESS training seems to typically be the best at recovering unknown planets during our tests.

The system is known from its S_{HK} values to have long-period activity cycles. Neither K2 nor TESS are likely to be sensitive to such long period signals, and this may explain the fairly precipitous dropoff of its sensitivity to injected planets between 60 and 100 days.

HD 31966

Our analysis of HD 31966, visible in Figure D.4, indicates that K2 photometry is more informative for removing stellar variability from RV data. It may be that the higher precision of K2 is contributing most, as HD 31966 is one of our least active targets. TESS photometry does not show clear, quasi-periodic signals, and the amplitude of our model is near the precision TESS achieves on HD 31966.

Strangely, the "RV detected" and "transiting planet" cases tell opposite stories for this system. In the former, K2 performs better when recovering injected planets near 60 days, and worse elsewhere. On the other hand, the latter sees TESS recovery improve near 60 days, and perform worse elsewhere. It may be that the choice of training dataset should be motivated in part by the nature of the exoplanets in the system.

HD 24040

Results pertaining to HD 24040 are visible in Figure D.5. The target is unique among our study in that it has known, RV-detected exoplanets that do not transit. These planets are long-period, and a trend in the data suggests the possible existence of another yet. Its K2 photometry either exhibits small fluctuations due to stellar variability, or there is some residual systematic signal. TESS data, too, exhibit low levels of variability. For these reasons, the injection recovery tests are somewhat ambiguous. Kepler and TESS see preference in the "fixed" planet case in different regimes, and rarely improve the model at all in the "RV-detected" planet case. In fact, in the latter case, our injection recovery tests failed even when the injected signal was large. This is unexpected, and difficult to explain. Most likely, the existence of long period giant planets interferes with our ability to recover injected signals, and the issue is amplified when the period of the signal is allowed to vary.

HD 106315

HD 106315 results can be seen in Figure D.6. Clear quasi-periodic variability in both K2 and TESS photometry can be seen, and the RV data too appear to vary with high amplitude. HD 106315 is a strange case, as it seems to have genuinely high variability in both photometry and RVs, and yet it fares better when trained on K2, rather than TESS as we might expect. The most likely culprit is the poor precision of our NEID RVs, especially as compared to our other targets. The archival HARPS data is much more precise than our NEID data, and closer in time to K2 photometry. This is likely the reason that K2 training performs better.

HD 119291

Interestingly, our analysis of HD 119291 (Figure D.7) suggests TESS training is superior for this target. TESS photometry is not abundant, and the K2 photometry for this target appears to be less contaminated with sytematics than for some of our other targets, all which would suggest the opposite result. It seems that the simultaneous, highly precise NEID RVs contribute enough to the injection-recovery tests that TESS training is more important for this system.

It is also interesting to note a dramatic improvement in sensitivity to injected planets between 30 and 60 days, that then falls. The predicted rotation period falls in this regime, though our GP models all adhere to lower periods. Most likely, a real activity signal at this period constructively interferes with our injected planets, amplifying our sensitivity.

All Targets

First we examine the three Kepler targets, HD 173701, Kepler-21, and Kepler-37. The first conclusion that we can make is that for low-amplitude injected signals, the GP training has little effect. This is not surprising, as low-amplitude planets are challenging to recover in even a quiet dataset. In such fits, the activity model is not the dominant source of uncertainty, rather it is the number and precision of the RVs. Perhaps more surprising, all three datasets see little-to-no improvement over the untrained fits for short period, high amplitude signals (with the exception of high amplitudes for Kepler-37). Why might this be? Such injected signals are expected to be recovered most easily, and so it may be that no matter how well the activity signals is constrained, the injected planet is recovered about as well in all fits. Interestingly, for longer period injected planets, Kepler seems to be the best photometric dataset to train on, despite its age. The longer observation baseline, higher precision, and sensitivity to longer-period signals beats out any advantage recent TESS photometry might

provide, despite our recent, simultaneous NEID RVs.

The K2-trained targets paint a less clear picture. Of the five, HD 4256 and HD 119291 have a clear preference for TESS training, while HD 31966 and HD 106315 benefit more from K2 training. HD 24040 has no clearly winning dataset. HD 106315's preference may be the easiest to explain: its NEID RVs are the least precise in our dataset, and it seems plausible that the advantages of training on TESS (mainly simultaneity with NEID) are diminished when the NEID data are less constraining of the RV model. HD 119291 and HD 4256 both have highly precise NEID RVs, likely emphasizing the importance of NEID simultaneity. HD 31966 is confusing from this angle, however, as its NEID RVs are the most precise in the dataset, and we have achieved the largest number of simultaneous RVs. Perhaps the best explanation is the fact that it has the smallest amplitude of activity contamination, similar to HD 24040. Examining the $\log R'_{HK}$ values in Table 6.1, this seems probable. $\log R'_{HK}$ values can be a good measure of stellar activity [153], and HD 119291 and HD 4256 have the largest values in the K2 target list. The advantages of training on simultaneous photometry seem to diminish as activity contamination becomes smaller.

Comparing the "transiting" planet fits to the "RV detected," we can see that GP training has a larger effect, typically, for the latter case across the board. This is unsurprising: when the period and phase of the undetected planet is uncertain, it is more difficult for an untrained GP to distinguish stellar activity from the injected planet. Thus, training a GP on photometry has extra benefit when searching for non-transiting planets.

Kepler and TESS photometry have many different qualities. Kepler photometry is much longer in baseline, higher in precision, and sensitive to longer period stellar activity signals, but is temporally distant from many of our most precise RVs. Despite this, training an activity model on Kepler photometry consistently recovers injected planet signals more strongly than when activity models are trained on TESS. This sensitivity increase seems to uptick above half of a TESS sector length, which may suggest that the short baseline of

TESS observations is the largest hindrance to mitigating activity.

K2 targets often better recover injected planets when trained on TESS. The K2 mission has significantly shorter baseline than Kepler (typically ~ 80 days), though it is still much longer than a typical TESS sector. K2 data are also notoriously contaminated with systematic effects. A GP activity model, when trained on such a dataset, might attempt to remove signals that originate from K2 systematic effects from RV data, despite their absence. This, combined with K2's shorter baseline when compared to Kepler, seems to hinder K2's other advantages.

6.5.2 Are Simultaneous RVs Beneficial?

We are also interested in exploring the benefit of simultaneously acquired RVs. It is commonly expected that RVs acquired simultaneously with photometry are ideal, as photometry can be used to constrain stellar activity signals in RVs as they are happening. Simultaneous RVs can be very challenging to acquire, however, and their true benefit may be small. Many analyses today utilize disparate datasets with a variety of RV and photometric instruments, further diminishing the probable benefit of simultaneously acquired RVs.

We performed a series of injection-recovery tests trained on simultaneous TESS photometry, as well as on non-simultaneous TESS photometry (refer to §6.4.3 for details). We take the median BF preferring the injected-planet model from our simultaneous-TESS and non-simultaneous-TESS analyses, and we use these numbers as a metric of how well the training is identifying injected planets across period-K amplitude space. We then take the difference between the simultaneous and non-simultaneous BFs in Figure 6.3.

A clear pattern is hard to distinguish. Simultaneous photometry is *not* the clearly better dataset with which to train an activity model. HD 173701 sees improvement in both

"transiting" planet and "RV-detected" planet cases, but Kepler-21 and HD 24040 both benefit most from training on the non-simultaneous dataset. The other targets see a mix of both, and the two cases are not even consistent across targets. What patterns exist?

Kepler-21 may be the easiest case to explain. NEID RVs of Kepler-21 are less precise than the archival HARPS-N RVs, so the benefit of simultaneous NEID-TESS training is likely reduced. Additionally, archival HARPS-N RVs are simultaneous with Kepler, further reducing the importance of simultaneous NEID data. It may be that the non-simultaneous TESS sectors happened to observe the star when its activity cycle was more similar to Kepler photometry, creating a preference for that TESS training dataset.

HD 24040 is an irregular case. Our injection recovery analysis (Figure D.5) is the most unusual of all of our targets, and we theorize that the system is not ideally suited for such. The presence of long-period, RV-detected planets seems to be interfering with the effectiveness of the Laplace Approximation, as even easily detectable injected planetary signals are not preferred in model comparison. Any conclusion taken from HD 24040 injection-recovery tests is likely suspect, and should be interpreted with caution.

HD 173701 and HD 4256 benefit the most from training on simultaneous photometry (though HD 4256 does not prefer this in the "transiting" planet case). These systems have the longest rotation periods in our sample ($>$ 30 days), and this may suggest some increased benefit for longer-period systems. With only six systems with which to compare results, we caution that a strong conclusion affirming this fact is not possible.

Kepler-37 sees significant improvement in the "transiting" planet case, but in the non-transiting scenario it is similar to HD 31966 in that it sees little difference in results no matter which TESS sectors it is trained on.

Overall, it is hard to claim a clear pattern. Our comparisons are most likely hindered by the different natures of our targets: different spectral types, rotation periods, and activity

levels make it difficult to identify exactly which quality is most improved, or hindered, by training on simultaneous photometry. The different qualities of the targets' archival data, too, probably affects the results, as Kepler-21, for example, has a great deal of archival HARPS-N data that are of similar precision to NEID. A future study, with a greater focus on similar stellar parameters and restricted to only the simultaneous, or near-simultaneous, RVs would likely be the best way to identify any real pattern, or lackthereof. We can conclude with confidence, however, that training data on simultaneous photometry is *not* necessarily the best way to remove stellar variability from RV data.

We conclude that if one is able to obtain enough RVs simultaneously with a photometric dataset to be able to independently recover a planetary signal, then that photometric dataset is likely the best to train upon. However, in the era of queue-scheduled RV observations, especially when utilizing data from a variety of RV instruments, one is likely better off obtaining additional RV observations in lieu of scheduling high priority time in order to achieve simultaneity. As a point of reference, the NEID queue assigns time priorities into five bins: 8% of time at priority 0, 17% at priority 1, 25% at priority 2, 25% at priority 3, and 50% at priority 4. Requesting high-priority time can seriously raise the cost of a telescope proposal, and if simultaneous RVs and photometry are unnecessary, it may not be required.

6.6 Summary

We perform an RV-photometry analysis of eight Kepler/K2 targets. We chose targets with known stellar activity contamination in order to study the best methods for mitigating stellar activity contamination in our RVs. We additionally obtained precise NEID observations of all targets simultaneously with TESS observations.

We then train stellar activity GP models on Kepler and TESS photometry, and use these

models to recover injected planet signals for our datasets. Finally, we experiment with the limits of temporal proximity for six of our targets, and we compare the results. We conclude:

1. Training stellar activity models on Kepler photometry is likely the best option when Kepler photometry is available, at least compared to TESS. Of our three Kepler targets, training on Kepler photometry improved the BF preferring injected planets by an average of 2.6 in the transiting planet case, and 3.7 in the RV-detected case.

2. Systems with longer rotation periods ($P_{rot} > 12$ days) and higher activity levels ($\sigma_{RV} > 5$ m s^{-1}) may benefit more from simultaneously acquired photometric observations.

3. Photometry simultaneous with RVs is *not* necessarily the best photometric dataset to use for activity mitigation. If one is able to obtain a larger quantity of RVs that are non-simultaneous (i.e. requesting lower priority time in a queue system) than can be acquired simultaneously, this will often better constrain an RV signal.

Chapter 7

Conclusion

The next generation of exoplanet science will be characterized by a deeper understanding of particular planets, in addition to a wider understanding of the populations and formation mechanisms that create the universe we see today. To expand our knowledge to the widest population of exoplanets, we must improve our instrument precision, as well as our analysis techniques. Most planets in the solar system would not be detectable if observed from one of our neighboring stars, a reminder that while we have discovered many exoplanets, many more remain outside of our reach. What's more, we still know precious little about even planets that were discovered decades ago. Bulk density is often the most detailed measured parameter we can estimate for any exoplanet, and this only if we have measurements of both mass and radius, far from a certainty. Many more planets have only one or the other, with no realistic prospect of amending this. Hubble and ground-based instruments have observed the atmosphere of some high SNR hot Jupiters, and JWST is currently observing the atmospheres of smaller transiting planets. Consequently, we have a basic understanding of some planetary atmospheres, though we are mostly restricted to climates far different than we see in the solar system. Even these measurements are clouded by degenericies and other sources of uncertainty, however, and we often can say very little about known planets

with great certainty.

To deeply understand exoplanets, we must utilize data from different sources. RV and photometric data are the most successful and abundant, though future missions will make direct imaging of reflected light of nearby exoplanets a possibility, and Gaia astrometry is already revolutionizing the way we can constrain the orbits of cold, distant planets. Even a single detection method, such as RVs, is typically spread over multiple observing instruments, making complete models today more complicated than ever. To widely and deeply understand exoplanets, we require analysis techniques that can combine multiple observing methods, techniques, instruments, and processes into a physical model that is consistent and manageable.

I began my study focusing on how photometry and RVs together can shed light, where photometry alone cannot. I began in §**??** with two M dwarf systems. I performed a deep analysis of both systems by combining not only TESS photometry, but ground based ARCTIC and RBO photometry in joint models with RV data. Even the RV data came from multiple instruments, already demonstrating how a complicated physical model is required to combine the physics of many datasets into one. We were able to constrain planet masses where, without RVs, we previously could not, and the ground-based photometry we acquired further improved the radii of the planets. Combined, we could examine aspects such as system bulk density, and with our orbital period measurements we could precisely measure equilibrium temperature and atmospheric flux values.

I continue in this vein in a more challenging system, GJ 3929, in §**??**. GJ 3929 is an exo-Venus that exhibited modest stellar variability, and contains a non-transiting exoplanet in its RV data. Exo-Venus's are particualrly important to study, as our ability to distinguish between a Venus-like and Earth-like planet is essential if we wish to characterize surface condtions with any reliability. GJ 3929 proved to be an interesting case where one dataset (RV) revealed a previously undetected planet not seen in the photometry. Such cases are not uncommon, as

all exoplanet detection methods have different sensitivities, and one method will often shed light where others could not. These problems will only grow larger as even more different datasets are combined, with myriad different precisions, susceptibility to stellar activity, and dimension.

I next turned my attention to stellar variability specifically, and how its different effects in different datasets can be used to understand stellar magnetic activity more deeply than any single dataset could alone. To start I focused on the system TOI-1136 in §4, a highly multiple TESS system with six known transiting exoplanets, and a possible seventh. The system is young ($\sim$ 700 Myr), and its RV and photometric data are highly contaminated with stellar variability signals. Furthermore, the unique resonance of the planets in the system contributed to large-amplitude TTV signals, adding to the complexity of any analysis. In order to best understand the true nature of TOI-1136, I combined transit timing data, RVs, and a GP model to account for stellar variability. If TOI-1136 were an older, quieter system, we likely could have characterized the system even more precisely, as the activity contamination was substantial. However, to truly understand the nature of exoplanet formation and evolution, we must study these young, multiple systems. Thus, we must study systems contaminated by stellar variability, and to do so, we must have practical techniques that separate stellar variability from exoplanet signals.

An effective way to do so is to utilize photometry to learn about stellar variability, rather than only looking for planetary transits. Photometric data is an abundant resource, and the relationship between photometric stellar variability caused by brightness variations, and RV variability caused by line shape variations, is well understood. How best to utilize this information, is less so. In §5, we perform a case study on Kepler-21, a Kepler system with know stellar activity contamination. We obtain NEID RV data simultaneous with TESS data, and we perform a wide variety of analyses of the system. We explore two primary methods of transferring stellar activity knowledge from photometry to RV data: namely

joint fits, and training a GP model on photometry before utilizing it on RVs. We found that both perform equally well for recovering the mass of the transiting exoplanet, but that training on Kepler photometry is still superior for discovering new planets.

We expand upon the Kepler-21 analysis in §6, by applying it to eight targets with Kepler/K2 photometry, and stellar activity contamination of their RVs. We perform injection-recovery tests to determine that, among multiple Kepler targets, Kepler photometry training indeed still appears superior when searching for additional exoplanets, but that this is less clear when utilizing K2 photometry. It seems that the tempral proximity of TESS to our new NEID RVs provides substantive advantage, despite K2/Kepler's increased precision and observing baseline. We also quantify the effects of simultaneous RVs, and confirm the widely held belief in the EPRV community: simultaneously acquired RVs and photometry are better for constraining and understanding stellar variability than when they are temporally distant.

The field of exoplanet science is consistently growing, and datasets with it. The same techniques that were effective ten years ago will not be effective on the challenging targets of today. To unravel the mysteries of exoplanet formation, evolution, and even more fundamental questions of life on other planets, we must refine not only our instruments, but our techniques. Multiple datasets can be utilized together to remove stellar variability, measure planet parameters that were impossible with only one dataset, and fully understand the nature of distant stellar systems. My studies on the combination of RV data, photometry, and astrometry show that data must be utilized in concert, and my final studies on stellar activity highlight the best ways to do so in the former datasets. The field still has a long way to go before the capability to detect Earth-like planets, but I have contributed a rung to the ladder that will eventually lead us there.

Bibliography

[1] E. Agol, C. Dorn, S. L. Grimm, M. Turbet, E. Ducrot, L. Delrez, M. Gillon, B.-O. Demory, A. Burdanov, K. Barkaoui, Z. Benkhaldoun, E. Bolmont, A. Burgasser, S. Carey, J. de Wit, D. Fabrycky, D. Foreman-Mackey, J. Haldemann, D. M. Hernandez, J. Ingalls, E. Jehin, Z. Langford, J. Leconte, S. M. Lederer, R. Luger, R. Malhotra, V. S. Meadows, B. M. Morris, F. J. Pozuelos, D. Queloz, S. N. Raymond, F. Selsis, M. Sestovic, A. H. M. J. Triaud, and V. Van Grootel. Refining the Transit-timing and Photometric Analysis of TRAPPIST-1: Masses, Radii, Densities, Dynamics, and Ephemerides. *Planetary Science Journal*, 2(1):1, Feb. 2021.

[2] E. Agol, R. Luger, and D. Foreman-Mackey. Analytic Planetary Transit Light Curves and Derivatives for Stars with Polynomial Limb Darkening. *Astronomical Journal*, 159(3):123, Mar. 2020.

[3] A. Aguichine, O. Mousis, M. Deleuil, and E. Marcq. Mass-Radius Relationships for Irradiated Ocean Planets. *The Astrophysical Journal*, 914(2):84, June 2021.

[4] S. Aigrain, J. Llama, T. Ceillier, M. L. d. Chagas, J. R. A. Davenport, R. A. García, K. L. Hay, A. F. Lanza, A. McQuillan, T. Mazeh, J. R. de Medeiros, M. B. Nielsen, and T. Reinhold. Testing the recovery of stellar rotation signals from Kepler light curves using a blind hare-and-hounds exercise. *Monthly Notices of the Royal Astronomical Society*, 450(3):3211–3226, July 2015.

[5] S. Aigrain, F. Pont, and S. Zucker. A simple method to estimate radial velocity variations due to stellar activity using photometry. *Monthly Notices of the Royal Astronomical Society*, 419(4):3147–3158, Feb. 2012.

[6] J. M. Akana Murphy, N. M. Batalha, N. Scarsdale, H. Isaacson, D. R. Ciardi, E. J. Gonzales, S. Giacalone, J. D. Twicken, A. Dattilo, T. Fetherolf, R. A. Rubenzahl, I. J. M. Crossfield, C. D. Dressing, B. Fulton, A. W. Howard, D. Huber, S. R. Kane, E. A. Petigura, P. Robertson, A. Roy, L. M. Weiss, C. Beard, A. Chontos, F. Dai, M. Rice, J. Van Zandt, J. Lubin, S. Blunt, A. S. Polanski, A. Behmard, P. A. Dalba, M. L. Hill, L. J. Rosenthal, C. L. Brinkman, A. W. Mayo, E. V. Turtelboom, I. Angelo, T. Močnik, M. G. MacDougall, D. Pidhorodetska, D. Tyler, M. R. Kosiarek, R. Holcomb, E. M. Louden, L. A. Hirsch, E. A. Gilbert, J. Anderson, and J. A. Valenti. The TESS-Keck Survey. XVI. Mass Measurements for 12 Planets in Eight Systems. *The Astronomical Journal*, 166(4):153, Oct. 2023.

[7] R. L. Akeson, X. Chen, D. Ciardi, M. Crane, J. Good, M. Harbut, E. Jackson, S. R. Kane, A. C. Laity, S. Leifer, M. Lynn, D. L. McElroy, M. Papin, P. Plavchan, S. V. Ramírez, R. Rey, K. von Braun, M. Wittman, M. Abajian, B. Ali, C. Beichman, A. Beekley, G. B. Berriman, S. Berukoff, G. Bryden, B. Chan, S. Groom, C. Lau, A. N. Payne, M. Regelson, M. Saucedo, M. Schmitz, J. Stauffer, P. Wyatt, and A. Zhang. The NASA Exoplanet Archive: Data and Tools for Exoplanet Research. *Publications of the Astronomical Society of the Pacific*, 125(930):989, Aug. 2013.

[8] F. Allard, D. Homeier, and B. Freytag. Models of very-low-mass stars, brown dwarfs and exoplanets. *Philosophical Transactions of the Royal Society of London Series A*, 370(1968):2765–2777, June 2012.

[9] J. M. Almenara, R. F. Díaz, X. Bonfils, and S. Udry. Absolute densities, masses, and radii of the WASP-47 system determined dynamically. *Astronomy and Astrophysics*, 595:L5, Oct. 2016.

[10] S. Ambikasaran, D. Foreman-Mackey, L. Greengard, D. W. Hogg, and M. O'Neil. Fast Direct Methods for Gaussian Processes. *IEEE Transactions on Pattern Analysis and Machine Intelligence*, 38:252, June 2015.

[11] D. R. Anderson, A. Collier Cameron, L. Delrez, A. P. Doyle, M. Gillon, C. Hellier, E. Jehin, M. Lendl, P. F. L. Maxted, N. Madhusudhan, F. Pepe, D. Pollacco, D. Queloz, D. Ségransan, B. Smalley, A. M. S. Smith, A. H. M. J. Triaud, O. D. Turner, S. Udry, and R. G. West. The discoveries of WASP-91b, WASP-105b and WASP-107b: Two warm Jupiters and a planet in the transition region between ice giants and gas giants. *Astronomy and Astrophysics*, 604:A110, Aug. 2017.

[12] G. Anglada-Escudé, P. J. Amado, J. Barnes, Z. M. Berdiñas, R. P. Butler, G. A. L. Coleman, I. de La Cueva, S. Dreizler, M. Endl, B. Giesers, S. V. Jeffers, J. S. Jenkins, H. R. A. Jones, M. Kiraga, M. Kürster, M. J. López-González, C. J. Marvin, N. Morales, J. Morin, R. P. Nelson, J. L. Ortiz, A. Ofir, S.-J. Paardekooper, A. Reiners, E. Rodríguez, C. Rodríguez-López, L. F. Sarmiento, J. P. Strachan, Y. Tsapras, M. Tuomi, and M. Zechmeister. A terrestrial planet candidate in a temperate orbit around Proxima Centauri. *Nature*, 536(7617):437–440, Aug. 2016.

[13] G. Anglada-Escudé, P. Arriagada, S. S. Vogt, E. J. Rivera, R. P. Butler, J. D. Crane, S. A. Shectman, I. B. Thompson, D. Minniti, N. Haghighipour, B. D. Carter, C. G. Tinney, R. A. Wittenmyer, J. A. Bailey, S. J. O'Toole, H. R. A. Jones, and J. S. Jenkins. A Planetary System around the nearby M Dwarf GJ 667C with At Least One Super-Earth in Its Habitable Zone. *The Astrophysical Journal Letters*, 751(1):L16, May 2012.

[14] G. Anglada-Escudé and R. P. Butler. The HARPS-TERRA Project. I. Description of the Algorithms, Performance, and New Measurements on a Few Remarkable Stars Observed by HARPS. *The Astrophysical Journal Supplement*, 200(2):15, June 2012.

[15] G. Anglada-Escudé, M. Tuomi, E. Gerlach, R. Barnes, R. Heller, J. S. Jenkins, S. Wende, S. S. Vogt, R. P. Butler, A. Reiners, and H. R. A. Jones. A dynamically-packed planetary system around GJ 667C with three super-Earths in its habitable zone. *Astronomy and Astrophysics*, 556:A126, Aug. 2013.

[16] P. J. Armitage. A Brief Overview of Planet Formation. In H. J. Deeg and J. A. Belmonte, editors, *Handbook of Exoplanets*, page 135. 2018.

[17] É. Artigau, J. Gagné, J. Faherty, L. Malo, M.-E. Naud, R. Doyon, D. Lafrenière, and Y. Beletsky. BANYAN. VI. Discovery of a Companion at the Brown Dwarf/Planet-Mass Limit to a Tucana-Horologium M Dwarf. *The Astrophysical Journal*, 806(2):254, June 2015.

[18] S. Ataiee and W. Kley. The role of disc torques in forming resonant planetary systems. *Astronomy and Astrophysics*, 635:A204, Mar. 2020.

[19] M. Auvergne, P. Bodin, L. Boisnard, J. T. Buey, S. Chaintreuil, G. Epstein, M. Jouret, T. Lam-Trong, P. Levacher, A. Magnan, R. Perez, P. Plasson, J. Plesseria, G. Peter, M. Steller, D. Tiphène, A. Baglin, P. Agogué, T. Appourchaux, D. Barbet, T. Beaufort, R. Bellenger, R. Berlin, P. Bernardi, D. Blouin, P. Boumier, F. Bonneau, R. Briet, B. Butler, R. Cautain, F. Chiavassa, V. Costes, J. Cuvilho, V. Cunha-Parro, F. de Oliveira Fialho, M. Decaudin, J. M. Defise, S. Djalal, A. Docclo, R. Drummond, O. Dupuis, G. Exil, C. Fauré, A. Gaboriaud, P. Gamet, P. Gavalda, E. Grolleau, L. Gueguen, V. Guivarc'h, P. Guterman, J. Hasiba, G. Huntzinger, H. Hustaix, C. Imbert, G. Jeanville, B. Johlander, L. Jorda, P. Journoud, F. Karioty, L. Kerjean, L. Lafond, V. Lapeyrere, P. Landiech, T. Larqué, P. Laudet, J. Le Merrer, L. Leporati, B. Leruyet, B. Levieuge, A. Llebaria, L. Martin, E. Mazy, J. M. Mesnager, J. P. Michel, J. P. Moalic, W. Monjoin, D. Naudet, S. Neukirchner, K. Nguyen-Kim, M. Ollivier, J. L. Orcesi, H. Ottacher, A. Oulali, J. Parisot, S. Perruchot, A. Piacentino, L. Pinheiro da Silva, J. Platzer, B. Pontet, A. Pradines, C. Quentin, U. Rohbeck, G. Rolland, F. Rollenhagen, R. Romagnan, N. Russ, R. Samadi, R. Schmidt, N. Schwartz, I. Sebbag, H. Smit, W. Sunter, M. Tello, P. Toulouse, B. Ulmer, O. Vandermarcq, E. Vergnault, R. Wallner, G. Waultier, and P. Zanatta. The CoRoT satellite in flight: description and performance. *Astronomy and Astrophysics*, 506(1):411–424, Oct. 2009.

[20] G. Bagnasco, M. Kolm, P. Ferruit, K. Honnen, J. Koehler, R. Lemke, M. Maschmann, M. Melf, G. Noyer, P. Rumler, J.-C. Salvignol, P. Strada, and M. Te Plate. Overview of the near-infrared spectrograph (NIRSpec) instrument on-board the James Webb Space Telescope (JWST). In J. B. Heaney and L. G. Burriesci, editors, *Cryogenic Optical Systems and Instruments XII*, volume 6692 of *Society of Photo-Optical Instrumentation Engineers (SPIE) Conference Series*, page 66920M, Sept. 2007.

[21] C. A. L. Bailer-Jones, J. Rybizki, M. Fouesneau, M. Demleitner, and R. Andrae. Estimating Distances from Parallaxes. V. Geometric and Photogeometric Distances to 1.47 Billion Stars in Gaia Early Data Release 3. *Astronomical Journal*, 161(3):147, Mar. 2021.

[22] C. A. L. Bailer-Jones, J. Rybizki, M. Fouesneau, G. Mantelet, and R. Andrae. Estimating Distance from Parallaxes. IV. Distances to 1.33 Billion Stars in Gaia Data Release 2. *Astronomical Journal*, 156(2):58, Aug. 2018.

[23] G. Bakos, R. W. Noyes, G. Kovács, K. Z. Stanek, D. D. Sasselov, and I. Domsa. Wide-Field Millimagnitude Photometry with the HAT: A Tool for Extrasolar Planet Detection. *Publications of the Astronomical Society of the Pacific*, 116(817):266–277, Mar. 2004.

[24] G. Á. Bakos, D. Bayliss, J. Bento, W. Bhatti, R. Brahm, Z. Csubry, N. Espinoza, J. D. Hartman, T. Henning, A. Jordán, L. Mancini, K. Penev, M. Rabus, P. Sarkis, V. Suc, M. de Val-Borro, G. Zhou, R. P. Butler, J. Crane, S. Durkan, S. Shectman, J. Kim, J. Lázár, I. Papp, P. Sári, G. Ricker, R. Vanderspek, D. W. Latham, S. Seager, J. N. Winn, J. Jenkins, A. D. Chacon, G. Fűrész, B. Goeke, J. Li, S. Quinn, E. V. Quintana, P. Tenenbaum, J. Teske, M. Vezie, L. Yu, C. Stockdale, P. Evans, and H. M. Relles. HATS-71b: A Giant Planet Transiting an M3 Dwarf Star in TESS Sector 1. *Astronomical Journal*, 159(6):267, June 2020.

[25] S. Ballard. Predicted Number, Multiplicity, and Orbital Dynamics of TESS M-dwarf Exoplanets. *Astronomical Journal*, 157(3):113, Mar. 2019.

[26] A. Baranne, D. Queloz, M. Mayor, G. Adrianzyk, G. Knispel, D. Kohler, D. Lacroix, J. P. Meunier, G. Rimbaud, and A. Vin. ELODIE: A spectrograph for accurate radial velocity measurements. *Astronomy and Astrophysics, Supplemental*, 119:373–390, Oct. 1996.

[27] T. Barclay, J. F. Rowe, J. J. Lissauer, D. Huber, F. Fressin, S. B. Howell, S. T. Bryson, W. J. Chaplin, J.-M. Désert, E. D. Lopez, G. W. Marcy, F. Mullally, D. Ragozzine, G. Torres, E. R. Adams, E. Agol, D. Barrado, S. Basu, T. R. Bedding, L. A. Buchhave, D. Charbonneau, J. L. Christiansen, J. Christensen-Dalsgaard, D. Ciardi, W. D. Cochran, A. K. Dupree, Y. Elsworth, M. Everett, D. A. Fischer, E. B. Ford, J. J. Fortney, J. C. Geary, M. R. Haas, R. Handberg, S. Hekker, C. E. Henze, E. Horch, A. W. Howard, R. C. Hunter, H. Isaacson, J. M. Jenkins, C. Karoff, S. D. Kawaler, H. Kjeldsen, T. C. Klaus, D. W. Latham, J. Li, J. Lillo-Box, M. N. Lund, M. Lundkvist, T. S. Metcalfe, A. Miglio, R. L. Morris, E. V. Quintana, D. Stello, J. C. Smith, M. Still, and S. E. Thompson. A sub-Mercury-sized exoplanet. *Nature*, 494(7438):452–454, Feb. 2013.

[28] S. C. C. Barros, H. Gosselin, J. Lillo-Box, D. Bayliss, E. Delgado Mena, B. Brugger, A. Santerne, D. J. Armstrong, V. Adibekyan, J. D. Armstrong, D. Barrado, J. Bento, I. Boisse, A. S. Bonomo, F. Bouchy, D. J. A. Brown, W. D. Cochran, A. Collier Cameron, M. Deleuil, O. Demangeon, R. F. Díaz, A. Doyle, X. Dumusque, D. Ehrenreich, N. Espinoza, F. Faedi, J. P. Faria, P. Figueira, E. Foxell, G. Hébrard, S. Hojjatpanah, J. Jackman, M. Lendl, R. Ligi, C. Lovis, C. Melo, O. Mousis, J. J. Neal, H. P. Osborn, D. Pollacco, N. C. Santos, R. Sefako, A. Shporer, S. G. Sousa, A. H. M. J. Triaud, S. Udry, A. Vigan, and A. Wyttenbach. Precise masses for the

transiting planetary system HD 106315 with HARPS. *Astronomy and Astrophysics*, 608:A25, Dec. 2017.

[29] F. A. Bastien, K. G. Stassun, J. Pepper, J. T. Wright, S. Aigrain, G. Basri, J. A. Johnson, A. W. Howard, and L. M. Walkowicz. Radial Velocity Variations of Photometrically Quiet, Chromospherically Inactive Kepler Stars: A Link between RV Jitter and Photometric Flicker. *The Astronomical Journal*, 147(2):29, Feb. 2014.

[30] N. E. Batalha, T. Lewis, J. J. Fortney, N. M. Batalha, E. Kempton, N. K. Lewis, and M. R. Line. The Precision of Mass Measurements Required for Robust Atmospheric Characterization of Transiting Exoplanets. *The Astrophysical Journal Letters*, 885(1):L25, Nov. 2019.

[31] N. E. Batalha, T. Lewis, J. J. Fortney, N. M. Batalha, E. Kempton, N. K. Lewis, and M. R. Line. The Precision of Mass Measurements Required for Robust Atmospheric Characterization of Transiting Exoplanets. *The Astrophysical Journal Letters*, 885(1):L25, Nov. 2019.

[32] N. E. Batalha, A. Mandell, K. Pontoppidan, K. B. Stevenson, N. K. Lewis, J. Kalirai, N. Earl, T. Greene, L. Albert, and L. D. Nielsen. PandExo: A Community Tool for Transiting Exoplanet Science with JWST & HST. *Publications of the Astronomical Society of the Pacific*, 129(976):064501, June 2017.

[33] K. Batygin. Capture of planets into mean-motion resonances and the origins of extrasolar orbital architectures. *Monthly Notices of the Royal Astronomical Society*, 451(3):2589–2609, Aug. 2015.

[34] K. Batygin and A. Morbidelli. Dissipative Divergence of Resonant Orbits. *The Astronomical Journal*, 145(1):1, Jan. 2013.

[35] J. L. Bean, S. N. Raymond, and J. E. Owen. The Nature and Origins of Sub-Neptune Size Planets. *Journal of Geophysical Research (Planets)*, 126(1):e06639, Jan. 2021.

[36] C. Beard. TOI-1136 Analysis Code, 2023.

[37] C. Beard. LApprox, 2024.

[38] C. Beard, P. Robertson, F. Dai, R. Holcomb, J. Lubin, J. M. Akana Murphy, N. M. Batalha, S. Blunt, I. Crossfield, C. Dressing, B. Fulton, A. W. Howard, D. Huber, H. Isaacson, S. R. Kane, G. Nowak, E. A. Petigura, A. Roy, R. A. Rubenzahl, L. M. Weiss, R. Barrena, A. Behmard, C. L. Brinkman, I. Carleo, A. Chontos, P. A. Dalba, T. Fetherolf, S. Giacalone, M. L. Hill, K. Kawauchi, J. Korth, R. Luque, M. G. MacDougall, A. W. Mayo, T. Močnik, G. Morello, F. Murgas, J. Orell-Miquel, E. Palle, A. S. Polanski, M. Rice, N. Scarsdale, D. Tyler, and J. Van Zandt. The TESS-Keck Survey. XVII. Precise Mass Measurements in a Young, High-multiplicity Transiting Planet System Using Radial Velocities and Transit Timing Variations. *The Astronomical Journal*, 167(2):70, Feb. 2024.

[39] C. Beard, P. Robertson, S. Kanodia, J. Libby-Roberts, C. I. Cañas, A. F. Gupta, R. Holcomb, S. Jones, H. A. Kobulnicky, A. S. J. Lin, J. Lubin, M. Maney, B. A. Parker, G. Stefánsson, W. D. Cochran, M. Endl, L. Hebb, S. Mahadevan, J. Wisniewski, C. F. Bender, S. A. Diddams, M. Everett, C. Fredrick, S. Halverson, F. Hearty, A. J. Metcalf, A. Monson, J. P. Ninan, A. Roy, M. Schutte, C. Schwab, and R. C. Terrien. TOI-1696 and TOI-2136: Constraining the Masses of Two Mini-Neptunes with the Habitable-Zone Planet Finder. *Astronomical Journal*, 163(6):286, June 2022.

[40] C. Beard, P. Robertson, S. Kanodia, J. Lubin, C. I. Cañas, A. F. Gupta, R. Holcomb, S. Jones, J. E. Libby-Roberts, A. S. J. Lin, S. Mahadevan, G. Stefánsson, C. F. Bender, C. H. Blake, W. D. Cochran, M. Endl, M. Everett, E. B. Ford, C. Fredrick, S. Halverson, L. Hebb, D. Li, S. E. Logsdon, J. Luhn, M. W. McElwain, A. J. Metcalf, J. P. Ninan, J. Rajagopal, A. Roy, M. Schutte, C. Schwab, R. C. Terrien, J. Wisniewski, and J. T. Wright. GJ 3929: High-precision Photometric and Doppler Characterization of an Exo-Venus and Its Hot, Mini-Neptune-mass Companion. *The Astrophysical Journal*, 936(1):55, Sept. 2022.

[41] J. C. Becker, A. Vanderburg, F. C. Adams, S. A. Rappaport, and H. M. Schwengeler. WASP-47: A Hot Jupiter System with Two Additional Planets Discovered by K2. *The Astrophysical Journal Letters*, 812(2):L18, Oct. 2015.

[42] E. C. Bellm, S. R. Kulkarni, M. J. Graham, R. Dekany, R. M. Smith, R. Riddle, F. J. Masci, G. Helou, T. A. Prince, S. M. Adams, C. Barbarino, T. Barlow, J. Bauer, R. Beck, J. Belicki, R. Biswas, N. Blagorodnova, D. Bodewits, B. Bolin, V. Brinnel, T. Brooke, B. Bue, M. Bulla, R. Burruss, S. B. Cenko, C.-K. Chang, A. Connolly, M. Coughlin, J. Cromer, V. Cunningham, K. De, A. Delacroix, V. Desai, D. A. Duev, G. Eadie, T. L. Farnham, M. Feeney, U. Feindt, D. Flynn, A. Franckowiak, S. Frederick, C. Fremling, A. Gal-Yam, S. Gezari, M. Giomi, D. A. Goldstein, V. Z. Golkhou, A. Goobar, S. Groom, E. Hacopians, D. Hale, J. Henning, A. Y. Q. Ho, D. Hover, J. Howell, T. Hung, D. Huppenkothen, D. Imel, W.-H. Ip, Ž. Ivezić, E. Jackson, L. Jones, M. Juric, M. M. Kasliwal, S. Kaspi, S. Kaye, M. S. P. Kelley, M. Kowalski, E. Kramer, T. Kupfer, W. Landry, R. R. Laher, C.-D. Lee, H. W. Lin, Z.-Y. Lin, R. Lunnan, M. Giomi, A. Mahabal, P. Mao, A. A. Miller, S. Monkewitz, P. Murphy, C.-C. Ngeow, J. Nordin, P. Nugent, E. Ofek, M. T. Patterson, B. Penprase, M. Porter, L. Rauch, U. Rebbapragada, D. Reiley, M. Rigault, H. Rodriguez, J. van Roestel, B. Rusholme, J. van Santen, S. Schulze, D. L. Shupe, L. P. Singer, M. T. Soumagnac, R. Stein, J. Surace, J. Sollerman, P. Szkody, F. Taddia, S. Terek, A. Van Sistine, S. van Velzen, W. T. Vestrand, R. Walters, C. Ward, Q.-Z. Ye, P.-C. Yu, L. Yan, and J. Zolkower. The Zwicky Transient Facility: System Overview, Performance, and First Results. *Publications of the Astronomical Society of the Pacific*, 131(995):018002, Jan. 2019.

[43] B. Benneke and S. Seager. Atmospheric Retrieval for Super-Earths: Uniquely Constraining the Atmospheric Composition with Transmission Spectroscopy. *The Astrophysical Journal*, 753(2):100, July 2012.

[44] O. Benomar, M. Bazot, M. B. Nielsen, L. Gizon, T. Sekii, M. Takata, H. Hotta, S. Hanasoge, K. R. Sreenivasan, and J. Christensen-Dalsgaard. Asteroseismic detection of latitudinal differential rotation in 13 Sun-like stars. *Science*, 361(6408):1231–1234, Sept. 2018.

[45] T. A. Berger, D. Huber, E. Gaidos, and J. L. van Saders. Revised Radii of Kepler Stars and Planets Using Gaia Data Release 2. *The Astrophysical Journal*, 866(2):99, Oct. 2018.

[46] T. A. Berger, D. Huber, E. Gaidos, J. L. van Saders, and L. M. Weiss. The Gaia-Kepler Stellar Properties Catalog. II. Planet Radius Demographics as a Function of Stellar Mass and Age. *The Astronomical Journal*, 160(3):108, Sept. 2020.

[47] T. A. Berger, D. Huber, E. Gaidos, J. L. van Saders, and L. M. Weiss. The Gaia-Kepler Stellar Properties Catalog. II. Planet Radius Demographics as a Function of Stellar Mass and Age. *The Astronomical Journal*, 160(3):108, Sept. 2020.

[48] T. A. Berger, D. Huber, J. L. van Saders, E. Gaidos, J. Tayar, and A. L. Kraus. The Gaia-Kepler Stellar Properties Catalog. I. Homogeneous Fundamental Properties for 186,301 Kepler Stars. *The Astronomical Journal*, 159(6):280, June 2020.

[49] M. Betancourt. A Conceptual Introduction to Hamiltonian Monte Carlo. *arXiv e-prints*, page arXiv:1701.02434, Jan. 2017.

[50] B. Bitsch, S. N. Raymond, L. A. Buchhave, A. Bello-Arufe, A. D. Rathcke, and A. D. Schneider. Dry or water world? How the water contents of inner sub-Neptunes constrain giant planet formation and the location of the water ice line. *Astronomy and Astrophysics*, 649:L5, May 2021.

[51] S. Blunt, A. Carvalho, T. J. David, C. Beichman, J. K. Zink, E. Gaidos, A. Behmard, L. G. Bouma, D. Cody, F. Dai, D. Foreman-Mackey, S. Grunblatt, A. W. Howard, M. Kosiarek, H. A. Knutson, R. A. Rubenzahl, C. Beard, A. Chontos, S. Giacalone, T. Hirano, M. C. Johnson, J. Lubin, J. M. Akana Murphy, E. A. Petigura, J. Van Zandt, and L. Weiss. Overfitting Affects the Reliability of Radial Velocity Mass Estimates of the V1298 Tau Planets. *The Astronomical Journal*, 166(2):62, Aug. 2023.

[52] S. Blunt, E. L. Nielsen, R. J. De Rosa, Q. M. Konopacky, D. Ryan, J. J. Wang, L. Pueyo, J. Rameau, C. Marois, F. Marchis, B. Macintosh, J. R. Graham, G. Duchêne, and A. C. Schneider. Orbits for the Impatient: A Bayesian Rejection-sampling Method for Quickly Fitting the Orbits of Long-period Exoplanets. *The Astronomical Journal*, 153(5):229, May 2017.

[53] A. J. Bohn, M. A. Kenworthy, C. Ginski, S. Rieder, E. E. Mamajek, T. Meshkat, M. J. Pecaut, M. Reggiani, J. de Boer, C. U. Keller, F. Snik, and J. Southworth. Two Directly Imaged, Wide-orbit Giant Planets around the Young, Solar Analog TYC 8998-760-1. *The Astrophysical Journal Letters*, 898(1):L16, July 2020.

[54] X. Bonfils, J. M. Almenara, R. Cloutier, A. Wünsche, N. Astudillo-Defru, Z. Berta-Thompson, F. Bouchy, D. Charbonneau, X. Delfosse, R. F. Díaz, J. Dittmann, R. Doyon, T. Forveille, J. Irwin, C. Lovis, M. Mayor, K. Menou, F. Murgas, E. Newton, F. Pepe, N. C. Santos, and S. Udry. Radial velocity follow-up of GJ1132 with HARPS. A precise mass for planet b and the discovery of a second planet. *Astronomy and Astrophysics*, 618:A142, Oct. 2018.

[55] X. Bonfils, X. Delfosse, S. Udry, N. C. Santos, T. Forveille, and D. Ségransan. Metallicity of M dwarfs. I. A photometric calibration and the impact on the mass-luminosity relation at the bottom of the main sequence. *Astronomy and Astrophysics*, 442(2):635–642, Nov. 2005.

[56] A. S. Bonomo, X. Dumusque, A. Massa, A. Mortier, R. Bongiolatti, L. Malavolta, A. Sozzetti, L. A. Buchhave, M. Damasso, R. D. Haywood, A. Morbidelli, D. W. Latham, E. Molinari, F. Pepe, E. Poretti, S. Udry, L. Affer, W. Boschin, D. Charbonneau, R. Cosentino, M. Cretignier, A. Ghedina, E. Lega, M. López-Morales, M. Margini, A. F. Martínez Fiorenzano, M. Mayor, G. Micela, M. Pedani, M. Pinamonti, K. Rice, D. Sasselov, R. Tronsgaard, and A. Vanderburg. Cold Jupiters and improved masses in 38 Kepler and K2 small planet systems from 3661 HARPS-N radial velocities. No excess of cold Jupiters in small planet systems. *Astronomy and Astrophysics*, 677:A33, Sept. 2023.

[57] W. J. Borucki, D. Koch, G. Basri, N. Batalha, T. Brown, D. Caldwell, J. Caldwell, J. Christensen-Dalsgaard, W. D. Cochran, E. DeVore, E. W. Dunham, A. K. Dupree, T. N. Gautier, J. C. Geary, R. Gilliland, A. Gould, S. B. Howell, J. M. Jenkins, Y. Kondo, D. W. Latham, G. W. Marcy, S. Meibom, H. Kjeldsen, J. J. Lissauer, D. G. Monet, D. Morrison, D. Sasselov, J. Tarter, A. Boss, D. Brownlee, T. Owen, D. Buzasi, D. Charbonneau, L. Doyle, J. Fortney, E. B. Ford, M. J. Holman, S. Seager, J. H. Steffen, W. F. Welsh, J. Rowe, H. Anderson, L. Buchhave, D. Ciardi, L. Walkowicz, W. Sherry, E. Horch, H. Isaacson, M. E. Everett, D. Fischer, G. Torres, J. A. Johnson, M. Endl, P. MacQueen, S. T. Bryson, J. Dotson, M. Haas, J. Kolodziejczak, J. Van Cleve, H. Chandrasekaran, J. D. Twicken, E. V. Quintana, B. D. Clarke, C. Allen, J. Li, H. Wu, P. Tenenbaum, E. Verner, F. Bruhweiler, J. Barnes, and A. Prsa. Kepler Planet-Detection Mission: Introduction and First Results. *Science*, 327(5968):977, Feb. 2010.

[58] W. J. Borucki, D. G. Koch, G. Basri, N. Batalha, T. M. Brown, S. T. Bryson, D. Caldwell, J. Christensen-Dalsgaard, W. D. Cochran, E. DeVore, E. W. Dunham, I. Gautier, Thomas N., J. C. Geary, R. Gilliland, A. Gould, S. B. Howell, J. M. Jenkins, D. W. Latham, J. J. Lissauer, G. W. Marcy, J. Rowe, D. Sasselov, A. Boss, D. Charbonneau, D. Ciardi, L. Doyle, A. K. Dupree, E. B. Ford, J. Fortney, M. J. Holman, S. Seager, J. H. Steffen, J. Tarter, W. F. Welsh, C. Allen, L. A. Buchhave, J. L. Christiansen, B. D. Clarke, S. Das, J.-M. Désert, M. Endl, D. Fabrycky, F. Fressin, M. Haas, E. Horch, A. Howard, H. Isaacson, H. Kjeldsen, J. Kolodziejczak, C. Kulesa, J. Li, P. W. Lucas, P. Machalek, D. McCarthy, P. MacQueen, S. Meibom, T. Miquel, A. Prsa, S. N. Quinn, E. V. Quintana, D. Ragozzine, W. Sherry, A. Shporer,

P. Tenenbaum, G. Torres, J. D. Twicken, J. Van Cleve, L. Walkowicz, F. C. Witteborn, and M. Still. Characteristics of Planetary Candidates Observed by Kepler. II. Analysis of the First Four Months of Data. *The Astrophysical Journal*, 736(1):19, July 2011.

[59] W. J. Borucki and A. L. Summers. The photometric method of detecting other planetary systems. *Icarus*, 58(1):121–134, Apr. 1984.

[60] J. Bradbury, R. Frostig, P. Hawkins, M. J. Johnson, C. Leary, D. Maclaurin, G. Necula, A. Paszke, J. VanderPlas, S. Wanderman-Milne, and Q. Zhang. JAX: composable transformations of Python+NumPy programs, 2018.

[61] T. D. Brandt. The Hipparcos-Gaia Catalog of Accelerations. *Astrophysical Journal, Supplement*, 239(2):31, Dec. 2018.

[62] T. D. Brandt. The Hipparcos-Gaia Catalog of Accelerations: Gaia EDR3 Edition. *Astrophysical Journal, Supplement*, 254(2):42, June 2021.

[63] T. M. Brown, N. Baliber, F. B. Bianco, M. Bowman, B. Burleson, P. Conway, M. Crellin, É. Depagne, J. De Vera, B. Dilday, D. Dragomir, M. Dubberley, J. D. Eastman, M. Elphick, M. Falarski, S. Foale, M. Ford, B. J. Fulton, J. Garza, E. L. Gomez, M. Graham, R. Greene, B. Haldeman, E. Hawkins, B. Haworth, R. Haynes, M. Hidas, A. E. Hjelstrom, D. A. Howell, J. Hygelund, T. A. Lister, R. Lobdill, J. Martinez, D. S. Mullins, M. Norbury, J. Parrent, R. Paulson, D. L. Petry, A. Pickles, V. Posner, W. E. Rosing, R. Ross, D. J. Sand, E. S. Saunders, J. Shobbrook, A. Shporer, R. A. Street, D. Thomas, Y. Tsapras, J. R. Tufts, S. Valenti, K. Vander Horst, Z. Walker, G. White, and M. Willis. Las Cumbres Observatory Global Telescope Network. *Publications of the Astronomical Society of the Pacific*, 125(931):1031, Sept. 2013.

[64] C. J. Burke, J. L. Christiansen, F. Mullally, S. Seader, D. Huber, J. F. Rowe, J. L. Coughlin, S. E. Thompson, J. Catanzarite, B. D. Clarke, T. D. Morton, D. A. Caldwell, S. T. Bryson, M. R. Haas, N. M. Batalha, J. M. Jenkins, P. Tenenbaum, J. D. Twicken, J. Li, E. Quintana, T. Barclay, C. E. Henze, W. J. Borucki, S. B. Howell, and M. Still. Terrestrial Planet Occurrence Rates for the Kepler GK Dwarf Sample. *The Astrophysical Journal*, 809(1):8, Aug. 2015.

[65] C. J. Burke, A. Levine, M. Fausnaugh, R. Vanderspek, T. Barclay, J. E. Libby-Roberts, B. Morris, B. Sipocz, M. Owens, A. D. Feinstein, and J. Camacho. TESS-Point: High precision TESS pointing tool, Mar. 2020.

[66] A. Burrows, S. Halverson, J. C. Siegel, C. Gilbertson, J. Luhn, J. Burt, C. F. Bender, A. Roy, R. C. Terrien, S. Vangstein, S. Mahadevan, J. T. Wright, P. Robertson, E. B. Ford, G. Stefánsson, J. P. Ninan, C. H. Blake, M. W. McElwain, C. Schwab, and J. Zhao. The Death of Vulcan: NEID Reveals That the Planet Candidate Orbiting HD 26965 Is Stellar Activity. *The Astronomical Journal*, 167(5):243, May 2024.

[67] J. A. Burt, L. D. Nielsen, S. N. Quinn, E. E. Mamajek, E. C. Matthews, G. Zhou, J. V. Seidel, C. X. Huang, E. Lopez, M. Soto, J. Otegi, K. G. Stassun, L. Kreidberg, K. A.

Collins, J. D. Eastman, J. E. Rodriguez, A. Vanderburg, S. P. Halverson, J. K. Teske, S. X. Wang, R. P. Butler, F. Bouchy, X. Dumusque, D. Segransen, S. A. Shectman, J. D. Crane, F. Feng, B. T. Montet, A. D. Feinstein, Y. Beletski, E. Flowers, M. N. Günther, T. Daylan, K. I. Collins, D. M. Conti, T. Gan, E. L. N. Jensen, J. F. Kielkopf, T.-G. Tan, R. Helled, C. Dorn, J. Haldemann, J. J. Lissauer, G. R. Ricker, R. Vanderspek, D. W. Latham, S. Seager, J. N. Winn, J. M. Jenkins, J. D. Twicken, J. C. Smith, P. Tenenbaum, S. Cartwright, T. Barclay, J. Pepper, G. Esquerdo, and W. Fong. TOI-824 b: A New Planet on the Lower Edge of the Hot Neptune Desert. *Astronomical Journal*, 160(4):153, Oct. 2020.

[68] R. P. Butler and G. W. Marcy. A Planet Orbiting 47 Ursae Majoris. *The Astrophysical Journall*, 464:L153, June 1996.

[69] R. P. Butler, G. W. Marcy, E. Williams, H. Hauser, and P. Shirts. Three New "51 Pegasi-Type" Planets. *The Astrophysical Journall*, 474(2):L115–L118, Jan. 1997.

[70] R. P. Butler, G. W. Marcy, E. Williams, C. McCarthy, P. Dosanjh, and S. S. Vogt. Attaining Doppler Precision of 3 M s-1. *Publications of the ASP*, 108:500, June 1996.

[71] R. P. Butler, S. S. Vogt, G. Laughlin, J. A. Burt, E. J. Rivera, M. Tuomi, J. Teske, P. Arriagada, M. Diaz, B. Holden, and S. Keiser. The LCES HIRES/Keck Precision Radial Velocity Exoplanet Survey. *The Astronomical Journal*, 153(5):208, May 2017.

[72] C. I. Cañas, S. Kanodia, C. F. Bender, S. Mahadevan, G. Stefánsson, W. D. Cochran, A. S. J. Lin, L. Powers, A. Monson, E. M. Green, B. A. Parker, T. N. Swaby, H. A. Kobulnicky, J. Wisniewski, A. F. Gupta, M. E. Everett, S. Jones, B. Anjakos, C. Beard, C. H. Blake, S. A. Diddams, Z. Dong, C. Fredrick, E. Hakemiamjad, L. Hebb, J. E. Libby-Roberts, S. E. Logsdon, M. W. McElwain, A. J. Metcalf, J. P. Ninan, J. Rajagopal, L. W. Ramsey, P. Robertson, A. Roy, J. Ruhle, C. Schwab, R. C. Terrien, and J. T. Wright. Two gas giants transiting M dwarfs confirmed with HPF and NEID. *arXiv e-prints*, page arXiv:2201.09963, Jan. 2022.

[73] J. Cabrera, S. Csizmadia, H. Lehmann, R. Dvorak, D. Gandolfi, H. Rauer, A. Erikson, C. Dreyer, P. Eigmüller, and A. Hatzes. The Planetary System to KIC 11442793: A Compact Analogue to the Solar System. *The Astrophysical Journal*, 781(1):18, Jan. 2014.

[74] B. L. Cale, M. Reefe, P. Plavchan, A. Tanner, E. Gaidos, J. Gagné, P. Gao, S. R. Kane, V. J. S. Béjar, N. Lodieu, G. Anglada-Escudé, I. Ribas, E. Pallé, A. Quirrenbach, P. J. Amado, A. Reiners, J. A. Caballero, M. Rosa Zapatero Osorio, S. Dreizler, A. W. Howard, B. J. Fulton, S. Xuesong Wang, K. I. Collins, M. El Mufti, J. Wittrock, E. A. Gilbert, T. Barclay, B. Klein, E. Martioli, R. Wittenmyer, D. Wright, B. Addison, T. Hirano, M. Tamura, T. Kotani, N. Narita, D. Vermilion, R. A. Lee, C. Geneser, J. Teske, S. N. Quinn, D. W. Latham, G. A. Esquerdo, M. L. Calkins, P. Berlind, F. Zohrabi, C. Stibbards, S. Kotnana, J. Jenkins, J. D. Twicken, C. Henze, R. Kidwell, C. Burke, J. Villaseñor, and P. Boyd. Diving Beneath the Sea of Stellar Activity: Chromatic Radial Velocities of the Young AU Mic Planetary System. *The Astronomical Journal*, 162(6):295, Dec. 2021.

[75] A. Castro González, E. Díez Alonso, J. Menéndez Blanco, J. H. Livingston, J. P. de Leon, S. L. Suárez Gómez, C. González Gutiérrez, F. García Riesgo, L. Bonavera, F. J. Iglesias Rodríguez, R. Muñiz, M. E. Everett, N. J. Scott, S. B. Howell, D. R. Ciardi, E. J. Gonzales, J. E. Schlieder, and F. J. de Cos Juez. Planetary candidates transiting cool dwarf stars from campaigns 12 to 15 of K2. *Monthly Notices of the Royal Astronomical Society*, 499(4):5416–5441, Dec. 2020.

[76] H. M. Cegla, C. A. Watson, S. Shelyag, M. Mathioudakis, and S. Moutari. Stellar Surface Magnetoconvection as a Source of Astrophysical Noise. III. Sun-as-a-Star Simulations and Optimal Noise Diagnostics. *The Astrophysical Journal*, 879(1):55, July 2019.

[77] W. J. Chaplin, H. M. Cegla, C. A. Watson, G. R. Davies, and W. H. Ball. Filtering Solar-Like Oscillations for Exoplanet Detection in Radial Velocity Observations. *The Astronomical Journal*, 157(4):163, Apr. 2019.

[78] D. Charbonneau, T. M. Brown, D. W. Latham, and M. Mayor. Detection of Planetary Transits Across a Sun-like Star. *The Astrophysical Journal Letters*, 529(1):L45–L48, Jan. 2000.

[79] S. Chatterjee and E. B. Ford. Planetesimal Interactions Can Explain the Mysterious Period Ratios of Small Near-Resonant Planets. *The Astrophysical Journal*, 803(1):33, Apr. 2015.

[80] J. Chen and D. Kipping. Probabilistic Forecasting of the Masses and Radii of Other Worlds. *The Astrophysical Journal*, 834(1):17, Jan. 2017.

[81] A. Claret, P. H. Hauschildt, and S. Witte. New limb-darkening coefficients for PHOENIX/1D model atmospheres. I. Calculations for 1500 K $\leq$ T_{eff} $\leq$ 4800 K Kepler, CoRot, Spitzer, uvby, UBVRIJHK, Sloan, and 2MASS photometric systems. *Astronomy and Astrophysics*, 546:A14, Oct. 2012.

[82] A. Claret, P. H. Hauschildt, and S. Witte. New limb-darkening coefficients for Phoenix/1d model atmospheres. II. Calculations for 5000 K $\leq$ T_{eff} $\leq$ 10 000 K Kepler, CoRot, Spitzer, uvby, UBVRIJHK, Sloan, and 2MASS photometric systems. *Astronomy and Astrophysics*, 552:A16, Apr. 2013.

[83] S. A. Clough, M. W. Shephard, E. J. Mlawer, J. S. Delamere, M. J. Iacono, K. Cady-Pereira, S. Boukabara, and P. D. Brown. Atmospheric radiative transfer modeling: a summary of the AER codes. *Journal of Quantitative Spectroscopy and Radiative Transfer*, 91(2):233–244, Mar. 2005.

[84] R. Cloutier and K. Menou. Evolution of the Radius Valley around Low-mass Stars from Kepler and K2. *Astronomical Journal*, 159(5):211, May 2020.

[85] A. Collier Cameron, D. Pollacco, R. A. Street, T. A. Lister, R. G. West, D. M. Wilson, F. Pont, D. J. Christian, W. I. Clarkson, B. Enoch, A. Evans, A. Fitzsimmons, C. A. Haswell, C. Hellier, S. T. Hodgkin, K. Horne, J. Irwin, S. R. Kane, F. P. Keenan,

A. J. Norton, N. R. Parley, J. Osborne, R. Ryans, I. Skillen, and P. J. Wheatley. A fast hybrid algorithm for exoplanetary transit searches. *Monthly Notices of the Royal Astronomical Society*, 373(2):799–810, Dec. 2006.

[86] K. A. Collins, J. F. Kielkopf, K. G. Stassun, and F. V. Hessman. AstroImageJ: Image Processing and Photometric Extraction for Ultra-precise Astronomical Light Curves. *Astronomical Journal*, 153(2):77, Feb. 2017.

[87] J. Colomé, K. Casteels, I. Ribas, and X. Francisco. The TJO-OAdM Robotic Observatory: the scheduler. In N. M. Radziwill and A. Bridger, editors, *Software and Cyberinfrastructure for Astronomy*, volume 7740 of *Society of Photo-Optical Instrumentation Engineers (SPIE) Conference Series*, page 77403K, July 2010.

[88] R. Cosentino, C. Lovis, F. Pepe, A. Collier Cameron, D. W. Latham, E. Molinari, S. Udry, N. Bezawada, M. Black, A. Born, N. Buchschacher, D. Charbonneau, P. Figueira, M. Fleury, A. Galli, A. Gallie, X. Gao, A. Ghedina, C. Gonzalez, M. Gonzalez, J. Guerra, D. Henry, K. Horne, I. Hughes, D. Kelly, M. Lodi, D. Lunney, C. Maire, M. Mayor, G. Micela, M. P. Ordway, J. Peacock, D. Phillips, G. Piotto, D. Pollacco, D. Queloz, K. Rice, C. Riverol, L. Riverol, J. San Juan, D. Sasselov, D. Segransan, A. Sozzetti, D. Sosnowska, B. Stobie, A. Szentgyorgyi, A. Vick, and L. Weber. Harps-N: the new planet hunter at TNG. In *Proceedings of the SPIE*, volume 8446 of *Society of Photo-Optical Instrumentation Engineers (SPIE) Conference Series*, page 84461V, Sept. 2012.

[89] R. Cosentino, C. Lovis, F. Pepe, A. Collier Cameron, D. W. Latham, E. Molinari, S. Udry, N. Bezawada, M. Black, A. Born, N. Buchschacher, D. Charbonneau, P. Figueira, M. Fleury, A. Galli, A. Gallie, X. Gao, A. Ghedina, C. Gonzalez, M. Gonzalez, J. Guerra, D. Henry, K. Horne, I. Hughes, D. Kelly, M. Lodi, D. Lunney, C. Maire, M. Mayor, G. Micela, M. P. Ordway, J. Peacock, D. Phillips, G. Piotto, D. Pollacco, D. Queloz, K. Rice, C. Riverol, L. Riverol, J. San Juan, D. Sasselov, D. Segransan, A. Sozzetti, D. Sosnowska, B. Stobie, A. Szentgyorgyi, A. Vick, and L. Weber. Harps-N: the new planet hunter at TNG. In I. S. McLean, S. K. Ramsay, and H. Takami, editors, *Ground-based and Airborne Instrumentation for Astronomy IV*, volume 8446 of *Society of Photo-Optical Instrumentation Engineers (SPIE) Conference Series*, page 84461V, Sept. 2012.

[90] C. J. Crockett, N. I. Mahmud, L. Prato, C. M. Johns-Krull, D. T. Jaffe, P. M. Hartigan, and C. A. Beichman. A Search for Giant Planet Companions to T Tauri Stars. *The Astrophysical Journal*, 761(2):164, Dec. 2012.

[91] I. J. M. Crossfield, D. R. Ciardi, H. Isaacson, A. W. Howard, E. A. Petigura, L. M. Weiss, B. J. Fulton, E. Sinukoff, J. E. Schlieder, D. Mawet, G. Ruane, I. de Pater, K. de Kleer, A. G. Davies, J. L. Christiansen, C. D. Dressing, L. Hirsch, B. Benneke, J. R. Crepp, M. Kosiarek, J. Livingston, E. Gonzales, C. A. Beichman, and H. A. Knutson. Two Small Transiting Planets and a Possible Third Body Orbiting HD 106315. *The Astronomical Journal*, 153(6):255, June 2017.

[92] I. J. M. Crossfield, W. Waalkes, E. R. Newton, N. Narita, P. Muirhead, K. Ment, E. Matthews, A. Kraus, V. Kostov, M. R. Kosiarek, S. R. Kane, H. Isaacson, S. Halverson, E. Gonzales, M. Everett, D. Dragomir, K. A. Collins, A. Chontos, D. Berardo, J. G. Winters, J. N. Winn, N. J. Scott, B. Rojas-Ayala, A. C. Rizzuto, E. A. Petigura, M. Peterson, T. Mocnik, T. Mikal-Evans, N. Mehrle, R. Matson, M. Kuzuhara, J. Irwin, D. Huber, C. Huang, S. Howell, A. W. Howard, T. Hirano, B. J. Fulton, T. Dupuy, C. D. Dressing, P. A. Dalba, D. Charbonneau, J. Burt, Z. Berta-Thompson, B. Benneke, N. Watanabe, J. D. Twicken, M. Tamura, J. Schlieder, S. Seager, M. E. Rose, G. Ricker, E. Quintana, S. Lépine, D. W. Latham, T. Kotani, J. M. Jenkins, Y. Hori, K. Colon, and D. A. Caldwell. A Super-Earth and Sub-Neptune Transiting the Late-type M Dwarf LP 791-18. *The Astrophysical Journal Letters*, 883(1):L16, Sept. 2019.

[93] S. Curiel, G. N. Ortiz-León, A. J. Mioduszewski, and J. Sanchez-Bermudez. 3D Orbital Architecture of a Dwarf Binary System and Its Planetary Companion. *The Astronomical Journal*, 164(3):93, Sept. 2022.

[94] R. M. Cutri, M. F. Skrutskie, S. van Dyk, C. A. Beichman, J. M. Carpenter, T. Chester, L. Cambresy, T. Evans, J. Fowler, J. Gizis, E. Howard, J. Huchra, T. Jarrett, E. L. Kopan, J. D. Kirkpatrick, R. M. Light, K. A. Marsh, H. McCallon, S. Schneider, R. Stiening, M. Sykes, M. Weinberg, W. A. Wheaton, S. Wheelock, and N. Zacarias. *2MASS All Sky Catalog of point sources.* 2003.

[95] F. Dai, K. Masuda, C. Beard, P. Robertson, M. Goldberg, K. Batygin, L. Bouma, J. J. Lissauer, E. Knudstrup, S. Albrecht, A. W. Howard, H. A. Knutson, E. A. Petigura, L. M. Weiss, H. Isaacson, M. H. Kristiansen, H. Osborn, S. Wang, X.-Y. Wang, A. Behmard, M. Greklek-McKeon, S. Vissapragada, N. M. Batalha, C. L. Brinkman, A. Chontos, I. Crossfield, C. Dressing, T. Fetherolf, B. Fulton, M. L. Hill, D. Huber, S. R. Kane, J. Lubin, M. MacDougall, A. Mayo, T. Močnik, J. M. Akana Murphy, R. A. Rubenzahl, N. Scarsdale, D. Tyler, J. V. Zandt, A. S. Polanski, H. M. Schwengeler, I. A. Terentev, P. Benni, A. Bieryla, D. Ciardi, B. Falk, E. Furlan, E. Girardin, P. Guerra, K. M. Hesse, S. B. Howell, J. Lillo-Box, E. C. Matthews, J. D. Twicken, J. Villaseñor, D. W. Latham, J. M. Jenkins, G. R. Ricker, S. Seager, R. Vanderspek, and J. N. Winn. TOI-1136 is a Young, Coplanar, Aligned Planetary System in a Pristine Resonant Chain. *The Astronomical Journal*, 165(2):33, Feb. 2023.

[96] F. Dai, K. Masuda, C. Beard, P. Robertson, M. Goldberg, K. Batygin, L. Bouma, J. J. Lissauer, E. Knudstrup, S. Albrecht, A. W. Howard, H. A. Knutson, E. A. Petigura, L. M. Weiss, H. Isaacson, M. H. Kristiansen, H. Osborn, S. Wang, X.-Y. Wang, A. Behmard, M. Greklek-McKeon, S. Vissapragada, N. M. Batalha, C. L. Brinkman, A. Chontos, I. Crossfield, C. Dressing, T. Fetherolf, B. Fulton, M. L. Hill, D. Huber, S. R. Kane, J. Lubin, M. MacDougall, A. Mayo, T. Močnik, J. M. Akana Murphy, R. A. Rubenzahl, N. Scarsdale, D. Tyler, J. V. Zandt, A. S. Polanski, H. M. Schwengeler, I. A. Terentev, P. Benni, A. Bieryla, D. Ciardi, B. Falk, E. Furlan, E. Girardin, P. Guerra, K. M. Hesse, S. B. Howell, J. Lillo-Box, E. C. Matthews, J. D. Twicken, J. Villaseñor, D. W. Latham, J. M. Jenkins, G. R. Ricker, S. Seager,

R. Vanderspek, and J. N. Winn. TOI-1136 is a Young, Coplanar, Aligned Planetary System in a Pristine Resonant Chain. *The Astronomical Journal*, 165(2):33, Feb. 2023.

[97] F. Dai, J. N. Winn, D. Gandolfi, S. X. Wang, J. K. Teske, J. Burt, S. Albrecht, O. Barragán, W. D. Cochran, M. Endl, M. Fridlund, A. P. Hatzes, T. Hirano, L. A. Hirsch, M. C. Johnson, A. B. Justesen, J. Livingston, C. M. Persson, J. Prieto-Arranz, A. Vanderburg, R. Alonso, G. Antoniciello, P. Arriagada, R. P. Butler, J. Cabrera, J. D. Crane, F. Cusano, S. Csizmadia, H. Deeg, S. B. Dieterich, P. Eigmüller, A. Erikson, M. E. Everett, A. Fukui, S. Grziwa, E. W. Guenther, G. W. Henry, S. B. Howell, J. A. Johnson, J. Korth, M. Kuzuhara, N. Narita, D. Nespral, G. Nowak, E. Palle, M. Pätzold, H. Rauer, P. Montañés Rodríguez, S. A. Shectman, A. M. S. Smith, I. B. Thompson, V. Van Eylen, M. W. Williamson, and R. A. Wittenmyer. The Discovery and Mass Measurement of a New Ultra-short-period Planet: K2-131b. *The Astronomical Journal*, 154(6):226, Dec. 2017.

[98] J. M. A. Danby. *Fundamentals of celestial mechanics*. 1988.

[99] G. D'Angelo, W. Kley, and T. Henning. Orbital Migration and Mass Accretion of Protoplanets in Three-dimensional Global Computations with Nested Grids. *The Astrophysical Journal*, 586(1):540–561, Mar. 2003.

[100] G. R. Davies, V. Silva Aguirre, T. R. Bedding, R. Handberg, M. N. Lund, W. J. Chaplin, D. Huber, T. R. White, O. Benomar, S. Hekker, S. Basu, T. L. Campante, J. Christensen-Dalsgaard, Y. Elsworth, C. Karoff, H. Kjeldsen, M. S. Lundkvist, T. S. Metcalfe, and D. Stello. Oscillation frequencies for 35 Kepler solar-type planet-hosting stars using Bayesian techniques and machine learning. *Monthly Notices of the Royal Astronomical Society*, 456(2):2183–2195, Feb. 2016.

[101] K. M. Deck, E. Agol, M. J. Holman, and D. Nesvorný. TTVFast: An Efficient and Accurate Code for Transit Timing Inversion Problems. *The Astrophysical Journal*, 787(2):132, June 2014.

[102] D. Deming, A. Wilkins, P. McCullough, A. Burrows, J. J. Fortney, E. Agol, I. Dobbs-Dixon, N. Madhusudhan, N. Crouzet, J.-M. Desert, R. L. Gilliland, K. Haynes, H. A. Knutson, M. Line, Z. Magic, A. M. Mandell, S. Ranjan, D. Charbonneau, M. Clampin, S. Seager, and A. P. Showman. Infrared Transmission Spectroscopy of the Exoplanets HD 209458b and XO-1b Using the Wide Field Camera-3 on the Hubble Space Telescope. *The Astrophysical Journal*, 774(2):95, Sept. 2013.

[103] P. Dierckx. *Curve and surface fitting with splines*. Oxford University Press, 1995.

[104] C. D. Dressing and D. Charbonneau. The Occurrence of Potentially Habitable Planets Orbiting M Dwarfs Estimated from the Full Kepler Dataset and an Empirical Measurement of the Detection Sensitivity. *The Astrophysical Journal*, 807(1):45, July 2015.

[105] X. Dumusque, I. Boisse, and N. C. Santos. SOAP 2.0: A Tool to Estimate the Photometric and Radial Velocity Variations Induced by Stellar Spots and Plages. *The Astrophysical Journal*, 796(2):132, Dec. 2014.

[106] X. Dumusque, O. Turner, C. Dorn, J. D. Eastman, R. Allart, V. Adibekyan, S. Sousa, N. C. Santos, C. Mordasini, V. Bourrier, F. Bouchy, A. Coffinet, M. D. Davies, R. F. Díaz, M. M. Fausnaugh, A. Glidden, N. Guerrero, C. E. Henze, J. M. Jenkins, D. W. Latham, C. Lovis, M. Mayor, F. Pepe, E. V. Quintana, G. R. Ricker, P. Rowden, D. Segransan, A. S. Mascareño, S. Seager, J. D. Twicken, S. Udry, R. K. Vanderspek, and J. N. Winn. Hot, rocky and warm, puffy super-Earths orbiting TOI-402 (HD 15337). *Astronomy and Astrophysics*, 627:A43, July 2019.

[107] A. H. Dymont, X. Yu, K. Ohno, X. Zhang, and J. J. Fortney. Cleaning our Hazy Lens: Statistical Trends in Transmission Spectra of Warm Exoplanets. *arXiv e-prints*, page arXiv:2112.06173, Dec. 2021.

[108] J. Eastman, B. S. Gaudi, and E. Agol. EXOFAST: A Fast Exoplanetary Fitting Suite in IDL. *Publications of the Astronomical Society of the Pacific*, 125(923):83, Jan. 2013.

[109] M. Endl, P. Robertson, W. D. Cochran, P. J. MacQueen, B. P. Bowler, K. E. Franson, R. Holcomb, C. Beard, H. Isaacson, A. W. Howard, and J. Lubin. A Jupiter Analog Orbiting The Nearby M Dwarf GJ 463. *The Astronomical Journal*, 164(6):238, Dec. 2022.

[110] N. Espinoza, D. Bayliss, J. D. Hartman, G. Á. Bakos, A. Jordán, G. Zhou, L. Mancini, R. Brahm, S. Ciceri, W. Bhatti, Z. Csubry, M. Rabus, K. Penev, J. Bento, M. de Val-Borro, T. Henning, B. Schmidt, V. Suc, D. J. Wright, C. G. Tinney, T. G. Tan, and R. Noyes. HATS-25b through HATS-30b: A Half-dozen New Inflated Transiting Hot Jupiters from the HATSouth Survey. *Astronomical Journal*, 152(4):108, Oct. 2016.

[111] N. Espinoza, D. Kossakowski, and R. Brahm. juliet: a versatile modelling tool for transiting and non-transiting exoplanetary systems. *Monthly Notices of the Royal Astronomical Society*, 490(2):2262–2283, Dec. 2019.

[112] L. J. Esteves, E. J. W. De Mooij, and R. Jayawardhana. Optical Phase Curves of Kepler Exoplanets. *The Astrophysical Journal*, 772(1):51, July 2013.

[113] T. J. Fauchez, M. Turbet, G. L. Villanueva, E. T. Wolf, G. Arney, R. K. Kopparapu, A. Lincowski, A. Mandell, J. de Wit, D. Pidhorodetska, S. D. Domagal-Goldman, and K. B. Stevenson. Impact of Clouds and Hazes on the Simulated JWST Transmission Spectra of Habitable Zone Planets in the TRAPPIST-1 System. *The Astrophysical Journal*, 887(2):194, Dec. 2019.

[114] A. D. Feinstein, B. T. Montet, D. Foreman-Mackey, M. E. Bedell, N. Saunders, J. L. Bean, J. L. Christiansen, C. Hedges, R. Luger, D. Scolnic, and J. V. d. M. Cardoso. eleanor: An Open-source Tool for Extracting Light Curves from the TESS Full-frame Images. *Publications of the Astronomical Society of the Pacific*, 131(1003):094502, Sept. 2019.

[115] F. Feng, M. Tuomi, H. R. A. Jones, J. Barnes, G. Anglada-Escudé, S. S. Vogt, and R. P. Butler. Color Difference Makes a Difference: Four Planet Candidates around τ Ceti. *The Astronomical Journal*, 154(4):135, Oct. 2017.

[116] E. L. Fitzpatrick. Correcting for the Effects of Interstellar Extinction. *Publications of the Astronomical Society of the Pacific*, 111(755):63–75, Jan. 1999.

[117] C. Fontanive, K. N. Allers, B. Pantoja, B. Biller, S. Dubber, Z. Zhang, T. Dupuy, M. C. Liu, and L. Albert. A Wide Planetary-mass Companion to a Young Low-mass Brown Dwarf in Ophiuchus. *The Astrophysical Journal Letters*, 905(2):L14, Dec. 2020.

[118] G. Foo, D. M. Palacios, and J. Swartzlander, Grover A. Optical vortex coronagraph. *Optics Letters*, 30(24):3308–3310, Dec. 2005.

[119] E. B. Ford. Improving the Efficiency of Markov Chain Monte Carlo for Analyzing the Orbits of Extrasolar Planets. *The Astrophysical Journal*, 642(1):505–522, May 2006.

[120] D. Foreman-Mackey. Scalable Backpropagation for Gaussian Processes using Celerite. *Research Notes of the American Astronomical Society*, 2(1):31, Feb. 2018.

[121] D. Foreman-Mackey. Scalable Backpropagation for Gaussian Processes using Celerite. *Research Notes of the American Astronomical Society*, 2(1):31, Feb. 2018.

[122] D. Foreman-Mackey, E. Agol, S. Ambikasaran, and R. Angus. Fast and Scalable Gaussian Process Modeling with Applications to Astronomical Time Series. *The Astronomical Journal*, 154(6):220, Dec. 2017.

[123] D. Foreman-Mackey, E. Agol, S. Ambikasaran, and R. Angus. Fast and Scalable Gaussian Process Modeling with Applications to Astronomical Time Series. *Astronomical Journal*, 154:220, Dec. 2017.

[124] D. Foreman-Mackey, E. Agol, S. Ambikasaran, and R. Angus. Fast and Scalable Gaussian Process Modeling with Applications to Astronomical Time Series. *Astronomical Journal*, 154:220, Dec. 2017.

[125] D. Foreman-Mackey, D. W. Hogg, D. Lang, and J. Goodman. emcee: The MCMC Hammer. *Publications of the Astronomical Society of the Pacific*, 125(925):306, Mar. 2013.

[126] D. Foreman-Mackey, D. W. Hogg, D. Lang, and J. Goodman. emcee: The MCMC Hammer. *Publications of the ASP*, 125(925):306, Mar. 2013.

[127] D. Foreman-Mackey, R. Luger, E. Agol, T. Barclay, L. G. Bouma, T. D. Brandt, I. Czekala, T. J. David, J. Dong, E. A. Gilbert, T. A. Gordon, C. Hedges, D. R. Hey, B. M. Morris, A. M. Price-Whelan, and A. B. Savel. exoplanet: Gradient-based probabilistic inference for exoplanet data & other astronomical time series. *arXiv e-prints*, page arXiv:2105.01994, May 2021.

[128] D. Foreman-Mackey, R. Luger, E. Agol, T. Barclay, L. G. Bouma, T. D. Brandt, I. Czekala, T. J. David, J. Dong, E. A. Gilbert, T. A. Gordon, C. Hedges, D. R. Hey, B. M. Morris, A. M. Price-Whelan, and A. B. Savel. 'exoplanet': Gradient-based probabilistic inference for exoplanet data & other astronomical time series. *Journal of Open Source Software*, 6(62):3285, 2021.

[129] D. Foreman-Mackey, A. Savel, R. Luger, E. Agol, I. Czekala, A. Price-Whelan, C. Hedges, E. Gilbert, L. Bouma, T. D. Brandt, and T. Barclay. exoplanet-dev/exoplanet v0.5.1, June 2021.

[130] Y. G. C. Frensch, G. Lo Curto, F. Bouchy, M. Mayor, G. Hébrard, C. Lovis, C. Moutou, F. A. Pepe, D. Queloz, N. Santos, D. Segransan, S. Udry, and N. Unger. The HARPS search for southern extra-solar planets. XLVII. Five Jupiter-mass planets in long-period orbits, one highly irradiated Neptune, one brown dwarf, and five stellar binaries. *Astronomy and Astrophysics*, 675:A173, July 2023.

[131] F. Fressin, G. Torres, D. Charbonneau, S. T. Bryson, J. Christiansen, C. D. Dressing, J. M. Jenkins, L. M. Walkowicz, and N. M. Batalha. The False Positive Rate of Kepler and the Occurrence of Planets. *The Astrophysical Journal*, 766(2):81, Apr. 2013.

[132] Y. Fujii, D. Angerhausen, R. Deitrick, S. Domagal-Goldman, J. L. Grenfell, Y. Hori, S. R. Kane, E. Pallé, H. Rauer, N. Siegler, K. Stapelfeldt, and K. B. Stevenson. Exoplanet Biosignatures: Observational Prospects. *Astrobiology*, 18(6):739–778, June 2018.

[133] B. J. Fulton, E. A. Petigura, S. Blunt, and E. Sinukoff. RadVel: The Radial Velocity Modeling Toolkit. *Publications of the Astronomical Society of the Pacific*, 130(986):044504, Apr. 2018.

[134] B. J. Fulton, E. A. Petigura, A. W. Howard, H. Isaacson, G. W. Marcy, P. A. Cargile, L. Hebb, L. M. Weiss, J. A. Johnson, T. D. Morton, E. Sinukoff, I. J. M. Crossfield, and L. A. Hirsch. The California-Kepler Survey. III. A Gap in the Radius Distribution of Small Planets. *Astronomical Journal*, 154(3):109, Sept. 2017.

[135] B. J. Fulton, L. M. Weiss, E. Sinukoff, H. Isaacson, A. W. Howard, G. W. Marcy, G. W. Henry, B. P. Holden, and R. I. Kibrick. Three Super-Earths Orbiting HD 7924. *The Astrophysical Journal*, 805(2):175, June 2015.

[136] E. Furlan, D. R. Ciardi, M. E. Everett, M. Saylors, J. K. Teske, E. P. Horch, S. B. Howell, G. T. van Belle, L. A. Hirsch, I. Gautier, T. N., E. R. Adams, D. Barrado, K. M. S. Cartier, C. D. Dressing, A. K. Dupree, R. L. Gilliland, J. Lillo-Box, P. W. Lucas, and J. Wang. Erratum: "The Kepler Follow-up Observation Program. I. A Catalog of Companions to Kepler Stars from High-resolution Imaging" (¡A href="https://doi.org/10.3847/1538-3881/153/2/71"¿2017, AJ, 153, 71¡/A¿). *Astronomical Journal*, 153(4):201, Apr. 2017.

[137] Gaia Collaboration, A. G. A. Brown, A. Vallenari, T. Prusti, J. H. J. de Bruijne, C. Babusiaux, C. A. L. Bailer-Jones, M. Biermann, D. W. Evans, L. Eyer, F. Jansen,

C. Jordi, S. A. Klioner, U. Lammers, L. Lindegren, X. Luri, F. Mignard, C. Panem, D. Pourbaix, S. Randich, P. Sartoretti, H. I. Siddiqui, C. Soubiran, F. van Leeuwen, N. A. Walton, F. Arenou, U. Bastian, M. Cropper, R. Drimmel, D. Katz, M. G. Lattanzi, J. Bakker, C. Cacciari, J. Castañeda, L. Chaoul, N. Cheek, F. De Angeli, C. Fabricius, R. Guerra, B. Holl, E. Masana, R. Messineo, N. Mowlavi, K. Nienartowicz, P. Panuzzo, J. Portell, M. Riello, G. M. Seabroke, P. Tanga, F. Thévenin, G. Gracia-Abril, G. Comoretto, M. Garcia-Reinaldos, D. Teyssier, M. Altmann, R. Andrae, M. Audard, I. Bellas-Velidis, K. Benson, J. Berthier, R. Blomme, P. Burgess, G. Busso, B. Carry, A. Cellino, G. Clementini, M. Clotet, O. Creevey, M. Davidson, J. De Ridder, L. Delchambre, A. Dell'Oro, C. Ducourant, J. Fernández-Hernández, M. Fouesneau, Y. Frémat, L. Galluccio, M. García-Torres, J. González-Núñez, J. J. González-Vidal, E. Gosset, L. P. Guy, J. L. Halbwachs, N. C. Hambly, D. L. Harrison, J. Hernández, D. Hestroffer, S. T. Hodgkin, A. Hutton, G. Jasniewicz, A. Jean-Antoine-Piccolo, S. Jordan, A. J. Korn, A. Krone-Martins, A. C. Lanzafame, T. Lebzelter, W. Löffler, M. Manteiga, P. M. Marrese, J. M. Martín-Fleitas, A. Moitinho, A. Mora, K. Muinonen, J. Osinde, E. Pancino, T. Pauwels, J. M. Petit, A. Recio-Blanco, P. J. Richards, L. Rimoldini, A. C. Robin, L. M. Sarro, C. Siopis, M. Smith, A. Sozzetti, M. Süveges, J. Torra, W. van Reeven, U. Abbas, A. Abreu Aramburu, S. Accart, C. Aerts, G. Altavilla, M. A. Álvarez, R. Alvarez, J. Alves, R. I. Anderson, A. H. Andrei, E. Anglada Varela, E. Antiche, T. Antoja, B. Arcay, T. L. Astraatmadja, N. Bach, S. G. Baker, L. Balaguer-Núñez, P. Balm, C. Barache, C. Barata, D. Barbato, F. Barblan, P. S. Barklem, D. Barrado, M. Barros, M. A. Barstow, S. Bartholomé Muñoz, J. L. Bassilana, U. Becciani, M. Bellazzini, A. Berihuete, S. Bertone, L. Bianchi, O. Bienaymé, S. Blanco-Cuaresma, T. Boch, C. Boeche, A. Bombrun, R. Borrachero, D. Bossini, S. Bouquillon, G. Bourda, A. Bragaglia, L. Bramante, M. A. Breddels, A. Bressan, N. Brouillet, T. Brüsemeister, E. Brugaletta, B. Bucciarelli, A. Burlacu, D. Busonero, A. G. Butkevich, R. Buzzi, E. Caffau, R. Cancelliere, G. Cannizzaro, T. Cantat-Gaudin, R. Carballo, T. Carlucci, J. M. Carrasco, L. Casamiquela, M. Castellani, A. Castro-Ginard, P. Charlot, L. Chemin, A. Chiavassa, G. Cocozza, G. Costigan, S. Cowell, F. Crifo, M. Crosta, C. Crowley, J. Cuypers, C. Dafonte, Y. Damerdji, A. Dapergolas, P. David, M. David, P. de Laverny, F. De Luise, R. De March, D. de Martino, R. de Souza, A. de Torres, J. Debosscher, E. del Pozo, M. Delbo, A. Delgado, H. E. Delgado, P. Di Matteo, S. Diakite, C. Diener, E. Distefano, C. Dolding, P. Drazinos, J. Durán, B. Edvardsson, H. Enke, K. Eriksson, P. Esquej, G. Eynard Bontemps, C. Fabre, M. Fabrizio, S. Faigler, A. J. Falcão, M. Farràs Casas, L. Federici, G. Fedorets, P. Fernique, F. Figueras, F. Filippi, K. Findeisen, A. Fonti, E. Fraile, M. Fraser, B. Frézouls, M. Gai, S. Galleti, D. Garabato, F. García-Sedano, A. Garofalo, N. Garralda, A. Gavel, P. Gavras, J. Gerssen, R. Geyer, P. Giacobbe, G. Gilmore, S. Girona, G. Giuffrida, F. Glass, M. Gomes, M. Granvik, A. Gueguen, A. Guerrier, J. Guiraud, R. Gutiérrez-Sánchez, R. Haigron, D. Hatzidimitriou, M. Hauser, M. Haywood, U. Heiter, A. Helmi, J. Heu, T. Hilger, D. Hobbs, W. Hofmann, G. Holland, H. E. Huckle, A. Hypki, V. Icardi, K. Janßen, G. Jevardat de Fombelle, P. G. Jonker, Á. L. Juhász, F. Julbe, A. Karampelas, A. Kewley, J. Klar, A. Kochoska, R. Kohley, K. Kolenberg, M. Kontizas, E. Kontizas,

S. E. Koposov, G. Kordopatis, Z. Kostrzewa-Rutkowska, P. Koubsky, S. Lambert, A. F. Lanza, Y. Lasne, J. B. Lavigne, Y. Le Fustec, C. Le Poncin-Lafitte, Y. Lebreton, S. Leccia, N. Leclerc, I. Lecoeur-Taibi, H. Lenhardt, F. Leroux, S. Liao, E. Licata, H. E. P. Lindstrøm, T. A. Lister, E. Livanou, A. Lobel, M. López, S. Managau, R. G. Mann, G. Mantelet, O. Marchal, J. M. Marchant, M. Marconi, S. Marinoni, G. Marschalkó, D. J. Marshall, M. Martino, G. Marton, N. Mary, D. Massari, G. Matijevič, T. Mazeh, P. J. McMillan, S. Messina, D. Michalik, N. R. Millar, D. Molina, R. Molinaro, L. Molnár, P. Montegriffo, R. Mor, R. Morbidelli, T. Morel, D. Morris, A. F. Mulone, T. Muraveva, I. Musella, G. Nelemans, L. Nicastro, L. Noval, W. O'Mullane, C. Ordénovic, D. Ordóñez-Blanco, P. Osborne, C. Pagani, I. Pagano, F. Pailler, H. Palacin, L. Palaversa, A. Panahi, M. Pawlak, A. M. Piersimoni, F. X. Pineau, E. Plachy, G. Plum, E. Poggio, E. Poujoulet, A. Prša, L. Pulone, E. Racero, S. Ragaini, N. Rambaux, M. Ramos-Lerate, S. Regibo, C. Reylé, F. Riclet, V. Ripepi, A. Riva, A. Rivard, G. Rixon, T. Roegiers, M. Roelens, M. Romero-Gómez, N. Rowell, F. Royer, L. Ruiz-Dern, G. Sadowski, T. Sagristà Sellés, J. Sahlmann, J. Salgado, E. Salguero, N. Sanna, T. Santana-Ros, M. Sarasso, H. Savietto, M. Schultheis, E. Sciacca, M. Segol, J. C. Segovia, D. Ségransan, I. C. Shih, L. Siltala, A. F. Silva, R. L. Smart, K. W. Smith, E. Solano, F. Solitro, R. Sordo, S. Soria Nieto, J. Souchay, A. Spagna, F. Spoto, U. Stampa, I. A. Steele, H. Steidelmüller, C. A. Stephenson, H. Stoev, F. F. Suess, J. Surdej, L. Szabados, E. Szegedi-Elek, D. Tapiador, F. Taris, G. Tauran, M. B. Taylor, R. Teixeira, D. Terrett, P. Teyssandier, W. Thuillot, A. Titarenko, F. Torra Clotet, C. Turon, A. Ulla, E. Utrilla, S. Uzzi, M. Vaillant, G. Valentini, V. Valette, A. van Elteren, E. Van Hemelryck, M. van Leeuwen, M. Vaschetto, A. Vecchiato, J. Veljanoski, Y. Viala, D. Vicente, S. Vogt, C. von Essen, H. Voss, V. Votruba, S. Voutsinas, G. Walmsley, M. Weiler, O. Wertz, T. Wevers, Ł. Wyrzykowski, A. Yoldas, M. Žerjal, H. Ziaeepour, J. Zorec, S. Zschocke, S. Zucker, C. Zurbach, and T. Zwitter. Gaia Data Release 2. Summary of the contents and survey properties. *Astronomy and Astrophysics*, 616:A1, Aug. 2018.

[138] Gaia Collaboration, A. G. A. Brown, A. Vallenari, T. Prusti, J. H. J. de Bruijne, C. Babusiaux, M. Biermann, O. L. Creevey, D. W. Evans, L. Eyer, A. Hutton, F. Jansen, C. Jordi, S. A. Klioner, U. Lammers, L. Lindegren, X. Luri, F. Mignard, C. Panem, D. Pourbaix, S. Randich, P. Sartoretti, C. Soubiran, N. A. Walton, F. Arenou, C. A. L. Bailer-Jones, U. Bastian, M. Cropper, R. Drimmel, D. Katz, M. G. Lattanzi, F. van Leeuwen, J. Bakker, C. Cacciari, J. Castañeda, F. De Angeli, C. Ducourant, C. Fabricius, M. Fouesneau, Y. Frémat, R. Guerra, A. Guerrier, J. Guiraud, A. Jean-Antoine Piccolo, E. Masana, R. Messineo, N. Mowlavi, C. Nicolas, K. Nienartowicz, F. Pailler, P. Panuzzo, F. Riclet, W. Roux, G. M. Seabroke, R. Sordo, P. Tanga, F. Thévenin, G. Gracia-Abril, J. Portell, D. Teyssier, M. Altmann, R. Andrae, I. Bellas-Velidis, K. Benson, J. Berthier, R. Blomme, E. Brugaletta, P. W. Burgess, G. Busso, B. Carry, A. Cellino, N. Cheek, G. Clementini, Y. Damerdji, M. Davidson, L. Delchambre, A. Dell'Oro, J. Fernández-Hernández, L. Galluccio, P. García-Lario, M. Garcia-Reinaldos, J. González-Núñez, E. Gosset, R. Haigron, J. L. Halbwachs, N. C. Hambly, D. L. Harrison, D. Hatzidimitriou, U. Heiter, J. Hernández, D. Hestroffer, S. T. Hodgkin, B. Holl, K. Janßen, G. Jevardat de Fombelle, S. Jordan,

A. Krone-Martins, A. C. Lanzafame, W. Löffler, A. Lorca, M. Manteiga, O. Marchal, P. M. Marrese, A. Moitinho, A. Mora, K. Muinonen, P. Osborne, E. Pancino, T. Pauwels, J. M. Petit, A. Recio-Blanco, P. J. Richards, M. Riello, L. Rimoldini, A. C. Robin, T. Roegiers, J. Rybizki, L. M. Sarro, C. Siopis, M. Smith, A. Sozzetti, A. Ulla, E. Utrilla, M. van Leeuwen, W. van Reeven, U. Abbas, A. Abreu Aramburu, S. Accart, C. Aerts, J. J. Aguado, M. Ajaj, G. Altavilla, M. A. Álvarez, J. Álvarez Cid-Fuentes, J. Alves, R. I. Anderson, E. Anglada Varela, T. Antoja, M. Audard, D. Baines, S. G. Baker, L. Balaguer-Núñez, E. Balbinot, Z. Balog, C. Barache, D. Barbato, M. Barros, M. A. Barstow, S. Bartolomé, J. L. Bassilana, N. Bauchet, A. Baudesson-Stella, U. Becciani, M. Bellazzini, M. Bernet, S. Bertone, L. Bianchi, S. Blanco-Cuaresma, T. Boch, A. Bombrun, D. Bossini, S. Bouquillon, A. Bragaglia, L. Bramante, E. Breedt, A. Bressan, N. Brouillet, B. Bucciarelli, A. Burlacu, D. Busonero, A. G. Butkevich, R. Buzzi, E. Caffau, R. Cancelliere, H. Cánovas, T. Cantat-Gaudin, R. Carballo, T. Carlucci, M. I. Carnerero, J. M. Carrasco, L. Casamiquela, M. Castellani, A. Castro-Ginard, P. Castro Sampol, L. Chaoul, P. Charlot, L. Chemin, A. Chiavassa, M. R. L. Cioni, G. Comoretto, W. J. Cooper, T. Cornez, S. Cowell, F. Crifo, M. Crosta, C. Crowley, C. Dafonte, A. Dapergolas, M. David, P. David, P. de Laverny, F. De Luise, R. De March, J. De Ridder, R. de Souza, P. de Teodoro, A. de Torres, E. F. del Peloso, E. del Pozo, M. Delbo, A. Delgado, H. E. Delgado, J. B. Delisle, P. Di Matteo, S. Diakite, C. Diener, E. Distefano, C. Dolding, D. Eappachen, B. Edvardsson, H. Enke, P. Esquej, C. Fabre, M. Fabrizio, S. Faigler, G. Fedorets, P. Fernique, A. Fienga, F. Figueras, C. Fouron, F. Fragkoudi, E. Fraile, F. Franke, M. Gai, D. Garabato, A. Garcia-Gutierrez, M. García-Torres, A. Garofalo, P. Gavras, E. Gerlach, R. Geyer, P. Giacobbe, G. Gilmore, S. Girona, G. Giuffrida, R. Gomel, A. Gomez, I. Gonzalez-Santamaria, J. J. González-Vidal, M. Granvik, R. Gutiérrez-Sánchez, L. P. Guy, M. Hauser, M. Haywood, A. Helmi, S. L. Hidalgo, T. Hilger, N. Hładczuk, D. Hobbs, G. Holland, H. E. Huckle, G. Jasniewicz, P. G. Jonker, J. Juaristi Campillo, F. Julbe, L. Karbevska, P. Kervella, S. Khanna, A. Kochoska, M. Kontizas, G. Kordopatis, A. J. Korn, Z. Kostrzewa-Rutkowska, K. Kruszyńska, S. Lambert, A. F. Lanza, Y. Lasne, J. F. Le Campion, Y. Le Fustec, Y. Lebreton, T. Lebzelter, S. Leccia, N. Leclerc, I. Lecoeur-Taibi, S. Liao, E. Licata, E. P. Lindstrøm, T. A. Lister, E. Livanou, A. Lobel, P. Madrero Pardo, S. Managau, R. G. Mann, J. M. Marchant, M. Marconi, M. M. S. Marcos Santos, S. Marinoni, F. Marocco, D. J. Marshall, L. Martin Polo, J. M. Martín-Fleitas, A. Masip, D. Massari, A. Mastrobuono-Battisti, T. Mazeh, P. J. McMillan, S. Messina, D. Michalik, N. R. Millar, A. Mints, D. Molina, R. Molinaro, L. Molnár, P. Montegriffo, R. Mor, R. Morbidelli, T. Morel, D. Morris, A. F. Mulone, D. Munoz, T. Muraveva, C. P. Murphy, I. Musella, L. Noval, C. Ordénovic, G. Orrù, J. Osinde, C. Pagani, I. Pagano, L. Palaversa, P. A. Palicio, A. Panahi, M. Pawlak, X. Peñalosa Esteller, A. Penttilä, A. M. Piersimoni, F. X. Pineau, E. Plachy, G. Plum, E. Poggio, E. Poretti, E. Poujoulet, A. Prša, L. Pulone, E. Racero, S. Ragaini, M. Rainer, C. M. Raiteri, N. Rambaux, P. Ramos, M. Ramos-Lerate, P. Re Fiorentin, S. Regibo, C. Reylé, V. Ripepi, A. Riva, G. Rixon, N. Robichon, C. Robin, M. Roelens, L. Rohrbasser, M. Romero-Gómez, N. Rowell, F. Royer, K. A. Rybicki, G. Sadowski, A. Sagristà Sellés, J. Sahlmann, J. Salgado, E. Salguero, N. Samaras, V. Sanchez Gimenez, N. Sanna, R. Santoveña, M. Sarasso, M. Schultheis, E. Sciacca, M. Segol,

J. C. Segovia, D. Ségransan, D. Semeux, S. Shahaf, H. I. Siddiqui, A. Siebert, L. Siltala, E. Slezak, R. L. Smart, E. Solano, F. Solitro, D. Souami, J. Souchay, A. Spagna, F. Spoto, I. A. Steele, H. Steidelmüller, C. A. Stephenson, M. Süveges, L. Szabados, E. Szegedi-Elek, F. Taris, G. Tauran, M. B. Taylor, R. Teixeira, W. Thuillot, N. Tonello, F. Torra, J. Torra, C. Turon, N. Unger, M. Vaillant, E. van Dillen, O. Vanel, A. Vecchiato, Y. Viala, D. Vicente, S. Voutsinas, M. Weiler, T. Wevers, Ł. Wyrzykowski, A. Yoldas, P. Yvard, H. Zhao, J. Zorec, S. Zucker, C. Zurbach, and T. Zwitter. Gaia Early Data Release 3. Summary of the contents and survey properties. *Astronomy and Astrophysics*, 649:A1, May 2021.

[139] Gaia Collaboration, T. Prusti, J. H. J. de Bruijne, A. G. A. Brown, A. Vallenari, C. Babusiaux, C. A. L. Bailer-Jones, U. Bastian, M. Biermann, D. W. Evans, L. Eyer, F. Jansen, C. Jordi, S. A. Klioner, U. Lammers, L. Lindegren, X. Luri, F. Mignard, D. J. Milligan, C. Panem, V. Poinsignon, D. Pourbaix, S. Randich, G. Sarri, P. Sartoretti, H. I. Siddiqui, C. Soubiran, V. Valette, F. van Leeuwen, N. A. Walton, C. Aerts, F. Arenou, M. Cropper, R. Drimmel, E. Høg, D. Katz, M. G. Lattanzi, W. O'Mullane, E. K. Grebel, A. D. Holland, C. Huc, X. Passot, L. Bramante, C. Cacciari, J. Castañeda, L. Chaoul, N. Cheek, F. De Angeli, C. Fabricius, R. Guerra, J. Hernández, A. Jean-Antoine-Piccolo, E. Masana, R. Messineo, N. Mowlavi, K. Nienartowicz, D. Ordóñez-Blanco, P. Panuzzo, J. Portell, P. J. Richards, M. Riello, G. M. Seabroke, P. Tanga, F. Thévenin, J. Torra, S. G. Els, G. Gracia-Abril, G. Comoretto, M. Garcia-Reinaldos, T. Lock, E. Mercier, M. Altmann, R. Andrae, T. L. Astraatmadja, I. Bellas-Velidis, K. Benson, J. Berthier, R. Blomme, G. Busso, B. Carry, A. Cellino, G. Clementini, S. Cowell, O. Creevey, J. Cuypers, M. Davidson, J. De Ridder, A. de Torres, L. Delchambre, A. Dell'Oro, C. Ducourant, Y. Frémat, M. García-Torres, E. Gosset, J. L. Halbwachs, N. C. Hambly, D. L. Harrison, M. Hauser, D. Hestroffer, S. T. Hodgkin, H. E. Huckle, A. Hutton, G. Jasniewicz, S. Jordan, M. Kontizas, A. J. Korn, A. C. Lanzafame, M. Manteiga, A. Moitinho, K. Muinonen, J. Osinde, E. Pancino, T. Pauwels, J. M. Petit, A. Recio-Blanco, A. C. Robin, L. M. Sarro, C. Siopis, M. Smith, K. W. Smith, A. Sozzetti, W. Thuillot, W. van Reeven, Y. Viala, U. Abbas, A. Abreu Aramburu, S. Accart, J. J. Aguado, P. M. Allan, W. Allasia, G. Altavilla, M. A. Álvarez, J. Alves, R. I. Anderson, A. H. Andrei, E. Anglada Varela, E. Antiche, T. Antoja, S. Antón, B. Arcay, A. Atzei, L. Ayache, N. Bach, S. G. Baker, L. Balaguer-Núñez, C. Barache, C. Barata, A. Barbier, F. Barblan, M. Baroni, D. Barrado y Navascués, M. Barros, M. A. Barstow, U. Becciani, M. Bellazzini, G. Bellei, A. Bello García, V. Belokurov, P. Bendjoya, A. Berihuete, L. Bianchi, O. Bienaymé, F. Billebaud, N. Blagorodnova, S. Blanco-Cuaresma, T. Boch, A. Bombrun, R. Borrachero, S. Bouquillon, G. Bourda, H. Bouy, A. Bragaglia, M. A. Breddels, N. Brouillet, T. Brüsemeister, B. Bucciarelli, F. Budnik, P. Burgess, R. Burgon, A. Burlacu, D. Busonero, R. Buzzi, E. Caffau, J. Cambras, H. Campbell, R. Cancelliere, T. Cantat-Gaudin, T. Carlucci, J. M. Carrasco, M. Castellani, P. Charlot, J. Charnas, P. Charvet, F. Chassat, A. Chiavassa, M. Clotet, G. Cocozza, R. S. Collins, P. Collins, G. Costigan, F. Crifo, N. J. G. Cross, M. Crosta, C. Crowley, C. Dafonte, Y. Damerdji, A. Dapergolas, P. David, M. David, P. De Cat, F. de Felice, P. de Laverny, F. De Luise, R. De March, D. de Martino,

R. de Souza, J. Debosscher, E. del Pozo, M. Delbo, A. Delgado, H. E. Delgado, F. di Marco, P. Di Matteo, S. Diakite, E. Distefano, C. Dolding, S. Dos Anjos, P. Drazinos, J. Durán, Y. Dzigan, E. Ecale, B. Edvardsson, H. Enke, M. Erdmann, D. Escolar, M. Espina, N. W. Evans, G. Eynard Bontemps, C. Fabre, M. Fabrizio, S. Faigler, A. J. Falcão, M. Farràs Casas, F. Faye, L. Federici, G. Fedorets, J. Fernández-Hernández, P. Fernique, A. Fienga, F. Figueras, F. Filippi, K. Findeisen, A. Fonti, M. Fouesneau, E. Fraile, M. Fraser, J. Fuchs, R. Furnell, M. Gai, S. Galleti, L. Galluccio, D. Garabato, F. García-Sedano, P. Garé, A. Garofalo, N. Garralda, P. Gavras, J. Gerssen, R. Geyer, G. Gilmore, S. Girona, G. Giuffrida, M. Gomes, A. González-Marcos, J. González-Núñez, J. J. González-Vidal, M. Granvik, A. Guerrier, P. Guillout, J. Guiraud, A. Gúrpide, R. Gutiérrez-Sánchez, L. P. Guy, R. Haigron, D. Hatzidimitriou, M. Haywood, U. Heiter, A. Helmi, D. Hobbs, W. Hofmann, B. Holl, G. Holland, J. A. S. Hunt, A. Hypki, V. Icardi, M. Irwin, G. Jevardat de Fombelle, P. Jofré, P. G. Jonker, A. Jorissen, F. Julbe, A. Karampelas, A. Kochoska, R. Kohley, K. Kolenberg, E. Kontizas, S. E. Koposov, G. Kordopatis, P. Koubsky, A. Kowalczyk, A. Krone-Martins, M. Kudryashova, I. Kull, R. K. Bachchan, F. Lacoste-Seris, A. F. Lanza, J. B. Lavigne, C. Le Poncin-Lafitte, Y. Lebreton, T. Lebzelter, S. Leccia, N. Leclerc, I. Lecoeur-Taibi, V. Lemaitre, H. Lenhardt, F. Leroux, S. Liao, E. Licata, H. E. P. Lindstrøm, T. A. Lister, E. Livanou, A. Lobel, W. Löffler, M. López, A. Lopez-Lozano, D. Lorenz, T. Loureiro, I. MacDonald, T. Magalhães Fernandes, S. Managau, R. G. Mann, G. Mantelet, O. Marchal, J. M. Marchant, M. Marconi, J. Marie, S. Marinoni, P. M. Marrese, G. Marschalkó, D. J. Marshall, J. M. Martín-Fleitas, M. Martino, N. Mary, G. Matijevič, T. Mazeh, P. J. McMillan, S. Messina, A. Mestre, D. Michalik, N. R. Millar, B. M. H. Miranda, D. Molina, R. Molinaro, M. Molinaro, L. Molnár, M. Moniez, P. Montegriffo, D. Monteiro, R. Mor, A. Mora, R. Morbidelli, T. Morel, S. Morgenthaler, T. Morley, D. Morris, A. F. Mulone, T. Muraveva, I. Musella, J. Narbonne, G. Nelemans, L. Nicastro, L. Noval, C. Ordénovic, J. Ordieres-Meré, P. Osborne, C. Pagani, I. Pagano, F. Pailler, H. Palacin, L. Palaversa, P. Parsons, T. Paulsen, M. Pecoraro, R. Pedrosa, H. Pentikäinen, J. Pereira, B. Pichon, A. M. Piersimoni, F. X. Pineau, E. Plachy, G. Plum, E. Poujoulet, A. Prša, L. Pulone, S. Ragaini, S. Rago, N. Rambaux, M. Ramos-Lerate, P. Ranalli, G. Rauw, A. Read, S. Regibo, F. Renk, C. Reylé, R. A. Ribeiro, L. Rimoldini, V. Ripepi, A. Riva, G. Rixon, M. Roelens, M. Romero-Gómez, N. Rowell, F. Royer, A. Rudolph, L. Ruiz-Dern, G. Sadowski, T. Sagristà Sellés, J. Sahlmann, J. Salgado, E. Salguero, M. Sarasso, H. Savietto, A. Schnorhk, M. Schultheis, E. Sciacca, M. Segol, J. C. Segovia, D. Segransan, E. Serpell, I. C. Shih, R. Smareglia, R. L. Smart, C. Smith, E. Solano, F. Solitro, R. Sordo, S. Soria Nieto, J. Souchay, A. Spagna, F. Spoto, U. Stampa, I. A. Steele, H. Steidelmüller, C. A. Stephenson, H. Stoev, F. F. Suess, M. Süveges, J. Surdej, L. Szabados, E. Szegedi-Elek, D. Tapiador, F. Taris, G. Tauran, M. B. Taylor, R. Teixeira, D. Terrett, B. Tingley, S. C. Trager, C. Turon, A. Ulla, E. Utrilla, G. Valentini, A. van Elteren, E. Van Hemelryck, M. van Leeuwen, M. Varadi, A. Vecchiato, J. Veljanoski, T. Via, D. Vicente, S. Vogt, H. Voss, V. Votruba, S. Voutsinas, G. Walmsley, M. Weiler, K. Weingrill, D. Werner, T. Wevers, G. Whitehead, Ł. Wyrzykowski, A. Yoldas, M. Žerjal, S. Zucker, C. Zurbach, T. Zwitter, A. Alecu, M. Allen, C. Allende Prieto, A. Amorim, G. Anglada-Escudé,

V. Arsenijevic, S. Azaz, P. Balm, M. Beck, H. H. Bernstein, L. Bigot, A. Bijaoui, C. Blasco, M. Bonfigli, G. Bono, S. Boudreault, A. Bressan, S. Brown, P. M. Brunet, P. Bunclark, R. Buonanno, A. G. Butkevich, C. Carret, C. Carrion, L. Chemin, F. Chéreau, L. Corcione, E. Darmigny, K. S. de Boer, P. de Teodoro, P. T. de Zeeuw, C. Delle Luche, C. D. Domingues, P. Dubath, F. Fodor, B. Frézouls, A. Fries, D. Fustes, D. Fyfe, E. Gallardo, J. Gallegos, D. Gardiol, M. Gebran, A. Gomboc, A. Gómez, E. Grux, A. Gueguen, A. Heyrovsky, J. Hoar, G. Iannicola, Y. Isasi Parache, A. M. Janotto, E. Joliet, A. Jonckheere, R. Keil, D. W. Kim, P. Klagyivik, J. Klar, J. Knude, O. Kochukhov, I. Kolka, J. Kos, A. Kutka, V. Lainey, D. LeBouquin, C. Liu, D. Loreggia, V. V. Makarov, M. G. Marseille, C. Martayan, O. Martinez-Rubi, B. Massart, F. Meynadier, S. Mignot, U. Munari, A. T. Nguyen, T. Nordlander, P. Ocvirk, K. S. O'Flaherty, A. Olias Sanz, P. Ortiz, J. Osorio, D. Oszkiewicz, A. Ouzounis, M. Palmer, P. Park, E. Pasquato, C. Peltzer, J. Peralta, F. Péturaud, T. Pieniluoma, E. Pigozzi, J. Poels, G. Prat, T. Prod'homme, F. Raison, J. M. Rebordao, D. Risquez, B. Rocca-Volmerange, S. Rosen, M. I. Ruiz-Fuertes, F. Russo, S. Sembay, I. Serraller Vizcaino, A. Short, A. Siebert, H. Silva, D. Sinachopoulos, E. Slezak, M. Soffel, D. Sosnowska, V. Straižys, M. ter Linden, D. Terrell, S. Theil, C. Tiede, L. Troisi, P. Tsalmantza, D. Tur, M. Vaccari, F. Vachier, P. Valles, W. Van Hamme, L. Veltz, J. Virtanen, J. M. Wallut, R. Wichmann, M. I. Wilkinson, H. Ziaeepour, and S. Zschocke. The Gaia mission. *Astronomy and Astrophysics*, 595:A1, Nov. 2016.

[140] Gaia Collaboration, A. Vallenari, A. G. A. Brown, T. Prusti, J. H. J. de Bruijne, F. Arenou, C. Babusiaux, M. Biermann, O. L. Creevey, C. Ducourant, D. W. Evans, L. Eyer, R. Guerra, A. Hutton, C. Jordi, S. A. Klioner, U. L. Lammers, L. Lindegren, X. Luri, F. Mignard, C. Panem, D. Pourbaix, S. Randich, P. Sartoretti, C. Soubiran, P. Tanga, N. A. Walton, C. A. L. Bailer-Jones, U. Bastian, R. Drimmel, F. Jansen, D. Katz, M. G. Lattanzi, F. van Leeuwen, J. Bakker, C. Cacciari, J. Castañeda, F. De Angeli, C. Fabricius, M. Fouesneau, Y. Frémat, L. Galluccio, A. Guerrier, U. Heiter, E. Masana, R. Messineo, N. Mowlavi, C. Nicolas, K. Nienartowicz, F. Pailler, P. Panuzzo, F. Riclet, W. Roux, G. M. Seabroke, R. Sordoørcit, F. Thévenin, G. Gracia-Abril, J. Portell, D. Teyssier, M. Altmann, R. Andrae, M. Audard, I. Bellas-Velidis, K. Benson, J. Berthier, R. Blomme, P. W. Burgess, D. Busonero, G. Busso, H. Cánovas, B. Carry, A. Cellino, N. Cheek, G. Clementini, Y. Damerdji, M. Davidson, P. de Teodoro, M. Nuñez Campos, L. Delchambre, A. Dell'Oro, P. Esquej, J. Fernández-Hernández, E. Fraile, D. Garabato, P. García-Lario, E. Gosset, R. Haigron, J. L. Halbwachs, N. C. Hambly, D. L. Harrison, J. Hernández, D. Hestroffer, S. T. Hodgkin, B. Holl, K. Janßen, G. Jevardat de Fombelle, S. Jordan, A. Krone-Martins, A. C. Lanzafame, W. Löffler, O. Marchal, P. M. Marrese, A. Moitinho, K. Muinonen, P. Osborne, E. Pancino, T. Pauwels, A. Recio-Blanco, C. Reylé, M. Riello, L. Rimoldini, T. Roegiers, J. Rybizki, L. M. Sarro, C. Siopis, M. Smith, A. Sozzetti, E. Utrilla, M. van Leeuwen, U. Abbas, P. Ábrahám, A. Abreu Aramburu, C. Aerts, J. J. Aguado, M. Ajaj, F. Aldea-Montero, G. Altavilla, M. A. Álvarez, J. Alves, F. Anders, R. I. Anderson, E. Anglada Varela, T. Antoja, D. Baines, S. G. Baker, L. Balaguer-Núñez, E. Balbinot, Z. Balog, C. Barache, D. Barbato,

M. Barros, M. A. Barstow, S. Bartolomé, J. L. Bassilana, N. Bauchet, U. Becciani, M. Bellazzini, A. Berihuete, M. Bernet, S. Bertone, L. Bianchi, A. Binnenfeld, S. Blanco-Cuaresma, A. Blazere, T. Boch, A. Bombrun, D. Bossini, S. Bouquillon, A. Bragaglia, L. Bramante, E. Breedt, A. Bressan, N. Brouillet, E. Brugaletta, B. Bucciarelli, A. Burlacu, A. G. Butkevich, R. Buzzi, E. Caffau, R. Cancelliere, T. Cantat-Gaudin, R. Carballo, T. Carlucci, M. I. Carnerero, J. M. Carrasco, L. Casamiquela, M. Castellani, A. Castro-Ginard, L. Chaoul, P. Charlot, L. Chemin, V. Chiaramida, A. Chiavassa, N. Chornay, G. Comoretto, G. Contursi, W. J. Cooper, T. Cornez, S. Cowell, F. Crifo, M. Cropper, M. Crosta, C. Crowley, C. Dafonte, A. Dapergolas, M. David, P. David, P. de Laverny, F. De Luise, R. De March, J. De Ridder, R. de Souza, A. de Torres, E. F. del Peloso, E. del Pozo, M. Delbo, A. Delgado, J. B. Delisle, C. Demouchy, T. E. Dharmawardena, P. Di Matteo, S. Diakite, C. Diener, E. Distefano, C. Dolding, B. Edvardsson, H. Enke, C. Fabre, M. Fabrizio, S. Faigler, G. Fedorets, P. Fernique, A. Fienga, F. Figueras, Y. Fournier, C. Fouron, F. Fragkoudi, M. Gai, A. Garcia-Gutierrez, M. Garcia-Reinaldos, M. García-Torres, A. Garofalo, A. Gavel, P. Gavras, E. Gerlach, R. Geyer, P. Giacobbe, G. Gilmore, S. Girona, G. Giuffrida, R. Gomel, A. Gomez, J. González-Núñez, I. González-Santamaría, J. J. González-Vidal, M. Granvik, P. Guillout, J. Guiraud, R. Gutiérrez-Sánchez, L. P. Guy, D. Hatzidimitriou, M. Hauser, M. Haywood, A. Helmer, A. Helmi, M. H. Sarmiento, S. L. Hidalgo, T. Hilger, N. Hładczuk, D. Hobbs, G. Holland, H. E. Huckle, K. Jardine, G. Jasniewicz, A. Jean-Antoine Piccolo, Ó. Jiménez-Arranz, A. Jorissen, J. Juaristi Campillo, F. Julbe, L. Karbevska, P. Kervella, S. Khanna, M. Kontizas, G. Kordopatis, A. J. Korn, Á. Kóspál, Z. Kostrzewa-Rutkowska, K. Kruszyńska, M. Kun, P. Laizeau, S. Lambert, A. F. Lanza, Y. Lasne, J. F. Le Campion, Y. Lebreton, T. Lebzelter, S. Leccia, N. Leclerc, I. Lecoeur-Taibi, S. Liao, E. L. Licata, H. E. P. Lindstrøm, T. A. Lister, E. Livanou, A. Lobel, A. Lorca, C. Loup, P. Madrero Pardo, A. Magdaleno Romeo, S. Managau, R. G. Mann, M. Manteiga, J. M. Marchant, M. Marconi, J. Marcos, M. M. S. Marcos Santos, D. Marín Pina, S. Marinoni, F. Marocco, D. J. Marshall, L. M. Polo, J. M. Martín-Fleitas, G. Marton, N. Mary, A. Masip, D. Massari, A. Mastrobuono-Battisti, T. Mazeh, P. J. McMillan, S. Messina, D. Michalik, N. R. Millar, A. Mints, D. Molina, R. Molinaro, L. Molnár, G. Monari, M. Monguió, P. Montegriffo, A. Montero, R. Mor, A. Mora, R. Morbidelli, T. Morel, D. Morris, T. Muraveva, C. P. Murphy, I. Musella, Z. Nagy, L. Noval, F. Ocaña, A. Ogden, C. Ordenovic, J. O. Osinde, C. Pagani, I. Pagano, L. Palaversa, P. A. Palicio, L. Pallas-Quintela, A. Panahi, S. Payne-Wardenaar, X. Peñalosa Esteller, A. Penttilä, B. Pichon, A. M. Piersimoni, F. X. Pineau, E. Plachy, G. Plum, E. Poggio, A. Prša, L. Pulone, E. Racero, S. Ragaini, M. Rainer, C. M. Raiteri, N. Rambaux, P. Ramos, M. Ramos-Lerate, P. Re Fiorentin, S. Regibo, P. J. Richards, C. Rios Diaz, V. Ripepi, A. Riva, H. W. Rix, G. Rixon, N. Robichon, A. C. Robin, C. Robin, M. Roelens, H. R. O. Rogues, L. Rohrbasser, M. Romero-Gómez, N. Rowell, F. Royer, D. Ruz Mieres, K. A. Rybicki, G. Sadowski, A. Sáez Núñez, A. Sagristà Sellés, J. Sahlmann, E. Salguero, N. Samaras, V. Sanchez Gimenez, N. Sanna, R. Santoveña, M. Sarasso, M. Schultheis, E. Sciacca, M. Segol, J. C. Segovia, D. Ségransan, D. Semeux, S. Shahaf, H. I. Siddiqui, A. Siebert, L. Siltala, A. Silvelo, E. Slezak, I. Slezak, R. L. Smart, O. N. Snaith, E. Solano, F. Solitro, D. Souami, J. Souchay, A. Spagna, L. Spina, F. Spoto,

I. A. Steele, H. Steidelmüller, C. A. Stephenson, M. Süveges, J. Surdej, L. Szabados, E. Szegedi-Elek, F. Taris, M. B. Taylo, R. Teixeira, L. Tolomei, N. Tonello, F. Torra, J. Torra, G. Torralba Elipe, M. Trabucchi, A. T. Tsounis, C. Turon, A. Ulla, N. Unger, M. V. Vaillant, E. van Dillen, W. van Reeven, O. Vanel, A. Vecchiato, Y. Viala, D. Vicente, S. Voutsinas, M. Weiler, T. Wevers, L. Wyrzykowski, A. Yoldas, P. Yvard, H. Zhao, J. Zorec, S. Zucker, and T. Zwitter. Gaia Data Release 3: Summary of the content and survey properties. *arXiv e-prints*, page arXiv:2208.00211, July 2022.

[141] Gaia Collaboration, A. Vallenari, A. G. A. Brown, T. Prusti, J. H. J. de Bruijne, F. Arenou, C. Babusiaux, M. Biermann, O. L. Creevey, C. Ducourant, D. W. Evans, L. Eyer, R. Guerra, A. Hutton, C. Jordi, S. A. Klioner, U. L. Lammers, L. Lindegren, X. Luri, F. Mignard, C. Panem, D. Pourbaix, S. Randich, P. Sartoretti, C. Soubiran, P. Tanga, N. A. Walton, C. A. L. Bailer-Jones, U. Bastian, R. Drimmel, F. Jansen, D. Katz, M. G. Lattanzi, F. van Leeuwen, J. Bakker, C. Cacciari, J. Castañeda, F. De Angeli, C. Fabricius, M. Fouesneau, Y. Frémat, L. Galluccio, A. Guerrier, U. Heiter, E. Masana, R. Messineo, N. Mowlavi, C. Nicolas, K. Nienartowicz, F. Pailler, P. Panuzzo, F. Riclet, W. Roux, G. M. Seabroke, R. Sordo, F. Thévenin, G. Gracia-Abril, J. Portell, D. Teyssier, M. Altmann, R. Andrae, M. Audard, I. Bellas-Velidis, K. Benson, J. Berthier, R. Blomme, P. W. Burgess, D. Busonero, G. Busso, H. Cánovas, B. Carry, A. Cellino, N. Cheek, G. Clementini, Y. Damerdji, M. Davidson, P. de Teodoro, M. Nuñez Campos, L. Delchambre, A. Dell'Oro, P. Esquej, J. Fernández-Hernández, E. Fraile, D. Garabato, P. García-Lario, E. Gosset, R. Haigron, J. L. Halbwachs, N. C. Hambly, D. L. Harrison, J. Hernández, D. Hestroffer, S. T. Hodgkin, B. Holl, K. Janßen, G. Jevardat de Fombelle, S. Jordan, A. Krone-Martins, A. C. Lanzafame, W. Löffler, O. Marchal, P. M. Marrese, A. Moitinho, K. Muinonen, P. Osborne, E. Pancino, T. Pauwels, A. Recio-Blanco, C. Reylé, M. Riello, L. Rimoldini, T. Roegiers, J. Rybizki, L. M. Sarro, C. Siopis, M. Smith, A. Sozzetti, E. Utrilla, M. van Leeuwen, U. Abbas, P. Ábrahám, A. Abreu Aramburu, C. Aerts, J. J. Aguado, M. Ajaj, F. Aldea-Montero, G. Altavilla, M. A. Álvarez, J. Alves, F. Anders, R. I. Anderson, E. Anglada Varela, T. Antoja, D. Baines, S. G. Baker, L. Balaguer-Núñez, E. Balbinot, Z. Balog, C. Barache, D. Barbato, M. Barros, M. A. Barstow, S. Bartolomé, J. L. Bassilana, N. Bauchet, U. Becciani, M. Bellazzini, A. Berihuete, M. Bernet, S. Bertone, L. Bianchi, A. Binnenfeld, S. Blanco-Cuaresma, A. Blazere, T. Boch, A. Bombrun, D. Bossini, S. Bouquillon, A. Bragaglia, L. Bramante, E. Breedt, A. Bressan, N. Brouillet, E. Brugaletta, B. Bucciarelli, A. Burlacu, A. G. Butkevich, R. Buzzi, E. Caffau, R. Cancelliere, T. Cantat-Gaudin, R. Carballo, T. Carlucci, M. I. Carnerero, J. M. Carrasco, L. Casamiquela, M. Castellani, A. Castro-Ginard, L. Chaoul, P. Charlot, L. Chemin, V. Chiaramida, A. Chiavassa, N. Chornay, G. Comoretto, G. Contursi, W. J. Cooper, T. Cornez, S. Cowell, F. Crifo, M. Cropper, M. Crosta, C. Crowley, C. Dafonte, A. Dapergolas, M. David, P. David, P. de Laverny, F. De Luise, R. De March, J. De Ridder, R. de Souza, A. de Torres, E. F. del Peloso, E. del Pozo, M. Delbo, A. Delgado, J. B. Delisle, C. Demouchy, T. E. Dharmawardena, P. Di Matteo, S. Diakite, C. Diener, E. Distefano, C. Dolding, B. Edvardsson, H. Enke, C. Fabre, M. Fabrizio, S. Faigler, G. Fedorets, P. Fernique, A. Fienga, F. Figueras, Y. Fournier, C. Fouron, F. Fragkoudi,

M. Gai, A. Garcia-Gutierrez, M. Garcia-Reinaldos, M. García-Torres, A. Garofalo, A. Gavel, P. Gavras, E. Gerlach, R. Geyer, P. Giacobbe, G. Gilmore, S. Girona, G. Giuffrida, R. Gomel, A. Gomez, J. González-Núñez, I. González-Santamaría, J. J. González-Vidal, M. Granvik, P. Guillout, J. Guiraud, R. Gutiérrez-Sánchez, L. P. Guy, D. Hatzidimitriou, M. Hauser, M. Haywood, A. Helmer, A. Helmi, M. H. Sarmiento, S. L. Hidalgo, T. Hilger, N. Hładczuk, D. Hobbs, G. Holland, H. E. Huckle, K. Jardine, G. Jasniewicz, A. Jean-Antoine Piccolo, Ó. Jiménez-Arranz, A. Jorissen, J. Juaristi Campillo, F. Julbe, L. Karbevska, P. Kervella, S. Khanna, M. Kontizas, G. Kordopatis, A. J. Korn, Á. Kóspál, Z. Kostrzewa-Rutkowska, K. Kruszyńska, M. Kun, P. Laizeau, S. Lambert, A. F. Lanza, Y. Lasne, J. F. Le Campion, Y. Lebreton, T. Lebzelter, S. Leccia, N. Leclerc, I. Lecoeur-Taibi, S. Liao, E. L. Licata, H. E. P. Lindstrøm, T. A. Lister, E. Livanou, A. Lobel, A. Lorca, C. Loup, P. Madrero Pardo, A. Magdaleno Romeo, S. Managau, R. G. Mann, M. Manteiga, J. M. Marchant, M. Marconi, J. Marcos, M. M. S. Marcos Santos, D. Marín Pina, S. Marinoni, F. Marocco, D. J. Marshall, L. Martin Polo, J. M. Martín-Fleitas, G. Marton, N. Mary, A. Masip, D. Massari, A. Mastrobuono-Battisti, T. Mazeh, P. J. McMillan, S. Messina, D. Michalik, N. R. Millar, A. Mints, D. Molina, R. Molinaro, L. Molnár, G. Monari, M. Monguió, P. Montegriffo, A. Montero, R. Mor, A. Mora, R. Morbidelli, T. Morel, D. Morris, T. Muraveva, C. P. Murphy, I. Musella, Z. Nagy, L. Noval, F. Ocaña, A. Ogden, C. Ordenovic, J. O. Osinde, C. Pagani, I. Pagano, L. Palaversa, P. A. Palicio, L. Pallas-Quintela, A. Panahi, S. Payne-Wardenaar, X. Peñalosa Esteller, A. Penttilä, B. Pichon, A. M. Piersimoni, F. X. Pineau, E. Plachy, G. Plum, E. Poggio, A. Prša, L. Pulone, E. Racero, S. Ragaini, M. Rainer, C. M. Raiteri, N. Rambaux, P. Ramos, M. Ramos-Lerate, P. Re Fiorentin, S. Regibo, P. J. Richards, C. Rios Diaz, V. Ripepi, A. Riva, H. W. Rix, G. Rixon, N. Robichon, A. C. Robin, C. Robin, M. Roelens, H. R. O. Rogues, L. Rohrbasser, M. Romero-Gómez, N. Rowell, F. Royer, D. Ruz Mieres, K. A. Rybicki, G. Sadowski, A. Sáez Núñez, A. Sagristà Sellés, J. Sahlmann, E. Salguero, N. Samaras, V. Sanchez Gimenez, N. Sanna, R. Santoveña, M. Sarasso, M. Schultheis, E. Sciacca, M. Segol, J. C. Segovia, D. Ségransan, D. Semeux, S. Shahaf, H. I. Siddiqui, A. Siebert, L. Siltala, A. Silvelo, E. Slezak, I. Slezak, R. L. Smart, O. N. Snaith, E. Solano, F. Solitro, D. Souami, J. Souchay, A. Spagna, L. Spina, F. Spoto, I. A. Steele, H. Steidelmüller, C. A. Stephenson, M. Süveges, J. Surdej, L. Szabados, E. Szegedi-Elek, F. Taris, M. B. Taylor, R. Teixeira, L. Tolomei, N. Tonello, F. Torra, J. Torra, G. Torralba Elipe, M. Trabucchi, A. T. Tsounis, C. Turon, A. Ulla, N. Unger, M. V. Vaillant, E. van Dillen, W. van Reeven, O. Vanel, A. Vecchiato, Y. Viala, D. Vicente, S. Voutsinas, M. Weiler, T. Wevers, Ł. Wyrzykowski, A. Yoldas, P. Yvard, H. Zhao, J. Zorec, S. Zucker, and T. Zwitter. Gaia Data Release 3. Summary of the content and survey properties. *Astronomy and Astrophysics*, 674:A1, June 2023.

[142] T. Gan, A. Soubkiou, S. X. Wang, Z. Benkhaldoun, S. Mao, É. Artigau, P. Fouqué, S. Giacalone, C. A. Theissen, C. Aganze, K. A. Collins, A. Shporer, K. Barkaoui, M. Ghachoui, S. B. Howell, C. Lamman, O. D. S. Demangeon, A. Burdanov, C. Cadieux, J. Chouqar, K. I. Collins, N. J. Cook, L. Delrez, B.-O. Demory, R. Doyon, G. Dransfield, C. D. Dressing, E. Ducrot, J. Fan, L. Garcia, H. Gill, M. Gillon, C. L. Gnilka, Y. Gómez Maqueo Chew, M. N. Günther, C. E. Henze, C. X. Huang, E. Jehin,

E. L. N. Jensen, Z. Lin, J. McCormac, C. A. Murray, P. Niraula, P. P. Pedersen, F. J. Pozuelos, D. Queloz, B. V. Rackham, A. B. Savel, N. Schanche, R. P. Schwarz, D. Sebastian, S. Thompson, M. Timmermans, A. H. M. J. Triaud, M. Vezie, R. D. Wells, J. de Wit, G. R. Ricker, R. Vanderspek, D. W. Latham, S. Seager, J. N. Winn, and J. M. Jenkins. TESS discovery of a sub-Neptune orbiting a mid-M dwarf TOI-2136. *arXiv e-prints*, page arXiv:2202.10024, Feb. 2022.

[143] J. P. Gardner, J. C. Mather, M. Clampin, R. Doyon, M. A. Greenhouse, H. B. Hammel, J. B. Hutchings, P. Jakobsen, S. J. Lilly, K. S. Long, J. I. Lunine, M. J. McCaughrean, M. Mountain, J. Nella, G. H. Rieke, M. J. Rieke, H.-W. Rix, E. P. Smith, G. Sonneborn, M. Stiavelli, H. S. Stockman, R. A. Windhorst, and G. S. Wright. The James Webb Space Telescope. *Space Science Reviews*, 123(4):485–606, Apr. 2006.

[144] F. Genest, D. Lafrenière, A. Boucher, A. Darveau-Bernier, R. Doyon, É. Artigau, and N. Cook. On the Effect of Stellar Activity on Low-resolution Transit Spectroscopy and the use of High Resolution as Mitigation. *The Astronomical Journal*, 163(5):231, May 2022.

[145] S. R. Gibson, A. W. Howard, G. W. Marcy, J. Edelstein, E. H. Wishnow, and C. L. Poppett. KPF: Keck Planet Finder. In C. J. Evans, L. Simard, and H. Takami, editors, *Ground-based and Airborne Instrumentation for Astronomy VI*, volume 9908 of *Society of Photo-Optical Instrumentation Engineers (SPIE) Conference Series*, page 990870, Aug. 2016.

[146] C. Gilbertson, E. B. Ford, and X. Dumusque. Toward Extremely Precise Radial Velocities. I. Simulated Solar Spectra for Testing Exoplanet Detection Algorithms. *Research Notes of the American Astronomical Society*, 4(4):59, Apr. 2020.

[147] H. A. C. Giles, A. Collier Cameron, and R. D. Haywood. A Kepler study of starspot lifetimes with respect to light-curve amplitude and spectral type. *Monthly Notices of the Royal Astronomical Society*, 472(2):1618–1627, Dec. 2017.

[148] M. Gillon, E. Jehin, S. M. Lederer, L. Delrez, J. de Wit, A. Burdanov, V. Van Grootel, A. J. Burgasser, A. H. M. J. Triaud, C. Opitom, B.-O. Demory, D. K. Sahu, D. Bardalez Gagliuffi, P. Magain, and D. Queloz. Temperate Earth-sized planets transiting a nearby ultracool dwarf star. *Nature*, 533(7602):221–224, May 2016.

[149] M. Gillon, A. H. M. J. Triaud, B.-O. Demory, E. Jehin, E. Agol, K. M. Deck, S. M. Lederer, J. de Wit, A. Burdanov, J. G. Ingalls, E. Bolmont, J. Leconte, S. N. Raymond, F. Selsis, M. Turbet, K. Barkaoui, A. Burgasser, M. R. Burleigh, S. J. Carey, A. Chaushev, C. M. Copperwheat, L. Delrez, C. S. Fernandes, D. L. Holdsworth, E. J. Kotze, V. Van Grootel, Y. Almleaky, Z. Benkhaldoun, P. Magain, and D. Queloz. Seven temperate terrestrial planets around the nearby ultracool dwarf star TRAPPIST-1. *Nature*, 542(7642):456–460, Feb. 2017.

[150] P. Goldreich and S. Soter. Q in the Solar System. *Icarus*, 5(1):375–389, Jan. 1966.

[151] P. Goldreich and S. Tremaine. Disk-satellite interactions. *The Astrophysical Journal*, 241:425–441, Oct. 1980.

[152] E. Golub, M. Everett, S. E. Logsdon, J. Rajagopal, and E. Timmermann. An automated scheduling software package and queue system for the NEID radial velocity spectrometer. In D. S. Adler, R. L. Seaman, and C. R. Benn, editors, *Observatory Operations: Strategies, Processes, and Systems VIII*, volume 11449, page 114491F. International Society for Optics and Photonics, SPIE, 2020.

[153] J. Gomes da Silva, N. C. Santos, X. Bonfils, X. Delfosse, T. Forveille, and S. Udry. Long-term magnetic activity of a sample of M-dwarf stars from the HARPS program. I. Comparison of activity indices. *Astronomy and Astrophysics*, 534:A30, Oct. 2011.

[154] J. Goodman and J. Weare. Ensemble samplers with affine invariance. *Communications in Applied Mathematics and Computational Science*, 5(1):65–80, Jan. 2010.

[155] D. F. Gray, S. L. Baliunas, G. W. Lockwood, and B. A. Skiff. The Activity Cycle of sigma Draconis. *The Astrophysical Journal*, 400:681, Dec. 1992.

[156] G. M. Green, E. Schlafly, C. Zucker, J. S. Speagle, and D. Finkbeiner. A 3D Dust Map Based on Gaia, Pan-STARRS 1, and 2MASS. *The Astrophysical Journal*, 887(1):93, Dec. 2019.

[157] T. P. Greene, T. J. Bell, E. Ducrot, A. Dyrek, P.-O. Lagage, and J. J. Fortney. Thermal emission from the Earth-sized exoplanet TRAPPIST-1 b using JWST. *Nature*, 618(7963):39–42, June 2023.

[158] P. C. Gregory. An apodized Kepler periodogram for separating planetary and stellar activity signals. *Monthly Notices of the Royal Astronomical Society*, 458(3):2604–2633, May 2016.

[159] S. L. Grimm, B.-O. Demory, M. Gillon, C. Dorn, E. Agol, A. Burdanov, L. Delrez, M. Sestovic, A. H. M. J. Triaud, M. Turbet, É. Bolmont, A. Caldas, J. de Wit, E. Jehin, J. Leconte, S. N. Raymond, V. Van Grootel, A. J. Burgasser, S. Carey, D. Fabrycky, K. Heng, D. M. Hernandez, J. G. Ingalls, S. Lederer, F. Selsis, and D. Queloz. The nature of the TRAPPIST-1 exoplanets. *Astronomy and Astrophysics*, 613:A68, May 2018.

[160] S. K. Grunblatt, A. W. Howard, and R. D. Haywood. Determining the Mass of Kepler-78b with Nonparametric Gaussian Process Estimation. *The Astrophysical Journal*, 808(2):127, Aug. 2015.

[161] N. M. Guerrero, S. Seager, C. X. Huang, A. Vanderburg, A. Garcia Soto, I. Mireles, K. Hesse, W. Fong, A. Glidden, A. Shporer, D. W. Latham, K. A. Collins, S. N. Quinn, J. Burt, D. Dragomir, I. Crossfield, R. Vanderspek, M. Fausnaugh, C. J. Burke, G. Ricker, T. Daylan, Z. Essack, M. N. Günther, H. P. Osborn, J. Pepper, P. Rowden, L. Sha, J. Villanueva, Steven, D. A. Yahalomi, L. Yu, S. Ballard, N. M. Batalha, D. Berardo, A. Chontos, J. A. Dittmann, G. A. Esquerdo, T. Mikal-Evans,

R. Jayaraman, A. Krishnamurthy, D. R. Louie, N. Mehrle, P. Niraula, B. V. Rackham, J. E. Rodriguez, S. J. L. Rowden, C. Sousa-Silva, D. Watanabe, I. Wong, Z. Zhan, G. Zivanovic, J. L. Christiansen, D. R. Ciardi, M. A. Swain, M. B. Lund, S. E. Mullally, S. W. Fleming, D. R. Rodriguez, P. T. Boyd, E. V. Quintana, T. Barclay, K. D. Colón, S. A. Rinehart, J. E. Schlieder, M. Clampin, J. M. Jenkins, J. D. Twicken, D. A. Caldwell, J. L. Coughlin, C. Henze, J. J. Lissauer, R. L. Morris, M. E. Rose, J. C. Smith, P. Tenenbaum, E. B. Ting, B. Wohler, G. Á. Bakos, J. L. Bean, Z. K. Berta-Thompson, A. Bieryla, L. G. Bouma, L. A. Buchhave, N. Butler, D. Charbonneau, J. P. Doty, J. Ge, M. J. Holman, A. W. Howard, L. Kaltenegger, S. R. Kane, H. Kjeldsen, L. Kreidberg, D. N. C. Lin, C. Minsky, N. Narita, M. Paegert, A. Pál, E. Palle, D. D. Sasselov, A. Spencer, A. Sozzetti, K. G. Stassun, G. Torres, S. Udry, and J. N. Winn. The TESS Objects of Interest Catalog from the TESS Prime Mission. *The Astrophysical Journal Supplement*, 254(2):39, June 2021.

[162] K. Gullikson, S. Dodson-Robinson, and A. Kraus. Correcting for Telluric Absorption: Methods, Case Studies, and Release of the TelFit Code. *Astronomical Journal*, 148(3):53, Sept. 2014.

[163] M. N. Günther, F. J. Pozuelos, J. A. Dittmann, D. Dragomir, S. R. Kane, T. Daylan, A. D. Feinstein, C. X. Huang, T. D. Morton, A. Bonfanti, L. G. Bouma, J. Burt, K. A. Collins, J. J. Lissauer, E. Matthews, B. T. Montet, A. Vanderburg, S. Wang, J. G. Winters, G. R. Ricker, R. K. Vanderspek, D. W. Latham, S. Seager, J. N. Winn, J. M. Jenkins, J. D. Armstrong, K. Barkaoui, N. Batalha, J. L. Bean, D. A. Caldwell, D. R. Ciardi, K. I. Collins, I. Crossfield, M. Fausnaugh, G. Furesz, T. Gan, M. Gillon, N. Guerrero, K. Horne, S. B. Howell, M. Ireland, G. Isopi, E. Jehin, J. F. Kielkopf, S. Lepine, F. Mallia, R. A. Matson, G. Myers, E. Palle, S. N. Quinn, H. M. Relles, B. Rojas-Ayala, J. Schlieder, R. Sefako, A. Shporer, J. C. Suárez, T.-G. Tan, E. B. Ting, J. D. Twicken, and I. A. Waite. A super-Earth and two sub-Neptunes transiting the nearby and quiet M dwarf TOI-270. *Nature Astronomy*, 3:1099–1108, July 2019.

[164] S. Hadden and Y. Lithwick. Kepler Planet Masses and Eccentricities from TTV Analysis. *The Astronomical Journal*, 154(1):5, July 2017.

[165] S. Halverson, R. Terrien, S. Mahadevan, A. Roy, C. Bender, G. K. Stefánsson, A. Monson, E. Levi, F. Hearty, C. Blake, M. McElwain, C. Schwab, L. Ramsey, J. Wright, S. Wang, Q. Gong, and P. Roberston. A comprehensive radial velocity error budget for next generation Doppler spectrometers. In C. J. Evans, L. Simard, and H. Takami, editors, *Ground-based and Airborne Instrumentation for Astronomy VI*, volume 9908 of *Society of Photo-Optical Instrumentation Engineers (SPIE) Conference Series*, page 99086P, Aug. 2016.

[166] N. C. Hara, F. Bouchy, M. Stalport, I. Boisse, J. Rodrigues, J. B. Delisle, A. Santerne, G. W. Henry, L. Arnold, N. Astudillo-Defru, S. Borgniet, X. Bonfils, V. Bourrier, B. Brugger, B. Courcol, S. Dalal, M. Deleuil, X. Delfosse, O. Demangeon, R. F. Díaz, X. Dumusque, T. Forveille, G. Hébrard, M. J. Hobson, F. Kiefer, T. Lopez, L. Mignon, O. Mousis, C. Moutou, F. Pepe, J. Rey, N. C. Santos, D. Ségransan, S. Udry, and

P. A. Wilson. The SOPHIE search for northern extrasolar planets. XVI. HD 158259: A compact planetary system in a near-3:2 mean motion resonance chain. *Astronomy and Astrophysics*, 636:L6, Apr. 2020.

[167] N. C. Hara, G. Boué, J. Laskar, and A. C. M. Correia. Radial velocity data analysis with compressed sensing techniques. *Monthly Notices of the Royal Astronomical Society*, 464(1):1220–1246, Jan. 2017.

[168] C. K. Harada, C. D. Dressing, S. R. Kane, and B. Adami Ardestani. Setting the stage for the search for life with the Habitable Worlds Observatory: Properties of 164 promising planet survey targets. *arXiv e-prints*, page arXiv:2401.03047, Jan. 2024.

[169] K. K. Hardegree-Ullman, D. Apai, G. J. Bergsten, I. Pascucci, and M. López-Morales. Bioverse: A Comprehensive Assessment of the Capabilities of Extremely Large Telescopes to Probe Earth-like O_2 Levels in Nearby Transiting Habitable-zone Exoplanets. *The Astronomical Journal*, 165(6):267, June 2023.

[170] K. K. Hardegree-Ullman, D. Apai, G. J. Bergsten, I. Pascucci, and M. López-Morales. Bioverse: A Comprehensive Assessment of the Capabilities of Extremely Large Telescopes to Probe Earth-like O_2 Levels in Nearby Transiting Habitable-zone Exoplanets. *The Astronomical Journal*, 165(6):267, June 2023.

[171] K. K. Hardegree-Ullman, M. C. Cushing, P. S. Muirhead, and J. L. Christiansen. Kepler Planet Occurrence Rates for Mid-type M Dwarfs as a Function of Spectral Type. *Astronomical Journal*, 158(2):75, Aug. 2019.

[172] C. R. Harris, K. J. Millman, S. J. van der Walt, R. Gommers, P. Virtanen, D. Cournapeau, E. Wieser, J. Taylor, S. Berg, N. J. Smith, R. Kern, M. Picus, S. Hoyer, M. H. van Kerkwijk, M. Brett, A. Haldane, J. F. del Río, M. Wiebe, P. Peterson, P. Gérard-Marchant, K. Sheppard, T. Reddy, W. Weckesser, H. Abbasi, C. Gohlke, and T. E. Oliphant. Array programming with NumPy. *Nature*, 585(7825):357–362, Sept. 2020.

[173] R. D. Haywood, A. Collier Cameron, D. Queloz, S. C. C. Barros, M. Deleuil, R. Fares, M. Gillon, A. F. Lanza, C. Lovis, C. Moutou, F. Pepe, D. Pollacco, A. Santerne, D. Ségransan, and Y. C. Unruh. Planets and stellar activity: hide and seek in the CoRoT-7 system. *Monthly Notices of the Royal Astronomical Society*, 443(3):2517–2531, Sept. 2014.

[174] M. Y. He, E. B. Ford, and D. Ragozzine. Friends and Foes: Conditional Occurrence Rates of Exoplanet Companions and Their Impact on Radial Velocity Follow-up Surveys. *Astronomical Journal*, 162(5):216, Nov. 2021.

[175] G. W. Henry, G. W. Marcy, R. P. Butler, and S. S. Vogt. A Transiting "51 Peg-like" Planet. *The Astrophysical Journal Letters*, 529(1):L41–L44, Jan. 2000.

[176] T. J. Henry, W.-C. Jao, J. G. Winters, S. B. Dieterich, C. T. Finch, P. A. Ianna, A. R. Riedel, M. L. Silverstein, J. P. Subasavage, and E. H. Vrijmoet. The Solar

Neighborhood XLIV: RECONS Discoveries within 10 parsecs. *Astronomical Journal*, 155(6):265, June 2018.

[177] S. Hinkley, S. Lacour, G. D. Marleau, A. M. Lagrange, J. J. Wang, J. Kammerer, A. Cumming, M. Nowak, L. Rodet, T. Stolker, W. O. Balmer, S. Ray, M. Bonnefoy, P. Mollière, C. Lazzoni, G. Kennedy, C. Mordasini, R. Abuter, S. Aigrain, A. Amorim, R. Asensio-Torres, C. Babusiaux, M. Benisty, J. P. Berger, H. Beust, S. Blunt, A. Boccaletti, A. Bohn, H. Bonnet, G. Bourdarot, W. Brandner, F. Cantalloube, P. Caselli, B. Charnay, G. Chauvin, A. Chomez, E. Choquet, V. Christiaens, Y. Clénet, V. Coudé du Foresto, A. Cridland, P. Delorme, R. Dembet, A. Drescher, G. Duvert, A. Eckart, F. Eisenhauer, H. Feuchtgruber, F. Galland, P. Garcia, R. Garcia Lopez, T. Gardner, E. Gendron, R. Genzel, S. Gillessen, J. H. Girard, A. Grandjean, X. Haubois, G. Heißel, T. Henning, S. Hippler, M. Horrobin, M. Houllé, Z. Hubert, L. Jocou, M. Keppler, P. Kervella, L. Kreidberg, V. Lapeyrère, J. B. Le Bouquin, P. Léna, D. Lutz, A. L. Maire, F. Mang, A. Mérand, N. Meunier, J. D. Monnier, D. Mouillet, E. Nasedkin, T. Ott, G. P. P. L. Otten, C. Paladini, T. Paumard, K. Perraut, G. Perrin, F. Philipot, O. Pfuhl, N. Pourré, L. Pueyo, J. Rameau, E. Rickman, P. Rubini, Z. Rustamkulov, M. Samland, J. Shangguan, T. Shimizu, D. Sing, C. Straubmeier, E. Sturm, L. J. Tacconi, E. F. van Dishoeck, A. Vigan, F. Vincent, K. Ward-Duong, F. Widmann, E. Wieprecht, E. Wiezorrek, J. Woillez, S. Yazici, A. Young, and N. Zicher. Direct discovery of the inner exoplanet in the HD 206893 system. Evidence for deuterium burning in a planetary-mass companion. *Astronomy and Astrophysics*, 671:L5, Mar. 2023.

[178] M. Hippke and R. Heller. Optimized transit detection algorithm to search for periodic transits of small planets. *Astronomy and Astrophysics*, 623:A39, Mar. 2019.

[179] M. D. Hoffman and A. Gelman. The No-U-Turn Sampler: Adaptively Setting Path Lengths in Hamiltonian Monte Carlo. *arXiv e-prints*, page arXiv:1111.4246, Nov. 2011.

[180] S. Hojjatpanah, M. Oshagh, P. Figueira, N. C. Santos, E. M. Amazo-Gómez, S. G. Sousa, V. Adibekyan, B. Akinsanmi, O. Demangeon, J. Faria, J. Gomes da Silva, and N. Meunier. The correlation between photometric variability and radial velocity jitter. Based on TESS and HARPS observations. *Astronomy and Astrophysics*, 639:A35, July 2020.

[181] R. J. Holcomb, P. Robertson, P. Hartigan, R. J. Oelkers, and C. Robinson. SpinSpotter : An Automated Algorithm for Identifying Stellar Rotation Periods with Autocorrelation Analysis. *The Astrophysical Journal*, 936(2):138, Sept. 2022.

[182] F. Hormuth, S. Hippler, W. Brandner, K. Wagner, and T. Henning. AstraLux: the Calar Alto lucky imaging camera. In I. S. McLean and M. M. Casali, editors, *Ground-based and Airborne Instrumentation for Astronomy II*, volume 7014 of *Society of Photo-Optical Instrumentation Engineers (SPIE) Conference Series*, page 701448, July 2008.

[183] K. Horne. Status aand Prospects of Planetary Transit Searches: Hot Jupiters Galore. In D. Deming and S. Seager, editors, *Scientific Frontiers in Research on Extrasolar*

Planets, volume 294 of *Astronomical Society of the Pacific Conference Series*, pages 361–370, Jan. 2003.

[184] A. W. Howard, J. A. Johnson, G. W. Marcy, D. A. Fischer, J. T. Wright, D. Bernat, G. W. Henry, K. M. G. Peek, H. Isaacson, K. Apps, M. Endl, W. D. Cochran, J. A. Valenti, J. Anderson, and N. E. Piskunov. The California Planet Survey. I. Four New Giant Exoplanets. *The Astrophysical Journal*, 721(2):1467–1481, Oct. 2010.

[185] A. W. Howard, G. W. Marcy, S. T. Bryson, J. M. Jenkins, J. F. Rowe, N. M. Batalha, W. J. Borucki, D. G. Koch, E. W. Dunham, I. Gautier, Thomas N., J. Van Cleve, W. D. Cochran, D. W. Latham, J. J. Lissauer, G. Torres, T. M. Brown, R. L. Gilliland, L. A. Buchhave, D. A. Caldwell, J. Christensen-Dalsgaard, D. Ciardi, F. Fressin, M. R. Haas, S. B. Howell, H. Kjeldsen, S. Seager, L. Rogers, D. D. Sasselov, J. H. Steffen, G. S. Basri, D. Charbonneau, J. Christiansen, B. Clarke, A. Dupree, D. C. Fabrycky, D. A. Fischer, E. B. Ford, J. J. Fortney, J. Tarter, F. R. Girouard, M. J. Holman, J. A. Johnson, T. C. Klaus, P. Machalek, A. V. Moorhead, R. C. Morehead, D. Ragozzine, P. Tenenbaum, J. D. Twicken, S. N. Quinn, H. Isaacson, A. Shporer, P. W. Lucas, L. M. Walkowicz, W. F. Welsh, A. Boss, E. Devore, A. Gould, J. C. Smith, R. L. Morris, A. Prsa, T. D. Morton, M. Still, S. E. Thompson, F. Mullally, M. Endl, and P. J. MacQueen. Planet Occurrence within 0.25 AU of Solar-type Stars from Kepler. *Astrophysical Journal, Supplement*, 201(2):15, Aug. 2012.

[186] S. B. Howell, J. F. Rowe, S. T. Bryson, S. N. Quinn, G. W. Marcy, H. Isaacson, D. R. Ciardi, W. J. Chaplin, T. S. Metcalfe, M. J. P. F. G. Monteiro, T. Appourchaux, S. Basu, O. L. Creevey, R. L. Gilliland, P.-O. Quirion, D. Stello, H. Kjeldsen, J. Christensen-Dalsgaard, Y. Elsworth, R. A. García, G. Houdek, C. Karoff, J. Molenda-Żakowicz, M. J. Thompson, G. A. Verner, G. Torres, F. Fressin, J. R. Crepp, E. Adams, A. Dupree, D. D. Sasselov, C. D. Dressing, W. J. Borucki, D. G. Koch, J. J. Lissauer, D. W. Latham, L. A. Buchhave, I. Gautier, Thomas N., M. Everett, E. Horch, N. M. Batalha, E. W. Dunham, P. Szkody, D. R. Silva, K. Mighell, J. Holberg, J. Ballot, T. R. Bedding, H. Bruntt, T. L. Campante, R. Handberg, S. Hekker, D. Huber, S. Mathur, B. Mosser, C. Régulo, T. R. White, J. L. Christiansen, C. K. Middour, M. R. Haas, J. R. Hall, J. M. Jenkins, S. McCaulif, M. N. Fanelli, C. Kulesa, D. McCarthy, and C. E. Henze. Kepler-21b: A 1.6 R_{Earth} Planet Transiting the Bright Oscillating F Subgiant Star HD 179070. *The Astrophysical Journal*, 746(2):123, Feb. 2012.

[187] S. B. Howell, C. Sobeck, M. Haas, M. Still, T. Barclay, F. Mullally, J. Troeltzsch, S. Aigrain, S. T. Bryson, D. Caldwell, W. J. Chaplin, W. D. Cochran, D. Huber, G. W. Marcy, A. Miglio, J. R. Najita, M. Smith, J. D. Twicken, and J. J. Fortney. The K2 Mission: Characterization and Early Results. *Publications of the ASP*, 126(938):398, Apr. 2014.

[188] D. C. Hsu, E. B. Ford, and R. Terrien. Occurrence rates of planets orbiting M Stars: applying ABC to Kepler DR25, Gaia DR2, and 2MASS data. *Monthly Notices of the Royal Astronomical Society*, 498(2):2249–2262, Oct. 2020.

[189] D. Huber, J. Zinn, M. Bojsen-Hansen, M. Pinsonneault, C. Sahlholdt, A. Serenelli, V. Silva Aguirre, K. Stassun, D. Stello, J. Tayar, F. Bastien, T. R. Bedding, L. A. Buchhave, W. J. Chaplin, G. R. Davies, R. A. García, D. W. Latham, S. Mathur, B. Mosser, and S. Sharma. Asteroseismology and Gaia: Testing Scaling Relations Using 2200 Kepler Stars with TGAS Parallaxes. *The Astrophysical Journal*, 844(2):102, Aug. 2017.

[190] J. Huehnerhoff, W. Ketzeback, A. Bradley, J. Dembicky, C. Doughty, S. Hawley, C. Johnson, M. Klaene, E. Leon, R. McMillan, R. Owen, C. Sayres, T. Sheen, and A. Shugart. Astrophysical Research Consortium Telescope Imaging Camera (ARCTIC) facility optical imager for the Apache Point Observatory 3.5m telescope. 9908:99085H, Aug. 2016. Conference Name: Ground-based and Airborne Instrumentation for Astronomy VI.

[191] C. M. Hurvich and C.-L. Tsai. A corrected akaike information criterion for vector autoregressive model selection. *Journal of Time Series Analysis*, 14(3):271–279, 1993.

[192] J. Ih, E. M. R. Kempton, E. A. Whittaker, and M. Lessard. Constraining the Thickness of the Atmosphere of TRAPPIST-1 b from its JWST Secondary Eclipse Observation. *arXiv e-prints*, page arXiv:2305.10414, May 2023.

[193] A. Izidoro, B. Bitsch, S. N. Raymond, A. Johansen, A. Morbidelli, M. Lambrechts, and S. A. Jacobson. Formation of planetary systems by pebble accretion and migration. Hot super-Earth systems from breaking compact resonant chains. *Astronomy and Astrophysics*, 650:A152, June 2021.

[194] A. Izidoro, M. Ogihara, S. N. Raymond, A. Morbidelli, A. Pierens, B. Bitsch, C. Cossou, and F. Hersant. Breaking the chains: hot super-Earth systems from migration and disruption of compact resonant chains. *Monthly Notices of the Royal Astronomical Society*, 470(2):1750–1770, Sept. 2017.

[195] J. M. Jenkins. The Impact of Solar-like Variability on the Detectability of Transiting Terrestrial Planets. *The Astrophysical Journal*, 575(1):493–505, Aug. 2002.

[196] J. M. Jenkins, D. A. Caldwell, and W. J. Borucki. Some Tests to Establish Confidence in Planets Discovered by Transit Photometry. *The Astrophysical Journal*, 564(1):495–507, Jan. 2002.

[197] J. M. Jenkins, D. A. Caldwell, H. Chandrasekaran, J. D. Twicken, S. T. Bryson, E. V. Quintana, B. D. Clarke, J. Li, C. Allen, P. Tenenbaum, H. Wu, T. C. Klaus, C. K. Middour, M. T. Cote, S. McCauliff, F. R. Girouard, J. P. Gunter, B. Wohler, J. Sommers, J. R. Hall, A. K. Uddin, M. S. Wu, P. A. Bhavsar, J. Van Cleve, D. L. Pletcher, J. A. Dotson, M. R. Haas, R. L. Gilliland, D. G. Koch, and W. J. Borucki. Overview of the Kepler Science Processing Pipeline. *The Astrophysical Journall*, 713(2):L87–L91, Apr. 2010.

[198] J. M. Jenkins, J. D. Twicken, S. McCauliff, J. Campbell, D. Sanderfer, D. Lung, M. Mansouri-Samani, F. Girouard, P. Tenenbaum, T. Klaus, J. C. Smith, D. A.

Caldwell, A. D. Chacon, C. Henze, C. Heiges, D. W. Latham, E. Morgan, D. Swade, S. Rinehart, and R. Vanderspek. The TESS science processing operations center. In G. Chiozzi and J. C. Guzman, editors, *Software and Cyberinfrastructure for Astronomy IV*, volume 9913 of *Society of Photo-Optical Instrumentation Engineers (SPIE) Conference Series*, page 99133E, Aug. 2016.

[199] J. A. Johnson and K. Apps. On the Metal Richness of M Dwarfs with Planets. *The Astrophysical Journal*, 699(2):933–937, July 2009.

[200] S. E. Jones, G. Stefansson, K. Masuda, J. E. Libby-Roberts, C. N. Gardner, R. Holcomb, C. Beard, P. Robertson, C. I. Cañas, S. Mahadevan, S. Kanodia, A. S. J. Lin, H. A. Kobulnicky, B. A. Parker, C. F. Bender, W. D. Cochran, S. A. Diddams, R. B. Fernandes, A. F. Gupta, S. Halverson, S. L. Hawley, F. R. Hearty, L. Hebb, A. Kowalski, J. Lubin, A. Monson, J. P. Ninan, L. Ramsey, A. Roy, C. Schwab, R. C. Terrien, and J. Wisniewski. TOI-2015b: A Warm Neptune with Transit Timing Variations Orbiting an Active mid M Dwarf. *arXiv e-prints*, page arXiv:2310.11775, Oct. 2023.

[201] S. Jordan, P. B. Rimmer, O. Shorttle, and T. Constantinou. Photochemistry of Venus-like Planets Orbiting K- and M-dwarf Stars. *The Astrophysical Journal*, 922(1):44, Nov. 2021.

[202] S. R. Kane, R. K. Kopparapu, and S. D. Domagal-Goldman. On the Frequency of Potential Venus Analogs from Kepler Data. *The Astrophysical Journal Letters*, 794(1):L5, Oct. 2014.

[203] S. Kanodia, S. Mahadevan, L. W. Ramsey, G. K. Stefansson, A. J. Monson, F. R. Hearty, S. Blakeslee, E. Lubar, C. F. Bender, J. P. Ninan, D. Sterner, A. Roy, S. P. Halverson, and P. M. Robertson. Overview of the spectrometer optical fiber feed for the habitable-zone planet finder. In C. J. Evans, L. Simard, and H. Takami, editors, *Ground-based and Airborne Instrumentation for Astronomy VII*, volume 10702 of *Society of Photo-Optical Instrumentation Engineers (SPIE) Conference Series*, page 107026Q, Aug. 2018.

[204] S. Kanodia, G. Stefansson, C. I. Cañas, M. Maney, A. S. J. Lin, J. P. Ninan, S. Jones, A. Monson, B. A. Parker, H. A. Kobulnicky, J. Rothenberg, C. Beard, J. Lubin, P. Robertson, A. F. Gupta, S. Mahadevan, W. D. Cochran, C. F. Bender, S. A. Diddams, C. Fredrick, S. Halverson, S. Hawley, F. Hearty, L. Hebb, R. Kopparapu, A. J. Metcalf, L. W. Ramsey, A. Roy, C. Schwab, M. Schutte, R. C. Terrien, J. Wisniewski, and J. T. Wright. TOI-532b: The Habitable-zone Planet Finder confirms a Large Super Neptune in the Neptune Desert orbiting a metal-rich M-dwarf host. *Astronomical Journal*, 162(4):135, Oct. 2021.

[205] S. Kanodia, A. Wolfgang, G. K. Stefansson, B. Ning, and S. Mahadevan. Mass-Radius Relationship for M Dwarf Exoplanets: Comparing Nonparametric and Parametric Methods. *The Astrophysical Journal*, 882(1):38, Sept. 2019.

[206] S. Kanodia and J. Wright. Python Leap Second Management and Implementation of Precise Barycentric Correction (barycorrpy). *Research Notes of the American Astronomical Society*, 2(1):4, Jan. 2018.

[207] D. H. Kasper, T. G. Ellis, R. R. Yeigh, H. A. Kobulnicky, H. Jang-Condell, M. Kelley, G. J. Bucher, and J. S. Weger. Remote Operations and Nightly Automation of the Red Buttes Observatory. *Publications of the Astronomical Society of the Pacific*, 128:105005, Oct. 2016.

[208] R. E. Kass and A. E. Raftery. Bayes factors. *Journal of the American Statistical Association*, 90(430):773–795, 1995.

[209] R. E. Kass and A. E. Raftery. Bayes factors. *Journal of the American Statistical Association*, 90(430):773–795, 1995.

[210] J. F. Kasting, D. P. Whitmire, and R. T. Reynolds. Habitable Zones around Main Sequence Stars. *Icarus*, 101(1):108–128, Jan. 1993.

[211] Y. Kawashima, R. Hu, and M. Ikoma. Detectable Molecular Features above Hydrocarbon Haze via Transmission Spectroscopy with JWST: Case Studies of GJ 1214b-, GJ 436b-, HD 97658b-, and Kepler-51b-like Planets. *The Astrophysical Journal Letters*, 876(1):L5, May 2019.

[212] K. Kawauchi, F. Murgas, E. Palle, N. Narita, A. Fukui, T. Hirano, H. Parviainen, H. T. Ishikawa, N. Watanabe, E. Esparaza-Borges, M. Kuzuhara, J. Orell-Miquel, V. Krishnamurthy, M. Mori, T. Kagetani, Y. Zou, K. Isogai, J. H. Livingston, S. B. Howell, N. Crouzet, J. P. de Leon, T. Kimura, T. Kodama, J. Korth, S. Kurita, A. Laza-Ramos, R. Luque, A. Madrigal-Aguado, K. Miyakawa, G. Morello, T. Nishiumi, G. E. F. Rodríguez, M. Sánchez-Benavente, M. Stangret, H. Teng, Y. Terada, C. L. Gnilka, N. Guerrero, H. Harakawa, K. Hodapp, Y. Hori, M. Ikoma, S. Jacobson, M. Konishi, T. Kotani, T. Kudo, T. Kurokowa, N. Kusakabe, J. Nishikawa, M. Omiya, T. Serizawa, M. Tamura, A. Ueda, and S. Vievard. Validation and atmospheric exploration of the sub-Neptune TOI-2136b around a nearby M3 dwarf. *arXiv e-prints*, page arXiv:2202.10182, Feb. 2022.

[213] J. Kemmer, S. Dreizler, D. Kossakowski, S. Stock, A. Quirrenbach, J. A. Caballero, P. J. Amado, K. A. Collins, N. Espinoza, E. Herrero, J. M. Jenkins, D. W. Latham, J. Lillo-Box, N. Narita, E. Pallé, A. Reiners, I. Ribas, G. Ricker, E. Rodríguez, S. Seager, R. Vanderspek, R. Wells, J. Winn, F. J. Aceituno, V. J. S. Béjar, T. Barclay, P. Bluhm, P. Chaturvedi, C. Cifuentes, K. I. Collins, M. Cortés-Contreras, B. O. Demory, M. M. Fausnaugh, A. Fukui, Y. Gómez Maqueo Chew, D. Galadí-Enríquez, T. Gan, M. Gillon, A. Golovin, A. P. Hatzes, T. Henning, C. Huang, S. V. Jeffers, A. Kaminski, M. Kunimoto, M. Kürster, M. J. López-González, M. Lafarga, R. Luque, J. McCormac, K. Molaverdikhani, D. Montes, J. C. Morales, V. M. Passegger, S. Reffert, L. Sabin, P. Schöfer, N. Schanche, M. Schlecker, U. Schroffenegger, R. P. Schwarz, A. Schweitzer, A. Sota, P. Tenenbaum, T. Trifonov, S. Vanaverbeke, and M. Zechmeister. Discovery and mass measurement of the hot, transiting, Earth-sized planet, GJ 3929 b. *Astronomy and Astrophysics*, 659:A17, Mar. 2022.

[214] E. M. R. Kempton, J. L. Bean, D. R. Louie, D. Deming, D. D. B. Koll, M. Mansfield, J. L. Christiansen, M. López-Morales, M. R. Swain, R. T. Zellem, S. Ballard, T. Barclay, J. K. Barstow, N. E. Batalha, T. G. Beatty, Z. Berta-Thompson, J. Birkby, L. A. Buchhave, D. Charbonneau, N. B. Cowan, I. Crossfield, M. de Val-Borro, R. Doyon, D. Dragomir, E. Gaidos, K. Heng, R. Hu, S. R. Kane, L. Kreidberg, M. Mallonn, C. V. Morley, N. Narita, V. Nascimbeni, E. Pallé, E. V. Quintana, E. Rauscher, S. Seager, E. L. Shkolnik, D. K. Sing, A. Sozzetti, K. G. Stassun, J. A. Valenti, and C. von Essen. A Framework for Prioritizing the TESS Planetary Candidates Most Amenable to Atmospheric Characterization. *Publications of the Astronomical Society of the Pacific*, 130(993):114401, Nov. 2018.

[215] E. M. R. Kempton, R. Lupu, A. Owusu-Asare, P. Slough, and B. Cale. Exo-Transmit: An Open-Source Code for Calculating Transmission Spectra for Exoplanet Atmospheres of Varied Composition. *Publications of the Astronomical Society of the Pacific*, 129(974):044402, Apr. 2017.

[216] D. M. Kipping. Efficient, uninformative sampling of limb darkening coefficients for two-parameter laws. *Monthly Notices of the Royal Astronomical Society*, 435:2152–2160, Nov. 2013.

[217] C. S. Kochanek, B. J. Shappee, K. Z. Stanek, T. W. S. Holoien, T. A. Thompson, J. L. Prieto, S. Dong, J. V. Shields, D. Will, C. Britt, D. Perzanowski, and G. Pojmański. The All-Sky Automated Survey for Supernovae (ASAS-SN) Light Curve Server v1.0. *Publications of the Astronomical Society of the Pacific*, 129(980):104502, Oct. 2017.

[218] Q. M. Konopacky, T. S. Barman, B. A. Macintosh, and C. Marois. Detection of Carbon Monoxide and Water Absorption Lines in an Exoplanet Atmosphere. *Science*, 339(6126):1398–1401, Mar. 2013.

[219] Q. M. Konopacky, A. M. Ghez, T. S. Barman, E. L. Rice, I. Bailey, J. I., R. J. White, I. S. McLean, and G. Duchêne. High-precision Dynamical Masses of Very Low Mass Binaries. *The Astrophysical Journal*, 711(2):1087–1122, Mar. 2010.

[220] R. K. Kopparapu, R. Ramirez, J. F. Kasting, V. Eymet, T. D. Robinson, S. Mahadevan, R. C. Terrien, S. Domagal-Goldman, V. Meadows, and R. Deshpande. Habitable Zones around Main-sequence Stars: New Estimates. *The Astrophysical Journal*, 765(2):131, Mar. 2013.

[221] R. K. Kopparapu, R. M. Ramirez, J. SchottelKotte, J. F. Kasting, S. Domagal-Goldman, and V. Eymet. Habitable Zones around Main-sequence Stars: Dependence on Planetary Mass. *The Astrophysical Journal Letters*, 787(2):L29, June 2014.

[222] D. Kossakowski, J. Kemmer, P. Bluhm, S. Stock, J. A. Caballero, V. J. S. Béjar, C. C. Guillén, N. Lodieu, K. A. Collins, M. Oshagh, M. Schlecker, N. Espinoza, E. Pallé, T. Henning, L. Kreidberg, M. Kürster, P. J. Amado, D. R. Anderson, J. C. Morales, S. Cartwright, D. Charbonneau, P. Chaturvedi, C. Cifuentes, D. M. Conti, M. Cortés-Contreras, S. Dreizler, D. Galadí-Enríquez, P. Guerra, R. Hart, C. Hellier,

C. Henze, E. Herrero, S. V. Jeffers, J. M. Jenkins, E. L. N. Jensen, A. Kaminski, J. F. Kielkopf, M. Kunimoto, M. Lafarga, D. W. Latham, J. Lillo-Box, R. Luque, K. Molaverdikhani, D. Montes, G. Morello, E. H. Morgan, G. Nowak, A. Pavlov, M. Perger, E. V. Quintana, A. Quirrenbach, S. Reffert, A. Reiners, G. Ricker, I. Ribas, C. R. López, M. R. Z. Osorio, S. Seager, P. Schöfer, A. Schweitzer, T. Trifonov, S. Vanaverbeke, R. Vanderspek, R. West, J. Winn, and M. Zechmeister. TOI-1201 b: A mini-Neptune transiting a bright and moderately young M dwarf. *Astronomy and Astrophysics*, 656:A124, Dec. 2021.

[223] G. Kovács, S. Zucker, and T. Mazeh. A box-fitting algorithm in the search for periodic transits. *Astronomy and Astrophysics*, 391:369–377, Aug. 2002.

[224] R. P. Kraft. The Binary System Nova T Coronae Borealis. *The Astrophysical Journal*, 127:625, May 1958.

[225] L. Kreidberg, J. L. Bean, J.-M. Désert, B. Benneke, D. Deming, K. B. Stevenson, S. Seager, Z. Berta-Thompson, A. Seifahrt, and D. Homeier. Clouds in the atmosphere of the super-Earth exoplanet GJ1214b. *Nature*, 505(7481):69–72, Jan. 2014.

[226] L. Kreidberg, P. Mollière, I. J. M. Crossfield, D. P. Thorngren, Y. Kawashima, C. V. Morley, B. Benneke, T. Mikal-Evans, D. Berardo, M. R. Kosiarek, V. Gorjian, D. R. Ciardi, J. L. Christiansen, D. Dragomir, C. D. Dressing, J. J. Fortney, B. J. Fulton, T. P. Greene, K. K. Hardegree-Ullman, A. W. Howard, S. B. Howell, H. Isaacson, J. E. Krick, J. H. Livingston, J. D. Lothringer, F. Y. Morales, E. A. Petigura, J. E. Rodriguez, J. E. Schlieder, and L. M. Weiss. Tentative Evidence for Water Vapor in the Atmosphere of the Neptune-sized Exoplanet HD 106315c. *The Astronomical Journal*, 164(4):124, Oct. 2022.

[227] J. Krissansen-Totton. Implications of atmospheric non-detections for Trappist-1 inner planets on atmospheric retention prospects for outer planets. *arXiv e-prints*, page arXiv:2306.05397, June 2023.

[228] M. Lafarga, I. Ribas, C. Lovis, M. Perger, M. Zechmeister, F. F. Bauer, M. Kürster, M. Cortés-Contreras, J. C. Morales, E. Herrero, A. Rosich, D. Baroch, A. Reiners, J. A. Caballero, A. Quirrenbach, P. J. Amado, J. M. Alacid, V. J. S. Béjar, S. Dreizler, A. P. Hatzes, T. Henning, S. V. Jeffers, A. Kaminski, D. Montes, S. Pedraz, C. Rodríguez-López, and J. H. M. M. Schmitt. The CARMENES search for exoplanets around M dwarfs. Radial velocities and activity indicators from cross-correlation functions with weighted binary masks. *Astronomy and Astrophysics*, 636:A36, Apr. 2020.

[229] A. M. Lagrange, M. Desort, F. Galland, S. Udry, and M. Mayor. Extrasolar planets and brown dwarfs around A-F type stars. VI. High precision RV survey of early type dwarfs with HARPS. *Astronomy and Astrophysics*, 495(1):335–352, Feb. 2009.

[230] K. W. F. Lam, S. Csizmadia, N. Astudillo-Defru, X. Bonfils, D. Gandolfi, S. Padovan, M. Esposito, C. Hellier, T. Hirano, J. Livingston, F. Murgas, A. M. S. Smith, K. A. Collins, S. Mathur, R. A. Garcia, S. B. Howell, N. C. Santos, F. Dai, G. R. Ricker,

R. Vanderspek, D. W. Latham, S. Seager, J. N. Winn, J. M. Jenkins, S. Albrecht, J. M. Almenara, E. Artigau, O. Barragán, F. Bouchy, J. Cabrera, D. Charbonneau, P. Chaturvedi, A. Chaushev, J. L. Christiansen, W. D. Cochran, J. R. De Meideiros, X. Delfosse, R. F. Díaz, R. Doyon, P. Eigmüller, P. Figueira, T. Forveille, M. Fridlund, G. Gaisné, E. Goffo, I. Georgieva, S. Grziwa, E. Guenther, A. P. Hatzes, M. C. Johnson, P. Kabáth, E. Knudstrup, J. Korth, P. Lewin, J. J. Lissauer, C. Lovis, R. Luque, C. Melo, E. H. Morgan, R. Morris, M. Mayor, N. Narita, H. L. M. Osborne, E. Palle, F. Pepe, C. M. Persson, S. N. Quinn, H. Rauer, S. Redfield, J. E. Schlieder, D. Ségransan, L. M. Serrano, J. C. Smith, J. Šubjak, J. D. Twicken, S. Udry, V. Van Eylen, and M. Vezie. GJ 367b: A dense, ultrashort-period sub-Earth planet transiting a nearby red dwarf star. *Science*, 374(6572):1271–1275, Dec. 2021.

[231] M. Lambrechts and A. Johansen. Rapid growth of gas-giant cores by pebble accretion. *Astronomy and Astrophysics*, 544:A32, Aug. 2012.

[232] H. Lammer, F. Selsis, I. Ribas, E. F. Guinan, S. J. Bauer, and W. W. Weiss. Atmospheric Loss of Exoplanets Resulting from Stellar X-Ray and Extreme-Ultraviolet Heating. *The Astrophysical Journal Letters*, 598(2):L121–L124, Dec. 2003.

[233] S. K. Leggett, M. C. Liu, T. J. Dupuy, C. V. Morley, M. S. Marley, and D. Saumon. Resolved Spectroscopy of the T8.5 and Y0-0.5 Binary WISEPC J121756.91+162640.2AB. *The Astrophysical Journal*, 780(1):62, Jan. 2014.

[234] Z. Li, S. R. Hildebrandt, S. R. Kane, N. T. Zimmerman, J. H. Girard, J. Gonzalez-Quiles, and M. C. Turnbull. Direct Imaging of Exoplanets beyond the Radial Velocity Limit: Application to the HD 134987 System. *The Astronomical Journal*, 162(1):9, July 2021.

[235] A. R. Liddle. Information criteria for astrophysical model selection. *Monthly Notices of the Royal Astronomical Society*, 377(1):L74–L78, May 2007.

[236] Lightkurve Collaboration, J. V. d. M. Cardoso, C. Hedges, M. Gully-Santiago, N. Saunders, A. M. Cody, T. Barclay, O. Hall, S. Sagear, E. Turtelboom, J. Zhang, A. Tzanidakis, K. Mighell, J. Coughlin, K. Bell, Z. Berta-Thompson, P. Williams, J. Dotson, and G. Barentsen. Lightkurve: Kepler and TESS time series analysis in Python. Astrophysics Source Code Library, Dec. 2018.

[237] Lightkurve Collaboration, J. V. d. M. Cardoso, C. Hedges, M. Gully-Santiago, N. Saunders, A. M. Cody, T. Barclay, O. Hall, S. Sagear, E. Turtelboom, J. Zhang, A. Tzanidakis, K. Mighell, J. Coughlin, K. Bell, Z. Berta-Thompson, P. Williams, J. Dotson, and G. Barentsen. Lightkurve: Kepler and TESS time series analysis in Python. Astrophysics Source Code Library, Dec. 2018.

[238] A. P. Lincowski, V. S. Meadows, S. Zieba, L. Kreidberg, C. Morley, M. Gillon, F. Selsis, E. Agol, E. Bolmont, E. Ducrot, R. Hu, D. D. B. Koll, X. Lyu, A. Mandell, G. Suissa, and P. Tamburo. Potential Atmospheric Compositions of TRAPPIST-1 c Constrained by JWST/MIRI Observations at 15 μm. *The Astrophysical Journal Letters*, 955(1):L7, Sept. 2023.

[239] L. Lindegren and D. Dravins. Astrometric radial velocities for nearby stars. *Astronomy and Astrophysics*, 652:A45, Aug. 2021.

[240] L. Lindegren, J. Hernández, A. Bombrun, S. Klioner, U. Bastian, M. Ramos-Lerate, A. de Torres, H. Steidelmüller, C. Stephenson, D. Hobbs, U. Lammers, M. Biermann, R. Geyer, T. Hilger, D. Michalik, U. Stampa, P. J. McMillan, J. Castañeda, M. Clotet, G. Comoretto, M. Davidson, C. Fabricius, G. Gracia, N. C. Hambly, A. Hutton, A. Mora, J. Portell, F. van Leeuwen, U. Abbas, A. Abreu, M. Altmann, A. Andrei, E. Anglada, L. Balaguer-Núñez, C. Barache, U. Becciani, S. Bertone, L. Bianchi, S. Bouquillon, G. Bourda, T. Brüsemeister, B. Bucciarelli, D. Busonero, R. Buzzi, R. Cancelliere, T. Carlucci, P. Charlot, N. Cheek, M. Crosta, C. Crowley, J. de Bruijne, F. de Felice, R. Drimmel, P. Esquej, A. Fienga, E. Fraile, M. Gai, N. Garralda, J. J. González-Vidal, R. Guerra, M. Hauser, W. Hofmann, B. Holl, S. Jordan, M. G. Lattanzi, H. Lenhardt, S. Liao, E. Licata, T. Lister, W. Löffler, J. Marchant, J. M. Martin-Fleitas, R. Messineo, F. Mignard, R. Morbidelli, E. Poggio, A. Riva, N. Rowell, E. Salguero, M. Sarasso, E. Sciacca, H. Siddiqui, R. L. Smart, A. Spagna, I. Steele, F. Taris, J. Torra, A. van Elteren, W. van Reeven, and A. Vecchiato. Gaia Data Release 2. The astrometric solution. *Astronomy and Astrophysics*, 616:A2, Aug. 2018.

[241] J. J. Lissauer, D. Jontof-Hutter, J. F. Rowe, D. C. Fabrycky, E. D. Lopez, E. Agol, G. W. Marcy, K. M. Deck, D. A. Fischer, J. J. Fortney, S. B. Howell, H. Isaacson, J. M. Jenkins, R. Kolbl, D. Sasselov, D. R. Short, and W. F. Welsh. All Six Planets Known to Orbit Kepler-11 Have Low Densities. *The Astrophysical Journal*, 770(2):131, June 2013.

[242] J. J. Lissauer, G. W. Marcy, J. F. Rowe, S. T. Bryson, E. Adams, L. A. Buchhave, D. R. Ciardi, W. D. Cochran, D. C. Fabrycky, E. B. Ford, F. Fressin, J. Geary, R. L. Gilliland, M. J. Holman, S. B. Howell, J. M. Jenkins, K. Kinemuchi, D. G. Koch, R. C. Morehead, D. Ragozzine, S. E. Seader, P. G. Tanenbaum, G. Torres, and J. D. Twicken. Almost All of Kepler's Multiple-planet Candidates Are Planets. *The Astrophysical Journal*, 750(2):112, May 2012.

[243] J. J. Lissauer, D. Ragozzine, D. C. Fabrycky, J. H. Steffen, E. B. Ford, J. M. Jenkins, A. Shporer, M. J. Holman, J. F. Rowe, E. V. Quintana, N. M. Batalha, W. J. Borucki, S. T. Bryson, D. A. Caldwell, J. A. Carter, D. Ciardi, E. W. Dunham, J. J. Fortney, I. Gautier, Thomas N., S. B. Howell, D. G. Koch, D. W. Latham, G. W. Marcy, R. C. Morehead, and D. Sasselov. Architecture and Dynamics of Kepler's Candidate Multiple Transiting Planet Systems. *The Astrophysical Journal Supplement*, 197(1):8, Nov. 2011.

[244] Y. Lithwick, J. Xie, and Y. Wu. Extracting Planet Mass and Eccentricity from TTV Data. *The Astrophysical Journal*, 761(2):122, Dec. 2012.

[245] J. H. Livingston, M. Endl, F. Dai, W. D. Cochran, O. Barragan, D. Gandolfi, T. Hirano, S. Grziwa, A. M. S. Smith, S. Albrecht, J. Cabrera, S. Csizmadia, J. P. de Leon, H. Deeg, P. Eigmüller, A. Erikson, M. Everett, M. Fridlund, A. Fukui, E. W. Guenther, A. P. Hatzes, S. Howell, J. Korth, N. Narita, D. Nespral, G. Nowak, E. Palle,

M. Pätzold, C. M. Persson, J. Prieto-Arranz, H. Rauer, M. Tamura, V. Van Eylen, and J. N. Winn. 44 Validated Planets from K2 Campaign 10. *Astronomical Journal*, 156(2):78, Aug. 2018.

[246] N. R. Lomb. Least-Squares Frequency Analysis of Unequally Spaced Data. *Astrophysics and Space Science*, 39(2):447–462, Feb. 1976.

[247] E. D. Lopez and J. J. Fortney. Understanding the Mass-Radius Relation for Sub-neptunes: Radius as a Proxy for Composition. *The Astrophysical Journal*, 792(1):1, Sept. 2014.

[248] M. López-Morales, R. D. Haywood, J. L. Coughlin, L. Zeng, L. A. Buchhave, H. A. C. Giles, L. Affer, A. S. Bonomo, D. Charbonneau, A. Collier Cameron, R. Consentino, C. D. Dressing, X. Dumusque, P. Figueira, A. F. M. Fiorenzano, A. Harutyunyan, J. A. Johnson, D. W. Latham, E. D. Lopez, C. Lovis, L. Malavolta, M. Mayor, G. Micela, E. Molinari, A. Mortier, F. Motalebi, V. Nascimbeni, F. Pepe, D. F. Phillips, G. Piotto, D. Pollacco, D. Queloz, K. Rice, D. Sasselov, D. Segransan, A. Sozzetti, S. Udry, A. Vanderburg, and C. Watson. Kepler-21b: A Rocky Planet Around a V = 8.25 Magnitude Star. *Astronomical Journal*, 152(6):204, Dec. 2016.

[249] M. López-Morales, R. D. Haywood, J. L. Coughlin, L. Zeng, L. A. Buchhave, H. A. C. Giles, L. Affer, A. S. Bonomo, D. Charbonneau, A. Collier Cameron, R. Consentino, C. D. Dressing, X. Dumusque, P. Figueira, A. F. M. Fiorenzano, A. Harutyunyan, J. A. Johnson, D. W. Latham, E. D. Lopez, C. Lovis, L. Malavolta, M. Mayor, G. Micela, E. Molinari, A. Mortier, F. Motalebi, V. Nascimbeni, F. Pepe, D. F. Phillips, G. Piotto, D. Pollacco, D. Queloz, K. Rice, D. Sasselov, D. Segransan, A. Sozzetti, S. Udry, A. Vanderburg, and C. Watson. Kepler-21b: A Rocky Planet Around a V = 8.25 Magnitude Star. *The Astronomical Journal*, 152(6):204, Dec. 2016.

[250] C. X. Lu, K. C. Schlaufman, and S. Cheng. An Increase in Small-planet Occurrence with Metallicity for Late-type Dwarf Stars in the Kepler Field and Its Implications for Planet Formation. *Astronomical Journal*, 160(6):253, Dec. 2020.

[251] J. Lubin, P. Robertson, G. Stefansson, J. Ninan, S. Mahadevan, M. Endl, E. Ford, J. T. Wright, C. Beard, C. Bender, W. D. Cochran, S. A. Diddams, C. Fredrick, S. Halverson, S. Kanodia, A. J. Metcalf, L. Ramsey, A. Roy, C. Schwab, and R. Terrien. Stellar Activity Manifesting at a One-year Alias Explains Barnard b as a False Positive. *Astronomical Journal*, 162(2):61, Aug. 2021.

[252] J. Lubin, J. Van Zandt, R. Holcomb, L. M. Weiss, E. A. Petigura, P. Robertson, J. M. Akana Murphy, N. Scarsdale, K. Batygin, A. S. Polanski, N. M. Batalha, I. J. M. Crossfield, C. Dressing, B. Fulton, A. W. Howard, D. Huber, H. Isaacson, S. R. Kane, A. Roy, C. Beard, S. Blunt, A. Chontos, F. Dai, P. A. Dalba, K. Gary, S. Giacalone, M. L. Hill, A. Mayo, T. Močnik, M. R. Kosiarek, M. Rice, R. A. Rubenzahl, D. W. Latham, S. Seager, J. N. Winn, and K. Gary. TESS-Keck Survey. IX. Masses of Three Sub-Neptunes Orbiting HD 191939 and the Discovery of a Warm Jovian plus a Distant Substellar Companion. *Astronomical Journal*, 163(2):101, Feb. 2022.

[253] J. Lubin, J. Van Zandt, R. Holcomb, L. M. Weiss, E. A. Petigura, P. Robertson, J. M. Akana Murphy, N. Scarsdale, K. Batygin, A. S. Polanski, N. M. Batalha, I. J. M. Crossfield, C. Dressing, B. Fulton, A. W. Howard, D. Huber, H. Isaacson, S. R. Kane, A. Roy, C. Beard, S. Blunt, A. Chontos, F. Dai, P. A. Dalba, K. Gary, S. Giacalone, M. L. Hill, A. Mayo, T. Močnik, M. R. Kosiarek, M. Rice, R. A. Rubenzahl, D. W. Latham, S. Seager, J. N. Winn, and K. Gary. TESS-Keck Survey. IX. Masses of Three Sub-Neptunes Orbiting HD 191939 and the Discovery of a Warm Jovian plus a Distant Substellar Companion. *Astronomical Journal*, 163(2):101, Feb. 2022.

[254] R. Luger, E. Agol, D. Foreman-Mackey, D. P. Fleming, J. Lustig-Yaeger, and R. Deitrick. starry: Analytic Occultation Light Curves. *Astronomical Journal*, 157:64, Feb. 2019.

[255] R. Luger, E. Agol, E. Kruse, R. Barnes, A. Becker, D. Foreman-Mackey, and D. Deming. EVEREST: Pixel Level Decorrelation of K2 Light Curves. *The Astronomical Journal*, 152(4):100, Oct. 2016.

[256] R. Luger, M. Sestovic, E. Kruse, S. L. Grimm, B.-O. Demory, E. Agol, E. Bolmont, D. Fabrycky, C. S. Fernandes, V. Van Grootel, A. Burgasser, M. Gillon, J. G. Ingalls, E. Jehin, S. N. Raymond, F. Selsis, A. H. M. J. Triaud, T. Barclay, G. Barentsen, S. B. Howell, L. Delrez, J. de Wit, D. Foreman-Mackey, D. L. Holdsworth, J. Leconte, S. Lederer, M. Turbet, Y. Almleaky, Z. Benkhaldoun, P. Magain, B. M. Morris, K. Heng, and D. Queloz. A seven-planet resonant chain in TRAPPIST-1. *Nature Astronomy*, 1:0129, June 2017.

[257] R. Luque and E. Pallé. Density, not radius, separates rocky and water-rich small planets orbiting M dwarf stars. *Science*, 377(6611):1211–1214, Sept. 2022.

[258] R. Luque, E. Pallé, D. Kossakowski, S. Dreizler, J. Kemmer, N. Espinoza, J. Burt, G. Anglada-Escudé, V. J. S. Béjar, J. A. Caballero, K. A. Collins, K. I. Collins, M. Cortés-Contreras, E. Díez-Alonso, F. Feng, A. Hatzes, C. Hellier, T. Henning, S. V. Jeffers, L. Kaltenegger, M. Kürster, J. Madden, K. Molaverdikhani, D. Montes, N. Narita, G. Nowak, A. Ofir, M. Oshagh, H. Parviainen, A. Quirrenbach, S. Reffert, A. Reiners, C. Rodríguez-López, M. Schlecker, S. Stock, T. Trifonov, J. N. Winn, M. R. Zapatero Osorio, M. Zechmeister, P. J. Amado, D. R. Anderson, N. E. Batalha, F. F. Bauer, P. Bluhm, C. J. Burke, R. P. Butler, D. A. Caldwell, G. Chen, J. D. Crane, D. Dragomir, C. D. Dressing, S. Dynes, J. M. Jenkins, A. Kaminski, H. Klahr, T. Kotani, M. Lafarga, D. W. Latham, P. Lewin, S. McDermott, P. Montañés-Rodríguez, J. C. Morales, F. Murgas, E. Nagel, S. Pedraz, I. Ribas, G. R. Ricker, P. Rowden, S. Seager, S. A. Shectman, M. Tamura, J. Teske, J. D. Twicken, R. Vanderspeck, S. X. Wang, and B. Wohler. Planetary system around the nearby M dwarf GJ 357 including a transiting, hot, Earth-sized planet optimal for atmospheric characterization. *Astronomy and Astrophysics*, 628:A39, Aug. 2019.

[259] X. Luri, A. G. A. Brown, L. M. Sarro, F. Arenou, C. A. L. Bailer-Jones, A. Castro-Ginard, J. de Bruijne, T. Prusti, C. Babusiaux, and H. E. Delgado. Gaia Data Release 2. Using Gaia parallaxes. *Astronomy and Astrophysics*, 616:A9, Aug. 2018.

[260] B. Macintosh, J. R. Graham, T. Barman, R. J. De Rosa, Q. Konopacky, M. S. Marley, C. Marois, E. L. Nielsen, L. Pueyo, A. Rajan, J. Rameau, D. Saumon, J. J. Wang, J. Patience, M. Ammons, P. Arriaga, E. Artigau, S. Beckwith, J. Brewster, S. Bruzzone, J. Bulger, B. Burningham, A. S. Burrows, C. Chen, E. Chiang, J. K. Chilcote, R. I. Dawson, R. Dong, R. Doyon, Z. H. Draper, G. Duchêne, T. M. Esposito, D. Fabrycky, M. P. Fitzgerald, K. B. Follette, J. J. Fortney, B. Gerard, S. Goodsell, A. Z. Greenbaum, P. Hibon, S. Hinkley, T. H. Cotten, L. W. Hung, P. Ingraham, M. Johnson-Groh, P. Kalas, D. Lafreniere, J. E. Larkin, J. Lee, M. Line, D. Long, J. Maire, F. Marchis, B. C. Matthews, C. E. Max, S. Metchev, M. A. Millar-Blanchaer, T. Mittal, C. V. Morley, K. M. Morzinski, R. Murray-Clay, R. Oppenheimer, D. W. Palmer, R. Patel, M. D. Perrin, L. A. Poyneer, R. R. Rafikov, F. T. Rantakyrö, E. L. Rice, P. Rojo, A. R. Rudy, J. B. Ruffio, M. T. Ruiz, N. Sadakuni, L. Saddlemyer, M. Salama, D. Savransky, A. C. Schneider, A. Sivaramakrishnan, I. Song, R. Soummer, S. Thomas, G. Vasisht, J. K. Wallace, K. Ward-Duong, S. J. Wiktorowicz, S. G. Wolff, and B. Zuckerman. Discovery and spectroscopy of the young jovian planet 51 Eri b with the Gemini Planet Imager. *Science*, 350(6256):64–67, Oct. 2015.

[261] D. Magrin, R. Ragazzoni, H. Rauer, I. Pagano, V. Nascimbeni, G. Piotto, V. Viotto, D. Piazza, T. Bandy, S. Basso, W. Benz, M. Bergomi, F. Biondi, F. Borsa, A. Börner, A. Brandeker, M. Brändli, G. Bruno, J. Cabrera, F. Calderone, V. Cessa, S. Chinellato, T. De Roche, M. Dima, A. Erikson, J. Farinato, M. Ghigo, D. Greggio, M. Klebor, L. Marafatto, M. Munari, V. Mogulsky, M. Pertenais, G. Peter, E. Portaluri, M. Rieder, S. Rockstein, M. Schweitzer, D. Sicilia, G. Umbriaco, M. Wieser, A. M. Heras, F. Marliani, S. Pirrotta, M. Salatti, E. Tommasi, R. Bardazzi, E. Battistelli, M. Brotini, M. Burresi, E. Capuano, M. Marinai, A. Novi, and C. Català. PLATO: the ESA mission for exo-planets discovery. In M. Lystrup, H. A. MacEwen, G. G. Fazio, N. Batalha, N. Siegler, and E. C. Tong, editors, *Space Telescopes and Instrumentation 2018: Optical, Infrared, and Millimeter Wave*, volume 10698 of *Society of Photo-Optical Instrumentation Engineers (SPIE) Conference Series*, page 106984X, July 2018.

[262] S. Mahadevan, L. Ramsey, C. Bender, R. Terrien, J. T. Wright, S. Halverson, F. Hearty, M. Nelson, A. Burton, S. Redman, S. Osterman, S. Diddams, J. Kasting, M. Endl, and R. Deshpande. The habitable-zone planet finder: a stabilized fiber-fed NIR spectrograph for the Hobby-Eberly Telescope. In I. S. McLean, S. K. Ramsay, and H. Takami, editors, *Ground-based and Airborne Instrumentation for Astronomy IV*, volume 8446 of *Society of Photo-Optical Instrumentation Engineers (SPIE) Conference Series*, page 84461S, Sept. 2012.

[263] S. Mahadevan, L. W. Ramsey, R. Terrien, S. Halverson, A. Roy, F. Hearty, E. Levi, G. K. Stefansson, P. Robertson, C. Bender, C. Schwab, and M. Nelson. The Habitable-zone Planet Finder: A status update on the development of a stabilized fiber-fed near-infrared spectrograph for the for the Hobby-Eberly telescope. In S. K. Ramsay, I. S. McLean, and H. Takami, editors, *Ground-based and Airborne Instrumentation for Astronomy V*, volume 9147 of *Society of Photo-Optical Instrumentation Engineers (SPIE) Conference Series*, page 91471G, July 2014.

[264] E. Mamajek and K. Stapelfeldt. NASA Exoplanet Exploration Program (ExEP) Mission Star List for the Habitable Worlds Observatory (2023). *arXiv e-prints*, page arXiv:2402.12414, Feb. 2024.

[265] A. W. Mann, G. A. Feiden, E. Gaidos, T. Boyajian, and K. von Braun. How to Constrain Your M Dwarf: Measuring Effective Temperature, Bolometric Luminosity, Mass, and Radius. *The Astrophysical Journal*, 804(1):64, May 2015.

[266] C. Marois, B. Macintosh, T. Barman, B. Zuckerman, I. Song, J. Patience, D. Lafrenière, and R. Doyon. Direct Imaging of Multiple Planets Orbiting the Star HR 8799. *Science*, 322(5906):1348, Nov. 2008.

[267] F. J. Masci, R. R. Laher, B. Rusholme, D. L. Shupe, S. Groom, J. Surace, E. Jackson, S. Monkewitz, R. Beck, D. Flynn, S. Terek, W. Landry, E. Hacopians, V. Desai, J. Howell, T. Brooke, D. Imel, S. Wachter, Q.-Z. Ye, H.-W. Lin, S. B. Cenko, V. Cunningham, U. Rebbapragada, B. Bue, A. A. Miller, A. Mahabal, E. C. Bellm, M. T. Patterson, M. Jurić, V. Z. Golkhou, E. O. Ofek, R. Walters, M. Graham, M. M. Kasliwal, R. G. Dekany, T. Kupfer, K. Burdge, C. B. Cannella, T. Barlow, A. Van Sistine, M. Giomi, C. Fremling, N. Blagorodnova, D. Levitan, R. Riddle, R. M. Smith, G. Helou, T. A. Prince, and S. R. Kulkarni. The Zwicky Transient Facility: Data Processing, Products, and Archive. *Publications of the Astronomical Society of the Pacific*, 131(995):018003, Jan. 2019.

[268] T. Matsakos and A. Königl. On the Origin of the Sub-Jovian Desert in the Orbital-period-Planetary-mass Plane. *The Astrophysical Journal Letters*, 820(1):L8, Mar. 2016.

[269] D. Mawet, M. Fitzgerald, Q. Konopacky, C. Beichman, N. Jovanovic, R. Dekany, D. Hover, E. Chisholm, D. Ciardi, É. Artigau, R. Banyal, T. Beatty, B. Benneke, G. A. Blake, A. Burgasser, G. Canalizo, G. Chen, T. Do, G. Doppmann, R. Doyon, C. Dressing, M. Fang, T. Greene, L. Hillenbrand, A. Howard, S. Kane, T. Kataria, E. Kempton, H. Knutson, T. Kotani, D. Lafrenière, C. Liu, S. Nishiyama, G. Pandey, P. Plavchan, L. Prato, S. P. Rajaguru, P. Robertson, C. Salyk, B. Sato, E. Schlawin, S. Sengupta, T. Sivarani, W. Skidmore, M. Tamura, H. Terada, G. Vasisht, J. Wang, and H. Zhang. High-resolution Infrared Spectrograph for Exoplanet Characterization with the Keck and Thirty Meter Telescopes. In *Bulletin of the American Astronomical Society*, volume 51, page 134, Sept. 2019.

[270] A. W. Mayo, A. Vanderburg, D. W. Latham, A. Bieryla, T. D. Morton, L. A. Buchhave, C. D. Dressing, C. Beichman, P. Berlind, M. L. Calkins, D. R. Ciardi, I. J. M. Crossfield, G. A. Esquerdo, M. E. Everett, E. J. Gonzales, L. A. Hirsch, E. P. Horch, A. W. Howard, S. B. Howell, J. Livingston, R. Patel, E. A. Petigura, J. E. Schlieder, N. J. Scott, C. F. Schumer, E. Sinukoff, J. Teske, and J. G. Winters. 275 Candidates and 149 Validated Planets Orbiting Bright Stars in K2 Campaigns 0-10. *The Astronomical Journal*, 155(3):136, Mar. 2018.

[271] M. Mayor, F. Pepe, D. Queloz, F. Bouchy, G. Rupprecht, G. Lo Curto, G. Avila, W. Benz, J. L. Bertaux, X. Bonfils, T. Dall, H. Dekker, B. Delabre, W. Eckert,

M. Fleury, A. Gilliotte, D. Gojak, J. C. Guzman, D. Kohler, J. L. Lizon, A. Longinotti, C. Lovis, D. Megevand, L. Pasquini, J. Reyes, J. P. Sivan, D. Sosnowska, R. Soto, S. Udry, A. van Kesteren, L. Weber, and U. Weilenmann. Setting New Standards with HARPS. *The Messenger*, 114:20–24, Dec. 2003.

[272] M. Mayor and D. Queloz. A Jupiter-mass companion to a solar-type star. *Nature*, 378(6555):355–359, Nov. 1995.

[273] M. Mayor, D. Queloz, S. Udry, and J.-L. Halbwachs. From brown dwarfs to planets. In C. Batalli Cosmovici, S. Bowyer, and D. Werthimer, editors, *IAU Colloq. 161: Astronomical and Biochemical Origins and the Search for Life in the Universe*, page 313, Jan. 1997.

[274] T. Mazeh, T. Holczer, and S. Faigler. Dearth of short-period Neptunian exoplanets: A desert in period-mass and period-radius planes. *Astronomy and Astrophysics*, 589:A75, May 2016.

[275] B. E. McArthur, M. Endl, W. D. Cochran, G. F. Benedict, D. A. Fischer, G. W. Marcy, R. P. Butler, D. Naef, M. Mayor, D. Queloz, S. Udry, and T. E. Harrison. Detection of a Neptune-Mass Planet in the ρ^1 Cancri System Using the Hobby-Eberly Telescope. *The Astrophysical Journall*, 614(1):L81–L84, Oct. 2004.

[276] W. H. McCrea. The Origin of the Solar System. *Proceedings of the Royal Society of London Series A*, 256(1285):245–266, June 1960.

[277] C. McCully, N. H. Volgenau, D.-R. Harbeck, T. A. Lister, E. S. Saunders, M. L. Turner, R. J. Siiverd, and M. Bowman. Real-time processing of the imaging data from the network of Las Cumbres Observatory Telescopes using BANZAI. In J. C. Guzman and J. Ibsen, editors, *Software and Cyberinfrastructure for Astronomy V*, volume 10707 of *Society of Photo-Optical Instrumentation Engineers (SPIE) Conference Series*, page 107070K, July 2018.

[278] A. McQuillan, T. Mazeh, and S. Aigrain. Rotation Periods of 34,030 Kepler Main-sequence Stars: The Full Autocorrelation Sample. *Astrophysical Journal, Supplement*, 211(2):24, Apr. 2014.

[279] D. Mesa, R. Gratton, P. Kervella, M. Bonavita, S. Desidera, V. D'Orazi, S. Marino, A. Zurlo, and E. Rigliaco. AF Lep b: The lowest-mass planet detected by coupling astrometric and direct imaging data. *Astronomy and Astrophysics*, 672:A93, Apr. 2023.

[280] N. Meunier, M. Desort, and A. M. Lagrange. Using the Sun to estimate Earth-like planets detection capabilities . II. Impact of plages. *Astronomy and Astrophysics*, 512:A39, Mar. 2010.

[281] S. M. Mills and T. Mazeh. The Planetary Mass-Radius Relation and Its Dependence on Orbital Period as Measured by Transit Timing Variations and Radial Velocities. *The Astrophysical Journal Letters*, 839(1):L8, Apr. 2017.

[282] M. Mori and J. H. Livingston. A warm Sub-Neptune transiting the M3 dwarf TOI 1696. In *Posters from the TESS Science Conference II (TSC2*, page 85, July 2021.

[283] C. V. Morley, J. J. Fortney, M. S. Marley, K. Zahnle, M. Line, E. Kempton, N. Lewis, and K. Cahoy. Thermal Emission and Reflected Light Spectra of Super Earths with Flat Transmission Spectra. *The Atrophysical Journal*, 815(2):110, Dec. 2015.

[284] J. I. Moses, N. Madhusudhan, C. Visscher, and R. S. Freedman. Chemical Consequences of the C/O Ratio on Hot Jupiters: Examples from WASP-12b, CoRoT-2b, XO-1b, and HD 189733b. *The Astrophysical Journal*, 763(1):25, Jan. 2013.

[285] J. I. Moses, C. Visscher, J. J. Fortney, A. P. Showman, N. K. Lewis, C. A. Griffith, S. J. Klippenstein, M. Shabram, A. J. Friedson, M. S. Marley, and R. S. Freedman. Disequilibrium Carbon, Oxygen, and Nitrogen Chemistry in the Atmospheres of HD 189733b and HD 209458b. *The Astrophysical Journal*, 737(1):15, Aug. 2011.

[286] F. Motalebi, S. Udry, M. Gillon, C. Lovis, D. Ségransan, L. A. Buchhave, B. O. Demory, L. Malavolta, C. D. Dressing, D. Sasselov, K. Rice, D. Charbonneau, A. Collier Cameron, D. Latham, E. Molinari, F. Pepe, L. Affer, A. S. Bonomo, R. Cosentino, X. Dumusque, P. Figueira, A. F. M. Fiorenzano, S. Gettel, A. Harutyunyan, R. D. Haywood, J. Johnson, E. Lopez, M. Lopez-Morales, M. Mayor, G. Micela, A. Mortier, V. Nascimbeni, D. Philips, G. Piotto, D. Pollacco, D. Queloz, A. Sozzetti, A. Vanderburg, and C. A. Watson. The HARPS-N Rocky Planet Search. I. HD 219134 b: A transiting rocky planet in a multi-planet system at 6.5 pc from the Sun. *Astronomy and Astrophysics*, 584:A72, Dec. 2015.

[287] G. D. Mulders, I. Pascucci, and D. Apai. An Increase in the Mass of Planetary Systems around Lower-mass Stars. *The Astrophysical Journal*, 814(2):130, Dec. 2015.

[288] C. D. Murray and S. F. Dermott. *Solar system dynamics*. 1999.

[289] N. Narita, A. Fukui, T. Yamamuro, D. Harbeck, M. Bowman, M. Elphick, J. Nation, J. D. Armstrong, J. Han, S. Abe, M. Ikoma, K. Isogai, K. Kawauchi, S. Kurita, N. Kusakabe, J. de Leon, J. Livingston, M. Mori, T. Nishiumi, M. Tamura, N. Watanabe, N. Volgenau, E. Heinrich-Josties, S. Foale, M. Daily, C. McCully, A. Kirby, C. Smith, B. Haworth, P. Conway, L. Storrie-Lombardi, W. Rosing, J. Chatelain, E. Bachelet, M. Johnson, and M. Rabus. MuSCAT3: a 4-color simultaneous camera for the 2m Faulkes Telescope North. In *Society of Photo-Optical Instrumentation Engineers (SPIE) Conference Series*, volume 11447 of *Society of Photo-Optical Instrumentation Engineers (SPIE) Conference Series*, page 114475K, Dec. 2020.

[290] E. National Academies of Sciences and Medicine. *Pathways to Discovery in Astronomy and Astrophysics for the 2020s*. 2021.

[291] B. E. Nelson, E. B. Ford, J. Buchner, R. Cloutier, R. F. Díaz, J. P. Faria, N. C. Hara, V. M. Rajpaul, and S. Rukdee. Quantifying the Bayesian Evidence for a Planet in Radial Velocity Data. *The Astronomical Journal*, 159(2):73, Feb. 2020.

[292] R. P. Nelson. Planetary Migration in Protoplanetary Disks. In H. J. Deeg and J. A. Belmonte, editors, *Handbook of Exoplanets*, page 139. 2018.

[293] E. R. Newton, J. Irwin, D. Charbonneau, Z. K. Berta-Thompson, J. A. Dittmann, and A. A. West. The Rotation and Galactic Kinematics of Mid M Dwarfs in the Solar Neighborhood. *The Astrophysical Journal*, 821(2):93, Apr. 2016.

[294] M. Newville, T. Stensitzki, D. B. Allen, and A. Ingargiola. LMFIT: Non-Linear Least-Square Minimization and Curve-Fitting for Python. Zenodo, Sept. 2014.

[295] G. Nowak, R. Luque, H. Parviainen, E. Pallé, K. Molaverdikhani, V. J. S. Béjar, J. Lillo-Box, C. Rodríguez-López, J. A. Caballero, M. Zechmeister, V. M. Passegger, C. Cifuentes, A. Schweitzer, N. Narita, B. Cale, N. Espinoza, F. Murgas, D. Hidalgo, M. R. Zapatero Osorio, F. J. Pozuelos, F. J. Aceituno, P. J. Amado, K. Barkaoui, D. Barrado, F. F. Bauer, Z. Benkhaldoun, D. A. Caldwell, N. Casasayas Barris, P. Chaturvedi, G. Chen, K. A. Collins, K. I. Collins, M. Cortés-Contreras, I. J. M. Crossfield, J. P. de León, E. Díez Alonso, S. Dreizler, M. El Mufti, E. Esparza-Borges, Z. Essack, A. Fukui, E. Gaidos, M. Gillon, E. J. Gonzales, P. Guerra, A. Hatzes, T. Henning, E. Herrero, K. Hesse, T. Hirano, S. B. Howell, S. V. Jeffers, E. Jehin, J. M. Jenkins, A. Kaminski, J. Kemmer, J. F. Kielkopf, D. Kossakowski, T. Kotani, M. Kürster, M. Lafarga, D. W. Latham, N. Law, J. J. Lissauer, N. Lodieu, A. Madrigal-Aguado, A. W. Mann, B. Massey, R. A. Matson, E. Matthews, P. Montañés-Rodríguez, D. Montes, J. C. Morales, M. Mori, E. Nagel, M. Oshagh, S. Pedraz, P. Plavchan, D. Pollacco, A. Quirrenbach, S. Reffert, A. Reiners, I. Ribas, G. R. Ricker, M. E. Rose, M. Schlecker, J. E. Schlieder, S. Seager, M. Stangret, S. Stock, M. Tamura, A. Tanner, J. Teske, T. Trifonov, J. D. Twicken, R. Vanderspek, D. Watanabe, J. Wittrock, C. Ziegler, and F. Zohrabi. The CARMENES search for exoplanets around M dwarfs. Two planets on opposite sides of the radius gap transiting the nearby M dwarf LTT 3780. *Astronomy and Astrophysics*, 642:A173, Oct. 2020.

[296] R. W. Noyes, L. W. Hartmann, S. L. Baliunas, D. K. Duncan, and A. H. Vaughan. Rotation, convection, and magnetic activity in lower main-sequence stars. *The Astrophysical Journal*, 279:763–777, Apr. 1984.

[297] K. I. Öberg, R. Murray-Clay, and E. A. Bergin. The Effects of Snowlines on C/O in Planetary Atmospheres. *The Astrophysical Journal Letters*, 743(1):L16, Dec. 2011.

[298] C. Ostberg and S. R. Kane. Predicting the Yield of Potential Venus Analogs from TESS and Their Potential for Atmospheric Characterization. *Astronomical Journal*, 158(5):195, Nov. 2019.

[299] J. E. Owen and B. Campos Estrada. Testing exoplanet evaporation with multitransiting systems. *Monthly Notices of the Royal Astronomical Society*, 491(4):5287–5297, Feb. 2020.

[300] J. E. Owen and D. Lai. Photoevaporation and high-eccentricity migration created the sub-Jovian desert. *Monthly Notices of the Royal Astronomical Society*, 479(4):5012–5021, Oct. 2018.

[301] H. Parviainen, E. Palle, M. R. Zapatero-Osorio, G. Nowak, A. Fukui, F. Murgas, N. Narita, K. G. Stassun, J. H. Livingston, K. A. Collins, D. Hidalgo Soto, V. J. S. Béjar, J. Korth, M. Monelli, P. Montanes Rodriguez, N. Casasayas-Barris, G. Chen, N. Crouzet, J. P. de Leon, A. Hernandez, K. Kawauchi, P. Klagyivik, N. Kusakabe, R. Luque, M. Mori, T. Nishiumi, J. Prieto-Arranz, M. Tamura, N. Watanabe, T. Gan, K. I. Collins, E. L. N. Jensen, T. Barclay, J. P. Doty, J. M. Jenkins, D. W. Latham, M. Paegert, G. Ricker, D. R. Rodriguez, S. Seager, A. Shporer, R. Vanderspek, J. Villaseñor, J. N. Winn, B. Wohler, and I. Wong. TOI-519 b: A short-period substellar object around an M dwarf validated using multicolour photometry and phase curve analysis. *Astronomy and Astrophysics*, 645:A16, Jan. 2021.

[302] F. Pepe, M. Mayor, G. Rupprecht, G. Avila, P. Ballester, J. L. Beckers, W. Benz, J. L. Bertaux, F. Bouchy, B. Buzzoni, C. Cavadore, S. Deiries, H. Dekker, B. Delabre, S. D'Odorico, W. Eckert, J. Fischer, M. Fleury, M. George, A. Gilliotte, D. Gojak, J. C. Guzman, F. Koch, D. Kohler, H. Kotzlowski, D. Lacroix, J. Le Merrer, J. L. Lizon, G. Lo Curto, A. Longinotti, D. Megevand, L. Pasquini, P. Petitpas, M. Pichard, D. Queloz, J. Reyes, P. Richaud, J. P. Sivan, D. Sosnowska, R. Soto, S. Udry, E. Ureta, A. van Kesteren, L. Weber, U. Weilenmann, A. Wicenec, G. Wieland, J. Christensen-Dalsgaard, D. Dravins, A. Hatzes, M. Kürster, F. Paresce, and A. Penny. HARPS: ESO's coming planet searcher. Chasing exoplanets with the La Silla 3.6-m telescope. *The Messenger*, 110:9–14, Dec. 2002.

[303] F. A. Pepe, S. Cristiani, R. Rebolo Lopez, N. C. Santos, A. Amorim, G. Avila, W. Benz, P. Bonifacio, A. Cabral, P. Carvas, R. Cirami, J. Coelho, M. Comari, I. Coretti, V. De Caprio, H. Dekker, B. Delabre, P. Di Marcantonio, V. D'Odorico, M. Fleury, R. García, J. M. Herreros Linares, I. Hughes, O. Iwert, J. Lima, J.-L. Lizon, G. Lo Curto, C. Lovis, A. Manescau, C. Martins, D. Mégevand, A. Moitinho, P. Molaro, M. Monteiro, M. Monteiro, L. Pasquini, C. Mordasini, D. Queloz, J. L. Rasilla, J. M. Rebordão, S. Santana Tschudi, P. Santin, D. Sosnowska, P. Spanò, F. Tenegi, S. Udry, E. Vanzella, M. Viel, M. R. Zapatero Osorio, and F. Zerbi. ESPRESSO: the Echelle spectrograph for rocky exoplanets and stable spectroscopic observations. In I. S. McLean, S. K. Ramsay, and H. Takami, editors, *Ground-based and Airborne Instrumentation for Astronomy III*, volume 7735 of *Society of Photo-Optical Instrumentation Engineers (SPIE) Conference Series*, page 77350F, July 2010.

[304] M. Perryman. *The Exoplanet Handbook*. 2018.

[305] E. A. Petigura, J. G. Rogers, H. Isaacson, J. E. Owen, A. L. Kraus, J. N. Winn, M. G. MacDougall, A. W. Howard, B. Fulton, M. R. Kosiarek, L. M. Weiss, A. Behmard, and S. Blunt. The California-Kepler Survey. X. The Radius Gap as a Function of Stellar Mass, Metallicity, and Age. *Astronomical Journal*, 163(4):179, Apr. 2022.

[306] E. A. Petigura, E. Sinukoff, E. D. Lopez, I. J. M. Crossfield, A. W. Howard, J. M. Brewer, B. J. Fulton, H. T. Isaacson, D. R. Ciardi, S. B. Howell, M. E. Everett, E. P. Horch, L. A. Hirsch, L. M. Weiss, and J. E. Schlieder. Four Sub-Saturns with Dissimilar Densities: Windows into Planetary Cores and Envelopes. *Astronomical Journal*, 153(4):142, Apr. 2017.

[307] C. Petrovich, E. Deibert, and Y. Wu. Ultra-short-period Planets from Secular Chaos. *The Astronomical Journal*, 157(5):180, May 2019.

[308] C. Phillips, J. Wang, S. Kendrew, T. P. Greene, R. Hu, J. Valenti, W. R. Panero, and J. Schulze. Detecting Biosignatures in the Atmospheres of Gas Dwarf Planets with the James Webb Space Telescope. *arXiv e-prints*, page arXiv:2109.12132, Sept. 2021.

[309] P. Plavchan, T. Barclay, J. Gagné, P. Gao, B. Cale, W. Matzko, D. Dragomir, S. Quinn, D. Feliz, K. Stassun, I. J. M. Crossfield, D. A. Berardo, D. W. Latham, B. Tieu, G. Anglada-Escudé, G. Ricker, R. Vanderspek, S. Seager, J. N. Winn, J. M. Jenkins, S. Rinehart, A. Krishnamurthy, S. Dynes, J. Doty, F. Adams, D. A. Afanasev, C. Beichman, M. Bottom, B. P. Bowler, C. Brinkworth, C. J. Brown, A. Cancino, D. R. Ciardi, M. Clampin, J. T. Clark, K. Collins, C. Davison, D. Foreman-Mackey, E. Furlan, E. J. Gaidos, C. Geneser, F. Giddens, E. Gilbert, R. Hall, C. Hellier, T. Henry, J. Horner, A. W. Howard, C. Huang, J. Huber, S. R. Kane, M. Kenworthy, J. Kielkopf, D. Kipping, C. Klenke, E. Kruse, N. Latouf, P. Lowrance, B. Mennesson, M. Mengel, S. M. Mills, T. Morton, N. Narita, E. Newton, A. Nishimoto, J. Okumura, E. Palle, J. Pepper, E. V. Quintana, A. Roberge, V. Roccatagliata, J. E. Schlieder, A. Tanner, J. Teske, C. G. Tinney, A. Vanderburg, K. von Braun, B. Walp, J. Wang, S. X. Wang, D. Weigand, R. White, R. A. Wittenmyer, D. J. Wright, A. Youngblood, H. Zhang, and P. Zilberman. A planet within the debris disk around the pre-main-sequence star AU Microscopii. *Nature*, 582(7813):497–500, June 2020.

[310] M. J. D. Powell. Direct search algorithms for optimization calculations. *Acta Numerica*, 7:287–336, Jan. 1998.

[311] A. Quirrenbach, P. J. Amado, J. A. Caballero, R. Mundt, A. Reiners, I. Ribas, W. Seifert, M. Abril, J. Aceituno, F. J. Alonso-Floriano, M. Ammler-von Eiff, R. Antona Jiménez, H. Anwand-Heerwart, M. Azzaro, F. Bauer, D. Barrado, S. Becerril, V. J. S. Béjar, D. Benítez, Z. M. Berdiñas, M. C. Cárdenas, E. Casal, A. Claret, J. Colomé, M. Cortés-Contreras, S. Czesla, M. Doellinger, S. Dreizler, C. Feiz, M. Fernández, D. Galadí, M. C. Gálvez-Ortiz, A. García-Piquer, M. L. García-Vargas, R. Garrido, L. Gesa, V. Gómez Galera, E. González Álvarez, J. I. González Hernández, U. Grözinger, J. Guàrdia, E. W. Guenther, E. de Guindos, J. Gutiérrez-Soto, H. J. Hagen, A. P. Hatzes, P. H. Hauschildt, J. Helmling, T. Henning, D. Hermann, L. Hernández Castaño, E. Herrero, D. Hidalgo, G. Holgado, A. Huber, K. F. Huber, S. Jeffers, V. Joergens, E. de Juan, M. Kehr, R. Klein, M. Kürster, A. Lamert, S. Lalitha, W. Laun, U. Lemke, R. Lenzen, M. López del Fresno, B. López Martí, J. López-Santiago, U. Mall, H. Mandel, E. L. Martín, S. Martín-Ruiz, H. Martínez-Rodríguez, C. J. Marvin, R. J. Mathar, E. Mirabet, D. Montes, R. Morales Muñoz, A. Moya, V. Naranjo, A. Ofir, R. Oreiro, E. Pallé, J. Panduro, V. M. Passegger, A. Pérez-Calpena, D. Pérez Medialdea, M. Perger, M. Pluto, A. Ramón, R. Rebolo, P. Redondo, S. Reffert, S. Reinhardt, P. Rhode, H. W. Rix, F. Rodler, E. Rodríguez, C. Rodríguez-López, E. Rodríguez-Pérez, R. R. Rohloff, A. Rosich, E. Sánchez-Blanco, M. A. Sánchez Carrasco, J. Sanz-Forcada, L. F. Sarmiento, S. Schäfer, J. Schiller, C. Schmidt, J. H. M. M. Schmitt, E. Solano, O. Stahl, C. Storz, J. Stürmer, J. C.

Suárez, R. G. Ulbrich, G. Veredas, K. Wagner, J. Winkler, M. R. Zapatero Osorio, M. Zechmeister, F. J. Abellán de Paco, G. Anglada-Escudé, C. del Burgo, A. Klutsch, J. L. Lizon, M. López-Morales, J. C. Morales, M. A. C. Perryman, S. M. Tulloch, and W. Xu. CARMENES instrument overview. In S. K. Ramsay, I. S. McLean, and H. Takami, editors, *Ground-based and Airborne Instrumentation for Astronomy V*, volume 9147 of *Society of Photo-Optical Instrumentation Engineers (SPIE) Conference Series*, page 91471F, July 2014.

[312] V. Rajpaul, S. Aigrain, M. A. Osborne, S. Reece, and S. Roberts. A Gaussian process framework for modelling stellar activity signals in radial velocity data. *Monthly Notices of the Royal Astronomical Society*, 452(3):2269–2291, Sept. 2015.

[313] V. Rajpaul, L. A. Buchhave, and S. Aigrain. Pinning down the mass of Kepler-10c: the importance of sampling and model comparison. *Monthly Notices of the Royal Astronomical Society*, 471(1):L125–L130, Oct. 2017.

[314] V. M. Rajpaul, L. A. Buchhave, G. Lacedelli, K. Rice, A. Mortier, L. Malavolta, S. Aigrain, L. Borsato, A. W. Mayo, D. Charbonneau, M. Damasso, X. Dumusque, A. Ghedina, D. W. Latham, M. López-Morales, A. Magazzù, G. Micela, E. Molinari, F. Pepe, G. Piotto, E. Poretti, S. Rowther, A. Sozzetti, S. Udry, and C. A. Watson. A HARPS-N mass for the elusive Kepler-37d: a case study in disentangling stellar activity and planetary signals. *Monthly Notices of the Royal Astronomical Society*, 507(2):1847–1868, Oct. 2021.

[315] H. Rauer, C. Catala, C. Aerts, T. Appourchaux, W. Benz, A. Brandeker, J. Christensen-Dalsgaard, M. Deleuil, L. Gizon, M. J. Goupil, M. Güdel, E. Janot-Pacheco, M. Mas-Hesse, I. Pagano, G. Piotto, D. Pollacco, Ċ. Santos, A. Smith, J. C. Suárez, R. Szabó, S. Udry, V. Adibekyan, Y. Alibert, J. M. Almenara, P. Amaro-Seoane, M. A.-v. Eiff, M. Asplund, E. Antonello, S. Barnes, F. Baudin, K. Belkacem, M. Bergemann, G. Bihain, A. C. Birch, X. Bonfils, I. Boisse, A. S. Bonomo, F. Borsa, I. M. Brandão, E. Brocato, S. Brun, M. Burleigh, R. Burston, J. Cabrera, S. Cassisi, W. Chaplin, S. Charpinet, C. Chiappini, R. P. Church, S. Csizmadia, M. Cunha, M. Damasso, M. B. Davies, H. J. Deeg, R. F. Díaz, S. Dreizler, C. Dreyer, P. Eggenberger, D. Ehrenreich, P. Eigmüller, A. Erikson, R. Farmer, S. Feltzing, F. de Oliveira Fialho, P. Figueira, T. Forveille, M. Fridlund, R. A. García, P. Giommi, G. Giuffrida, M. Godolt, J. Gomes da Silva, T. Granzer, J. L. Grenfell, A. Grotsch-Noels, E. Günther, C. A. Haswell, A. P. Hatzes, G. Hébrard, S. Hekker, R. Helled, K. Heng, J. M. Jenkins, A. Johansen, M. L. Khodachenko, K. G. Kislyakova, W. Kley, U. Kolb, N. Krivova, F. Kupka, H. Lammer, A. F. Lanza, Y. Lebreton, D. Magrin, P. Marcos-Arenal, P. M. Marrese, J. P. Marques, J. Martins, S. Mathis, S. Mathur, S. Messina, A. Miglio, J. Montalban, M. Montalto, M. J. P. F. G. Monteiro, H. Moradi, E. Moravveji, C. Mordasini, T. Morel, A. Mortier, V. Nascimbeni, R. P. Nelson, M. B. Nielsen, L. Noack, A. J. Norton, A. Ofir, M. Oshagh, R. M. Ouazzani, P. Pápics, V. C. Parro, P. Petit, B. Plez, E. Poretti, A. Quirrenbach, R. Ragazzoni, G. Raimondo, M. Rainer, D. R. Reese, R. Redmer, S. Reffert, B. Rojas-Ayala, I. W. Roxburgh, S. Salmon, A. Santerne, J. Schneider, J. Schou, S. Schuh, H. Schunker, A. Silva-Valio,

R. Silvotti, I. Skillen, I. Snellen, F. Sohl, S. G. Sousa, A. Sozzetti, D. Stello, K. G. Strassmeier, M. Švanda, G. M. Szabó, A. Tkachenko, D. Valencia, V. Van Grootel, S. D. Vauclair, P. Ventura, F. W. Wagner, N. A. Walton, J. Weingrill, S. C. Werner, P. J. Wheatley, and K. Zwintz. The PLATO 2.0 mission. *Experimental Astronomy*, 38(1-2):249–330, Nov. 2014.

[316] S. N. Raymond, R. Barnes, and A. M. Mandell. Observable consequences of planet formation models in systems with close-in terrestrial planets. *Monthly Notices of the Royal Astronomical Society*, 384(2):663–674, Feb. 2008.

[317] A. Reiners, M. Zechmeister, J. A. Caballero, I. Ribas, J. C. Morales, S. V. Jeffers, P. Schöfer, L. Tal-Or, A. Quirrenbach, P. J. Amado, A. Kaminski, W. Seifert, M. Abril, J. Aceituno, F. J. Alonso-Floriano, M. Ammler-von Eiff, R. Antona, G. Anglada-Escudé, H. Anwand-Heerwart, B. Arroyo-Torres, M. Azzaro, D. Baroch, D. Barrado, F. F. Bauer, S. Becerril, V. J. S. Béjar, D. Benítez, Z. M. Berdinas, G. Bergond, M. Blümcke, M. Brinkmöller, C. del Burgo, J. Cano, M. C. Cárdenas Vázquez, E. Casal, C. Cifuentes, A. Claret, J. Colomé, M. Cortés-Contreras, S. Czesla, E. Díez-Alonso, S. Dreizler, C. Feiz, M. Fernández, I. M. Ferro, B. Fuhrmeister, D. Galadí-Enríquez, A. Garcia-Piquer, M. L. García Vargas, L. Gesa, V. Gómez Galera, J. I. González Hernández, R. González-Peinado, U. Grözinger, S. Grohnert, J. Guàrdia, E. W. Guenther, A. Guijarro, E. de Guindos, J. Gutiérrez-Soto, H. J. Hagen, A. P. Hatzes, P. H. Hauschildt, R. P. Hedrosa, J. Helmling, T. Henning, I. Hermelo, R. Hernández Arabí, L. Hernández Castaño, F. Hernández Hernando, E. Herrero, A. Huber, P. Huke, E. N. Johnson, E. de Juan, M. Kim, R. Klein, J. Klüter, A. Klutsch, M. Kürster, M. Lafarga, A. Lamert, M. Lampón, L. M. Lara, W. Laun, U. Lemke, R. Lenzen, R. Launhardt, M. López del Fresno, J. López-González, M. López-Puertas, J. F. López Salas, J. López-Santiago, R. Luque, H. Magán Madinabeitia, U. Mall, L. Mancini, H. Mandel, E. Marfil, J. A. Marín Molina, D. Maroto Fernández, E. L. Martín, S. Martín-Ruiz, C. J. Marvin, R. J. Mathar, E. Mirabet, D. Montes, M. E. Moreno-Raya, A. Moya, R. Mundt, E. Nagel, V. Naranjo, L. Nortmann, G. Nowak, A. Ofir, R. Oreiro, E. Pallé, J. Panduro, J. Pascual, V. M. Passegger, A. Pavlov, S. Pedraz, A. Pérez-Calpena, D. Pérez Medialdea, M. Perger, M. A. C. Perryman, M. Pluto, O. Rabaza, A. Ramón, R. Rebolo, P. Redondo, S. Reffert, S. Reinhart, P. Rhode, H. W. Rix, F. Rodler, E. Rodríguez, C. Rodríguez-López, A. Rodríguez Trinidad, R. R. Rohloff, A. Rosich, S. Sadegi, E. Sánchez-Blanco, M. A. Sánchez Carrasco, A. Sánchez-López, J. Sanz-Forcada, P. Sarkis, L. F. Sarmiento, S. Schäfer, J. H. M. M. Schmitt, J. Schiller, A. Schweitzer, E. Solano, O. Stahl, J. B. P. Strachan, J. Stürmer, J. C. Suárez, H. M. Tabernero, M. Tala, T. Trifonov, S. M. Tulloch, R. G. Ulbrich, G. Veredas, J. I. Vico Linares, F. Vilardell, K. Wagner, J. Winkler, V. Wolthoff, W. Xu, F. Yan, and M. R. Zapatero Osorio. The CARMENES search for exoplanets around M dwarfs. High-resolution optical and near-infrared spectroscopy of 324 survey stars. *Astronomy and Astrophysics*, 612:A49, Apr. 2018.

[318] G. R. Ricker, J. N. Winn, R. Vanderspek, D. W. Latham, G. Á. Bakos, J. L. Bean, Z. K. Berta-Thompson, T. M. Brown, L. Buchhave, N. R. Butler, R. P. Butler, W. J. Chaplin, D. Charbonneau, J. Christensen-Dalsgaard, M. Clampin, D. Deming, J. Doty,

N. De Lee, C. Dressing, E. W. Dunham, M. Endl, F. Fressin, J. Ge, T. Henning, M. J. Holman, A. W. Howard, S. Ida, J. M. Jenkins, G. Jernigan, J. A. Johnson, L. Kaltenegger, N. Kawai, H. Kjeldsen, G. Laughlin, A. M. Levine, D. Lin, J. J. Lissauer, P. MacQueen, G. Marcy, P. R. McCullough, T. D. Morton, N. Narita, M. Paegert, E. Palle, F. Pepe, J. Pepper, A. Quirrenbach, S. A. Rinehart, D. Sasselov, B. Sato, S. Seager, A. Sozzetti, K. G. Stassun, P. Sullivan, A. Szentgyorgyi, G. Torres, S. Udry, and J. Villasenor. Transiting Exoplanet Survey Satellite (TESS). *Journal of Astronomical Telescopes, Instruments, and Systems*, 1:014003, Jan. 2015.

[319] G. R. Ricker, J. N. Winn, R. Vanderspek, D. W. Latham, G. Á. Bakos, J. L. Bean, Z. K. Berta-Thompson, T. M. Brown, L. Buchhave, N. R. Butler, R. P. Butler, W. J. Chaplin, D. Charbonneau, J. Christensen-Dalsgaard, M. Clampin, D. Deming, J. Doty, N. De Lee, C. Dressing, E. W. Dunham, M. Endl, F. Fressin, J. Ge, T. Henning, M. J. Holman, A. W. Howard, S. Ida, J. M. Jenkins, G. Jernigan, J. A. Johnson, L. Kaltenegger, N. Kawai, H. Kjeldsen, G. Laughlin, A. M. Levine, D. Lin, J. J. Lissauer, P. MacQueen, G. Marcy, P. R. McCullough, T. D. Morton, N. Narita, M. Paegert, E. Palle, F. Pepe, J. Pepper, A. Quirrenbach, S. A. Rinehart, D. Sasselov, B. Sato, S. Seager, A. Sozzetti, K. G. Stassun, P. Sullivan, A. Szentgyorgyi, G. Torres, S. Udry, and J. Villasenor. Transiting Exoplanet Survey Satellite (TESS). *Journal of Astronomical Telescopes, Instruments, and Systems*, 1:014003, Jan. 2015.

[320] P. Robertson, T. Anderson, G. Stefansson, F. R. Hearty, A. Monson, S. Mahadevan, S. Blakeslee, C. Bender, J. P. Ninan, D. Conran, E. Levi, E. Lubar, A. Cole, A. Dykhouse, S. Kanodia, C. Nitroy, J. Smolsky, D. Tuggle, B. Blank, M. Nelson, C. Blake, S. Halverson, C. Henderson, K. F. Kaplan, D. Li, S. E. Logsdon, M. W. McElwain, J. Rajagopal, L. W. Ramsey, A. Roy, C. Schwab, R. Terrien, and J. T. Wright. Ultrastable environment control for the NEID spectrometer: design and performance demonstration. *Journal of Astronomical Telescopes, Instruments, and Systems*, 5:015003, Jan. 2019.

[321] P. Robertson, C. Bender, S. Mahadevan, A. Roy, and L. W. Ramsey. Proxima Centauri as a Benchmark for Stellar Activity Indicators in the Near-infrared. *The Astrophysical Journal*, 832(2):112, Dec. 2016.

[322] P. Robertson, S. Mahadevan, M. Endl, and A. Roy. Stellar activity masquerading as planets in the habitable zone of the M dwarf Gliese 581. *Science*, 345(6195):440–444, July 2014.

[323] P. Robertson, G. Stefansson, S. Mahadevan, M. Endl, W. D. Cochran, C. Beard, C. F. Bender, S. A. Diddams, N. Duong, E. B. Ford, C. Fredrick, S. Halverson, F. Hearty, R. Holcomb, L. Juan, S. Kanodia, J. Lubin, A. J. Metcalf, A. Monson, J. P. Ninan, J. Palafoutas, L. W. Ramsey, A. Roy, C. Schwab, R. C. Terrien, and J. T. Wright. Persistent Starspot Signals on M Dwarfs: Multiwavelength Doppler Observations with the Habitable-zone Planet Finder and Keck/HIRES. *The Astrophysical Journal*, 897(2):125, July 2020.

[324] J. G. Rogers, H. E. Schlichting, and J. E. Owen. Conclusive Evidence for a Population of Water Worlds around M Dwarfs Remains Elusive. *The Astrophysical Journal Letters*, 947(1):L19, Apr. 2023.

[325] L. A. Rogers, P. Bodenheimer, J. J. Lissauer, and S. Seager. Formation and Structure of Low-density exo-Neptunes. *The Astrophysical Journal*, 738(1):59, Sept. 2011.

[326] L. J. Rosenthal, B. J. Fulton, L. A. Hirsch, H. T. Isaacson, A. W. Howard, C. M. Dedrick, I. A. Sherstyuk, S. C. Blunt, E. A. Petigura, H. A. Knutson, A. Behmard, A. Chontos, J. R. Crepp, I. J. M. Crossfield, P. A. Dalba, D. A. Fischer, G. W. Henry, S. R. Kane, M. Kosiarek, G. W. Marcy, R. A. Rubenzahl, L. M. Weiss, and J. T. Wright. The California Legacy Survey. I. A Catalog of 178 Planets from Precision Radial Velocity Monitoring of 719 Nearby Stars over Three Decades. *The Astrophysical Journal Supplement Series*, 255(1):8, July 2021.

[327] S. H. Saar and R. A. Donahue. Activity-Related Radial Velocity Variation in Cool Stars. *The Astrophysical Journal*, 485(1):319–327, Aug. 1997.

[328] S. Sabotta, M. Schlecker, P. Chaturvedi, E. W. Guenther, I. Muñoz Rodríguez, J. C. Muñoz Sánchez, J. A. Caballero, Y. Shan, S. Reffert, I. Ribas, A. Reiners, A. P. Hatzes, P. J. Amado, H. Klahr, J. C. Morales, A. Quirrenbach, T. Henning, S. Dreizler, E. Pallé, M. Perger, M. Azzaro, S. V. Jeffers, A. Kaminski, M. Kürster, M. Lafarga, D. Montes, V. M. Passegger, and M. Zechmeister. The CARMENES search for exoplanets around M dwarfs. Planet occurrence rates from a subsample of 71 stars. *Astronomy and Astrophysics*, 653:A114, Sept. 2021.

[329] J. Salvatier, T. V. Wiecki, and C. Fonnesbeck. Probabilistic programming in python using pymc3. *PeerJ Computer Science*, 2:e55, 2016.

[330] M. Samland, P. Mollière, M. Bonnefoy, A. L. Maire, F. Cantalloube, A. C. Cheetham, D. Mesa, R. Gratton, B. A. Biller, Z. Wahhaj, J. Bouwman, W. Brandner, D. Melnick, J. Carson, M. Janson, T. Henning, D. Homeier, C. Mordasini, M. Langlois, S. P. Quanz, R. van Boekel, A. Zurlo, J. E. Schlieder, H. Avenhaus, J. L. Beuzit, A. Boccaletti, M. Bonavita, G. Chauvin, R. Claudi, M. Cudel, S. Desidera, M. Feldt, T. Fusco, R. Galicher, T. G. Kopytova, A. M. Lagrange, H. Le Coroller, P. Martinez, O. Moeller-Nilsson, D. Mouillet, L. M. Mugnier, C. Perrot, A. Sevin, E. Sissa, A. Vigan, and L. Weber. Spectral and atmospheric characterization of 51 Eridani b using VLT/SPHERE. *Astronomy and Astrophysics*, 603:A57, July 2017.

[331] R. F. Sanford. The Radial-Velocity Variation of UU Cassiopeiae. *The Astrophysical Journal*, 79:84, Jan. 1934.

[332] A. Santerne, L. Malavolta, M. R. Kosiarek, F. Dai, C. D. Dressing, X. Dumusque, N. C. Hara, T. A. Lopez, A. Mortier, A. Vanderburg, V. Adibekyan, D. J. Armstrong, D. Barrado, S. C. C. Barros, D. Bayliss, D. Berardo, I. Boisse, A. S. Bonomo, F. Bouchy, D. J. A. Brown, L. A. Buchhave, R. P. Butler, A. Collier Cameron, R. Cosentino, J. D. Crane, I. J. M. Crossfield, M. Damasso, M. R. Deleuil,

E. Delgado Mena, O. Demangeon, R. F. Díaz, J. F. Donati, P. Figueira, B. J. Fulton, A. Ghedina, A. Harutyunyan, G. Hébrard, L. A. Hirsch, S. Hojjatpanah, A. W. Howard, H. Isaacson, D. W. Latham, J. Lillo-Box, M. López-Morales, C. Lovis, A. F. Martinez Fiorenzano, E. Molinari, O. Mousis, C. Moutou, C. Nava, L. D. Nielsen, H. P. Osborn, E. A. Petigura, D. F. Phillips, D. L. Pollacco, E. Poretti, K. Rice, N. C. Santos, D. Ségransan, S. A. Shectman, E. Sinukoff, S. G. Sousa, A. Sozzetti, J. K. Teske, S. Udry, A. Vigan, S. X. Wang, C. A. Watson, L. M. Weiss, P. J. Wheatley, and J. N. Winn. An extremely low-density and temperate giant exoplanet. *arXiv e-prints*, page arXiv:1911.07355, Nov. 2019.

[333] J. Sanz-Forcada, G. Micela, I. Ribas, A. M. T. Pollock, C. Eiroa, A. Velasco, E. Solano, and D. García-Álvarez. Estimation of the XUV radiation onto close planets and their evaporation. *Astronomy and Astrophysics*, 532:A6, Aug. 2011.

[334] J. D. Scargle. Studies in astronomical time series analysis. II. Statistical aspects of spectral analysis of unevenly spaced data. *The Astrophysical Journal*, 263:835–853, Dec. 1982.

[335] M. Schofield, W. J. Chaplin, D. Huber, T. L. Campante, G. R. Davies, A. Miglio, W. H. Ball, T. Appourchaux, S. Basu, T. R. Bedding, J. Christensen-Dalsgaard, O. Creevey, R. A. García, R. Handberg, S. D. Kawaler, H. Kjeldsen, D. W. Latham, M. N. Lund, T. S. Metcalfe, G. R. Ricker, A. Serenelli, V. Silva Aguirre, D. Stello, and R. Vanderspek. The Asteroseismic Target List for Solar-like Oscillators Observed in 2 minute Cadence with the Transiting Exoplanet Survey Satellite. *The Astrophysical Journals*, 241(1):12, Mar. 2019.

[336] C. Schwab, A. Rakich, Q. Gong, S. Mahadevan, S. P. Halverson, A. Roy, R. C. Terrien, P. M. Robertson, F. R. Hearty, E. I. Levi, A. J. Monson, J. T. Wright, M. W. McElwain, C. F. Bender, C. H. Blake, J. Stürmer, Y. V. Gurevich, A. Chakraborty, and L. W. Ramsey. Design of NEID, an extreme precision Doppler spectrograph for WIYN. In C. J. Evans, L. Simard, and H. Takami, editors, *Ground-based and Airborne Instrumentation for Astronomy VI*, volume 9908 of *Society of Photo-Optical Instrumentation Engineers (SPIE) Conference Series*, page 99087H, Aug. 2016.

[337] E. W. Schwieterman, N. Y. Kiang, M. N. Parenteau, C. E. Harman, S. DasSarma, T. M. Fisher, G. N. Arney, H. E. Hartnett, C. T. Reinhard, S. L. Olson, V. S. Meadows, C. S. Cockell, S. I. Walker, J. L. Grenfell, S. Hegde, S. Rugheimer, R. Hu, and T. W. Lyons. Exoplanet Biosignatures: A Review of Remotely Detectable Signs of Life. *Astrobiology*, 18(6):663–708, June 2018.

[338] S. Seager, W. Bains, and R. Hu. A Biomass-based Model to Estimate the Plausibility of Exoplanet Biosignature Gases. *The Astrophysical Journal*, 775(2):104, Oct. 2013.

[339] S. Seager, W. Bains, and R. Hu. Biosignature Gases in H_2-dominated Atmospheres on Rocky Exoplanets. *The Astrophysical Journal*, 777(2):95, Nov. 2013.

[340] S. Seager and D. Deming. Exoplanet Atmospheres. *Annual Review of Astronomy and Astrophysics*, 48:631–672, Sept. 2010.

[341] C. J. Shallue and A. Vanderburg. Identifying Exoplanets with Deep Learning: A Five-planet Resonant Chain around Kepler-80 and an Eighth Planet around Kepler-90. *The Astronomical Journal*, 155(2):94, Feb. 2018.

[342] B. Shappee, J. Prieto, K. Z. Stanek, C. S. Kochanek, T. Holoien, J. Jencson, U. Basu, J. F. Beacom, D. Szczygiel, G. Pojmanski, J. Brimacombe, M. Dubberley, M. Elphick, S. Foale, E. Hawkins, D. Mullins, W. Rosing, R. Ross, and Z. Walker. All Sky Automated Survey for SuperNovae (ASAS-SN or "Assassin"). In *American Astronomical Society Meeting Abstracts #223*, volume 223 of *American Astronomical Society Meeting Abstracts*, page 236.03, Jan. 2014.

[343] B. J. Shappee, J. L. Prieto, D. Grupe, C. S. Kochanek, K. Z. Stanek, G. De Rosa, S. Mathur, Y. Zu, B. M. Peterson, R. W. Pogge, S. Komossa, M. Im, J. Jencson, T. W. S. Holoien, U. Basu, J. F. Beacom, D. M. Szczygieł, J. Brimacombe, S. Adams, A. Campillay, C. Choi, C. Contreras, M. Dietrich, M. Dubberley, M. Elphick, S. Foale, M. Giustini, C. Gonzalez, E. Hawkins, D. A. Howell, E. Y. Hsiao, M. Koss, K. M. Leighly, N. Morrell, D. Mudd, D. Mullins, J. M. Nugent, J. Parrent, M. M. Phillips, G. Pojmanski, W. Rosing, R. Ross, D. Sand, D. M. Terndrup, S. Valenti, Z. Walker, and Y. Yoon. The Man behind the Curtain: X-Rays Drive the UV through NIR Variability in the 2013 Active Galactic Nucleus Outburst in NGC 2617. *The Astrophysical Journal*, 788(1):48, June 2014.

[344] M. Shetrone, M. E. Cornell, J. R. Fowler, N. Gaffney, B. Laws, J. Mader, C. Mason, S. Odewahn, B. Roman, S. Rostopchin, D. P. Schneider, J. Umbarger, and A. Westfall. Ten Year Review of Queue Scheduling of the Hobby-Eberly Telescope. *Publications of the Astronomical Society of the Pacific*, 119(855):556–566, May 2007.

[345] A. L. Shields, S. Ballard, and J. A. Johnson. The habitability of planets orbiting M-dwarf stars. *Physics Reports*, 663:1, Dec. 2016.

[346] V. Silva Aguirre, G. R. Davies, S. Basu, J. Christensen-Dalsgaard, O. Creevey, T. S. Metcalfe, T. R. Bedding, L. Casagrande, R. Handberg, M. N. Lund, P. E. Nissen, W. J. Chaplin, D. Huber, A. M. Serenelli, D. Stello, V. Van Eylen, T. L. Campante, Y. Elsworth, R. L. Gilliland, S. Hekker, C. Karoff, S. D. Kawaler, H. Kjeldsen, and M. S. Lundkvist. Ages and fundamental properties of Kepler exoplanet host stars from asteroseismology. *Monthly Notices of the Royal Astronomical Society*, 452(2):2127–2148, Sept. 2015.

[347] A. T. Sinclair. The orbital resonance amongst the Galilean satellites of Jupiter. *Monthly Notices of the Royal Astronomical Society*, 171:59–72, Apr. 1975.

[348] R. J. Siverd, T. G. Beatty, J. Pepper, J. D. Eastman, K. Collins, A. Bieryla, D. W. Latham, L. A. Buchhave, E. L. N. Jensen, J. R. Crepp, R. Street, K. G. Stassun, B. S. Gaudi, P. Berlind, M. L. Calkins, D. L. DePoy, G. A. Esquerdo, B. J. Fulton, G. Fűrész, J. C. Geary, A. Gould, L. Hebb, J. F. Kielkopf, J. L. Marshall, R. Pogge, K. Z. Stanek, R. P. Stefanik, A. H. Szentgyorgyi, M. Trueblood, P. Trueblood, A. M. Stutz, and J. L.

van Saders. KELT-1b: A Strongly Irradiated, Highly Inflated, Short Period, 27 Jupiter-mass Companion Transiting a Mid-F Star. *The Astrophysical Journal*, 761(2):123, Dec. 2012.

[349] W. Skidmore, TMT International Science Development Teams, and T. Science Advisory Committee. Thirty Meter Telescope Detailed Science Case: 2015. *Research in Astronomy and Astrophysics*, 15(12):1945, Dec. 2015.

[350] I. Snellen, R. de Kok, J. L. Birkby, B. Brandl, M. Brogi, C. Keller, M. Kenworthy, H. Schwarz, and R. Stuik. Combining high-dispersion spectroscopy with high contrast imaging: Probing rocky planets around our nearest neighbors. *Astonomy and Astrophysics*, 576:A59, Apr. 2015.

[351] C. Soubiran, G. Jasniewicz, L. Chemin, C. Zurbach, N. Brouillet, P. Panuzzo, P. Sartoretti, D. Katz, J. F. Le Campion, O. Marchal, D. Hestroffer, F. Thévenin, F. Crifo, S. Udry, M. Cropper, G. Seabroke, Y. Viala, K. Benson, R. Blomme, A. Jean-Antoine, H. Huckle, M. Smith, S. G. Baker, Y. Damerdji, C. Dolding, Y. Frémat, E. Gosset, A. Guerrier, L. P. Guy, R. Haigron, K. Janßen, G. Plum, C. Fabre, Y. Lasne, F. Pailler, C. Panem, F. Riclet, F. Royer, G. Tauran, T. Zwitter, A. Gueguen, and C. Turon. Gaia Data Release 2. The catalogue of radial velocity standard stars. *Astronomy and Astrophysics*, 616:A7, Aug. 2018.

[352] A. Sozzetti, M. Pinamonti, M. Damasso, S. Desidera, K. Biazzo, A. S. Bonomo, D. Nardiello, R. Gratton, A. F. Lanza, L. Malavolta, P. Giacobbe, L. Affer, A. Bignamini, F. Borsa, W. Boschin, M. Brogi, L. Cabona, R. Claudi, E. Covino, L. Di Fabrizio, A. Ghedina, A. Harutyunyan, C. Knapic, J. Maldonado, A. Maggio, L. Mancini, G. Mantovan, F. Marzari, S. Messina, G. Micela, E. Molinari, M. Montalto, L. Naponiello, I. Pagano, M. Pedani, G. Piotto, E. Poretti, G. Scandariato, R. Silvotti, and D. Turrini. The GAPS Programme at TNG. XLVII. A conundrum resolved: HIP 66074b/Gaia-3b characterised as a massive giant planet on a quasi-face-on and extremely elongated orbit. *Astronomy and Astrophysics*, 677:L15, Sept. 2023.

[353] S. Srinath, R. McGurk, C. Rockosi, R. Kupke, D. Gavel, G. Cabak, D. Cowley, M. Peck, C. Ratliff, E. Gates, D. Dillon, A. Norton, and M. Reining. Swimming with ShARCS: comparison of on-sky sensitivity with model predictions for ShaneAO on the Lick Observatory 3-meter telescope. In E. Marchetti, L. M. Close, and J.-P. Vran, editors, *Adaptive Optics Systems IV*, volume 9148 of *Society of Photo-Optical Instrumentation Engineers (SPIE) Conference Series*, page 91482Z, Aug. 2014.

[354] K. R. Stapelfeldt. Extrasolar planets and star formation: science opportunities for future ELTs. In P. Whitelock, M. Dennefeld, and B. Leibundgut, editors, *The Scientific Requirements for Extremely Large Telescopes*, volume 232, pages 149–158, Jan. 2006.

[355] K. G. Stassun, R. J. Oelkers, M. Paegert, G. Torres, J. Pepper, N. De Lee, K. Collins, D. W. Latham, P. S. Muirhead, J. Chittidi, B. Rojas-Ayala, S. W. Fleming, M. E. Rose, P. Tenenbaum, E. B. Ting, S. R. Kane, T. Barclay, J. L. Bean, C. E. Brassuer, D. Charbonneau, J. Ge, J. J. Lissauer, A. W. Mann, B. McLean, S. Mullally, N. Narita,

P. Plavchan, G. R. Ricker, D. Sasselov, S. Seager, S. Sharma, B. Shiao, A. Sozzetti, D. Stello, R. Vanderspek, G. Wallace, and J. N. Winn. The Revised TESS Input Catalog and Candidate Target List. *Astronomical Journal*, 158(4):138, Oct. 2019.

[356] K. G. Stassun, R. J. Oelkers, J. Pepper, M. Paegert, N. De Lee, G. Torres, D. W. Latham, S. Charpinet, C. D. Dressing, D. Huber, S. R. Kane, S. Lépine, A. Mann, P. S. Muirhead, B. Rojas-Ayala, R. Silvotti, S. W. Fleming, A. Levine, and P. Plavchan. The TESS Input Catalog and Candidate Target List. *Astronomical Journal*, 156(3):102, Sept. 2018.

[357] G. Stefánsson, C. Cañas, J. Wisniewski, P. Robertson, S. Mahadevan, M. Maney, S. Kanodia, C. Beard, C. F. Bender, P. Brunt, J. C. Clemens, W. Cochran, S. A. Diddams, M. Endl, E. B. Ford, C. Fredrick, S. Halverson, F. Hearty, L. Hebb, J. Huehnerhoff, J. Jennings, K. Kaplan, E. Levi, E. Lubar, A. J. Metcalf, A. Monson, B. Morris, J. P. Ninan, C. Nitroy, L. Ramsey, A. Roy, C. Schwab, S. Sigurdsson, R. Terrien, and J. T. Wright. A Sub-Neptune-sized Planet Transiting the M2.5 Dwarf G 9-40: Validation with the Habitable-zone Planet Finder. *Astronomical Journal*, 159(3):100, Mar. 2020.

[358] G. Stefansson, F. Hearty, P. Robertson, S. Mahadevan, T. Anderson, E. Levi, C. Bender, M. Nelson, A. Monson, B. Blank, S. Halverson, C. Henderson, L. Ramsey, A. Roy, C. Schwab, and R. Terrien. A Versatile Technique to Enable Sub-milli-Kelvin Instrument Stability for Precise Radial Velocity Measurements: Tests with the Habitable-zone Planet Finder. *The Astrophysical Journal*, 833(2):175, Dec. 2016.

[359] G. Stefánsson, R. Kopparapu, A. Lin, S. Mahadevan, C. I. Cañas, S. Kanodia, J. P. Ninan, W. D. Cochran, M. Endl, L. Hebb, J. Wisniewski, A. Gupta, M. Everett, C. F. Bender, S. A. Diddams, E. B. Ford, C. Fredrick, S. Halverson, F. Hearty, E. Levi, M. Maney, A. J. Metcalf, A. Monson, L. W. Ramsey, P. Robertson, A. Roy, C. Schwab, R. C. Terrien, and J. T. Wright. A Mini-Neptune and a Radius Valley Planet Orbiting the Nearby M2 Dwarf TOI-1266 in Its Venus Zone: Validation with the Habitable-zone Planet Finder. *Astronomical Journal*, 160(6):259, Dec. 2020.

[360] G. Stefansson, S. Mahadevan, L. Hebb, J. Wisniewski, J. Huehnerhoff, B. Morris, S. Halverson, M. Zhao, J. Wright, J. O'rourke, H. Knutson, S. Hawley, S. Kanodia, Y. Li, L. M. Z. Hagen, L. J. Liu, T. Beatty, C. Bender, P. Robertson, J. Dembicky, C. Gray, W. Ketzeback, R. McMillan, and T. Rudyk. Toward Space-like Photometric Precision from the Ground with Beam-shaping Diffusers. *The Astrophysical Journal*, 848:9, Oct. 2017.

[361] G. Stefánsson, S. Mahadevan, M. Maney, J. P. Ninan, P. Robertson, J. Rajagopal, F. Haase, L. Allen, E. B. Ford, J. Winn, A. Wolfgang, R. I. Dawson, J. Wisniewski, C. F. Bender, C. Cañas, W. Cochran, S. A. Diddams, C. Fredrick, S. Halverson, F. Hearty, L. Hebb, S. Kanodia, E. Levi, A. J. Metcalf, A. Monson, L. Ramsey, A. Roy, C. Schwab, R. Terrien, and J. T. Wright. The Habitable Zone Planet Finder Reveals a High Mass and Low Obliquity for the Young Neptune K2-25b. *Astronomical Journal*, 160(4):192, Oct. 2020.

[362] G. Stefansson, S. Mahadevan, C. Petrovich, J. N. Winn, S. Kanodia, S. C. Millholland, M. Maney, C. I. Cañas, J. Wisniewski, P. Robertson, J. P. Ninan, E. B. Ford, C. F. Bender, C. H. Blake, H. Cegla, W. D. Cochran, S. A. Diddams, J. Dong, M. Endl, C. Fredrick, S. Halverson, F. Hearty, L. Hebb, T. Hirano, A. S. J. Lin, S. E. Logsdon, E. Lubar, M. W. McElwain, A. J. Metcalf, A. Monson, J. Rajagopal, L. W. Ramsey, A. Roy, C. Schwab, H. Schweiker, R. C. Terrien, and J. T. Wright. The Warm Neptune GJ 3470b has a Polar Orbit. *arXiv e-prints*, page arXiv:2111.01295, Nov. 2021.

[363] G. Stefànsson, S. Mahadevan, C. Petrovich, J. N. Winn, S. Kanodia, S. C. Millholland, M. Maney, C. I. Cañas, J. Wisniewski, P. Robertson, J. P. Ninan, E. B. Ford, C. F. Bender, C. H. Blake, H. Cegla, W. D. Cochran, S. A. Diddams, J. Dong, M. Endl, C. Fredrick, S. Halverson, F. Hearty, L. Hebb, T. Hirano, A. S. J. Lin, S. E. Logsdon, E. Lubar, M. W. McElwain, A. J. Metcalf, A. Monson, J. Rajagopal, L. W. Ramsey, A. Roy, C. Schwab, H. Schweiker, R. C. Terrien, and J. T. Wright. The Warm Neptune GJ 3470b Has a Polar Orbit. *The Astrophysical Journal Letters*, 931(2):L15, June 2022.

[364] G. Stefansson, S. Mahadevan, J. Wisniewski, Y. Li, L. Hebb, B. Morris, S. Halverson, A. Monson, and P. Robertson. Extreme precision photometry from the ground with beam-shaping diffusers for K2, TESS, and beyond. In C. J. Evans, L. Simard, and H. Takami, editors, *Ground-based and Airborne Instrumentation for Astronomy VII*, volume 10702, pages 1518 – 1533. International Society for Optics and Photonics, SPIE, 2018.

[365] J. H. Steffen. Sensitivity bias in the mass-radius distribution from transit timing variations and radial velocity measurements. *Monthly Notices of the Royal Astronomical Society*, 457(4):4384–4392, Apr. 2016.

[366] M. C. Stumpe, J. C. Smith, J. E. Van Cleve, J. D. Twicken, T. S. Barclay, M. N. Fanelli, F. R. Girouard, J. M. Jenkins, J. J. Kolodziejczak, S. D. McCauliff, and R. L. Morris. Kepler Presearch Data Conditioning I—Architecture and Algorithms for Error Correction in Kepler Light Curves. *Publications of the Astronomical Society of the Pacific*, 124(919):985, Sept. 2012.

[367] P. A. Sturrock and J. D. Scargle. False-alarm Probability in Relation to Oversampled Power Spectra, with Application to Super-Kamiokande Solar Neutrino Data. *The Astrophysical Journal*, 718(1):527–529, July 2010.

[368] A. Suárez Mascareño, M. Damasso, N. Lodieu, A. Sozzetti, V. J. S. Béjar, S. Benatti, M. R. Zapatero Osorio, G. Micela, R. Rebolo, S. Desidera, F. Murgas, R. Claudi, J. I. González Hernández, L. Malavolta, C. del Burgo, V. D'Orazi, P. J. Amado, D. Locci, H. M. Tabernero, F. Marzari, D. S. Aguado, D. Turrini, C. Cardona Guillén, B. Toledo-Padrón, A. Maggio, J. Aceituno, F. F. Bauer, J. A. Caballero, P. Chinchilla, E. Esparza-Borges, E. González-Álvarez, T. Granzer, R. Luque, E. L. Martín, G. Nowak, M. Oshagh, E. Pallé, H. Parviainen, A. Quirrenbach, A. Reiners, I. Ribas, K. G. Strassmeier, M. Weber, and M. Mallonn. Rapid contraction of giant planets orbiting the 20-million-year-old star V1298 Tau. *Nature Astronomy*, 6:232–240, Dec. 2021.

[369] P. W. Sullivan, J. N. Winn, Z. K. Berta-Thompson, D. Charbonneau, D. Deming, C. D. Dressing, D. W. Latham, A. M. Levine, P. R. McCullough, T. Morton, G. R. Ricker, R. Vanderspek, and D. Woods. The Transiting Exoplanet Survey Satellite: Simulations of Planet Detections and Astrophysical False Positives. *The Astrophysical Journal*, 809(1):77, Aug. 2015.

[370] C. J. F. Ter Braak. A Markov Chain Monte Carlo version of the genetic algorithm Differential Evolution: easy Bayesian computing for real parameter spaces. *Statistics and Computing*, 16(3):239–249, Sept. 2006.

[371] C. Terquem and J. C. B. Papaloizou. Migration and the Formation of Systems of Hot Super-Earths and Neptunes. *The Astrophysical Journal*, 654(2):1110–1120, Jan. 2007.

[372] Theano Development Team. Theano: A Python framework for fast computation of mathematical expressions. *arXiv e-prints*, abs/1605.02688, May 2016.

[373] A. E. L. Thomas, W. J. Chaplin, G. R. Davies, R. Howe, Á. R. G. Santos, Y. Elsworth, A. Miglio, T. Campante, and M. S. Cunha. Asteroseismic constraints on active latitudes of solar-type stars: HD 173701 has active bands at higher latitudes than the Sun. *Monthly Notices of the Royal Astronomical Society*, 485(3):3857–3868, May 2019.

[374] C. G. Tinney, R. P. Butler, G. W. Marcy, H. R. A. Jones, A. J. Penny, C. McCarthy, B. D. Carter, and D. A. Fischer. Three Low-Mass Planets from the Anglo-Australian Planet Search. *The Astrophysical Journal*, 623(2):1171–1179, Apr. 2005.

[375] Q. H. Tran, M. Bedell, D. Foreman-Mackey, and R. Luger. Joint Modeling of Radial Velocities and Photometry with a Gaussian Process Framework. *arXiv e-prints*, page arXiv:2305.00988, May 2023.

[376] R. Trotta. Bayes in the sky: Bayesian inference and model selection in cosmology. *Contemporary Physics*, 49(2):71–104, Mar. 2008.

[377] E. V. Turtelboom, L. M. Weiss, C. D. Dressing, G. Nowak, E. Pallé, C. Beard, S. Blunt, C. Brinkman, A. Chontos, Z. R. Claytor, F. Dai, P. A. Dalba, S. Giacalone, E. Gonzales, C. K. Harada, M. L. Hill, R. Holcomb, J. Korth, J. Lubin, T. Masseron, M. MacDougall, A. W. Mayo, T. Močnik, J. M. Akana Murphy, A. S. Polanski, M. Rice, R. A. Rubenzahl, N. Scarsdale, K. G. Stassun, D. B. Tyler, J. V. Zandt, I. J. M. Crossfield, H. J. Deeg, B. Fulton, D. Gandolfi, A. W. Howard, D. Huber, H. Isaacson, S. R. Kane, K. W. F. Lam, R. Luque, E. L. Martín, G. Morello, J. Orell-Miquel, E. A. Petigura, P. Robertson, A. Roy, V. Van Eylen, D. Baker, A. A. Belinski, A. Bieryla, D. R. Ciardi, K. A. Collins, N. Cutting, D. J. Della-Rose, T. B. Ellingsen, E. Furlan, T. Gan, C. L. Gnilka, P. Guerra, S. B. Howell, M. Jimenez, D. W. Latham, M. Larivière, K. V. Lester, J. Lillo-Box, L. Luker, C. R. Mann, P. P. Plavchan, B. Safonov, B. Skinner, I. A. Strakhov, J. M. Wittrock, D. A. Caldwell, Z. Essack, J. M. Jenkins, E. V. Quintana, G. R. Ricker, R. Vanderspek, S. Seager, and J. N.

Winn. The TESS-Keck Survey. XI. Mass Measurements for Four Transiting Sub-Neptunes Orbiting K Dwarf TOI-1246. *The Astronomical Journal*, 163(6):293, June 2022.

[378] J. D. Twicken, J. M. Jenkins, S. E. Seader, P. Tenenbaum, J. C. Smith, L. S. Brownston, C. J. Burke, J. H. Catanzarite, B. D. Clarke, M. T. Cote, F. R. Girouard, T. C. Klaus, J. Li, S. D. McCauliff, R. L. Morris, B. Wohler, J. R. Campbell, A. Kamal Uddin, K. A. Zamudio, A. Sabale, S. T. Bryson, D. A. Caldwell, J. L. Christiansen, J. L. Coughlin, M. R. Haas, C. E. Henze, D. T. Sanderfer, and S. E. Thompson. Detection of Potential Transit Signals in 17 Quarters of Kepler Data: Results of the Final Kepler Mission Transiting Planet Search (DR25). *The Astronomical Journal*, 152(6):158, Dec. 2016.

[379] D. Valencia, T. Guillot, V. Parmentier, and R. S. Freedman. Bulk Composition of GJ 1214b and Other Sub-Neptune Exoplanets. *The Astrophysical Journal*, 775(1):10, Sept. 2013.

[380] V. Van Eylen, C. Agentoft, M. S. Lundkvist, H. Kjeldsen, J. E. Owen, B. J. Fulton, E. Petigura, and I. Snellen. An asteroseismic view of the radius valley: stripped cores, not born rocky. *Monthly Notices of the Royal Astronomical Society*, 479(4):4786–4795, Oct. 2018.

[381] V. Van Eylen, S. Albrecht, X. Huang, M. G. MacDonald, R. I. Dawson, M. X. Cai, D. Foreman-Mackey, M. S. Lundkvist, V. Silva Aguirre, I. Snellen, and J. N. Winn. The Orbital Eccentricity of Small Planet Systems. *The Astronomical Journal*, 157(2):61, Feb. 2019.

[382] V. Van Eylen, N. Astudillo-Defru, X. Bonfils, J. Livingston, T. Hirano, R. Luque, K. W. F. Lam, A. B. Justesen, J. N. Winn, D. Gandolfi, G. Nowak, E. Palle, S. Albrecht, F. Dai, B. Campos Estrada, J. E. Owen, D. Foreman-Mackey, M. Fridlund, J. Korth, S. Mathur, T. Forveille, T. Mikal-Evans, H. L. M. Osborne, C. S. K. Ho, J. M. Almenara, E. Artigau, O. Barragán, S. C. C. Barros, F. Bouchy, J. Cabrera, D. A. Caldwell, D. Charbonneau, P. Chaturvedi, W. D. Cochran, S. Csizmadia, M. Damasso, X. Delfosse, J. R. De Medeiros, R. F. Díaz, R. Doyon, M. Esposito, G. Fűrész, P. Figueira, I. Georgieva, E. Goffo, S. Grziwa, E. Guenther, A. P. Hatzes, J. M. Jenkins, P. Kabath, E. Knudstrup, D. W. Latham, B. Lavie, C. Lovis, R. E. Mennickent, S. E. Mullally, F. Murgas, N. Narita, F. A. Pepe, C. M. Persson, S. Redfield, G. R. Ricker, N. C. Santos, S. Seager, L. M. Serrano, A. M. S. Smith, A. Suárez Mascareño, J. Subjak, J. D. Twicken, S. Udry, R. Vanderspek, and M. R. Zapatero Osorio. Masses and compositions of three small planets orbiting the nearby M dwarf L231-32 (TOI-270) and the M dwarf radius valley. *Monthly Notices of the Royal Astronomical Society*, 507(2):2154–2173, Oct. 2021.

[383] S. R. Vaughan, T. D. Gebhard, K. Bott, S. L. Casewell, N. B. Cowan, D. S. Doelman, M. Kenworthy, J. Mazoyer, M. A. Millar-Blanchaer, V. J. H. Trees, D. M. Stam, O. Absil, L. Altinier, P. Baudoz, R. Belikov, A. Bidot, J. L. Birkby, M. J. Bonse, B. Brandl, A. Carlotti, E. Choquet, D. van Dam, N. Desai, K. Fogarty, J. Fowler,

K. van Gorkom, Y. Gutierrez, O. Guyon, S. Y. Haffert, O. Herscovici-Schiller, A. Hours, R. Juanola-Parramon, E. Kleisioti, L. König, M. van Kooten, M. Krasteva, I. Laginja, R. Landman, L. Leboulleux, D. Mouillet, M. N'Diaye, E. H. Por, L. Pueyo, and F. Snik. Chasing rainbows and ocean glints: Inner working angle constraints for the Habitable Worlds Observatory. *Monthly Notices of the Royal Astronomical Society*, 524(4):5477–5485, Oct. 2023.

[384] P. Virtanen, R. Gommers, T. E. Oliphant, M. Haberland, T. Reddy, D. Cournapeau, E. Burovski, P. Peterson, W. Weckesser, J. Bright, S. J. van der Walt, M. Brett, J. Wilson, K. J. Millman, N. Mayorov, A. R. J. Nelson, E. Jones, R. Kern, E. Larson, C. J. Carey, İ. Polat, Y. Feng, E. W. Moore, J. VanderPlas, D. Laxalde, J. Perktold, R. Cimrman, I. Henriksen, E. A. Quintero, C. R. Harris, A. M. Archibald, A. H. Ribeiro, F. Pedregosa, P. van Mulbregt, and SciPy 1.0 Contributors. SciPy 1.0: Fundamental Algorithms for Scientific Computing in Python. *Nature Methods*, 17:261–272, 2020.

[385] P. Virtanen, R. Gommers, T. E. Oliphant, M. Haberland, T. Reddy, D. Cournapeau, E. Burovski, P. Peterson, W. Weckesser, J. Bright, S. J. van der Walt, M. Brett, J. Wilson, K. J. Millman, N. Mayorov, A. R. J. Nelson, E. Jones, R. Kern, E. Larson, C. J. Carey, İ. Polat, Y. Feng, E. W. Moore, J. VanderPlas, D. Laxalde, J. Perktold, R. Cimrman, I. Henriksen, E. A. Quintero, C. R. Harris, A. M. Archibald, A. H. Ribeiro, F. Pedregosa, P. van Mulbregt, and SciPy 1.0 Contributors. SciPy 1.0: Fundamental Algorithms for Scientific Computing in Python. *Nature Methods*, 17:261–272, 2020.

[386] S. S. Vogt, S. L. Allen, B. C. Bigelow, L. Bresee, B. Brown, T. Cantrall, A. Conrad, M. Couture, C. Delaney, H. W. Epps, D. Hilyard, D. F. Hilyard, E. Horn, N. Jern, D. Kanto, M. J. Keane, R. I. Kibrick, J. W. Lewis, J. Osborne, G. H. Pardeilhan, T. Pfister, T. Ricketts, L. B. Robinson, R. J. Stover, D. Tucker, J. Ward, and M. Z. Wei. HIRES: the high-resolution echelle spectrometer on the Keck 10-m Telescope. In D. L. Crawford and E. R. Craine, editors, *Instrumentation in Astronomy VIII*, volume 2198 of *Society of Photo-Optical Instrumentation Engineers (SPIE) Conference Series*, page 362, June 1994.

[387] S. S. Vogt, S. L. Allen, B. C. Bigelow, L. Bresee, B. Brown, T. Cantrall, A. Conrad, M. Couture, C. Delaney, H. W. Epps, D. Hilyard, D. F. Hilyard, E. Horn, N. Jern, D. Kanto, M. J. Keane, R. I. Kibrick, J. W. Lewis, J. Osborne, G. H. Pardeilhan, T. Pfister, T. Ricketts, L. B. Robinson, R. J. Stover, D. Tucker, J. Ward, and M. Z. Wei. HIRES: the high-resolution echelle spectrometer on the Keck 10-m Telescope. In D. L. Crawford and E. R. Craine, editors, *Instrumentation in Astronomy VIII*, volume 2198 of *Society of Photo-Optical Instrumentation Engineers (SPIE) Conference Series*, page 362, June 1994.

[388] S. S. Vogt, M. Radovan, R. Kibrick, R. P. Butler, B. Alcott, S. Allen, P. Arriagada, M. Bolte, J. Burt, J. Cabak, K. Chloros, D. Cowley, W. Deich, B. Dupraw, W. Earthman, H. Epps, S. Faber, D. Fischer, E. Gates, D. Hilyard, B. Holden,

K. Johnston, S. Keiser, D. Kanto, M. Katsuki, L. Laiterman, K. Lanclos, G. Laughlin, J. Lewis, C. Lockwood, P. Lynam, G. Marcy, M. McLean, J. Miller, T. Misch, M. Peck, T. Pfister, A. Phillips, E. Rivera, D. Sandford, M. Saylor, R. Stover, M. Thompson, B. Walp, J. Ward, J. Wareham, M. Wei, and C. Wright. APF—The Lick Observatory Automated Planet Finder. *Publications of the Astronomical Society of the Pacific*, 126(938):359, Apr. 2014.

[389] W. C. Waalkes, Z. K. Berta-Thompson, K. A. Collins, A. D. Feinstein, B. M. Tofflemire, B. Rojas-Ayala, M. L. Silverstein, E. Newton, G. R. Ricker, R. Vanderspek, D. W. Latham, S. Seager, J. N. Winn, J. M. Jenkins, J. Christiansen, R. F. Goeke, A. M. Levine, H. P. Osborn, S. A. Rinehart, M. E. Rose, E. B. Ting, J. D. Twicken, K. Barkaoui, J. L. Bean, C. Briceño, D. R. Ciardi, K. I. Collins, D. Conti, T. Gan, M. Gillon, G. Isopi, E. Jehin, E. L. N. Jensen, J. F. Kielkopf, N. Law, F. Mallia, A. W. Mann, B. T. Montet, F. J. Pozuelos, H. Relles, J. E. Libby-Roberts, and C. Ziegler. TOI 122b and TOI 237b: Two Small Warm Planets Orbiting Inactive M Dwarfs Found by TESS. *Astronomical Journal*, 161(1):13, Jan. 2021.

[390] J. J. Wang, S. Ginzburg, B. Ren, N. Wallack, P. Gao, D. Mawet, C. Z. Bond, S. Cetre, P. Wizinowich, R. J. De Rosa, G. Ruane, M. C. Liu, O. Absil, C. Alvarez, C. Baranec, É. Choquet, M. Chun, D. Defrère, J.-R. Delorme, G. Duchêne, P. Forsberg, A. Ghez, O. Guyon, D. N. B. Hall, E. Huby, A. Jolivet, R. Jensen-Clem, N. Jovanovic, M. Karlsson, S. Lilley, K. Matthews, F. Ménard, T. Meshkat, M. Millar-Blanchaer, H. Ngo, G. Orban de Xivry, C. Pinte, S. Ragland, E. Serabyn, E. V. Catalán, J. Wang, E. Wetherell, J. P. Williams, M. Ygouf, and B. Zuckerman. Keck/NIRC2 L'-band Imaging of Jovian-mass Accreting Protoplanets around PDS 70. *The Astronomical Journal*, 159(6):263, June 2020.

[391] S. Wang, D.-H. Wu, T. Barclay, and G. P. Laughlin. Updated Masses for the TRAPPIST-1 Planets. *arXiv e-prints*, page arXiv:1704.04290, Apr. 2017.

[392] L. M. Weiss. *The Masses and Orbital Dynamics of Exoplanets*. PhD thesis, University of California, Berkeley, Jan. 2016.

[393] L. M. Weiss, F. Dai, D. Huber, J. M. Brewer, K. A. Collins, D. R. Ciardi, E. C. Matthews, C. Ziegler, S. B. Howell, N. M. Batalha, I. J. M. Crossfield, C. Dressing, B. Fulton, A. W. Howard, H. Isaacson, S. R. Kane, E. A. Petigura, P. Robertson, A. Roy, R. A. Rubenzahl, J. D. Twicken, Z. R. Claytor, K. G. Stassun, M. G. MacDougall, A. Chontos, S. Giacalone, P. A. Dalba, T. Mocnik, M. L. Hill, C. Beard, J. M. Akana Murphy, L. J. Rosenthal, A. Behmard, J. Van Zandt, J. Lubin, M. R. Kosiarek, M. B. Lund, J. L. Christiansen, R. A. Matson, C. A. Beichman, J. E. Schlieder, E. J. Gonzales, C. Briceño, N. Law, A. W. Mann, K. I. Collins, P. Evans, A. Fukui, E. L. N. Jensen, F. Murgas, N. Narita, E. Palle, H. Parviainen, R. P. Schwarz, T.-G. Tan, J. S. Acton, E. M. Bryant, A. Chaushev, S. Gill, P. Eigmüller, J. Jenkins, G. Ricker, S. Seager, and J. N. Winn. The TESS-Keck Survey. II. An Ultra-short-period Rocky Planet and Its Siblings Transiting the Galactic Thick-disk Star TOI-561. *Astronomical Journal*, 161(2):56, Feb. 2021.

[394] L. M. Weiss, K. M. Deck, E. Sinukoff, E. A. Petigura, E. Agol, E. J. Lee, J. C. Becker, A. W. Howard, H. Isaacson, I. J. M. Crossfield, B. J. Fulton, L. Hirsch, and B. Benneke. New Insights on Planet Formation in WASP-47 from a Simultaneous Analysis of Radial Velocities and Transit Timing Variations. *The Astronomical Journal*, 153(6):265, June 2017.

[395] L. M. Weiss, L. A. Rogers, H. T. Isaacson, E. Agol, G. W. Marcy, J. F. Rowe, D. Kipping, B. J. Fulton, J. J. Lissauer, A. W. Howard, and D. Fabrycky. Revised Masses and Densities of the Planets around Kepler-10. *The Astrophysical Journal*, 819(1):83, Mar. 2016.

[396] R. D. Wells, B. V. Rackham, N. Schanche, R. Petrucci, Y. Gómez Maqueo Chew, B. O. Demory, A. J. Burgasser, R. Burn, F. J. Pozuelos, M. N. Günther, L. Sabin, U. Schroffenegger, M. A. Gómez-Muñoz, K. G. Stassun, V. Van Grootel, S. B. Howell, D. Sebastian, A. H. M. J. Triaud, D. Apai, I. Plauchu-Frayn, C. A. Guerrero, P. F. Guillén, A. Landa, G. Melgoza, F. Montalvo, H. Serrano, H. Riesgo, K. Barkaoui, A. Bixel, A. Burdanov, W. P. Chen, P. Chinchilla, K. A. Collins, T. Daylan, J. de Wit, L. Delrez, M. Dévora-Pajares, J. Dietrich, G. Dransfield, E. Ducrot, M. Fausnaugh, E. Furlan, P. Gabor, T. Gan, L. Garcia, M. Ghachoui, S. Giacalone, A. B. Gibbs, M. Gillon, C. Gnilka, R. Gore, N. Guerrero, T. Henning, K. Hesse, E. Jehin, J. M. Jenkins, D. W. Latham, K. Lester, J. McCormac, C. A. Murray, P. Niraula, P. P. Pedersen, D. Queloz, G. Ricker, D. R. Rodriguez, A. Schroeder, R. P. Schwarz, N. Scott, S. Seager, C. A. Theissen, S. Thompson, M. Timmermans, J. D. Twicken, and J. N. Winn. A large sub-Neptune transiting the thick-disk M4 V TOI-2406. *Astronomy and Astrophysics*, 653:A97, Sept. 2021.

[397] A. Wolszczan and D. A. Frail. A planetary system around the millisecond pulsar PSR1257 + 12. *Nature*, 355(6356):145–147, Jan. 1992.

[398] E. L. Wright, P. R. M. Eisenhardt, A. K. Mainzer, M. E. Ressler, R. M. Cutri, T. Jarrett, J. D. Kirkpatrick, D. Padgett, R. S. McMillan, M. Skrutskie, S. A. Stanford, M. Cohen, R. G. Walker, J. C. Mather, D. Leisawitz, I. Gautier, Thomas N., I. McLean, D. Benford, C. J. Lonsdale, A. Blain, B. Mendez, W. R. Irace, V. Duval, F. Liu, D. Royer, I. Heinrichsen, J. Howard, M. Shannon, M. Kendall, A. L. Walsh, M. Larsen, J. G. Cardon, S. Schick, M. Schwalm, M. Abid, B. Fabinsky, L. Naes, and C.-W. Tsai. The Wide-field Infrared Survey Explorer (WISE): Mission Description and Initial On-orbit Performance. *Astronomical Journal*, 140(6):1868–1881, Dec. 2010.

[399] J. T. Wright and P. Robertson. The Third Workshop on Extremely Precise Radial Velocities: The New Instruments. *Research Notes of the American Astronomical Society*, 1(1):51, Dec. 2017.

[400] H. Wu, J. D. Twicken, P. Tenenbaum, B. D. Clarke, J. Li, E. V. Quintana, C. Allen, H. Chandrasekaran, J. M. Jenkins, D. A. Caldwell, B. Wohler, F. Girouard, S. McCauliff, M. T. Cote, and T. C. Klaus. Data validation in the Kepler Science Operations Center pipeline. In N. M. Radziwill and A. Bridger, editors, *Software*

and Cyberinfrastructure for Astronomy, volume 7740 of *Society of Photo-Optical Instrumentation Engineers (SPIE) Conference Series*, page 774019, July 2010.

[401] G.-Y. Xiao, Y.-J. Liu, H.-Y. Teng, W. Wang, T. D. Brandt, G. Zhao, F. Zhao, M. Zhai, and Q. Gao. The Masses of a Sample of Radial-velocity Exoplanets with Astrometric Measurements. *Research in Astronomy and Astrophysics*, 23(5):055022, May 2023.

[402] S. W. Yee, E. A. Petigura, and K. von Braun. Precision Stellar Characterization of FGKM Stars using an Empirical Spectral Library. *The Astrophysical Journal*, 836(1):77, Feb. 2017.

[403] X. Yu, C. He, X. Zhang, S. M. Hörst, A. H. Dymont, P. McGuiggan, J. I. Moses, N. K. Lewis, J. J. Fortney, P. Gao, E. M. R. Kempton, S. E. Moran, C. V. Morley, D. Powell, J. A. Valenti, and V. Vuitton. Haze evolution in temperate exoplanet atmospheres through surface energy measurements. *Nature Astronomy*, 5:822–831, July 2021.

[404] M. Zechmeister and M. Kürster. The generalised Lomb-Scargle periodogram. A new formalism for the floating-mean and Keplerian periodograms. *Astronomy and Astrophysics*, 496(2):577–584, Mar. 2009.

[405] M. Zechmeister, A. Reiners, P. J. Amado, M. Azzaro, F. F. Bauer, V. J. S. Béjar, J. A. Caballero, E. W. Guenther, H. J. Hagen, S. V. Jeffers, A. Kaminski, M. Kürster, R. Launhardt, D. Montes, J. C. Morales, A. Quirrenbach, S. Reffert, I. Ribas, W. Seifert, L. Tal-Or, and V. Wolthoff. Spectrum radial velocity analyser (SERVAL). High-precision radial velocities and two alternative spectral indicators. *Astronomy and Astrophysics*, 609:A12, Jan. 2018.

[406] L. Zeng, S. B. Jacobsen, D. D. Sasselov, M. I. Petaev, A. Vanderburg, M. Lopez-Morales, J. Perez-Mercader, T. R. Mattsson, G. Li, M. Z. Heising, A. S. Bonomo, M. Damasso, T. A. Berger, H. Cao, A. Levi, and R. D. Wordsworth. Growth model interpretation of planet size distribution. *Proceedings of the National Academy of Science*, 116(20):9723–9728, May 2019.

[407] Z. Zhang, M. C. Liu, Z. R. Claytor, W. M. J. Best, T. J. Dupuy, and R. J. Siverd. The Second Discovery from the COCONUTS Program: A Cold Wide-orbit Exoplanet around a Young Field M Dwarf at 10.9 pc. *The Astrophysical Journal Letters*, 916(2):L11, Aug. 2021.

[408] S. Zieba, L. Kreidberg, E. Ducrot, M. Gillon, C. Morley, L. Schaefer, P. Tamburo, D. D. B. Koll, X. Lyu, L. Acuña, E. Agol, A. R. Iyer, R. Hu, A. P. Lincowski, V. S. Meadows, F. Selsis, E. Bolmont, A. M. Mandell, and G. Suissa. No thick carbon dioxide atmosphere on the rocky exoplanet TRAPPIST-1 c. *Nature*, 620(7975):746–749, Aug. 2023.

Appendix A

Appendix for Chapter 2

A.1 Periodograms of Photometry and Activity Indicators for TOI-2136

Due to the possibility of activity interfering with our RV measurements of TOI-2136, we include plots of several activity indicators, as well as ZTF and ASAS-SN photometry. While these data are mostly uninformative, we include them here for completeness.

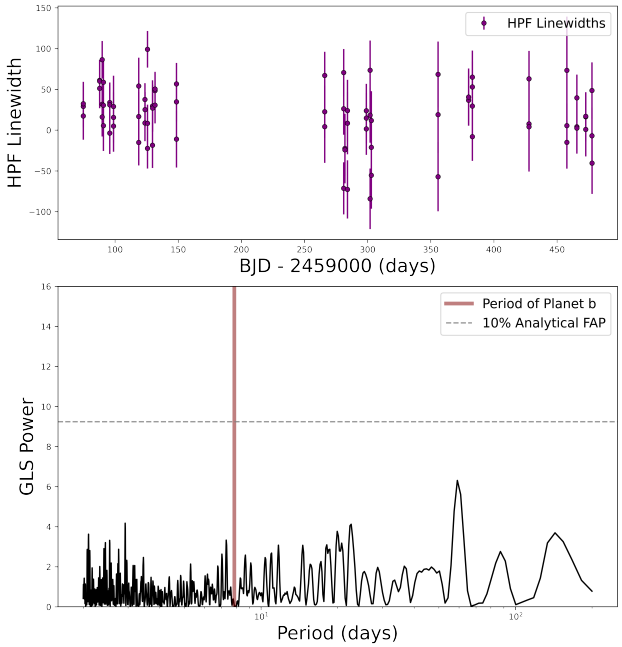

Figure A.1: Top: Scatterplot of HPF linewidths for TOI-2136. Bottom: GLS periodogram of TOI-2136 linewidths, with the period of planet b highlighted in red. Periodicities in linewidths can represent stellar variability, though we detect no significant periodicities in the HPF linewidths.

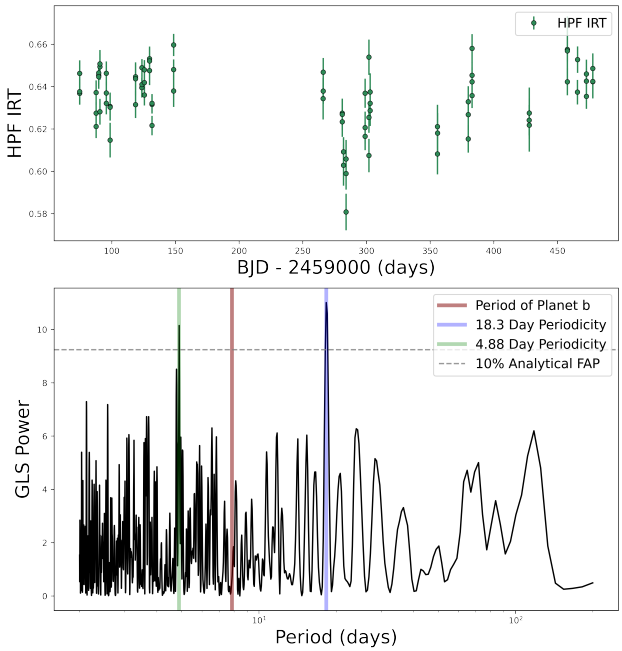

Figure A.2: Top: Scatterplot of the measured flux of the Calcium Infrared Triplet (Ca IRT) of TOI-2136, taken with HPF. Bottom: GLS periodogram of the data. We detect marginally strong periodicities at 4.88 days and 18.3 days, though neither seems related to the planet period, or the rotation period of the system.

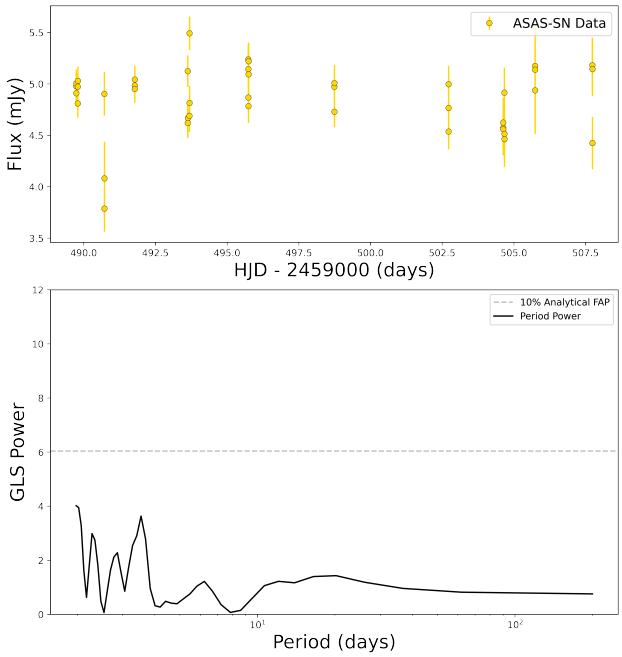

Figure A.3: Top: Flux data of TOI-2136 taken using ASAS-SN [217]. Bottom: GLS periodogram of the data. We detect no significant periodicities.

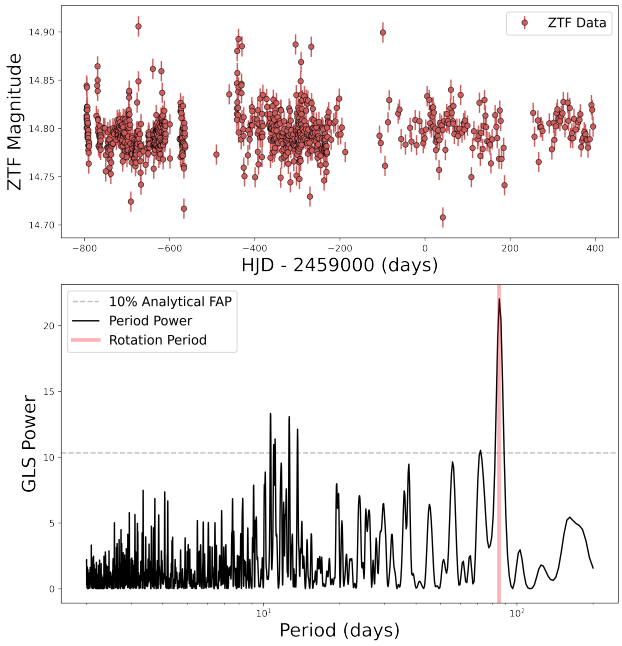

Figure A.4: Top: Photometric data taken using ZTF [267], after it has been sigma clipped for outliers. Bottom: GLS periodogram of the data. We detect a signifcant period at ~ 85 days which is probably associated with the rotation of the system.

Appendix B

Appendix for Chapter 3

We include a corner plot of a few of our model parameters in Figure B.1.

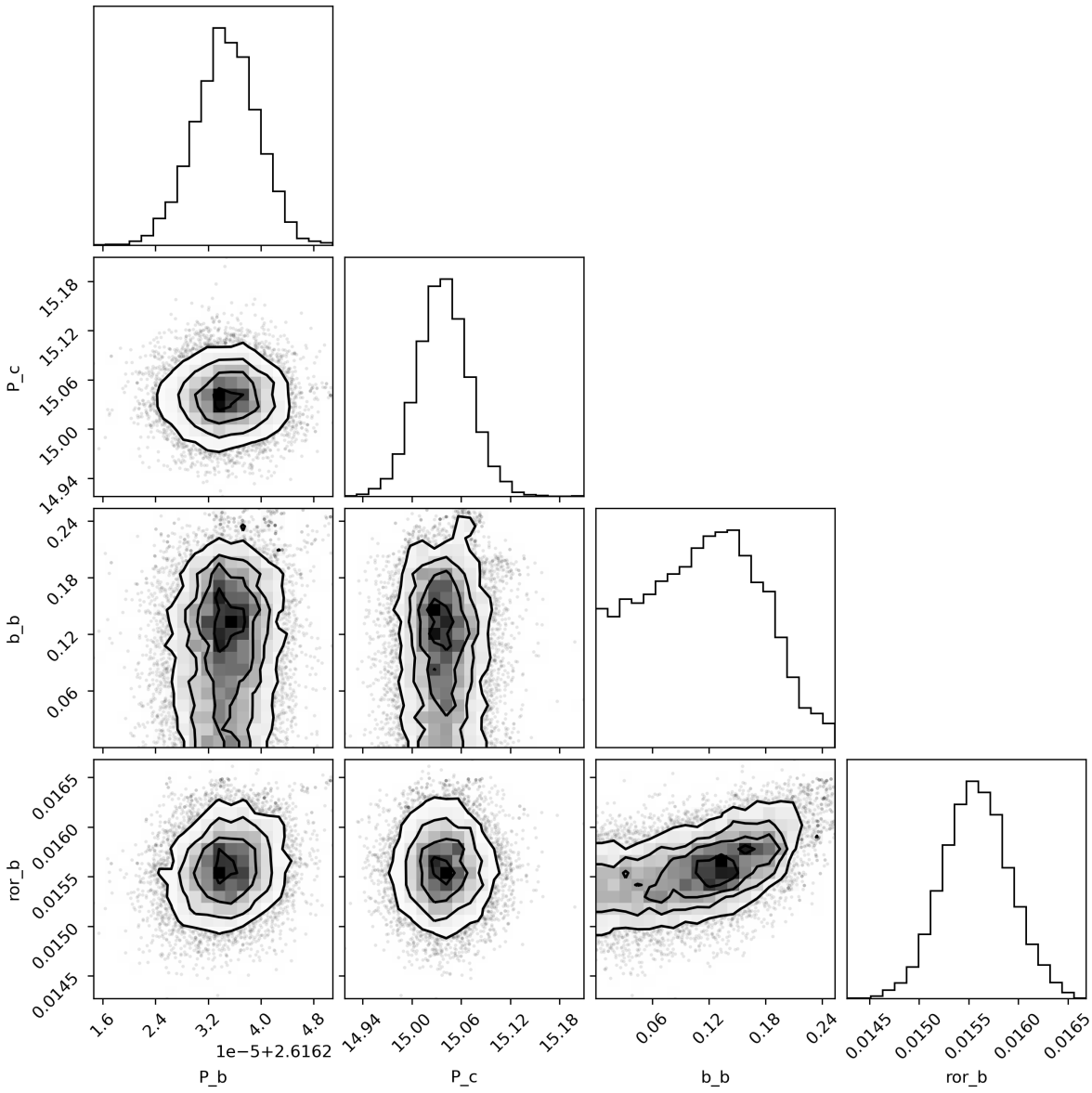

Figure B.1: We include a corner plot of a few key parameters generated during our joint fit. At the top of each column is a histogram of each parameter's values during the MCMC process, marginalized over other parameters.

Appendix C

Appendix for Chapter 4

We include a number of additional tables and figures in the appendix that may be of interest.

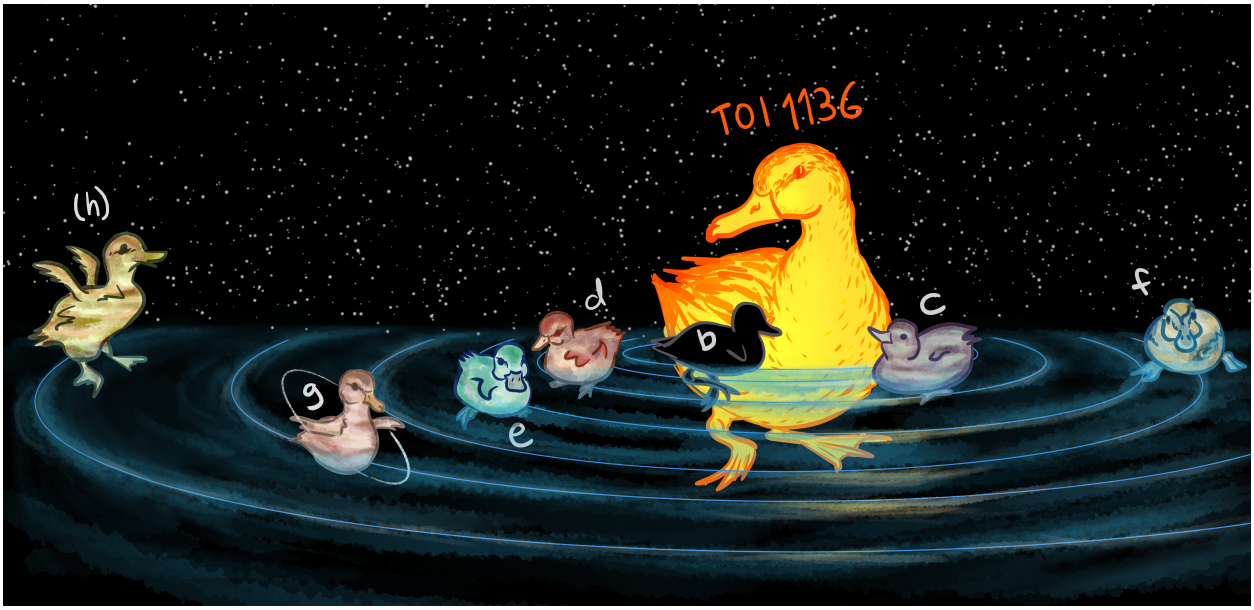

Figure C.1: Here we present an amusing rendition of the TOI-1136 system if each body in the system were a duck or duckling, created by co-author Rae Holcomb. We encourage any future promotions of work associated with TOI-1136 to use this graphic at their leisure.

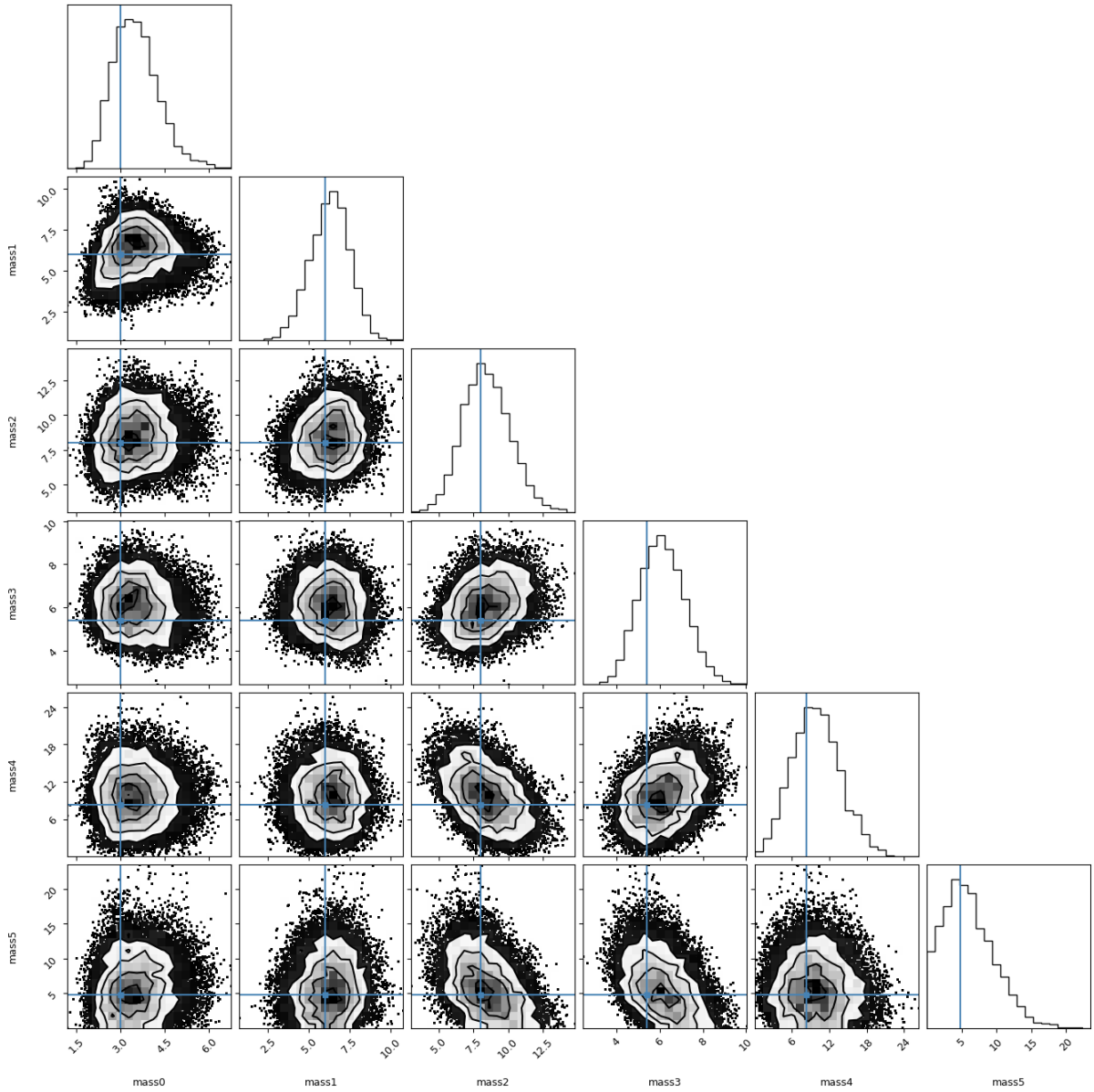

Figure C.2: Corner plot highlighting the mass fits to each planet in our adopted model. Blue lines indicate the value reported in D23.

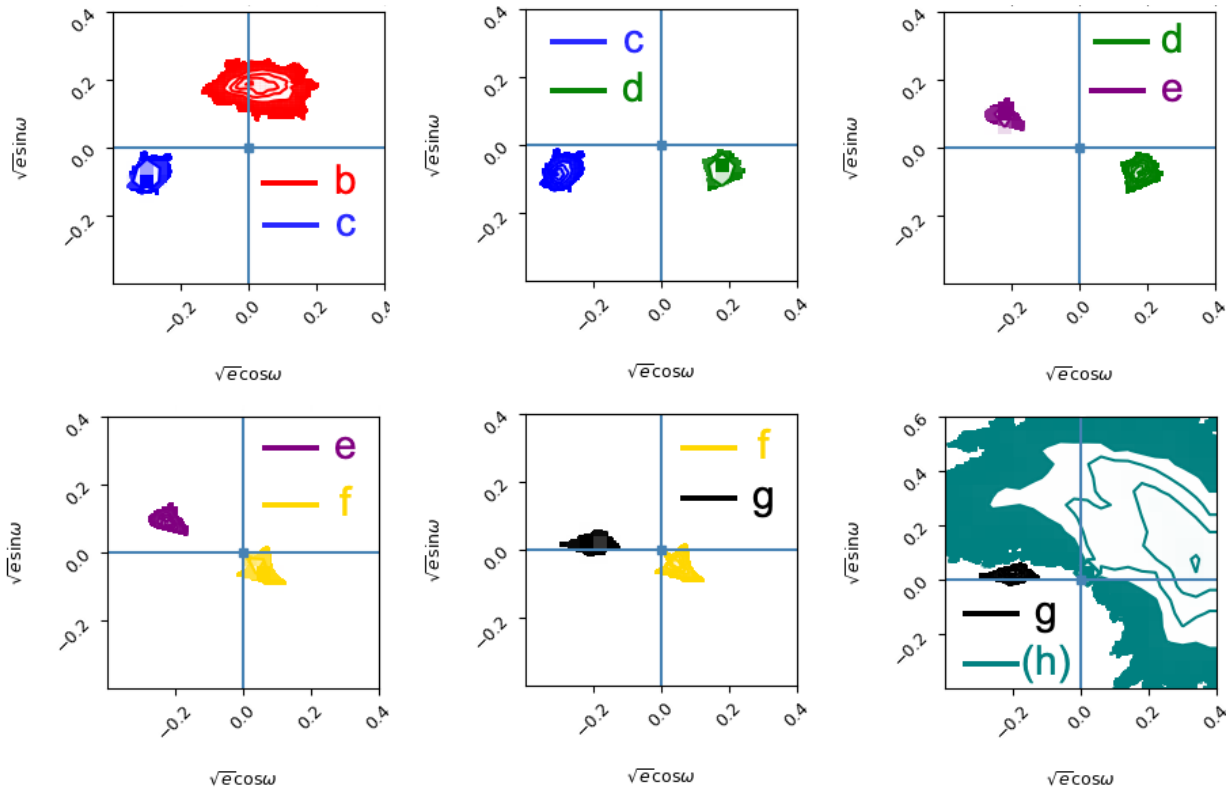

Figure C.3: We include comparisons of the $\sqrt{e}\cos\omega$ and $\sqrt{e}\sin\omega$ posteriors for each planet in the system. [34] predict that the argument of periastrons of neighboring planets should be anti-aligned when in resonance. Planets in the TOI-1136 system seem to generally follow this principle, a strong indicator that the system experienced Type-I migration.

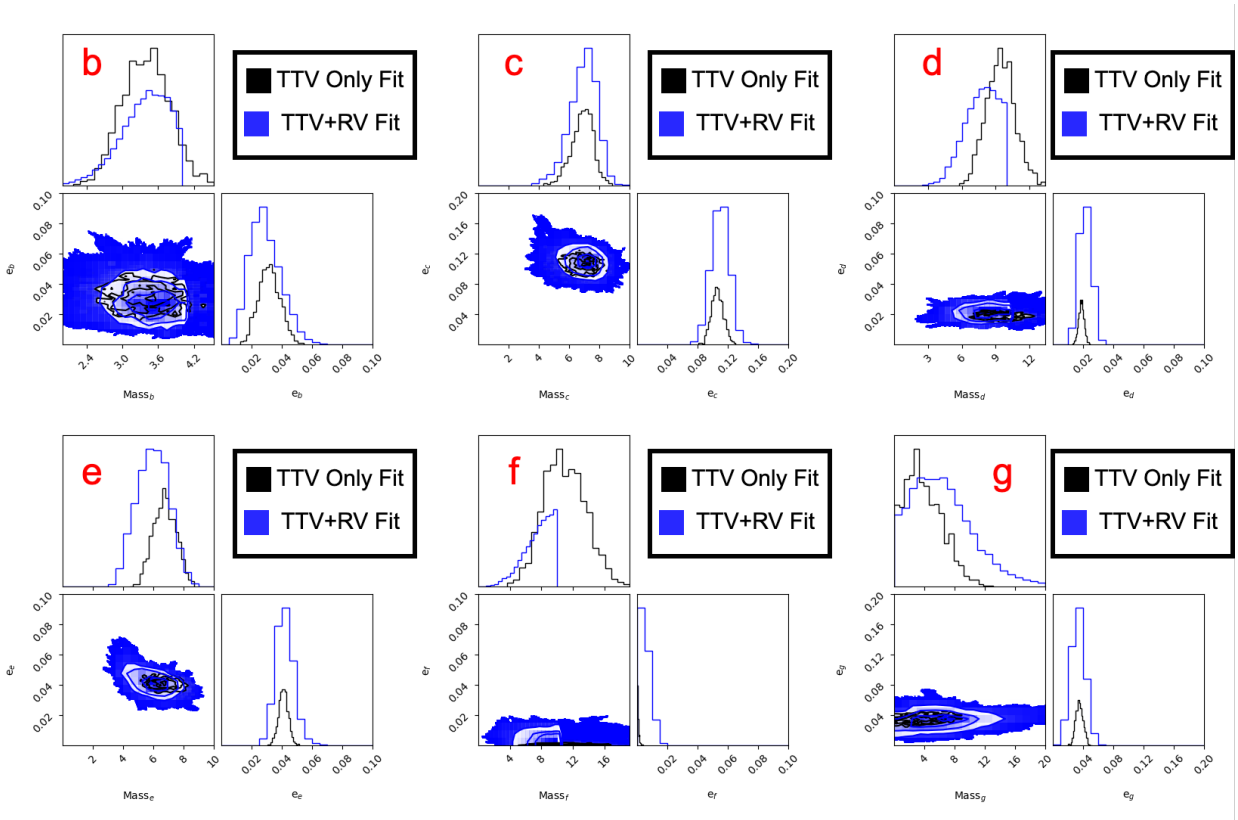

Figure C.4: A comparison of the posterior samples for mass and eccentricity of a TTV-only 6 planet fit, to our TTV + RV + GP 6 planet fit. The TTV-only posteriors are more precise in most cases, indicating that improved posterior estimates in our model are not necessarily due to inclusion of RVs, but may also be sampler-dependent.

Appendix D

Appendix for Chapter 6

We include summary plots for each of our targets.

Kepler-21

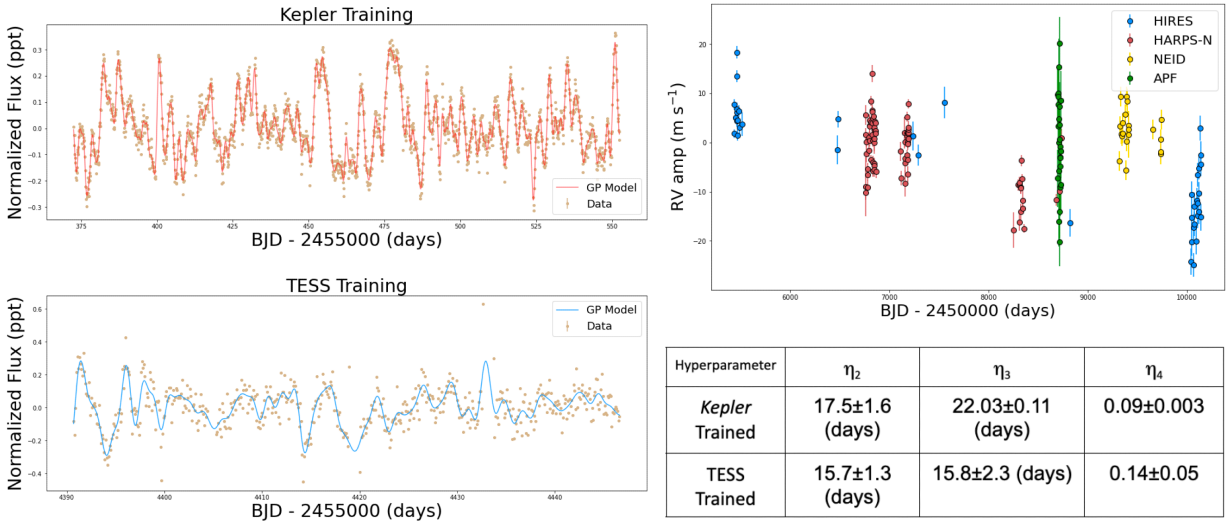

Hyperparameter	η_2	η_3	η_4
Kepler Trained	17.5±1.6 (days)	22.03±0.11 (days)	0.09±0.003
TESS Trained	15.7±1.3 (days)	15.8±2.3 (days)	0.14±0.05

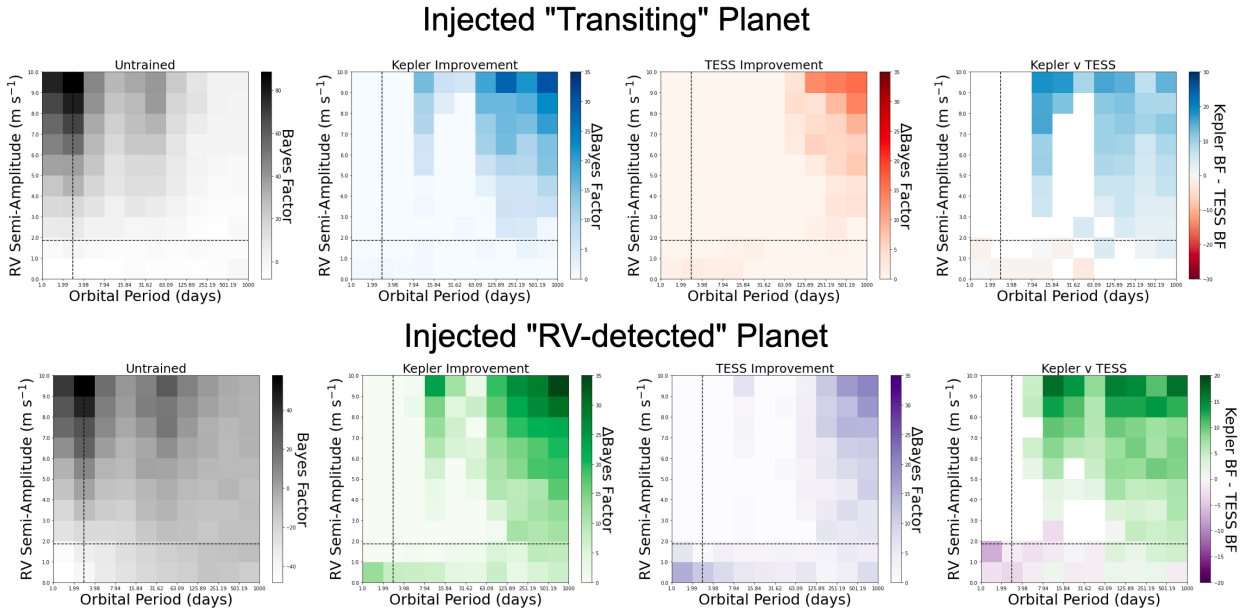

Figure D.1: We include a variety of plots summarizing our training and analysis of Kepler-21. Top Left: Kepler and TESS training data, as well as our best fit GP model overlaid. Top Right: RV time series and training posteriors. Bottom: Results of our injection-recovery analysis in the two cases described in §6.4. The left plots show the preference for models including the injected planet when no GP training is applied. The middle two plots show the improvements gained when training on Kepler or TESS. The rightmost plots highlight the differences between Kepler and TESS training.

Kepler-37

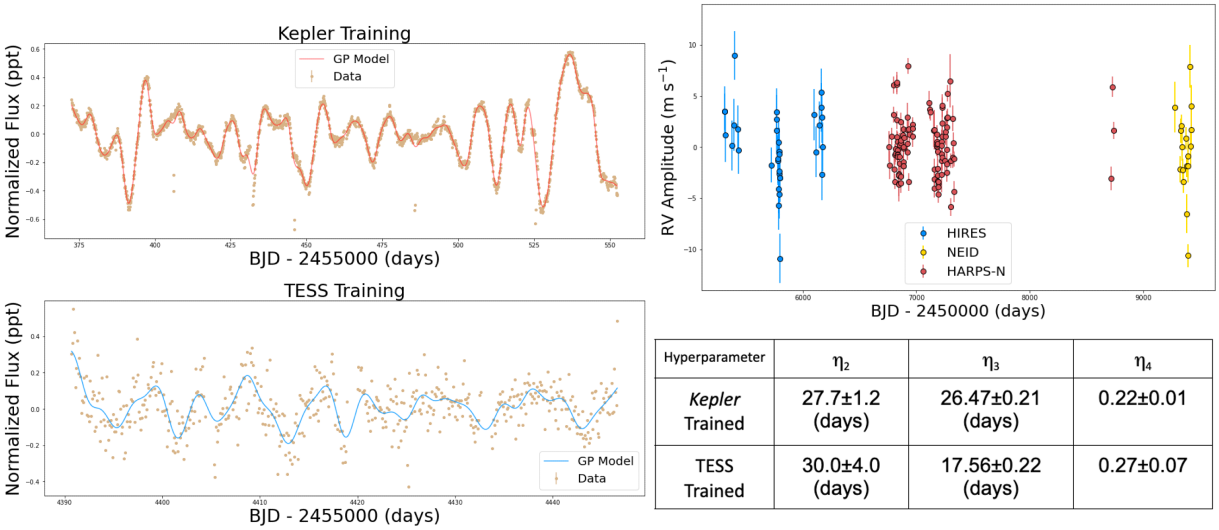

Hyperparameter	η_2	η_3	η_4
Kepler Trained	27.7±1.2 (days)	26.47±0.21 (days)	0.22±0.01
TESS Trained	30.0±4.0 (days)	17.56±0.22 (days)	0.27±0.07

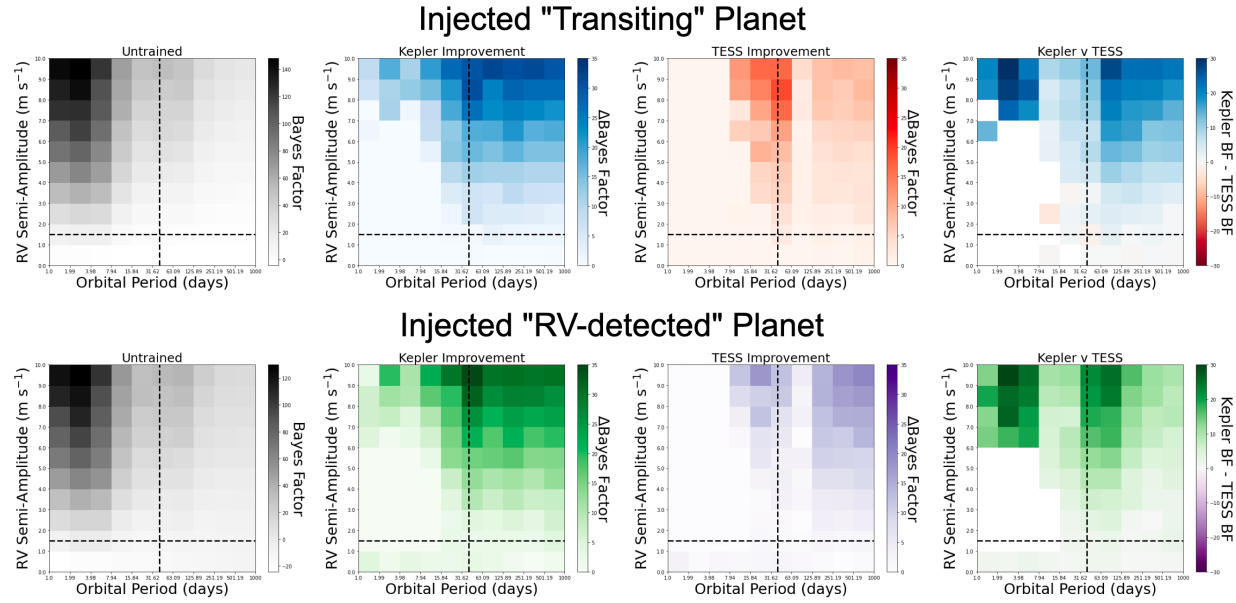

Figure D.2: We include a variety of plots summarizing our training and analysis of Kepler-37. Top Left: Kepler and TESS training data, as well as our best fit GP model overlaid. Top Right: RV time series and training posteriors. Bottom: Results of our injection-recovery analysis in the two cases described in §6.4. The left plots show the preference for models including the injected planet when no GP training is applied. The middle two plots show the improvements gained when training on Kepler or TESS. The rightmost plots highlight the differences between Kepler and TESS trainnig.

HD 4256

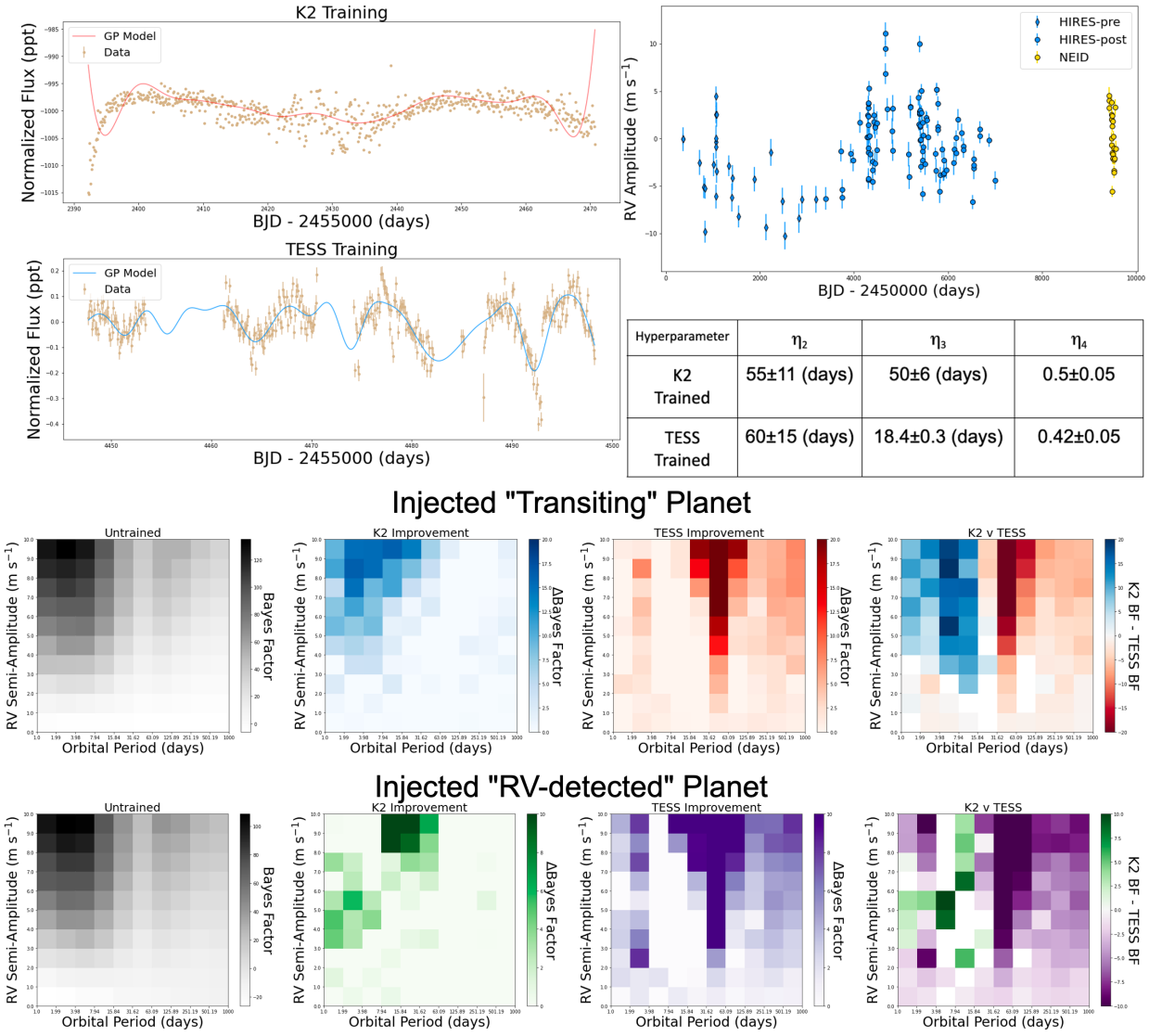

Hyperparameter	η_2	η_3	η_4
K2 Trained	55±11 (days)	50±6 (days)	0.5±0.05
TESS Trained	60±15 (days)	18.4±0.3 (days)	0.42±0.05

Figure D.3: We include a variety of plots summarizing our training and analysis of HD 4256. Top Left: K2 and TESS training data, as well as our best fit GP model overlaid. Top Right: RV time series and training posteriors. Bottom: Results of our injection-recovery analysis in the two cases described in §6.4. The left plots show the preference for models including the injected planet when no GP training is applied. The middle two plots show the improvements gained when training on K2 or TESS. The rightmost plots highlight the differences between Kepler and TESS training.

HD 31966

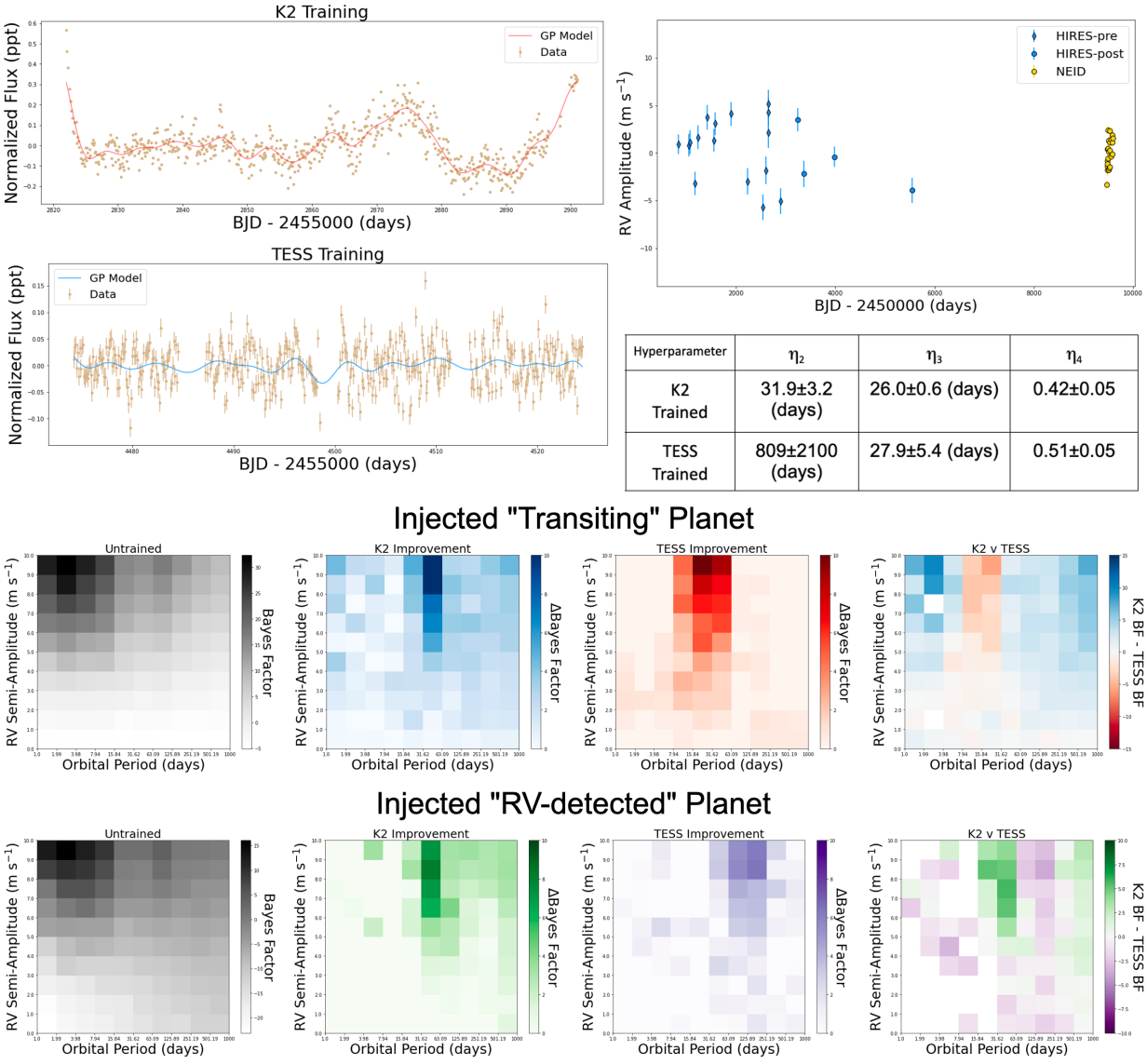

Hyperparameter	η_2	η_3	η_4
K2 Trained	31.9±3.2 (days)	26.0±0.6 (days)	0.42±0.05
TESS Trained	809±2100 (days)	27.9±5.4 (days)	0.51±0.05

Figure D.4: We include a variety of plots summarizing our training and analysis of HD 31966. Top Left: K2 and TESS training data, as well as our best fit GP model overlaid. Top Right: RV time series and training posteriors. Bottom: Results of our injection-recovery analysis in the two cases described in §6.4. The left plots show the preference for models including the injected planet when no GP training is applied. The middle two plots show the improvements gained when training on K2 or TESS. The rightmost plots highlight the differences between Kepler and TESS training.

HD 24040

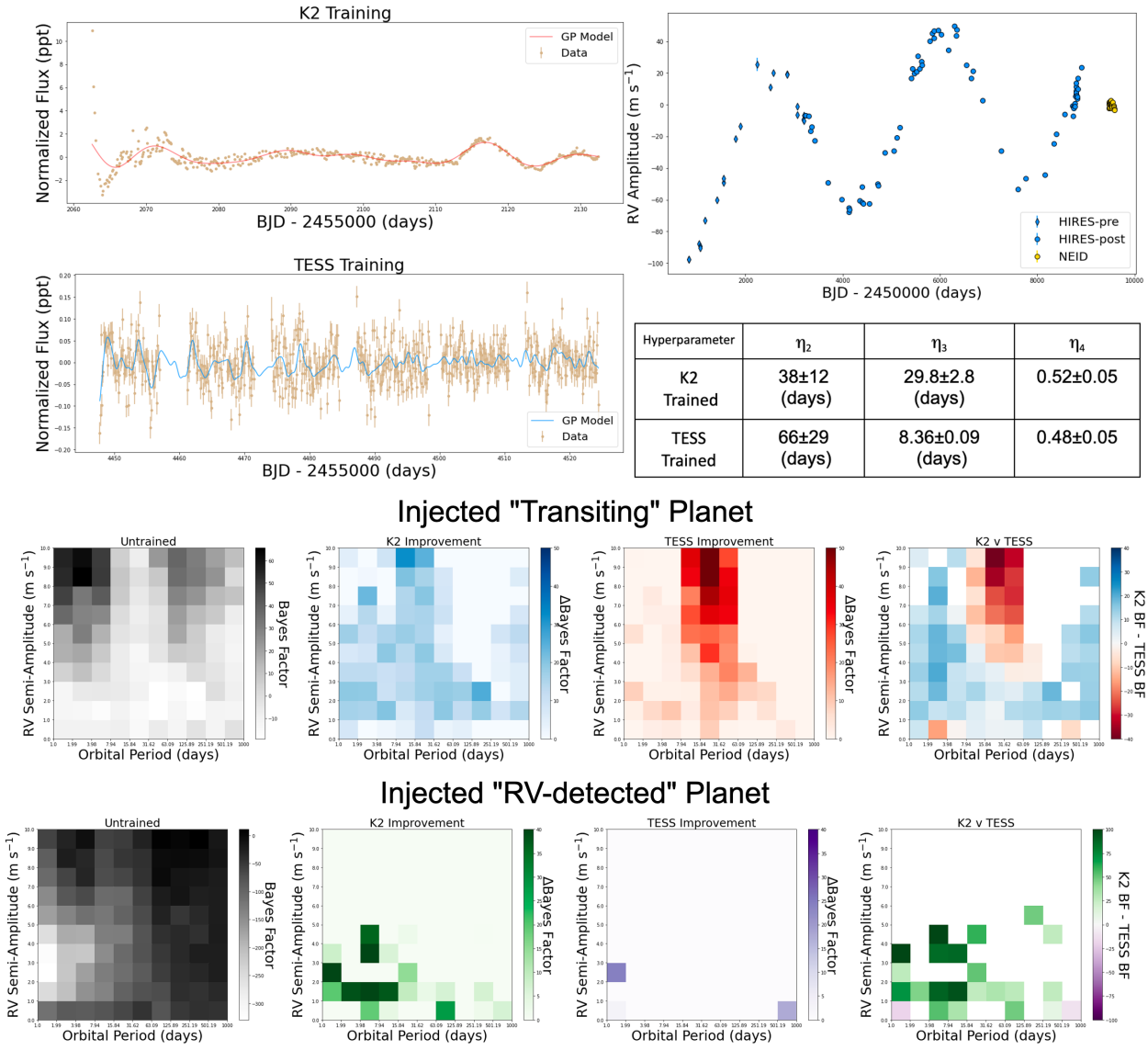

Hyperparameter	η_2	η_3	η_4
K2 Trained	38±12 (days)	29.8±2.8 (days)	0.52±0.05
TESS Trained	66±29 (days)	8.36±0.09 (days)	0.48±0.05

Figure D.5: We include a variety of plots summarizing our training and analysis of HD 24040. Top Left: K2 and TESS training data, as well as our best fit GP model overlaid. Top Right: RV time series and training posteriors. Bottom: Results of our injection-recovery analysis in the two cases described in §6.4. The left plots show the preference for models including the injected planet when no GP training is applied. The middle two plots show the improvements gained when training on K2 or TESS. The rightmost plots highlight the differences between Kepler and TESS training.

HD 106315

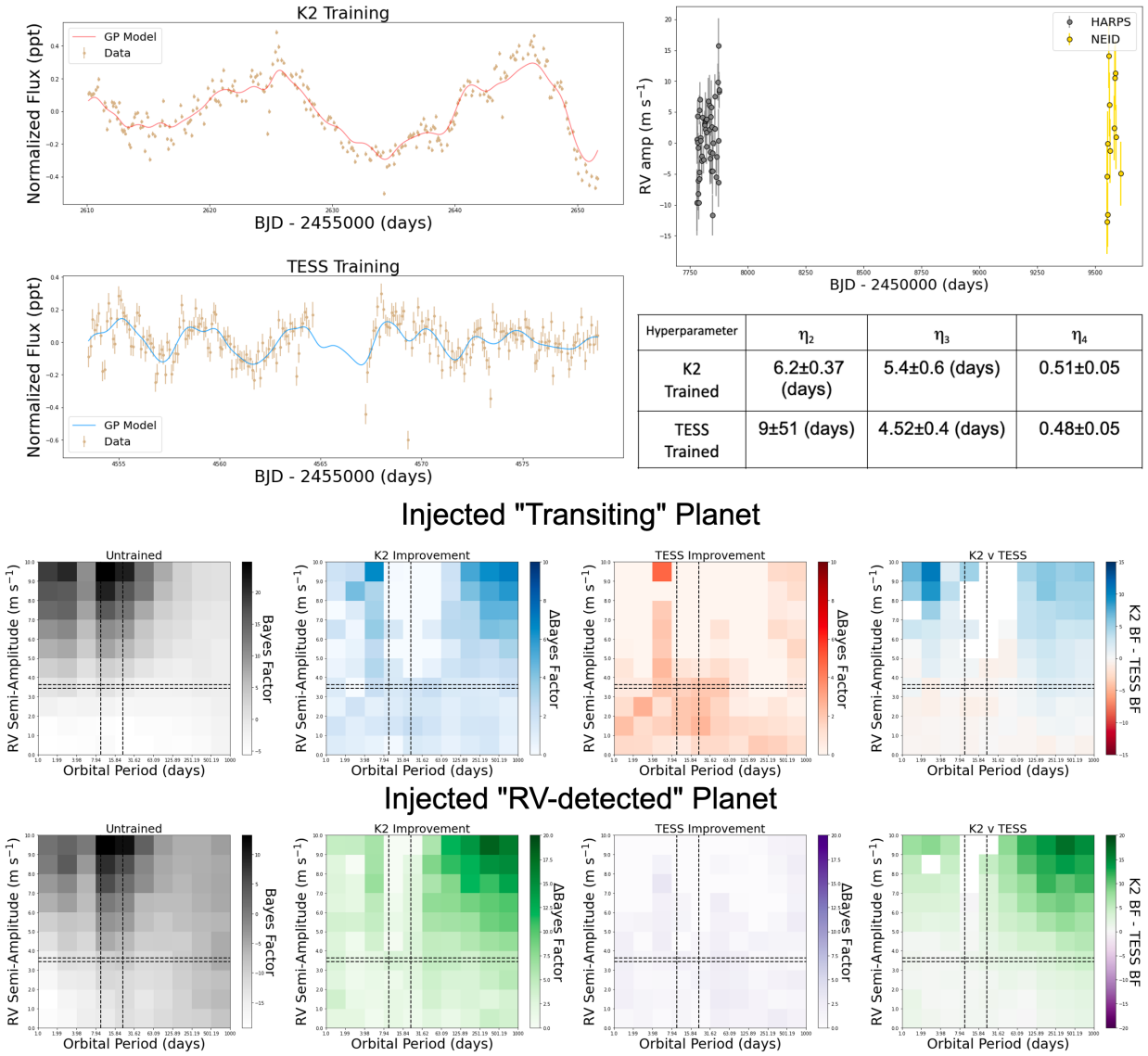

Hyperparameter	η_2	η_3	η_4
K2 Trained	6.2±0.37 (days)	5.4±0.6 (days)	0.51±0.05
TESS Trained	9±51 (days)	4.52±0.4 (days)	0.48±0.05

Figure D.6: We include a variety of plots summarizing our training and analysis of HD 106315. Top Left: K2 and TESS training data, as well as our best fit GP model overlaid. Top Right: RV time series and training posteriors. Bottom: Results of our injection-recovery analysis in the two cases described in §6.4. The left plots show the preference for models including the injected planet when no GP training is applied. The middle two plots show the improvements gained when training on K2 or TESS. The rightmost plots highlight the differences between Kepler and TESS training.

HD 119291

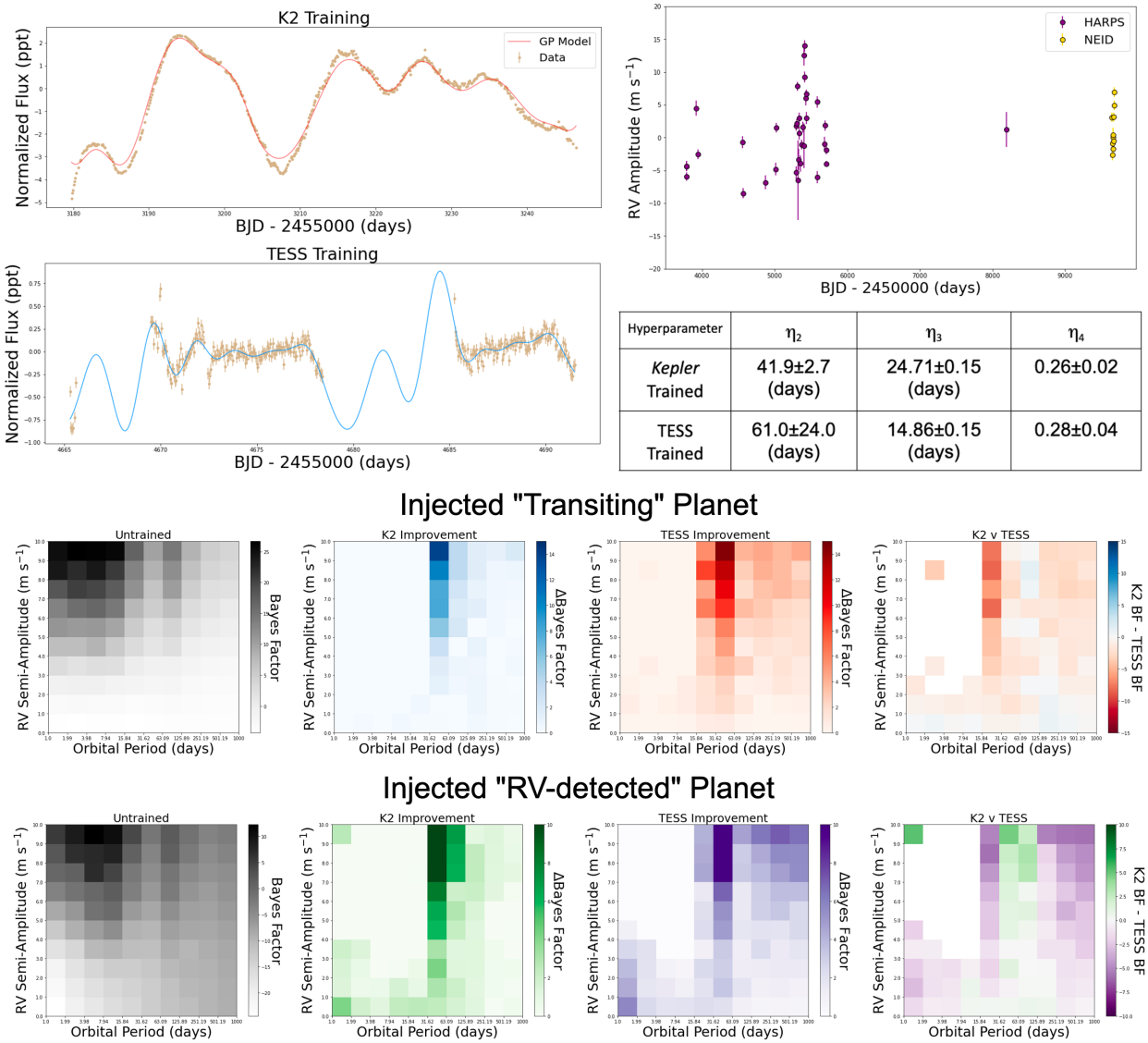

Hyperparameter	η_2	η_3	η_4
Kepler Trained	41.9±2.7 (days)	24.71±0.15 (days)	0.26±0.02
TESS Trained	61.0±24.0 (days)	14.86±0.15 (days)	0.28±0.04

Figure D.7: We include a variety of plots summarizing our training and analysis of HD 119291. Top Left: K2 and TESS training data, as well as our best fit GP model overlaid. Top Right: RV time series and training posteriors. Bottom: Results of our injection-recovery analysis in the two cases described in §6.4. The left plots show the preference for models including the injected planet when no GP training is applied. The middle two plots show the improvements gained when training on K2 or TESS. The rightmost plots highlight the differences between Kepler and TESS training.